Université de Paris XI-Orsay
Habilitation à diriger des Recherches

Études de la plasticité des solides cristallins par dynamique des dislocations à l'échelle mésoscopique

par

Benoit Devincre

Mémoire soutenu le 20/06/2005

devant le Jury composé de :

Prof. M. Condat (Rapporteur)
Dr. J. Rabier (Rapporteur)
Prof. A. Zaoui (Rapporteur)
Dr. T. Khan (Président)
Dr. J. Gil Sevillano (Examinateur)
Dr. L. Kubin (Examinateur)

Table des matières

Première partie .

Mémoire Scientifique

CHAPITRE 1

Introduction

1.1. Simulations multi-échelles

Au cours des dix dernières années, la recherche en sciences des matériaux a été le lieu d'émergence d'une nouvelle forme d'activité scientifique appelée *modélisation multiéchelles*. Un parcours rapide de la littérature montre que la finalité de cette nouvelle thématique est bien définie dans son principe. Il s'agit d'établir un lien entre d'une part notre compréhension d'un ou plusieurs phénomènes physiques élémentaires à l'échelle microscopique et d'autre part, au niveau macroscopique, un comportement bien caractérisé mais souvent mal compris.

L'étude de la déformation plastique des matériaux cristallins constitue une des problématiques où l'apport des modélisations multiéchelles, et plus particulièrement des simulations mésoscopiques, s'avère essentiel [1, 2, 3]. En effet, des divergences ou incompréhensions demeurent entre approches microscopiques (physiques) et macroscopiques (mécaniques) de ce phénomène important.

- Les modèles microscopiques sont souvent limités aux seuls aspects atomiques, liés à la structure de coeur des dislocations. Ils ne sont pas intégrés à plus grande échelle et il est difficile d'en tirer des prédictions sur le comportement global du matériau.
- Les modèles macroscopiques s'appuient sur la mécanique des milieux continus qui, certes, fournit aux ingénieurs une description quantitative, mais reste souvent phénoménologique et ne contenant pas les longueurs d'échelle associées aux aspects microstructuraux.

L'idée qu'une unification 'micro-macro' de la plasticité doit venir d'investigations aux échelles intermédiaires a été mise en évidence par de nombreux travaux dans les années 1970. Pour comprendre la plasticité d'un matériau cristallin, il faut être capable de prendre en compte simultanément certains détails importants de la nature discrète des dislocations (par exemple l'influence de la structure de coeur) et en même temps pouvoir considérer des éléments de volume suffisamment grands pour satisfaire les conditions d'existence d'un volume élémentaire représentatif tel que défini en mécanique des milieux continus. Bien que ce constat ait été effectué il y a plus de trente ans, l'étude formelle et précise de la plasticité, à l'échelle mésoscopique et dans le cadre d'un problématique multiéchelles, n'a réellement débuté que depuis une dizaine d'années. Ce retard peut s'expliquer de différentes manières. On cite souvent l'accroissement de la puissance de calcul comme étant à l'origine du développement des méthodes numériques. Nous y reviendrons, mais il ne faut pas non plus négliger l'évolution des techniques expérimentales et de la modélisation.

Au niveau microstructural ou microscopique, l'observation des dislocations et l'étude de leurs propriétés, s'est souvent limitée à la microscopie électronique en transmission (MET). La recherche s'est

progressivement focalisée sur l'étude du comportement des dislocations isolées, *post mortem* ou *in situ*, au détriment de leurs propriétés collectives. Parallèlement, les méthodes d'investigation de la mécanique du solide, de même que ses formalismes continus, ne permettaient pas d'aborder les aspects discrets de la déformation plastique. Cela a favorisé le développement de modèles mathématiquement cohérents, mais faisant souvent abstraction des connaissances les plus élémentaires issues de la théorie des dislocations.

Il est utile de rappeler que si la *dynamique des fluides* peut être traitée rigoureusement en résolvant un système d'équations différentielles, l'écoulement plastique ne peut pas se décrire par un formalisme équivalent. La plasticité des matériaux cristallins est un phénomène fortement dissipatif, souvent éloigné de l'équilibre thermodynamique et faisant intervenir conjointement des propriétés locales et des propriétés à longue distance. C'est donc un phénomène complexe, difficile à formaliser sur le plan théorique. De ce point de vue, les années 1970-1980 furent une période riche en propositions, mais sans réel aboutissement.

Depuis une quinzaine d'années, une nouvelle dynamique de recherche s'est établie. Les études expérimentales en métallurgie physique font appel à de nouveaux outils d'investigation comme la microscopie à effet de champ, la nano-indentation, la topographie X utilisant le rayonnement synchrotron, etc. Ces outils permettent de diversifier les échelles d'observation, de la plus petite à la plus grande. Par ailleurs, pour étudier finement les hétérogénéités de la déformation plastique, les mécaniciens font appel à des techniques de mesures de plus en plus fines, extensomètrie Laser, micro-grilles avec analyse d'images, microscopie à balayage couplée à l'analyse des électrons rétrodiffusés (MEB-EBSD), etc. Bien sûr, lorsqu'on arrive aux dimensions micrométriques et submicrométriques, la nature discrète de la déformation plastique ne peut plus être ignorée.

D'un point de vue théorique, beaucoup de choses ont également évolué et de nouveaux formalismes sont apparus. Il s'agit principalement de modèles mathématiques s'appuyant sur des concepts issus de la mécanique statistique et de l'analyse non linéaire [4, 5, 6, 7, 8, 9, 10, 11, 12]. De plus, une tendance forte de ces dernières années consiste à prendre en compte les spécificités microstructurales de chaque matériau. Cette évolution suppose que l'on reformule les lois constitutives de la plasticité pour y inclure l'influence d'une ou plusieurs longueurs caractéristiques et de paramètres physiques ou géométriques spécifiques, en plus des constantes élastiques [13, 14, 15, 16].

Plus récemment encore, le regain d'intérêt manifesté dans de nombreux laboratoires pour des problématiques faisant intervenir l'étude de la déformation plastique s'est vu concrétiser par l'émergence de nouveaux programmes de recherches internationaux ambitieux. Ces programmes ont pour objectif principal de prédire les propriétés mécaniques de tel ou tel matériau à partir d'une description remontant les échelles de temps et de longueur à partir du niveau atomique, voire électronique[1]. Une grande diversité de techniques expérimentales ou numériques intervient dans ces programmes, mais on peut remarquer qu'ils ont tous en commun l'utilisation de simulations de la *Dynamique des Dislocations* (DD).

Ainsi, ces simulations sont devenues en quelques années un point de passage obligé pour de nombreux programmes de recherche, car elles permettent d'intégrer de manière réaliste et à l'échelle mésoscopique toute la diversité des propriétés des dislocations rencontrée dans les matériaux. Après avoir identifié les propriétés élémentaires de dislocations par l'expérience ou par des simulations atomiques, ces simulations permettent de tester rapidement certaines hypothèses. Elles permettent aussi de proposer de nouveaux modèles d'après des observations faites '*in silico*' (à l'ordinateur) et dont l'équivalent expérimental serait très difficile, ou impossible, à réaliser.

[1] Par exemple, on peut citer les cas du molybdène dans le cadre du programme américain 'ASCI', du zirconium et des zircaloys dans le cadre du programme européen 'SIRENA', des aciers austénitiques et ferritiques dans le cadre du projet européen 'PERFECT', etc ...

1.2. Modéliser la déformation plastique

L'absence d'une théorie globale de la plasticité s'explique en grande partie par l'étendue des échelles de temps et de longueur mises en jeu : échelle atomique pour les propriétés gouvernées par la structure de coeur, échelle mésoscopique pour les interactions élastiques et les réactions intervenant au sein d'une microstructure, échelle macroscopique pour les contraintes liées à l'état de chargement et qui dépendent des conditions aux limites sur l'élément de volume considéré. Dans cette hiérarchie, nous venons de voir que les simulations mésoscopiques de la DD constituent une étape intermédiaire indispensable dans une approche "multi-échelles" de la plasticité reliant les aspects atomiques aux aspects continus.

Ces dernières années, plusieurs facteurs ont favorisé leur développement :

- D'une part, la progression spectaculaire des simulations atomiques (dynamique et statique moléculaire), et plus récemment des méthodes *ab initio* appliquées à l'étude des propriétés élémentaires de dislocations. Les résultats de ces simulations représentent potentiellement les données d'entrée pour des simulations de DD. L'explosion de la puissance de calcul disponible dans les laboratoires est naturellement à l'origine de cette évolution.
- D'autre part, une évolution toute aussi spectaculaire des modèles issus de la mécanique des milieux continus en vue d'utiliser le formalisme des dislocations soit pour les matériaux de structure, soit pour l'étude des effets de taille et des lois d'échelle en plasticité. L'intérêt récent porté aux matériaux nanostructurés et aux effets de confinement de la déformation plastique sur les propriétés mécaniques est en partie à l'origine de ces développements.
- Enfin, l'échelle spatiale de la DD coïncide avec celle des observations en MET. L'expansion des méthodes d'imagerie (rayonnement synchrotron, imagerie d'orientation ...) permet également d'obtenir des informations quantitatives à des dimensions caractéristiques qui peuvent être comparées directement aux résultats de la DD.

Les connaissances acquises à l'échelle atomique sont essentielles car la structure de coeur des dislocations varie fortement d'un matériau ou d'une classe de matériaux à l'autre, et c'est elle qui détermine en grande partie la mobilité d'une dislocation isolée. Ces connaissances peuvent être facilement incorporées dans des simulations de DD. En effet, il est toujours possible d'augmenter la résolution de ces simulations jusqu'à une échelle de longueur identique à celle des simulations atomiques. On peut alors paramétrer plus facilement les règles de simulation décrivant les propriétés des coeurs. Cette démarche permet, en principe, de reproduire une à une toutes les propriétés élémentaires des dislocations dans un matériau donné. Lorsque cette étape est achevée, les simulations du comportement collectif d'une grande densité de dislocations aux échelles supérieures ont un réel caractère prédictif, car aucune propriété supplémentaire ne doit être ajoutée ou ajustée lors d'un changement d'échelle (les propriétés élastiques ne sont pas ici considérées comme des propriétés ajustables).

Inversement, l'utilisation des simulations de DD à des échelles fines et en ne considérant que des propriétés issues de l'élasticité linéaire permet de quantifier l'influence réelle des propriétés de cœur. Différents exemples d'études s'inscrivant dans le cadre de cette approche sont rapportées dans ce mémoire. Il s'agit par exemple d'une comparaison directe entre un calcul de dynamique moléculaire et un calcul de DD sur la stabilité d'une jonction de Lomer. Ce travail a permis de montrer que la force motrice pour former une jonction et la stabilité de cette dernière, sont presque entièrement contrôlées par l'énergie élastique (cf. § 3.1).

De plus en plus d'études sont entreprises pour mesurer précisément la friction exercée par le réseau cristallin sur les dislocations. Cependant, il faut noter que notre compréhension théorique de ce phénomène dans certains matériaux, par exemple de structure cubique centrée (CC) ou hexagonale compacte (HC) est encore imparfaite (cf. § 4.1). Dans d'autres matériaux, les dislocations peuvent manifester parfois des propriétés de coeur exceptionnelles, conduisant à des effets d'alliage ou à la formation de configurations sessiles complexes (cf. § 3.2). Dans de tels cas, l'utilisation de la DD

permet d'évaluer la sensibilité de la réponse macroscopique aux paramètres physiques mal connus. Deux exemples d'études de ce type sont présentés dans la suite de ce texte.

Lorsque tous les éléments constitutifs d'un calcul de DD sont maîtrisés, c'est-à-dire que toutes les propriétés élémentaires des dislocations dans le matériau simulé ont été incorporées, les résultats de DD ont un réel caractère prédictif et quantitatif. La réponse simulée pour un type de chargement donné est unique et le modèle contient toutes les données nécessaires pour reproduire, par exemple, les effets de taille observés expérimentalement. Malheureusement, les dimensions volumiques simulées, de même que les taux de déformation qu'il est possible d'obtenir, sont relativement limités. La DD ne peut donc modéliser que les tous premiers stades de l'écoulement plastique.

Ces simulations sur un petit domaine de déformation permettent cependant une "mesure" fine des paramètres contenus dans les lois de comportement macroscopiques. Des simulations de DD permettent aussi de mesurer l'influence du mode de chargement sur la microstructure. C'est pourquoi, l'intérêt d'un rapprochement entre simulations de DD et modélisation macroscopique est double. D'une part, cela permet d'extrapoler les prédictions de la DD et ainsi de vérifier leur pertinence à de plus grandes déformations. D'autre part, cela permet d'éliminer les aspects phénoménologiques et d'élargir le domaine de validité des simulations ou calculs réalisés aux échelles supérieures. Au Chapitre 5 de ce mémoire, un exemple d'étude s'inscrivant dans cette démarche sera présenté pour les métaux de structure cubique face centrée (CFC).

Enfin, lorsqu'on sait précisément calculer le chargement induit sur les dislocations par des éléments microstructuraux tels qu'une surface libre, une interface, une interphase, un joint de grain ou une fissure, un autre domaine d'application s'ouvre à la DD. Il s'agit de la modélisation de la déformation plastique dans des volumes de petite dimension où l'hypothèse d'une densité continue de dislocations n'est plus satisfaite. Autrement dit, aux plus petites échelles, la déformation plastique est fortement hétérogène et sa nature discrète ne peut plus être négligée. Il ne fait aucun doute que ce domaine de recherche va rapidement se développer avec l'accent mis actuellement sur les nanomatériaux et l'intégration technologique de composants de structure de dimensions de plus en plus fines (couches minces, inter-connections, MEMS, etc). Le cas de la relaxation plastique des couches minces épitaxiées présenté en § 6.2 entre dans cette dernière catégorie.

Le présent mémoire scientifique est une synthèse non-exhaustive de mes travaux de recherche effectués au Laboratoire d'Etude des Microstructures (LEM, UMR 0104) entre les années 1994 et 2005. Ce travail s'inscrit dans le cadre d'une thématique originale initiée lors de mon affectation au LEM le 1er octobre 1994. Réalisés principalement en collaboration avec L. Kubin, ces travaux portent sur l'étude des défauts et de la déformation plastique des matériaux cristallins. L'objectif ultime de ces recherches est, en résumé, de parvenir à une description intégrée, ou multi-échelles, de la déformation plastique.

La suite de ce document est divisée en six parties. A l'exception du Chapitre 2 discutant les aspects méthodologique de la DD, qui est l'équivalent du chapitre "méthodes et techniques pour les études expérimentales", chaque chapitre commence par un rappel scientifique introduisant des travaux de recherche originaux. Ces derniers sont dans chaque chapitre soit résumés succinctement, soit présentées sous la forme de reproductions d'articles publiés. Donc, le lecteur trouvera dans ce texte quatre informations distinctes - une description de la méthode de la DD, - des rappels utiles sur la plasticité et les propriétés des dislocations, - des exemples de ce qui peut être entrepris avec la DD et enfin - une prospective finale définissant mon projet de recherche pour les années à venir et plus généralement des directions de recherche prometteuses pour la DD . De façon systématique le plan suivant est respecté :

- Le Chapitre 2 présente et discute la méthode de simulation de la dynamique des dislocations.
- Le Chapitre 3 rapporte les règles locales de la DD et des exemples portant sur les propriétés élémentaires des dislocations.

– Le Chapitre 4 est consacré à des études sur des matériaux où la déformation plastique est fortement influencée par la friction de réseau.
– Le Chapitre 5 traite de matériaux où la déformation plastique est gouvernée par les interactions entre dislocations.
– Le Chapitre 6 aborde le cas des matériaux à structure complexe, incluant d'autres défauts cristallins que les dislocations (surfaces, interfaces, joints de grains, etc).
– Enfin, le Chapitre 7 conclut ce mémoire par mon projet de recherche pour les années à venir.

CHAPITRE 2

Simulation de la Dynamique des Dislocations

2.1. Introduction

Il n'existe pas de solution unique pour construire un programme de simulation de Dynamique des Dislocations (DD)[1]. Les simulations tridimensionnelles sont récentes et il faudra sans doute encore attendre quelques années pour qu'un consensus se fasse entre les différents groupes de recherche concernés. Il est possible, cependant, d'identifier les principales forces et faiblesses des solutions existantes. Ce chapitre présente les principaux éléments constituant une simulation de DD. Des aspects techniques importants et qui ont fortement progressé ces dernières années sont discutés en détail ou reportés en annexe. Mon intention n'est pas de faire une présentation complète de tous les aspects méthodologiques d'un programme de DD, mais plutôt de faire apparaître les points les plus importants sur lesquels j'ai travaillé au cours de ces dernières années.

Dans un souci de concision, les approches bidimensionnelles de la DD ne sont pas présentées. Une partie de mon activité a également porté sur ces simulations qui peuvent permettre de répondre à des questions précises ou de défricher une problématique avant de réaliser des calculs 3-d plus complexes, mais aussi beaucoup plus réalistes.

De nombreux éléments des simulations 3-d sont des extensions de solutions numériques obtenues, souvent vers la fin des années 1960, pour les premières simulations en 2-d. Ainsi, les simulations d'aujourd'hui doivent beaucoup aux travaux de Brown [17], Foreman [18], Bacon [19, 20] et autres. De même, il est intéressant de noter que les chercheurs qui ont participé au développement des premières simulations en 3-d ont des cultures scientifiques différentes. Cette hétérogénéité peut sans doute expliquer la diversité des approches que l'on trouve dans la littérature.

Ce chapitre présente les aspects méthodologiques fondés sur la théorie élastique des dislocations. Cette composante forme l'ossature commune à toutes les simulations de DD et elle intervient quel que soit le matériau étudié. Les "règles locales", qui permettent la modélisation des propriétés non-élastiques des dislocations, et qui *in fine* introduisent la spécificité de chaque matériau, sont présentées dans les chapitres qui suivent.

[1] Dans la suite de ce chapitre, et par souci de simplification de l'écriture, l'acronyme DD désignera indifféramment la dynamique des dislocations ou une "simulation de la dynamique des dislocation".

2.2. Discrétisation des lignes de dislocations

Les principales différences entre codes de DD résident dans la procédure choisie pour discrétiser les lignes de dislocations. Idéalement, pour qu'un modèle de lignes soit performant, il doit satisfaire à deux conditions contradictoires. D'une part, on souhaite un modèle contenant le plus petit nombre possible de degrés de liberté, afin d'optimiser les calculs et de simplifier l'analyse des résultats. D'autre part, il faut une solution capable de reproduire les propriétés élémentaires des dislocations sans utiliser de trop fortes approximations. Par définition, il n'existe donc pas de modèle parfait et il est juste de dire que les solutions publiées peuvent correspondre à des choix optimisés pour tel ou tel type de problème.

Tous les modèles existants partent de l'idée d'un découpage (d'une discrétisation) des dislocations en sous-entités pour former des chaînes de segments modélisant idéalement la forme des lignes de dislocations. Les segments utilisés pour ce découpage sont généralement des portions de droites. Ce choix est dicté par des contraintes de performance numérique. En effet, dans le cadre de l'élasticité isotrope, on peut définir sous une forme analytique simple le champ de self-contrainte d'un segment de dislocation rectiligne [21, 22]. Cependant, avec la progression constante des moyens de calcul et la mise en oeuvre d'études nouvelles faisant intervenir des phénomènes où l'influence de l'élasticité anisotrope ne peut être négligée, d'autres solutions vont progressivement devenir attractives [23, 24, 25].

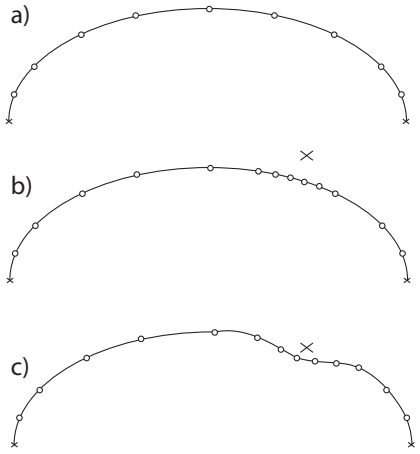

FIG. 2.1.: Illustration sur une source de Frank-Read du nombre de points d'intégrations, PI (marqués par un cercle), nécessaires pour résoudre efficacement une DD, indépendamment du modèle de ligne choisi. Le segment source initial est horizontal et de caractère vis. a) Pour une source isolée, c'est la self-contrainte qui fixe le nombre et la répartition des PIs. Il faut davantage de PIs par unité de longueur dans les sections coins à faible rayon de courbure, car le gradient de self-contrainte est plus fort. Dans ce cas simple, on voit qu'un critère de courbure de ligne suffit à distribuer les PIs. b) et c) Si la source se rapproche d'un obstacle (marqué d'une croix) associé à un champ élastique, comme un arbre de la forêt ou un précipité incohérent, il faut localement davantage de PIs pour déterminer correctement les forces s'exerçant sur la dislocation. Un critère en tension de ligne (critère en courbure) n'est donc plus suffisant.

L'objet élémentaire d'une DD est donc un segment de dislocation rectiligne. C'est le nombre de ces segments par unité de longueur qui définit le nombre de degrés de liberté attribués aux lignes de dislocations. À chaque segment est associé un ou plusieurs points d'intégration (PI) des forces sur les dislocations. En définitive, c'est dans le nombre et le positionnement des PIs que résident les différences majeures entre les divers modèles de DD. Parmi les solutions existantes, Il faut distinguer deux grands groupes :

- D'une part, il existe des modèles qui, par construction, n'imposent aucune contrainte sur le positionnement des PIs [23, 26, 27, 28, 29]. Cette approche permet une description simplifiée de la courbure des dislocations et donne une convergence rapide des résultats pour une boucle de dislocation isolée lorsque le nombre de segments augmente [30, 31]. L'argument le plus souvent avancé en faveur de cette approche est qu'elle donne une description précise des dislocations avec moins de segments et serait donc plus performante sur le plan numérique. Cet argument est en réalité inexact car le coût numérique d'une simulation n'est pas contrôlé par le nombre minimum de segments nécessaires à la description des lignes, mais par le nombre de PIs utilisés pour calculer les forces. Or, pour les problèmes faisant intervenir un grand nombre de dislocations, cette dernière quantité ne dépend pas de la courbure des lignes mais plutôt des fluctuations du champ de contrainte dans les plans de glissement. Cette remarque importante est illustrée sur la Fig. 2.1. En bref, il faut mettre plus de PIs là où le gradient de contrainte est fort, afin d'intégrer correctement la dynamique. Déterminer le nombre et la distribution des PIs par un calcul du rayon de courbure des dislocations n'est possible que dans le cas d'une dislocation isolée (beaucoup de codes de simulations continuent néanmoins d'utiliser cette solution).
- D'autre part, il existe une autre approche où les PIs ne peuvent occuper que des positions discrètes dans l'espace [30, 32, 33, 34, 35, 36, 37]. Ici, l'idée maîtresse est qu'il est numériquement contre-performant de calculer les forces aux PIs de façon continue dans l'espace. Mieux vaut définir une distance minimum entre PIs et ainsi travailler dans un espace Euclidien borné[2]. Cette distance est définie à l'aide d'un maillage sous-tendant la simulation, qui délimite les positions discrètes où peuvent résider les PIs. Cette approche équivaut à résoudre une dynamique de segments de longueurs et de caractère discrets, reliant des PIs sur un 'réseau' de simulation. Pour prendre en compte simplement la géométrie du glissement dans le matériau étudié on choisit un réseau de simulation homothétique de son réseau cristallin. Le paramètre de maille de la simulation peut être quelconque. Cependant, il peut être utilisé comme un garde-fou évitant le calcul des interactions entre segments à des distances telles que l'élasticité linéaire ne s'applique plus ou que l'amplitude des forces d'interaction nécessite des pas de temps extrêmement courts pour l'intégration de la dynamique. On évite ainsi l'utilisation de pas de temps trop petits.

En résumé, la première approche dite de *discrétisation continue* permet à priori une meilleure description des champs élastiques près des lignes de dislocations, puisque le caractère de ligne (la courbure) peut être décrit de manière quasi-continue. La seconde approche, dite de *discrétisation sur réseau* optimise l'intégration numérique en réduisant l'espace des solutions accessibles au mouvement des dislocations.

Enfin, il faut souligner que, quelle que soit la solution de discrétisation choisie, il faut pour certains matériaux différencier des directions cristallographiques privilégiées. Celles-ci se confondent généralement avec les directions de ligne où s'exerçe une forte friction de réseau, par exemple la direction vis dans les métaux de structure CC [35, 38]). De longs segments de dislocations sont alors 'rigidifiés' par une faible mobilité dans la direction normale à la ligne. Cette propriété qui se retrouve dans de nombreux matériaux réduit sensiblement les différences entre les diverses méthodes de discrétisation des lignes.

Les différentes générations de DD développées au LEM s'inscrivent toutes dans la famille des simulations utilisant une discrétisation sur réseau. Tout en restant dans la continuité du premier code de simulation '*coin-vis*' (deux directions de segments par système de glissement), les versions récentes permettent une description plus précise de la courbure des dislocations (quatre directions de

[2]La manipulation de nombres entiers par les ordinateurs est rapide et permet une optimisation des calculs en tabulant à l'avance un nombre fini d'opérations à effectuer

segments par système de glissement). On améliore ainsi le réalisme des simulations tout en réduisant les coûts de calcul. Le tout dernier code 3-d, qui met en jeu de nombreuses collaborations, permet de traiter non seulement les structures cristallines cubiques (CFC, CC, CD), mais aussi les structures hexagonale et orthorhombique. Ce code de simulation intitulé '*mM*' est depuis le début de l'année 2004 un logiciel libre distribué sans restriction dans le cadre d'une licence GPL (GNU Public Licence). Les paragraphes suivants discutent certaines spécificités de ce modèle.

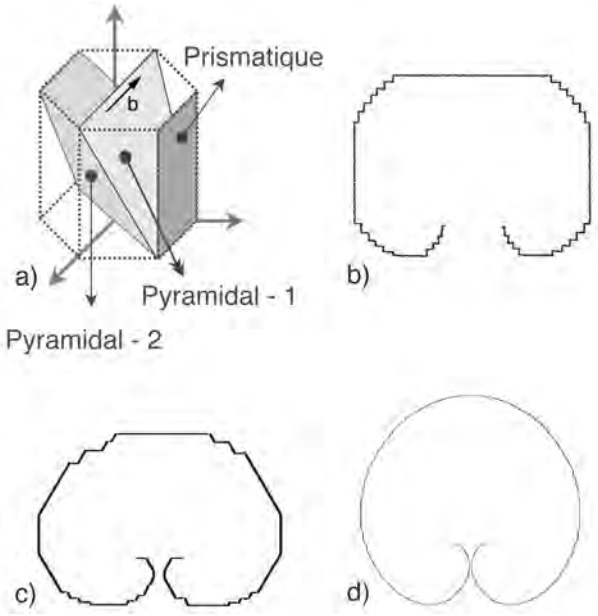

FIG. 2.2.: Discrétisations optimales en fonction des systèmes de glissement étudiés, dans le cas des discrétisations sur réseau. L'illustration est réalisée dans le cas d'une source de Frank-Read fonctionnant en l'absence de force de friction de réseau. a) La maille hexagonale du zirconium et ses principaux systèmes de glissement actifs à la température ambiante ($\vec{b}$ est le vecteur de Burgers). b) Si l'on doit étudier seulement le glissement prismatique, une discrétisation ne considérant que des directions de segments parallèles aux caractères vis et coin est suffisante. Ce modèle de ligne, dit 'coin-vis', permet de prendre en compte précisément l'influence de la friction de réseau (dans la direction vis) et des réactions entre plans de glissement (directions coins). Si l'on veut tenir compte de systèmes de glissement supplémentaires, comme le pyramidal-1 et le pyramidal-2, il est préférable d'inclure un certain nombre de directions de segments pertinentes comme les directions à l'intersection des plans de glissements. Dans le cas de zirconium, on prend en compte c) quatre directions par système de glissement pour simuler du glissement prismatique associé à du pyramidal-1 et en d) huit directions dans le cas le plus général.

2.3. Forces sur les segments de dislocation

La résolution du mouvement des dislocations s'effectue à partir des équations classiques de la mécanique Newtonienne. La prédiction du déplacement des segments construisant les lignes de dislocation repose sur le calcul des forces effectives auquel chaque segment est soumis. Le formalisme utilisé pour calculer ces quantités s'appuie sur la théorie élastique des dislocations. On néglige donc dans le calcul des forces les contributions provenant du coeur des dislocations. Cette simplification usuelle s'applique même à des éléments de volume de dimensions nanométriques, car l'énergie élastique est toujours très supérieure à l'énergie de coeur [21, 39].

La relation de Peach et Koehler, $F^{PK} = (\underline{\underline{\sigma}} \cdot \underline{b}) \wedge \underline{\xi}$, définit la forme générale de la force par unité

de longueur exercée par le tenseur de contraintes $\underline{\underline{\sigma}}$ sur une dislocation de vecteur de Burgers $\underline{b}$ et de direction unitaire $\underline{\xi}$. Pour déterminer la force vue par les dislocations, la force de Peach-Koehler est projetée dans les directions de glissement et de glissement dévié pour les portions de ligne vis et dans les directions de glissement et de montée pour les parties non vis. A ce jour, cependant, aucune simulation ne fait usage de la composante de montée. Excepté aux très hautes températures, la vitesse de montée d'une dislocation est très faible comparée à sa vitesse de glissement et il est difficile de prendre en compte simultanément ces deux mécanismes de déplacement.

C'est dans le calcul de la contrainte locale $\underline{\underline{\sigma}}$ aux PIs que réside le plus grande difficulté numérique de la DD. Ce calcul doit impérativement être précis et performant. La résolution de l'équilibre mécanique d'un solide disloqué est un problème difficile pour lequel il n'existe pas toujours de solutions analytiques [40]. C'est pourquoi la solution choisie pour chaque étude dépend des conditions aux limites et de chargement simulées. Comme discuté ci-dessous, il existe, en pratique, une sorte de hiérarchie dans la complexité du calcul des forces.

2.3.1. Approximations de la tension de ligne

Le champ de self-contrainte d'une dislocation étant singulier, il est difficile de calculer la contribution à la force de Peach-Koehler des sections de ligne là où le champ de contrainte diverge. De plus, toutes les procédures de discrétisation utilisant des segments rectiligne sous-estiment l'énergie de ligne W en éliminant localement la courbure des dislocations. Ce point est critique lorsqu'un modèle utilise, pour optimiser les calculs, de longs segments et de fortes désorientations angulaires entre segments [21]. C'est pourquoi, la contribution à la force de Peach-Koehler des segments voisins d'un PI est en pratique remplacée par un calcul de tension de ligne locale [41].

Si, comme dans les simulations de Foreman-Makin [42], on limite le calcul des forces à cette seule contribution, la solution obtenue est alors celle d'un ensemble de lignes élastiques interconnectées mais n'interagissant pas entre elles. Le domaine de pertinence de ces calculs est difficile à anticiper, mais il existe des problèmes où cette approche simplifiée donne de bons résultats [41, 43].

En élasticité isotrope, on utilise souvent une méthode proposé par Brown [17, 18, 27]. Cette méthode consiste à calculer la tension de ligne T associée à un arc de cercle passant par trois points (pas nécessairement des PIs) contigus sur une ligne de dislocation. La tension de ligne est alors calculée simplement au premier ordre non nul [21].

$$T = \frac{dW}{dl} = W + \frac{\partial^2 W}{\partial \alpha^2} \tag{2.1}$$

Dans l'Eq. 2.1, le terme de droite fait apparaître la dépendance angulaire de la tension de ligne qui, en élasticité isotrope, ne dépend que du caractère des dislocations, c'est-à-dire de l'angle α entre $\underline{\xi}$ et $\underline{b}$. Pour un arc de cercle Foreman [18] a proposé une formule simple :

$$T = \frac{\mu b}{4\pi(1-\nu)} \frac{1}{R}[(1+\nu) - 3\nu \sin^2\alpha) \ln(\frac{2\Lambda}{r_0}) - \nu \cos(2\alpha)] \tag{2.2}$$

où R est le rayon de courbure et $2\Lambda = R\theta$ la longueur de l'arc de cercle sous-tendu par l'angle θ. Cette expression donne une bonne estimation des forces sur une dislocation isolée [44] ou encore sur une configuration de quelques dislocations (cf. § 3.1). C'est pourquoi des simulations utilisent uniquement cette approximation pour calculer localement certaines propriétés élémentaires des dislocations. Par exemple, l'équilibre aux noeuds triples d'une jonction peut être déterminé en ne considérant que les tensions de lignes [45, 46]. Dans ce cas, mais aussi pour d'autres points particuliers comme l'extrémité d'une dislocation touchant une interface ou un point d'épinglage à l'intersection de deux plans de glissement, le calcul de l'arc de cercle décrivant la courbure des dislocations doit être traité de manière

spécifique (cf. [47, 48, 49]). Il y a plusieurs manières de résoudre ce problème, ce qui peut engendrer des différences entre résultats de différentes simulations.

L'extension du concept de tension de ligne locale au cas de l'élasticité anisotrope ne peut pas se faire de manière analytique, sauf cas particulier [50]. Le calcul des champs de contrainte et de déplacement d'une dislocation dans un milieu anisotrope passe en effet par la résolution numérique d'une équation du sixième degré [21, 51]. En pratique, on peut calculer numériquement les différents termes intervenant dans l'Eq. 2.1, par exemple avec le code *DisDi* de J. Douin [52]. Les résultats de ces calculs peuvent alors être tabulés pour différentes valeurs de α. En cours de simulation, la tension de ligne sera ensuite interpolée à l'aide d'un calcul d'arc de cercle similaire à celui utilisé pour des calculs isotropes [53]. Un exemple de simulation utilisant une telle procédure est donné au chapitre 6.2.

2.3.2. Self-contraintes dans un milieu élastique infini

La grande majorité des calculs de DD font l'hypothèse simplificatrice que le solide simulé est assimilable à un milieu élastique infini. Cette hypothèse permet, dans le cadre de l'élasticité isotrope, l'utilisation de formules mathématiques simples pour le calcul du champ de contrainte induit par chaque segment d'une boucle de dislocation ou d'une dislocation rectiligne infinie [21]. Conformément au principe de superposition des champs de l'élasticité linéaire, la tension de ligne calculée ci-dessus (§2.3.1) est alors complétée par une force de Peach-Koehler calculée aux PIs et prenant en compte le champ de contrainte associé à l'ensemble des segments de dislocations présents dans l'élément de volume simulé[3].

On trouvera en Annexe B1, un exemple d'expression du champ de self-contrainte pour des segments de dislocation droits. Cette formulation, que j'ai proposée avec M. Condat [30], est souvent utilisée car elle est facile à programmer, elle exprime le champ de contrainte de segments de dislocations dans un repère orthonormé unique et elle répond à de nombreuses exigences de performance numérique. Toujours dans l'hypothèse d'un milieu infini, des solutions numériques ont été développées pour déterminer le champ de contrainte de dislocations discrètes dans un milieu élastique anisotrope [24]. La comparaison entre les solutions isotrope et anisotrope montre que des différences significatives n'apparaissent qu'à de très faibles distances du coeur des dislocations (quelques nanomètres). Lorsqu'on s'éloigne du cœur, les différences s'estompent rapidement et dans une microstructure, elles sont négligeables par rapport à la distance moyenne entre dislocations ($1/\sqrt{\rho}$). C'est pourquoi, il est généralement admis que l'élasticité isotrope suffit pour calculer la contribution à longue portée des interactions entre dislocations dans un cristal déformé.

Pour satisfaire à l'hypothèse d'un milieu élastique infini, les conditions à appliquer aux limites des simulations constituent un point essentiel, difficile à résoudre [10, 54]. En effet, pour que le volume élémentaire considéré soit représentatif de la plasticité d'un élément de volume d'un monocristal ou d'un grain de grande dimension, il faut veiller à ce qu'aux limites

- le champ de contrainte et la tension de ligne des dislocations préservent leur continuité,
- les flux de dislocations soit correctement reproduits,
- et le libre parcours moyen des dislocations ne soit pas altéré.

Si en 2-d des conditions aux limites périodiques (CLPs) ont été utilisées très tôt [55, 56], en toute connaissance des artefacts possibles [57, 58], l'utilisation de ces mêmes CLPs en 3-d a été longtemps considérée comme problématique. La principale objection était qu'il est difficile de gérer la connectivité des lignes de dislocation aux limites d'une cellule de simulation périodique en 3-d dès que l'on a plus de trois systèmes de glissement actifs. Depuis le travail de Bulatov et al. [59], il a été montré qu'en réalité cette question de la connectivité des lignes est un faux problème. Aujourd'hui des CLPs sont utilisées dans la quasi-totalité des calculs dits "massifs".

[3] Lors de ce calcul, il faut éliminer la contribution des segments contigus sur la ligne puisque leur contribution est déjà incluse dans la tension de ligne locale

Cependant, comme montré dans notre article [60] reproduit en Annexe B2, l'utilisation de CLPs suppose qu'une attention particulière soit portée au calcul des contraintes à longue distance, au choix de la configuration initiale et à la forme de la boîte de simulation. En effet, sans précautions particulières, les CLPs limitent sensiblement le libre parcours moyen des dislocations car elles introduisent des auto-annihilations entre différentes portions d'une même ligne de dislocation (cf. figure 1 en annexe B2). Si l'on n'y prend garde, cet artefact altère l'évolution des densités de dislocations et, par conséquence, le durcissement d'écrouissage. Des solutions ont été proposées pour contrôler cet effet indésirable[4]. En pratique, les simulations doivent être arrêtées avant une déformation critique où l'on sait que les premiers artefacts apparaissent. La méthode la plus générale pour augmenter au maximum cette déformation critique consiste à déformer les cellules primaire de simulation ou encore à tourner les systèmes de glissement vis à vis du repère orthonormé utilisé dans les CLPs (cf. annexe B2).

La figure 2.3 illustre un aspect pratique des CLPs. L'espace simulé étant continûment périodique, il est possible de définir dans le solide des formes de cellules de simulation alternatives à la cellule primaire et qui sont topologiquement équivalentes. Chacune d'elle est de même volume que la cellule primaire et permet la reconstruction du milieu périodique. Ainsi, si l'on veut visualiser la trajectoire d'une dislocation sur de grande distance, il est généralement possible d'échanger la cellule primaire des simulations par une lame mince de grande dimension qui permet toujours un pavage exacte du solide périodique simulé.

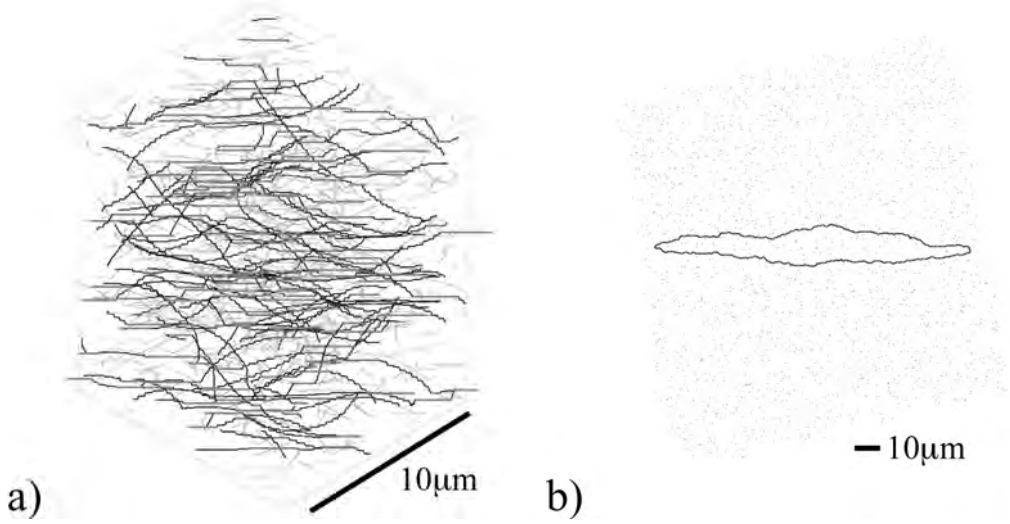

FIG. 2.3.: Extension d'une boucle de dislocation (ligne en gras) dans un volume simulé périodique contenant des dislocations dans deux systèmes de glissement latents, formant avec la boucle mobile des jonctions de même direction cristallographique. Cette configuration induit une forte hétérogénéité de mobilité sur les segments de la boucle. a) image 3-d de la cellule de simulation primaire après déformation. Divers fragments de la boucle y apparaissent, qui sont des répliques des fragments obtenus par le jeu des CLPs dans les différentes cellules. b) Le plan de glissement périodique dans lequel se développe la boucle de dislocation est obtenu en réalisant une section de l'ensemble du volume simulé. Dans cette lame mince, les dislocations qui coupent le plan de lame apparaissent comme des objets quasi-ponctuels.

[4]Les problèmes d'auto-annihilation et de formation de dipôles artificiellement stables ne peuvent pas être complètement éliminés. Par contre il est possible de contrôler la déformation critique pour laquelle ces problèmes apparaisssent, cf. Annexe B2

2.3.3. Optimisation du calcul des forces

Le champ de contrainte des dislocations étant un champ à longue portée $(1/r)$, il n'est pas justifié, en l'absence d'écrantage, d'introduire une distance de coupure dans le calcul des interactions élastiques. C'est pourquoi le coût de calcul des forces entre segments devient rapidement très important. Il croit comme $O(N^2)$ si N est le nombre de segments, la valeur de l'exposant mesurant ce qu'on appelle la complexité de la méthode. Au cours des années passées plusieurs solutions algorithmiques ont été apportées à ce problème. Les méthodes les plus intéressantes, qui sont incorporées dans le code de simulation "***mM***", sont maintenant brièvement discutées.

2.3.3.1. Méthode des multipôles

Une analogie simple entre interactions élastiques et forces gravitationnelle ou électrostatique, montre que si les segments n'ont pas une forte dispersion de longueurs, il est possible en DD d'utiliser un algorithme de calcul proposé par Greengard [61, 62] et plus connu sous le nom de "méthode des multipôles". Sous différentes formes, cet algorithme, s'applique à tous les problèmes à N corps et repose sur une idée simple. Lorsqu'on s'éloigne d'un segment, son champ de self-contrainte varie de plus en plus lentement dans l'espace. Ainsi, lorsqu'on veut connaître les forces d'interactions entre de nombreux segments éloignés les uns des autres, il est possible d'optimiser de manière simple et contrôlée le calcul en ne déterminant plus les contraintes sur chaque segment (chaque PI), mais seulement en un nombre plus restreint de points de référence. Les points de référence, ou pôles, de l'algorithme sont généralement situés au centre de sous-domaines régulièrement inscrits dans la cellule de simulation. L'ensemble des champs de contraintes issus de segments situés dans un sous-domaine est sommé sur les pôles et, comme il varie lentement dans le temps, il peut être actualisé avec un pas de temps plus grand que le pas de temps élémentaire de la simulation.

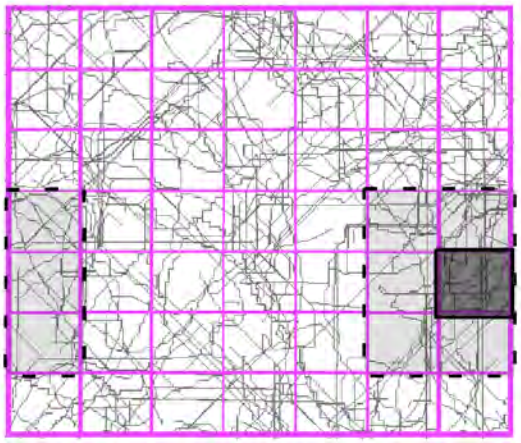

FIG. 2.4.: Illustration de la décomposition en domaines de la cellule de simulation défini pour la méthode multipôle. Les domaines dans la frontière en pointillé correspondent aux regions d'interactions à courtes distances vis à vis des segments contenu dans le domaine grisé. A l'intérieur de ces domaines tous les calculs sont réalisés de manière explicite. Les autres domaines sont considérés comme éloignés de la région grisé et les interactions élastiques entre segments sont remplacées par un calcul approché dont la nature dépend de la complexité du schéma multipôlaire mis en oeuvre (Fig. d'après R. Madec).

Cette méthode nécessite d'indexer efficacement l'appartenance des segments à telle ou telle région de l'espace. Une telle indexation est importante pour d'autres utilisations, car elle définit les notions de voisinage et de topologie. Sont considérés comme éloignés, deux segments dont les domaines respectifs

ne sont pas contigus. Cette décomposition en domaines permet de différencier les iinteractions à courte distance, qui ne peuvent être simplifiés, et à longue distance. L'analyse du gain numérique résultant est complexe et dépend de nombreux paramètres. Cependant, dans l'hypothèse d'une distribution homogène, on peut vérifier que la complexité du problème passe de $O(N^2)$ à $O(N^{3/2})$. Pour le lecteur intéressé, une démonstration rapide est donnée ci-dessous.

Soient, N,N_d, $CCD(N)$, $CLD(N)$ et δt, respectivement le nombre de segments, le nombre de sous-domaines, le coût d'un calcul à courte distance (CD), le coût d'un calcul à longue distance (LD) et δ la périodicité des calculs à longue distance vis à vis du pas de temps élémentaire.
Chaque segment possède $\frac{27*N}{N_d}$ segments voisins à CD, donc $CCD(N) = \frac{27*N^2}{N_d}$.
Comme les calculs à LD sont réalisés uniquement au centre des domaines, tous les δ pas de calcul, et que chaque domaine possède dans l'espace 26 domaines voisins, $CLD(N) = \frac{N_b}{\delta}(N - 27\frac{N}{N_d})$.
En faisant l'approximation $27\frac{N}{N_d} << N$, le coût total de la méthode décrite ci-dessus devient $C(N) = CCD(N) + CLD(N) = \frac{27*N^2}{N_d} + \frac{N_d*N}{\delta}$.
Pour un petit pas de $\delta = 3$, le minimum de cette fonction s'obtient pour $N_d = 3\sqrt{N}$ et vaut $C_{min} = 10N\sqrt{N}$. La complexité du problème est donc passée de $O(N^2)$ à $O(N^{3/2})$.

La solution présenté ci-dessus est la plus simple à mettre en oeuvre, mais aussi la plus performante lorsque le nombre de segments considéré n'est pas trop grand. Pour 20000 segments, on obtient une accélération des simulations d'un facteur compris entre 15 et 50, suivant la valeur de δ. Cette méthode peut être étendue à des ordres supérieurs comme $O(N \ln N)$ et $O(N)$ [63, 64].Pour cela il faut une récriture des formules définissant le champ de contrainte d'un segment de dislocation sous la forme d'une somme de produits de fonctions approximant la solution exacte. En d'autres termes, il faut remplacer mathématiquement la somme des segments d'un sous-domaine par quelques dislocations de Volterra dont le champ de contrainte reproduit le plus précisément possible la solution vraie. Le défaut de cette procédure est que pour avoir une bonne précision dans tous les cas possibles, il faut parfois considérer un grand nombre de pôles, ce qui fait croître fortement le terme constant intervenant devant la complexité de la solution (par exemple, la solution $O(N^{3/2})$ est affectée d'un facteur 10). Wang et al. [64] ont montré qu'une accélération globale d'un facteur 100 peut être atteinte dans certain cas. Le mérite essentiel de cette dernière solution est de donner à la DD la possibilité pratique de réaliser des calculs avec plusieurs centaines de milliers de segments [65].

2.3.3.2. Parallélisation

Depuis les années 1970, les ordinateurs diminuent en taille, gagnent en puissance de calcul et voient leur coût d'achat se réduire. Il n'est donc plus inhabituel de trouver au sein des laboratoires de recherche des petites "fermes" de machines dont la puissance de calcul totale est importante. Pour utiliser la pleine puissance de ces installations, il est nécessaire de récrire (paralléliser) les codes de simulations. Comme pour la méthode d'optimisation discutée ci-dessus, il existe plusieurs schémas de parallélisation possibles et la performance obtenue dépend du problème simulé et du type de machines utilisées (machines à mémoire partagée, machines à mémoire distribuée, etc). Parmi les solutions existantes, on distingue trois grands schémas liés la manière dont la charge de travail est distribuée entre les machines :

– La solution la plus classique est celle dite de "décomposition de domaines" [65, 66]. Elle consiste à partager l'espace en domaines, de taille variable en cours de calcul, et à donner à chaque processeur la charge de calcul liée aux segments d'un ou plusieurs domaines. La force de cette approche est quelle est déjà utilisée dans de nombreux autres problèmes de physique. Sa faiblesse bien connue est que les performances dépendent sensiblement du nombre de processeurs mis en jeu. Idéalement, pour un calcul 3-d, il faut un nombre de machines croissant comme une puissance cubique entière.

– La seconde solution s'attache à prendre en compte la topologie des lignes de dislocations et à garder au niveau de chaque machines la notion de chaînage de segments. Ainsi on impose à chaque processeur de résoudre la dynamique d'un paquet de lignes de dislocations, indépendamment de leur position dans l'espace. Il semble que cette solution ne soit utilisée que dans un seul code existant (PARANOID [46]). Sa force est certainement sa simplicité de mise en oeuvre. Sa principale faiblesse est de ne pas pouvoir se conjuguer facilement avec les méthodes des multipôles.
– La dernière solution, qui est utilisée dans "***mM***", repose sur l'idée d'un équilibre optimum des charges (load balancing) en relation avec l'algorithme de Greengard. La mise en œuvre suppose une évaluation des coûts de calculs de chaque segment, en différenciant les interactions à longue et courte distances. A partir de ce calcul et de la décomposition en domaines, il est possible de distribuer sur chaque processeur, proportionnellement à sa rapidité, un nombre de segment fonction de temps de calculs évalués. L'avantage de cette solution est qu'elle est indépendante du nombre de processeurs utilisés et permet de prendre en compte facilement des hétérogénéités dans la distribution spatiale des dislocations. Sa faiblesse est de se focaliser sur le coût de calcul des forces d'interactions, sans prendre en compte de possibles déséquilibres de charge induits par le traitement des réactions de contact.

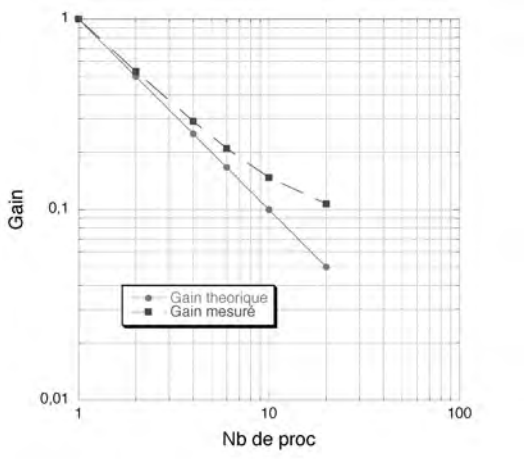

FIG. 2.5.: Mesure du gain (inverse de l'accélération) obtenu en fonction du nombre de processeurs avec "***mM***" et pour une microstructure contenant 18000 segments. Au delà de dix processeurs, le gain obtenu s'écarte rapidement de la valeur théorique. Avec un plus grand nombre de segments, il est possible d'utiliser de manière efficace un plus grand nombre de processeurs.

La parallélisation des codes de DD, au même titre que les optimisations algorithmiques, constitue une étape incontournable pour réaliser des simulations avec un grand nombre de dislocations. Il est important de garder à l'esprit que la déformation plastique est un problème non conservatif où la densité de dislocations (le nombre de segments) augmente très rapidement. C'est pourquoi, une parallélisation des codes de simulation est nécessaire pour améliorer les performances (les solutions optimales font appel à un nombre de processeurs croissant au cours de la déformation), et surtout pour augmenter la déformation maximale obtenue pour un temps de calcul raisonnable. Sur la figure 2.5, le gain obtenu sur "***mM***" pour une microstructure de 18000 segments est porté en fonction du nombre de processeurs. Avec dix processeurs, l'accélération effective mesurée est d'un facteur huit.

2.3.3.3. Sous-intégration dynamique

Durant un essai de déformation, la densité de dislocations mobiles est souvent faible devant la densité totale. En effet, la grande majorité des segments ne se déplace que pendant une petite fraction du temps simulé. Le reste du temps, ces segments sont bloqués pour différentes raisons :

- ils sont immobilisé par des obstacles cristallins (joint de grains, interfaces, précipités incohérents, etc),
- ils se trouvent dans un minimum local d'énergie (jonctions, dipôles, obstacles élastiques, etc),
- ou bien, plus généralement, la tension de ligne équilibre les forces dans le sens du mouvement.

Quel que soit le problème étudié, il faut donc considérer pour les segments un temps de vol moyen, qui fixe le pas d'intégration de la DD, ainsi que des temps d'attentes pendant lesquels il suffit de vérifier si les lignes tendent à se déplacer. La notion de sous-intégration dynamique repose sur l'hypothèse d'une tolérance de la DD vis-à-vis de l'instant où un segment est remobilisé. Cette idée est développée ci-dessous en détaillant l'algorithme utilisé dans le code ***mM*** :

1. Soit Δt le pas de temps élémentaire et $x\Delta t$ un intervalle de temps de surveillance.
2. Soit F_{im}, un seuil de force au-dessous duquel un segment peut être considéré comme pratiquement immobile.
3. Si pendant ≈ 3 pas de Δt consécutifs[5] la force sur un segment est plus petite que F_{im}, ce segment est considéré comme immobile.
4. Pendant un temps $(x-3)\Delta t$, la force sur ce segment n'est plus réévaluée.
5. A la fin de ce temps, le segment immobilisé est positionné en fonction des petits déplacements cumulés pendant les $(x-3)$ pas. Cet unique déplacement est donc fonction de la dernière évaluation des forces effectuée avant d'immobiliser un segment. Si la force était alors nulle, le déplacement à ce pas est nul. Ensuite, le segment est considéré comme de nouveau mobile et la procédure est réitérée.

Cette procédure s'avère très utile quand de nombreux segments sont immobilisés par des obstacles infranchissables. Elle n'affecte pas de manière notable l'intégration de la dynamique si elle est bien paramétrée. Elle équivaut seulement à utiliser un pas de temps plus grand pour les segments qui ne participent pas ou peu à la déformation plastique. Sa principale force est de déterminer, à la volée, la population de segments dont la dynamique peut être intégrée avec un pas de temps plus grand. Grâce à cette méthode, une accélération d'un facteur 5 a été mesurée lors de l'étude de la déformation plastique de polycristaux, où de très nombreux segments s'empilent aux joints de grains.

En conclusion de cette partie, il faut souligner que la combinaison des trois optimisations présentées plus haut, méthode des multipôles, parallélisation et sous-intégration dynamqiue, conduit à une accélération moyenne des simulations d'un facteur 1000 environ. Ce progrès, obtenu au cours des toutes dernières années, a été principalement mis au service de calculs de plus en plus précis, c'est-à-dire avec davantage de PIs par unité de longueur.

2.3.4. Conditions aux limites complexes

Van der Giessen et Needleman [67] ont été les premiers à discuter l'importance d'un traitement précis des conditions aux limites "mécaniques" en DD. Les forces sur les dislocations étant des forces de configuration, c'est la résolution du problème mécanique aux limites de la structure étudiée qui fixe ces forces. Celles-ci doivent être compatibles avec les conditions d'équilibre du solide en présence ou en l'absence de travaux internes ou externes. Or, ce calcul devient complexe et ne peut plus être

[5] Le test d'immobilité dois être répété plusieurs fois pour ne pas prendre en compte des segments oscillant autour d'un minimum local d'énergie.

résolu analytiquement si le volume simulé, de dimensions finies, contient des surfaces, des interfaces ou si le chargement imposé (en déplacement ou en forces) s'effectue sur une surface de morphologie complexe. Différentes solutions existent à ce problème et sont brièvement décrites ci-dessous. Une de mes publications discutant les mérites respectifs des deux principales méthodes de couplage entre DD et élément finis (EF) est ensuite reproduite. Cette discussion est importante, car il s'agit d'un aspect méthodologique de la DD encore en forte évolution et qui conditionne la faisabilité d'une partie des études discutées dans mon projet de recherche développé au Chapitre 7.

2.3.4.1. Approximation de la tension de ligne

Quel que soit le milieu étudié, la DD utilise toujours un traitement local de la tension de ligne. Comme discuté plus haut, cette approximation est nécessaire pour calculer la contribution des segments de dislocations de part et d'autre des PIs lors du calcul des forces. Or, lorsqu'une dislocation s'approche d'une discontinuité cristalline (surface, fissure, interface, etc), une variation de la tension de ligne doit être prise en compte car l'énergie élastique diffère de part et d'autre de ce défaut.

Par exemple, lorsqu'une dislocation émerge à une surface libre de toute sollicitation, on sait que les forces s'exerçant sur les lignes proches de la surface modifient la structure de coeur des dislocations [68] et imposent une réorientation qui minimise l'énergie élastique [21, 69]. Comme je l'ai montré dans ma thèse [47], ces effets peuvent être reproduits de manière simple. Pour cela on suppose qu'une surface libre induit sur l'extrémité libre des dislocations une tension de ligne de direction constante différenciée pour chaque système de glissement[6]. Cette solution simple a été utilisée par exemple par Schwarz et col. pour l'étude des propriétés des dislocations dans les couches minces de silicium et donne des résultats bien meilleurs que toute description empirique [27, 70]. Il ne faut cependant pas oublier que l'effet de la force image ne se limite pas aux dislocations qui touchent la surface et qu'il faut également traiter la force image sur les dislocations proches d'une surface mais qui n'émergent pas. Notons aussi que cette solution approchée est plus difficile à mettre en œuvre lorsqu'on étudie des matériaux très anisotropes du point de vue élastique.

Dans le cas de dislocations traversant une interphase ou touchant une surface contrainte, des approximations sur la tension de ligne sont toujours possibles, mais elles deviennent très complexes (cf. l'étude par de Koning et col. sur le franchissementnt d'un joint de grain par une dislocation [71, 72]).

En pratique, la simple modification de la tension de ligne en élasticité isotrope constitue une assez bonne approximation qui permet de reproduire l'essentiel des propriétés physiques induite par la présence d'interfaces. C'est une solution simple à implémenter et qui n'implique pas de surcoût de calcul important. C'est pourquoi, malgré ses imperfections, elle est souvent utilisée [28, 73, 74].

2.3.4.2. Compensation de surface

Une méthode permettant un calcul plus rigoureux des forces dans un solide disloqué et contenant une ou plusieurs surfaces a été proposé par Fivel et col. [75, 76]. Cette méthode, qui s'inspire de la solution de Boussinesq-Cerruti dans un milieu semi-infini, consiste à imposer des forces ponctuelles "compensatrices" en surface pour équilibrer le solide en présence de forces internes. Couplée avec l'approximation de la tension de ligne discutée plus haut, cette approche permet un calcul très précis de la force image. Malheureusement, son coût numérique élevé la restreint à des études ne faisant intervenir qu'un petit nombre de dislocations [70, 76]. C'est pourquoi, deux autres méthodes s'inspirant

[6] Ainsi, si l'on applique aux extrémités libres des dislocations une tension de ligne constante dans la directions vis, les sections de ligne proches de la surface vont se redresser dans la direction vis et éliminer toute courbure en surface pour minimiser l'énergie de ligne. Il faut noter que la direction correspondant au vrai minimum d'énergie pour une dislocation émergente n'est pas exactement la direction vis mais fait un angle compris entre la direction de $\underline{b}$ et la normale à la surface dans le plan de glissement [27].

de cette solution, moins précises mais beaucoup plus performantes, ont été développées.

La première méthode consiste à équilibrer surfaces et interfaces dans un milieu fini avec une 'mosaïque' de boucles de dislocations de Volterra (l'amplitude et la direction du vecteur de Burgers de chaque boucle est quelconque). Cette méthode tridiemensionnelle dérive de la solution classique qui consiste à décrire le champ élastique d'une fissure en 2-d par un empilement de dislocations de Volterra. Ainsi, à chaque pas de simulation et avec l'aide d'un algorithme de minimisation, on calcule les vecteurs de Burgers qui vont équilibrer les contraintes normales à la surface au centre de chaque petite boucle. Une fois le réseau de boucles de Volterra construit, il est possible de calculer correctement les forces de Peach-Koehler sur les dislocations si l'on prend en compte le champ de contraintes du réseau de dislocations de surface [77, 78, 79].

La seconde méthode s'appuie sur le formalisme performant et bien connu et des éléments finis ou des éléments frontières. Pour cela, il faut mailler le volume simulé pour déterminer des points d'intégration sur les surfaces ou interfaces. D'après le champ de contrainte mesuré en ces points il est possible de réaliser l'équilibre du volume étudié en imposant des chargements de surface. Cette solution initialement utilisée en 2-d est souvent nommée 'méthode de superposition' [67, 80, 81, 82]. Elle est maintenant souvent utilisée en 3-d. On notera seulement que, suivant les auteurs, il existe d'importantes différences dans la manière de prendre en compte le chargement appliqué [49, 83, 84, 85, 86, 87, 88]. La méthode de superposition est présentée plus en détail dans l'article reproduit dans le paragraphe suivant.

2.3.4.3. Le modèle discret-continu

Une solution alternative pour le calcul des forces sur les dislocations dans un solide fini consiste à ne plus rechercher des corrections aux champs de contrainte des dislocations dans un milieu infini, mais à calculer directement le "vrai" champ de contrainte par des méthodes numériques comme la méthode des éléments finis (EF), ou la méthode de champs de phase si l'on souhaite travailler dans l'espace de Fourier. Ces méthodes sont toutes issues de la théorie des "Eigenstrains" de Mura [40]. Une approche de ce type utilisant les EF a été développée à l'ONERA lors des travaux de thèse de C. Lemarchand et S. Groh (collaboration entre le LEM et DMSE) [25, 37, 53, 89, 90]. L'article reproduit ci-après [90] contient une discussion des forces et faiblesses de notre modèle 'discret-continu' et une comparaison avec la méthode de superposition.

BOUNDARY PROBLEMS IN DD SIMULATIONS

B. DEVINCRE[1], A. ROOS[2] AND S. GROH[1]
[1]*LEM, CNRS-ONERA, 29 av. de la division Leclerc, 92322 Chatillon Cedex, France*
[2]*DMSE/LCME, ONERA, 29 av. de la division Leclerc, 92322 Chatillon Cedex, France*

Abstract. Over the years, different approaches have been developed to calculate the state of mechanical equilibrium in a dislocated finite body. The purpose of this paper is to show the common aspects among the approaches used with Dislocation Dynamics simulations, as well as their distinctitive features. Given the uniqueness of the solution, an attempt is made to explicitly illustrate how it is translated within the different existing frameworks. Two approaches are distinguished according to whether the stress singularity along the dislocations lines is homogenized or not. It is shown that the solution to be preferred depends on the problems at hand.

1. Introduction

Over the years, different methods have been developed to calculate the state of mechanical equilibrium in a dislocated finite body. Recently, such studies were found to be useful for the development of exact 3D simulations of dislocation dynamics (DD). In this paper, a critical review of the existing numerical solutions is carried out. Such solutions are based on the *superposition method* [1, 2, 3, 4] and the *Discrete-Continuous Model* (DCM) [5, 6]. Although the underlying physical problem is the same, and therefore also its mechanical solution, these methods follow different strategies. As a consequence, it is not always clear how and where exactly they differ or are similar. Our purpose is here to establish their common features and their differences in a concise manner, as well as to determine their preferential domain of application. By lack of space, the case of simulations making use of periodic boundary conditions, as well as the recent phase-field approaches used to model dislocation dynamics, are not considered.

Throughout this study, use is made of normal type (a) to denote scalar quantities and of bold characters ($\mathbf{a}$) for vectors. Second order tensors are underlined ($\underline{a}$), and fourth order tensors are doubly underlined $\underline{\underline{a}}$.

2. Statement of the problem

2.1. DISLOCATIONS IN A CONTINUUM MEDIUM

Following the seminal work of Mura [7], dislocations can be regarded as line defects causing eigenstresses in an elastic medium. For each dislocation, a volume C is defined, which surrounds the line and its slip trace (see figure 1). Within this volume (of penny shape with constant thickness h in the direction $\mathbf{n}$, normal to the dislocation slip plane) an eigenstrain field, $\underline{\varepsilon}^p$, exists that leaves into the medium a plastic deformation in the form of a displacement shift (or shear). The direction and the magnitude of this plastic shear are characterized by the Burgers vector, $\mathbf{b}$. Outside C and at the boundary ∂C, the eigenstrain $\underline{\varepsilon}^p$ is by definition equal to zero. When a small volume element v included in V is sheared by several dislocation segments i, the associated eigenstrain is denoted by $\underline{\varepsilon}^p_v = \sum_i \underline{\varepsilon}^{p,i}$. One must realize that the dislocation core properties are not accounted for in this framework, but this is not a problem in what follows since the dislocation core structure has a weak influence on the boundary value problem.

In a few ideal cases, such as dislocations in an infinite elastic medium and with a Heaviside step function as eigenstrain solution, the mechanical problem of the equilibrium state of a dislocated body can be solved analytically. This development is reported in many textbooks (see for instance [7]) and is, therefore, not be reproduced here. One must only keep in mind that the solutions for $\underline{\sigma}^\infty$ and $\underline{\varepsilon}^\infty$ are relatively simple and are commonly used to predict the elastic properties of dislocations [8].

2.2. MECHANICAL EQUILIBRIUM IN A FINITE BODY

Van der Giessen and Needleman [1] were the first to emphasize the importance of the boundary value problem in mesoscopic simulations of plastic deformation. Indeed, DD codes, in their standard formulation, use for reason of simplicity and code efficiency analytical forms justified only in an isotropic infinite body. When a finite body is concerned, or when there are internal interfaces, this simple solution is *a priori* no longer valid and the true boundary value problem (BVP) has to be solved.

Consider, as in figure 1, a computational volume V, which may contain elastic inclusions of volume V^* and dislocations (line segments i) in a matrix phase $V^M = V - V^*$. The elastic properties of the matrix are governed by the fourth-order tensor $\underline{\underline{L}}^M$, while the elastic modulus tensor of the inclusion

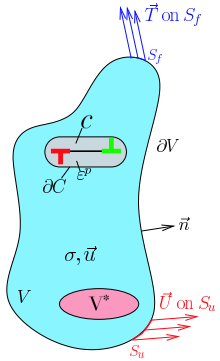

Figure 1. Statement of the mechanical problem. A description of all quantities can be found in the text. In mechanical equilibrium all fields must satisfy equation (1).

is denoted $\underline{\underline{L}}^*$. Tractions $\mathbf{T}$ can be prescribed at the boundary S_f, and displacements $\mathbf{U}$ at the boundary S_u. The latter may also include a plastic displacement $\mathbf{u}^p$ induced by dislocations that moved out of the volume V in an earlier deformation stage. The outward normal to the surface is denoted by $\mathbf{n}$.

In the absence of overall body forces, the equilibrium state of the total volume is described by the stress field $\underline{\sigma}$ and the total strain field $\underline{\varepsilon}$ that must satisfy:

$$\left\{\begin{array}{rcl} \nabla\cdot\underline{\sigma} & = & \mathbf{0} \\ \underline{\sigma}\cdot\mathbf{n} & = & \mathbf{T} \text{ at } S_f \\ \mathbf{u} & = & \mathbf{U} \text{ at } S_u \\ \nabla\mathbf{u} & = & \underline{\varepsilon} \\ \underline{\sigma} & = & \underline{\underline{L}}^M : (\underline{\varepsilon} - \underline{\varepsilon}^p) \text{ in } V^M \\ \underline{\sigma} & = & \underline{\underline{L}}^* : \underline{\varepsilon} \text{ in } V^* \end{array}\right. \tag{1}$$

3. Solution strategies for DD simulations

Depending upon the precision required and on the nature of the problem to be solved, different numerical methods are available for computing field that satisfy equations (1). Two approaches are particularly well adapted to DD simulations and have been the object of several applications. Both of them make use of a coupling with a Finite Element (FE) code, but the resolution of the algebraic equations involved is not attached to any particular method.

For instance, Boundary Elements, Finite Volume or Element Free Galerkin methods could be a good alternative to the classical FE approach.

3.1. THE DISCRETE-CONTINUOUS MODEL

The Discrete-Continuous Model (DCM) was the first solution effectively used in conjunction with 3D simulations of dislocation dynamics [5, 6]. In this method, a FE code computes directly the displacement field satisfying equations (1), making use of the plastic strain, $\underline{\varepsilon}^p$, yielded by the DD simulation. Thus the DD code serves as a substitute for the constitutive form used in standard FE frameworks. The most difficult part of the coupling consists in setting conditions that leave the possibility for the FE mesh to capture the complexity of the elastic fields involved during plastic deformation. Two important steps of the computational method must be distinguished: a homogenization procedure for the calculation of $\underline{\varepsilon}^p$ and an interpolation procedure for the calculation of $\underline{\sigma}$.

The homogenization procedure is certainly the most critical part of the method, and a publication has been dedicated to it[9]. In consistency with the framework recalled in § 2.1, the plastic shear associated with the motion of dislocations is extended over a slab of thickness h. This is formally equivalent to replacing one dislocation by a continuum distribution of parallel infinitesimal dislocations, or to distributing the eigenstrains $\underline{\varepsilon}^{p,i}$ of each dislocation i over a large slab, rather than on an infinitely thin plate. Within the slab of typical thickness $h = 3\, v_G^{1/3}$ (v_G is the elementary volume associated to the Gauss points in the FE mesh), the Burgers vector can be split linearly or with the help of a shape function that helps localizing the dislocation slip plane in the FE mesh. In what follows, only the linear solution will be considered for the sake of simplicity, although a polynomial solution is preferred in the practice.

When a dislocation segment i belonging to the slip system of normal $\mathbf{n}$ and Burgers vector $\mathbf{b}^i$ moves, it generates increments of resolved plastic shear. These increments, $\Delta\gamma^i_{n,e}$, are homogenized within the elementary volumes $v_{G,e}$ of the Gauss points e according to:

$$\Delta\gamma^i_{n,e} = \frac{(b^i/h)v^i_{int,e}}{v_{G,e}} \tag{2}$$

where $v^i_{int,e}$ is the volume of intersection between the sheared slab of segment i and a volume $v_{G,e}$. Notice that C^i and $v^i_{int,e}$ are related by:

$$C^i = \sum_e v^i_{int,e} \tag{3}$$

Then, the plastic strain increment at each Gauss point of the FE mesh is the sum of the contributions of all the segments i of unit shear direction $\mathbf{l}^i = \mathbf{b}^i/b^i$ and moving in $v_{G,e}$:

$$\Delta\underline{\varepsilon}^p_{,e} = \sum_i \Delta\gamma^i_{n,e}(\mathbf{l}^i \otimes \mathbf{n}^i)^{sym} \tag{4}$$

Finally, to obtain the total plastic strain at step k, the sum of all increments from step 0 to step k is needed:

$$\underline{\varepsilon}^p_{,e} = \sum_0^k \Delta\underline{\varepsilon}^p_{,e} \tag{5}$$

Once $\underline{\varepsilon}^p$ is defined at each Gauss point of the FE mesh, the problem of the equilibrium state (Eq. 1) can be solved in a conventional manner. The only modification made with respect to an ordinary FE explicit scheme is that the increments of total deformation $\Delta\underline{\varepsilon}_{,e}$ need to be computed simultaneously everywhere in the FE mesh. This modification is necessary for the DD simulation.

The second critical procedure of the DCM is the interpolation step. This operation is not specific to the DCM and exists in the other approach discussed below. Nevertheless, this procedure is more critical in the DCM case where the FE mesh is strongly deformed. To compute the Peach-Koehler force on each dislocation, the stresses calculated at the Gauss points, $\underline{\sigma}_{,e}$, must be interpolated at reference points along the dislocation line. The quality of this interpolation strongly influences the dynamics of the dislocations. It is directly related to the flexibility offered by the polynomial shape functions associated with the FE mesh. For this reason, mesh elements containing a large number of nodes and Gauss points are required. Typically, the DCM calculations make use of elements consisting of 20 nodes - 27 Gauss points.

3.2. THE SUPERPOSITION METHOD

This approach was first used by Van der Giessen and Needleman [1] for 2-D simulations, but is now applied to 3-D simulations [2, 3, 4]. The basic objective of this method is to enable an accurate description of the dislocation-dislocation interactions at short distances, while, at the same time, simplifying as much as possible the computations delivered to the FE code. In rough terms, the idea is to eliminate from the FE mesh the elastic singularity associated to the dislocation fields. This can be done by extracting the singular solutions for dislocations in an infinite body, $\underline{\sigma}^\infty$ and $\mathbf{u}^\infty$ (see § 2.1) from the whole mechanical problem.

More precisely, the simulated problem (cf. fig. 1) is decomposed into two sub-problems. The first sub-problem is that of interacting dislocations in a homogeneous, isotropic, infinite solid, the ($\widetilde{}$) fields, and the second one is the complementary problem of accounting for the initial non-homogeneous body, but without dislocations and with modified boundary conditions, the ($\widehat{}$) fields. The state of the simulated body is then re-written as the superposition of two fields:

$$\begin{array}{rcl} \mathbf{u} & = & \widehat{\mathbf{u}} + \widetilde{\mathbf{u}} \\ \underline{\varepsilon} & = & \underline{\widehat{\varepsilon}} + \underline{\widetilde{\varepsilon}} \\ \underline{\sigma} & = & \underline{\widehat{\sigma}} + \underline{\widetilde{\sigma}} \end{array} \tag{6}$$

Note that the fields of the ($\widetilde{}$) sub-problem may be decomposed again into two contributions:

$$\begin{array}{rcl} \widetilde{\mathbf{u}} & = & \mathbf{u}^\infty + \mathbf{u}^b \\ \underline{\widetilde{\varepsilon}} & = & \underline{\varepsilon}^\infty + \underline{\varepsilon}^b \\ \underline{\widetilde{\sigma}} & = & \underline{\sigma}^\infty \end{array} \tag{7}$$

where the additional fields $\mathbf{u}^b$ and $\underline{\varepsilon}^b$ exist only at the boundary and account for the body shape transformation. Indeed, each time a dislocation moves out of the finite body, it vanishes at the surface leaving a step of magnitude b, and the shape of the finite body is changed. Accounting for this dislocation-boundary interaction is one of the most difficult parts of the superposition method. Among possible solutions, the concept of virtual dislocations developed by Weygand *et al.* [10] is extremely useful. To avoid the cumputation of $\mathbf{u}^b$ and $\underline{\varepsilon}^b$, it is suggested that the outgoing dislocations should never be eliminated, but accumulated outside the simulated body, at virtual coordinates consistent with the dislocation slip planes. The benefit of that procedure is that displacements at the boundary are computed in the same manner as in the volume.

Then, the governing equations for the ($\widetilde{}$) fields are, by construction, free of boundary conditions and can be summarized as follows:

$$\left\{ \begin{array}{rcll} \nabla\cdot\underline{\widetilde{\sigma}} & = & \mathbf{0} & \\ \underline{\widetilde{\sigma}} & = & \underline{\underline{\underline{\underline{L}}}} : \underline{\widetilde{\varepsilon}} & \text{in } V = V^M \cup V^* \\ \underline{\widetilde{\varepsilon}} & = & \nabla\widetilde{\mathbf{u}} & \end{array} \right. \tag{8}$$

With the help of equations (1), (6) and (8), we can now define the equations governing the sub-problem for the ($\widehat{}$) fields:

i) in V

$$\begin{array}{rcl} \nabla\cdot\underline{\sigma}=\mathbf{0} & <=> & \nabla\cdot(\underline{\widehat{\sigma}}+\underline{\widetilde{\sigma}})=\nabla\cdot\underline{\widehat{\sigma}}+\nabla\cdot\underline{\widetilde{\sigma}}=\nabla\cdot\underline{\widehat{\sigma}} \\ & => & \nabla\cdot\underline{\widehat{\sigma}}=\mathbf{0} \end{array} \tag{9}$$

and

$$\begin{array}{rcl} \underline{\varepsilon}=\underline{\widehat{\varepsilon}}+\underline{\widetilde{\varepsilon}}=\nabla\mathbf{u} & <=> & \underline{\varepsilon}-\underline{\widetilde{\varepsilon}}=\nabla\mathbf{u}-\nabla\widetilde{\mathbf{u}} \\ & => & \underline{\widehat{\varepsilon}}=\nabla\widehat{\mathbf{u}} \end{array} \tag{10}$$

ii) at the boundary we have on S_f:

$$\begin{array}{rcl} \underline{\sigma}\cdot\mathbf{n}=\mathbf{T} & <=> & \underline{\widehat{\sigma}}\cdot\mathbf{n}=\mathbf{T}-\underline{\widetilde{\sigma}}\cdot\mathbf{n} \\ & => & \underline{\widehat{\sigma}}\cdot\mathbf{n}=\mathbf{T}-\widetilde{\mathbf{T}} \end{array} \tag{11}$$

and on S_u:

$$\begin{array}{rcl} \mathbf{u} & = & \widehat{\mathbf{u}}+\widetilde{\mathbf{u}}=\mathbf{u}^{app} \\ & => & \widehat{\mathbf{u}}=\mathbf{u}^{app}-\widetilde{\mathbf{u}} \end{array} \tag{12}$$

iii) finally, keeping in mind that $\underline{\varepsilon}^p$ is non-zero only inside C and that the thickness of C tends to zero when the analytical solutions hold, we have in V^M:

$$\begin{array}{rcl} \underline{\sigma}=\underline{\underline{L}}:(\underline{\varepsilon}-\underline{\varepsilon}^p) & = & \underline{\underline{L}}:(\underline{\widehat{\varepsilon}}+\underline{\widetilde{\varepsilon}}-\underline{\varepsilon}^p)=\underline{\underline{L}}:(\underline{\widehat{\varepsilon}}+\underline{\widetilde{\varepsilon}})=\underline{\underline{L}}:\underline{\widehat{\varepsilon}}+\underline{\widetilde{\sigma}} \\ & => & \underline{\widehat{\sigma}}=\underline{\underline{L}}:\underline{\widehat{\varepsilon}} \end{array} \tag{13}$$

and in V^*:

$$\begin{array}{rcl} \underline{\sigma}=\underline{\widehat{\sigma}}+\underline{\widetilde{\sigma}} & = & \underline{\underline{L}}^*:\underline{\varepsilon}=\underline{\underline{L}}^*:(\underline{\widehat{\varepsilon}}+\underline{\widetilde{\varepsilon}}) \\ & => & \underline{\widehat{\sigma}}=\underline{\underline{L}}^*:\underline{\widehat{\varepsilon}}+(\underline{\underline{L}}^*-\underline{\underline{L}}):\underline{\widetilde{\varepsilon}} \end{array} \tag{14}$$

In summary, the equilibrium state equations for the ($\widehat{\ }$) sub-problem are:

$$\left\{\begin{array}{rcl} \nabla\cdot\underline{\widehat{\sigma}} & = & \mathbf{0} \\ \underline{\widehat{\sigma}}\cdot\mathbf{n} & = & \mathbf{T}^{app}-\underline{\sigma}^{\infty}\cdot\mathbf{n} \quad \text{at } S_f \\ \widehat{\mathbf{u}} & = & \mathbf{U}^{app}-\widetilde{\mathbf{u}} \quad \text{at } S_u \\ \nabla\widehat{\mathbf{u}} & = & \underline{\widehat{\varepsilon}} \\ \underline{\widehat{\sigma}} & = & \underline{\underline{L}}:\underline{\widehat{\varepsilon}} \quad \text{in } V^M \\ \underline{\widehat{\sigma}} & = & \underline{\underline{L}}^*:\underline{\widehat{\varepsilon}}+(\underline{\underline{L}}^*-\underline{\underline{L}}):\underline{\widetilde{\varepsilon}} \quad \text{in } V^* \end{array}\right. \tag{15}$$

By resolving this elastic problem with a FE meshing, and adding the analytical solutions of the ($\widetilde{\ }$) fields problem to that solution, i.e. by adding σ^{∞}, $\varepsilon^{\infty}[+\varepsilon^b]$ and $\mathbf{u}^{\infty}[+\mathbf{u}^b]$, one can determine solutions for the total problem as defined in equations (1).

4. Discussion

In this section the strengths and weaknesses of the BVP solutions presented in §3 are compared. The discussion is based on the authors' recent evaluations and validation tests. We tried, as much as possible, to restrict our comments to general features independent of the coding details of the simulations.

In terms of CPU, the comparison of the DCM and the superposition method is usually in favor of the last one. Indeed, as mentioned in §3.1, the DCM requires a more detailed meshing (i.e. more elements with many nodes and Gauss points) and, therefore, larger computations. Also, the superposition method requires only data transfer between the DD and FE codes at the boundary elements of the mesh, whereas, the DCM imposes data transfer everywhere. From a practical viewpoint, the implementation of DD-FE coupling based on the superposition approach is easier to realize, but this last point may depend on the FE code that is used. From a theoretical point of view, the two approaches are perfectly equivalent with one exception; calculations in an elastically anisotropic medium can be realized much more easily using the DCM approach. Indeed, for the superposition solution to be efficient, analytical forms are required for the displacement field of dislocation segments and for anisotropic media a general solution does not exist. In contrast, elastic anisotropy is easily taken into account with the DCM by only changing one input of the DCM calculation: the tensor of elastic moduli of the considered material. As a result, computing times are virtually the same for isotropic and anisotropic simulations.

To obtain the stress at an arbitrary position in the simulated body, FEs are using shape functions which interpolate the stresses calculated at Gauss points. A basic hypothesis of the classical FE method imposes that these shape functions are continuous within the elements. Since the dislocation fields vary as the inverse of the distance to the line, the resulting singularities at the dislocation line cannot be exactly accounted for. For instance, our tests show that quadratic elements (i.e. with a polynomial shape function of order two) become inaccurate at distances from a dislocation line of the order of $v_G^{1/3}$. This is why, without correction, the DCM cannot precisely account for dislocation-dislocation contact and short distance interactions. An immediate solution to this problem consists in refining the mesh and, consequently, decreasing the homogenization thickness h around the dislocation lines. The latter is directly linked to the size of finite element mesh and to v_G. However, this leads rapidly to useless simulations in term of computation times, especially in 3D. Alternatively, we can use in the DCM analytical forms for segment-segment elastic interactions at short distances (i.e. when two segments are at a distance smaller than 1.7 $v_G^{1/3}$).

This additional force contribution to the dislocation dynamics simulation can be regarded as a constitutive rule caring of the lack of accuracy of the FE mesh at short distance.

It is interesting to note that the above problem of the DCM approach turns into an advantage when dislocation segments are close to boundaries. Indeed, in the superposition approach the boundary conditions on S_f and/or S_u contain an image contribution proportional to minus σ^∞ and $\mathbf{u}^\infty$, respectively. When a dislocation approaches the boundary, these contributions diverge, and in fact become infinite when dislocations touch a Gauss point at the boundary. To precisely account for this surface effect requires an accurate subtraction of the large ($\widetilde{\ }$) and ($\widehat{\ }$) fields, hence a remeshing of the boundaries close to the points where segments are emerging [11]. Without such a procedure, important errors arise on the amplitude of the image force (the nodes at the surface elements cannot accommodate the important elastic displacement imposed by the emerging dislocations). To the best knowledge of the authors, no satisfactory solution to this problem has been published yet. On the other hand, as a result of the homogenization procedure, such difficulty is not met within the DCM approach. The only limitation is that the amplitude of the image force close to the surface may be smaller than the elastic prediction because of the smoothing of the shape functions.

Lastly, as emphasized by equation (14), the existence of elastic inclusions in the simulated body impose additional computations to the superposition approach and makes it less attractive by comparison to the DCM scheme, since the latter is transparent to this problem. As discussed in reference [1] and [12], in the case of the superposition approach, two-phase problems impose the calculation of the so-called polarization stresses in the inclusions, $\widehat{\underline{p}} = (\underline{\underline{L}}^* - \underline{\underline{L}}) : \widetilde{\underline{\varepsilon}} = (\underline{\underline{L}}^* : \underline{\underline{L}}^{-1} - \underline{\underline{I}}) : \widetilde{\underline{\sigma}}$. Hence, the number of analytical calculations of the $\widetilde{\underline{\sigma}}$ solutions at each step of the simulation is significantly increased (in addition to the boundary calculation, the stress field of each segments must be calculated at each Gauss points in V^*).

5. Conclusion

In this paper, we provide a non-exhaustive list of advantages and disadvantages of the two numerical approaches used to solve boundary value problems in DD simulations, respectively the DCM and the superposition method. During these early stages of development of these simulation techniques, our aim was to draw the contour of their domains of excellence. Based on the comments made in §4, our recommendation to those starting in this field could be to try first the superposition method. This approach is easy to implement, delivers precise results and is efficient in terms of

CPU for simple problems. Then, for those interested in problems with a large density of dislocations and complex materials (e.g. multiphase materials, materials with strong elastic anisotropy materials, materials exhibiting plastic strain localization, ...) our preference would go to the second approach. Indeed, the DCM is numerically competitive (even faster) with large numbers of segments. Furthermore, with its concept of plastic strain homogenization,it provides an interesting self-consistent description of plasticity compatible with mesoscopic (discrete) and macroscopic(continuous) modeling of solid mechanics.

6. Acknowledgments

The authors wish to thank J-L. Chaboche, F. Feyel and L.P. Kubin for helpful discussions.

References

1. E. Van der Giessen and A. Needleman, Model. Simul. Mater. Sci. Eng. **3**, 689 (1995).
2. D. Weygand, E. Van der Giessen and A. Needleman, Mat. Sci. Eng. **A309-310**, 420 (2001).
3. C.S. Shin, M.C. Fivel and K.H. Oh, J. Phys. IV France **11**, Pr5-27 (2001).
4. H. Yasin, H.M. Zbib and M.A. Khaleel, Mat. Sci. Eng. **A309-310**, 294 (2001).
5. C. Lemarchand, B. Devincre, L.P. Kubin and J.L. Chaboche, MRS Symposium Proceedings **538**, 63 (1999).
6. C. Lemarchand, Ph.D. Thesis, University of Paris VI (1999).
7. T. Mura,"Micromechanics of defects in solids", Second edition, Kluwer Academic Publishers (1993).
8. J.P. Hirth and J. Lothe,"Theory of dislocations", Second edition, John Wiley and Sons (1982).
9. C. Lemarchand, B. Devincre and L.P. Kubin, Journal of the Mechanics and Physics of Solids **49**, 1969 (2001).
10. D. Weygand, L.H. Friedman, E. Van der Giessen, A. Needleman, Model. and Simu. in Mat. Sci. and Eng. **10**, 437 (2002).
11. M.C. Fivel, T.J. Gosling and G.R. Canova Model. Simul. Mater. Sci. Eng. **4**, 581 (1996).
12. C.S. Shin, M.C. Fivel and K.H. Oh J. Phys. IV France **11**, 27 (2001).

2.4. Intégration des équations du mouvement

Dans les matériaux à faible friction de réseau, les dislocations peuvent se déplacer rapidement entre obstacles. Quand cette vitesse, v, reste faible devant la vitesse du son, c_t, dans le matériau, $v < c_t/2$, l'ensemble des mécanismes physiques déterminant le mouvement des dislocations en régime permanent peut être modélisé par un coefficient de frottement visqueux, $B(T)$ (cf. § 4.1). Ce coefficient tient compte essentiellement des diverses interactions des dislocations avec les phonons et, à basse température, avec les électrons. Les valeurs de ce coefficient peuvent être déterminées expérimentalement pour un petit nombre de matériaux [91, 92], et théoriquement par des modèles mésoscopiques [91] ou à l'aide de simulations atomiques [93, 94]. Dans le cas du cuivre, qui est le matériau le plus étudié, les diverses estimations convergent vers $B(300\text{K}) \approx 1.5 \times 10^{-5}$ Pa s.

Ce coefficient de frottement connu, l'équation du mouvement d'une section de ligne de dislocation de direction x et qui se déplace suivant la direction u s'écrit :

$$m\frac{\partial^2 u}{\partial t^2} + B(T)\frac{\partial u}{\partial t} = \tau^* b + \frac{\Gamma}{R} \tag{2.3}$$

Tous les termes de l'équation (2.3) sont exprimés par unité de longueur de dislocation. Les deux termes à gauche de l'égalité représentent respectivement, les effets d'inertie et de frottement visqueux. Lorsque la vitesse est inférieure à $c_t/2$, les effets relativistes associés aux déplacement des dislocations à grande vitesse peuvent être négligés. La masse effective d'une dislocation est alors $m \approx m_o \approx \rho_o b^2$, où ρ_o est la densité du matériau. A droite de l'égalité, la force totale sur les dislocations est décomposée en deux termes qui sont respectivement la force de Peach-Koehler effective, contenant notamment l'effet de la contrainte appliquée, τ_a, dont on a retiré la tension de ligne locale. Cette dernière quantité s'écrit Γ/R et dépend de u et de x via le rayon de courbure R. L'équation (2.3) est l'équation maîtresse du modèle des cordes vibrantes de Granato et Lücke [95]. Dans le cas le plus général, elle doit être intégrée numériquement. Cependant, dans le cas des modélisations mésoscopiques, des simplifications peuvent être faites.

En présence d'un frottement visqueux, on suppose dans un calcul traditionnel que les dislocations se déplacent en restant rectilignes, de manière à éviter de calculer la tension de ligne. L'équation (2.3) se réduit alors à une forme simplifiée fonction de la vitesse, $v(t)$, de la ligne :

$$m_o\frac{dv}{\mathrm{d}t} + B(T)v = \tau^* b \tag{2.4}$$

La solution unique de cette équation diférentielle est de la forme :

$$v = v_s[1 - \exp(-t/t_o)], \tag{2.5}$$

où v_s une vitesse de régime stationnaire, et t_o un temps caractéristique pour atteindre cette vitesse. Ces deux quantités sont donnés par

$$v_s = \tau^* b/B(T) \quad \text{et} \quad t_o = \rho_o b^2/B(T). \tag{2.6}$$

Dans le cas du cuivre ($\rho_o = 8 \times 10^3\,\mathrm{kg\,m^{-3}}$, $b = 2.55 \times 10^{-10}\,\mathrm{m}$ et pour une contrainte appliquée projetée $\tau^* \approx \tau_a = 1\mathrm{MPa}$), la vitesse de régime stationnaire, $v_s \approx \tau^* \times 2.\,10^{-5} \approx 20\mathrm{m\,s^{-1}}$, est atteinte après un temps caractéristique $t_o = 10^{-10} - 10^{-11}$ s à 300 K. En fait, Le pas de temps élémentaire de la DD étant généralement plus grand ou du même ordre de grandeur que t_o, les dislocations sont toujours en régime stationnaire et il est justifié de négliger les effets d'inertie. Cela est d'autant plus vrai que dans la DD, il faut retirer la tension de ligne de la force de Peach-Koehler effective, car la courbure locale des dislocations est prise en compte. L'équation du mouvement (2.6) se réduit alors à une forme linéaire simple :

$$v = \frac{\tau^* b}{B(T)} \tag{2.7}$$

Cette expression est celle la plus souvent utilisée pour décrire le glissement des dislocations, pour des matériaux comme les CFC où la force de frottement de réseau est négligeable. Son domaine de validité doit, en tout rigueur, être restreint aux sollicitations où l'approximation de régime stationnaire est justifiée. Si on utilise une simulation de DD à des échelles fines se rapprochant des dimensions interatomiques [94] ou lorsqu'on considère de très grandes vitesses de déformation, il faut revenir à l'équation (2.4). De même, lorsque le glissement des dislocations met en jeu des mécanismes thermiquement activés, l'équation (2.7) doit être remplacée par des lois de vitesse semi-phénoménologiques (lois d'Arrhenius) qui, toujours dans une hypothèse de régime stationnaire, reproduisent le caractère stochastique du franchissement d'obstacles. Un exemple de telles lois de mobilité est donné au Chapitre 4 (§ 4.2.2), dans le cas de la plasticité des monocristaux de zirconium.

Lorsque l'approximation de régime stationnaire est valide, la trajectoire des segments de dislocation définie par leur coordonnée $r(t)$ au temps t, peut être calculée au temps, $t_{n+1} = t_n + \Delta t$, à l'aide d'un schéma d'intégration explicite d'Euler :

$$r(t + \Delta t) = r(t) + v(t)\Delta t \tag{2.8}$$

si l'on veut prendre en compte les effets d'inertie, il faut utiliser des algorithmes d'intégration plus sophistiqués comme l'algorithme de Verlet ou celui de Runge-Kutta.

Pour des raisons de simplicité, l'intégration des équations du mouvement est souvent traitée de façon locale. Durant un pas de simulation Δt, le déplacement de chaque segment d'une ligne de dislocation est appliqué indépendamment des déplacements de ses segments voisins. Cependant, en toute rigueur, et pour augmenter le pas de temps des simulations, il est possible d'amortir les fluctuations des vitesses le long des lignes en corrélant les déplacements de segments voisins. Par analogie avec la méthode des éléments finis à une dimension, le principe des travaux virtuels permet de définir dans ce cas la vitesse à un point d'intégration PI sur un segment [86, 96] :

$$v_{PI} = (N_{PI_p} v_{PI_p} \underline{d_{PI_p}} + N_{PI} v_{PI} \underline{d_{PI}} + N_{PI_s} v_{PI_s} \underline{d_{PI_s}}).\underline{d_{PI}} \tag{2.9}$$

où PI_p et PI_s désignent respectivement les points d'intégrations sur les segments "précédant" et "suivant" le segment contenant PI. $\underline{d}$ est le vecteur direction de glissement normal à la ligne aux points d'intégration et N une fonction de forme linéaire définissant le poids numérique à attribuer à chacun des trois points d'intégration en fonction de la longueur des segments.

Pour terminer cette discussion, il faut mentionner qu'au cours de l'intégration des équations du mouvement, des vitesses de segments beaucoup trop importantes et irréalistes peuvent être occasionnellement obtenues pour des géométries de ligne mal relaxées[7]. Pour assurer la stabilité de l'intégration et ne pas trop réduire le pas de temps des simulations, une vitesse maximale à ne pas dépasser est imposée à tous les segments. Cette vitesse de coupure est choisie de manière à ne pas affecter le comportement d'ensemble de la simulation (par exemple $v_{max} \approx c_t/2$).

2.5. Conditions initiales et données de sortie des simulations

Les simulations de DD sont basées sur la théorie élastique, qui est continue, et les seules échelles de dimension présentes sont le vecteur de Burgers des dislocations ou le paramètre de maille du réseau cristallin. On peut donc passer continûment de la simulation d'un élément de volume de quelques dizaines de vecteur de Burgers de côté, à celle de volumes beaucoup plus grands en augmentant le pas

[7] Ces configurations de ligne sont inévitables et apparaissent par exemple après l'annihilation de deux lignes ou encore durant la formation et la destruction d'une jonction entre deux dislocations.

de discrétisation des lignes. La dimension maximale de l'élément de volume pouvant être simulé est définie au cas par cas. Elle dépend du nombre de segments (approximativement la densité de dislocations) estimé en fin de simulation et de la longueur caractéristique des fluctuations de la contrainte dans le matériau [8]. En règle générale, les volumes simulés ont une dimension qui va de $(10\mu m)^3$ dans la plupart des matériaux jusqu'à $(100\mu m)^3$ pour les matériaux les plus favorables, comme le silicium où la densité initiale de dislocations est beaucoup plus faible que dans les métaux.

Dans de très nombreuses simulations la microstructure servant de configuration initiale est constituée d'une distribution aléatoire de sources de Frank-Read, c'est-à-dire de segments de dislocations ancrés à leurs extrémités. Ce type de configuration est fréquemment utilisé, car il est simple, mais il pose problème dans certains cas. Ainsi, dans les CFC, la longueur L_s des segments sources doit être grande par rapport à la distance moyenne entre dislocations ($L_s > 5\rho^{-1/2}$) sous peine de voir la contrainte critique de Frank-Read affecter la contrainte d'écoulement. Cependant, en fixant une longueur L_s relativement grande, on permet durant les premiers pas de simulation la formation des jonctions de longueur très supérieure à $\rho^{-1/2}$. De même, une microstructure initiale de dislocations contenant beaucoup de point d'ancrages sera difficile à relaxer et influencera fortement et durablement la déformation plastique.

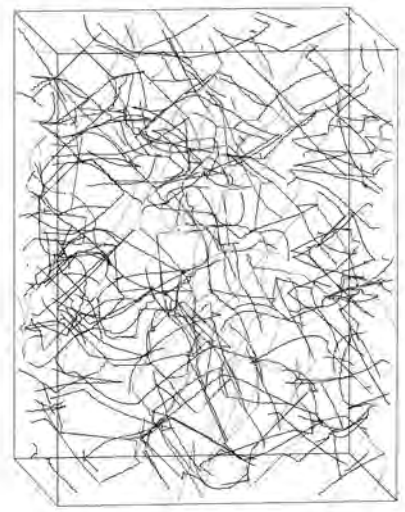

FIG. 2.6.: Exemple de microstructure initiale relaxée. Cette configuration a été obtenue à partir d'une distribution aléatoire de boucles dipolaires et ne nécessite pas l'introduction de points d'ancrage artificiels.

En règle générale, pour réduire l'influence de ces conditions initiales, il faut prédéformer le volume simulé pour augmenter significativement la densité de dislocations. Il existe cependant une solution alternative à une prédéformation qui, il faut le noter, fait commencer les simulations avec un très grand nombre de segments et donc ralentit beaucoup les calculs. Cette solution est presque aussi simple qu'une distribution de sources et donne de bien meilleurs résultats lorsqu'elle peut être utilisée. Il s'agit d'une distribution de boucles dipolaires, c'est-à-dire quatre dislocations coins de même vecteur de Burgers connectées entre les plans primaire et dévié. Comme l'ont montré les simulations réalisées avec le modèle discret-continu [37], ce type de configuration initiale (cf. figure 2.6) permet de satisfaire rigoureusement les conditions d'équilibre mécanique d'un solide périodique et elle est facile

[8] La simulation de grandes déformations plastiques nécessite de réduire le nombre total de segments, donc la dimension du volume simulé. De même, pour une densité de dislocations fixée, les matériaux où la densité de dislocation est uniformément distribuée permettent d'utiliser de plus grands volumes simulés, car la longueur de discrétisation peut y être plus grande que dans les cas où les dislocations s'organisent de manière hétérogène

à relaxer puisqu'elle ne contient aucun point d'ancrage. Chaque segment des boucles contenu dans un plan de glissement peut fonctionner comme une sources ancrée sur les points à l'intersection entre les plans primaire et dévié[9].

En sortie de simulation, nous obtenons des informations sur la microstructure de dislocations et les quantités physiques locales ou globales qui lui sont associées, contraintes internes, densités de dislocations, distribution de la déformation, activité des systèmes de glissement, etc. Par ailleurs, on peut déterminer différents aspects de la réponse mécanique macroscopiques : courbe contrainte-déformation, vitesse de déformation, apparition d'instabilités plastiques, etc. Dans les années à venir les couplages entre DD et EF donneront accès à de nouvelles informations, comme les champs de rotation locaux ou les efforts de décohésion interfaciale.

En conclusion de ce chapitre, il faut souligner qu'un effort constant a été dédié ces dix dernières années à l'amélioration des performances et de la capacité prédictive des codes de DD. On peut extraire de mes travaux les cinq points les plus importants relatifs à ces récents développements techniques :

1. L'écriture d'un nouveau code de la dynamique des dislocations a été entrepris au LEM en fin 1998. Ce travail réalisé principalement dans le cadre de la thèse de R. Madec et du stage post-doctoral de G. Monnet était devenu nécessaire pour tirer parti de l'expérience accumulée et des progrès accomplis par l'informatique au fil des années. Cette nouvelle version permet une discrétisation accrue du caractère des lignes de dislocation (coin, vis et deux directions mixtes à 60°, cf. Fig. 2.2) et améliore la précision de la méthode tout en réduisant les coûts de calcul. Parmi les avantages de notre nouveau code, l'aspect le plus important est sans doute la possibilité de traiter précisément les réactions de contact entre dislocations. Ce point sera illustré au chapitre 3.
2. Le caractère linéaire des dislocations et le nombre important de systèmes de glissement potentiellement actifs ont longtemps bloqué le développement de conditions aux limites périodiques pour les simulations de DD. Cette insuffisance engendrait des artefacts de calcul et rendait difficile l'interprétation quantitative des simulations. Par exemple, des hétérogénéités de la densité de dislocations aux limites de la cellule de simulation réduisaient sensiblement la taille du volume simulé représentatif des conditions expérimentales. Ce problème a été résolu en 2000. Suite à un travail original de V. Bulatov et col. au Lawrence Livermore National Laboratory, nous avons développé une solution algorithmique élégante qui assure simultanément une continuité de la déformation plastique aux limites du volume simulé, une balance des flux de dislocations et un contrôle du libre parcours moyen effectif des dislocations.
3. Le nombre de segments de dislocations devant être pris en compte dans une simulation augmentant très rapidement avec la déformation plastique, des solutions algorithmiques telle que la méthode des multipôles et la parallèlisation des calculs sur plusieurs ordinateurs ont été développées pour repousser les limites des simulations.
4. Une généralisation cristallographique de notre méthode de discrétisation sur réseau, initialement dédiée aux structures CFC, a été réalisée. Le nouveau code 3-d permet de traiter non seulement les structures cristallines cubiques (CFC, CC, CD) mais aussi les structures hexagonale et orthorhombique. En distribuant librement notre logiciel et en favorisant son utilisation par un nombre de plus en plus important de groupes de recherches, nous souhaitons éprouver les solutions choisies au cours des années passées et, si possible, favoriser le développent de nouvelles étude en métallurgie physique et en mécanique.

[9] La contrainte de multiplication de ces sources est faible puisque la tension de ligne est minimale dans la direction coin

5. Afin de dépasser le stade du monocristal soumis à des contraintes uniaxiales et uniformes, il est nécessaire de pouvoir prendre en compte des situations impliquant soit des sources de contraintes internes (joints de grains, précipités), soit des chargements complexes. Cette "grande unification" entre les approches du physicien métallurgiste et celle du mécanicien est désormais réalisée en couplant la simulation de DD à un code d'éléments finis. Dans ce modèle "discret-continu" (MDC), la partie EF traite tous les problèmes élastiques (conditions d'équilibre de forces en surface et en volume, compatibilité des déformations), tandis que la composante plastique de la déformation est fournie par le code de dynamique des dislocations. En pratique, les problèmes de méthodologie posés par le couplage DD-EF sont assez complexes. Ils résultent de l'incompatibilité fondamentale entre l'approche continue ("rigidité" conceptuelle des maillages éléments finis) et l'approche discrète (divergence des champs élastiques sur les lignes de dislocation). La réalisation de ce couplage a nécessité deux thèses successives (C. Lemarchand et S. Groh), en collaboration avec J.L. Chaboche, F. Feyel et A. Roos à l'ONERA.

CHAPITRE 3

Règle locales et propriétés élémentaires des dislocations

Pour modéliser les propriétés liées à la structure de coeur des dislocations à l'échelle mésoscopique, il faut définir des *règles locales* qui imposent aux dislocations un comportement ne relevant pas de l'élasticité linéaire. Les deux plus importantes d'entre elles concernent le glissement dévié et la relation entre contrainte locale et vitesse. Le traitement des intersections entre dislocations, qui n'est que faiblement lié à la structure de cœur, nécessite également des règles locales, sous la forme de *règles de contact*. La raison en est essentiellement pratique : un traitement purement élastique nécessiterait de réduire considérablement les pas de temps et les longueurs de discrétisation. A l'exception de la formation des jonctions, les mécanismes impliqués varient beaucoup d'un matériau à l'autre. Les règles locales doivent donc être redéfinies partiellement ou totalement pour chaque matériau étudié. Ainsi, elles jouent en DD un rôle similaire aux potentiels d'interaction dans les simulations de Dynamique Moléculaire. Au final, la capacité prédictive des simulations dépend beaucoup du soin apporté à l'élaboration de ces règles. Lorsqu'on réduit la dimensionnalité des simulations de 3-d à 2-d, il devient très difficile de conserver ce réalisme. C'est une des raisons pour lesquelles, la mise en oeuvre de simulations à 2-d doit être évité chaque fois que cela est possible.

Ce chapitre est consacré aux règles locales concernant les jonctions et le glissement dévié, et à deux applications dans lesquelles elles jouent un rôle prépondérant. La discussion des lois de vitesse thermiquement activées des dislocations dans les matériaux à forte friction de réseau est reportée au Chapitre 4. La loi de vitesse des métaux CFC donnée par l'équation 2.7 constitue également une règle locale.

3.1. Réactions de contact entre dislocations

La formation et de la destruction de jonctions entre dislocations est à priori un phénomène complexe à modéliser, qui fait intervenir des interactions élastiques et implique localement une reconstruction des lignes de dislocations. Cependant, on sait depuis longtemps [97], et cela a été vérifié récemment (cf. l'article reproduit ci-dessous) que la contribution des énergies de coeur à la formation de jonctions est négligeable [98, 99, 100]. C'est pourquoi, les réactions de contact entre dislocations peuvent être traitées à l'échelle mésoscopique comme une propriété purement élastique.

Un principe très général est que les règles locales pour les simulations doivent êtres simples et les moins interventionnistes possible. Pour décrire le mécanisme d'intersection des dislocations, on le décompose en quatre étapes :

- Tout d'abord, il faut anticiper et déterminer géométriquement le point où deux dislocations vont se croiser. Un soin important doit être apporté à la programmation de cette partie qui est en DD, après le calcul des contraintes, l'étape la plus consommatrice de CPU ($\approx 15\%$). Suivant le mode de discrétisation, différentes solutions algorithmiques existent. Malheureusement, aucune comparaison des forces et faiblesses de chacune d'entre elles n'a jamais été publiée.
- Ensuite, en fonction du vecteur de Burgers des dislocations, il faut établir une règle prédisant, si une jonction peut se former ou non. Construire une telle règle n'est pas chose simple car les configurations possibles sont nombreuses et ne dépendent pas uniquement du caractère des dislocations près du point de contact. On trouvera en annexe B3, un article illustrant ce point en détail. Il est donc difficile d'anticiper le résultat des intersections à partir d'une règle simple[1]. C'est pourquoi, la meilleure solution consiste à donner au point d'intersection tous les degrés de liberté utiles pour que la jonction puisse se former et s'allonger le long de la ligne d'intersection entre les plans de glissement des dislocations parentes. La direction de réaction est unique pour chaque couple de systèmes de glissement et cette information peut être tabulée pour chaque cristallographie.
- L'étape suivante consiste à vérifier s'il existe des forces pouvant provoquer l'allongement des dislocations dans la direction de jonction. Pour cela, il faut calculer précisément les forces de part et d'autre du point de contact, soit en raffinant la discrétisation des lignes, soit, plus efficacement, en introduisant des points d'intégration spéciaux ou additionnels sur les segments concernés. D'une simulation à l'autre et suivant le mode de discrétisation utilisé, les jonctions peuvent êtres décrites de deux manières différentes. Chaque couple de dislocations en interaction peut être remplacé localement par une ligne de dislocation sessile dont le vecteur de Burgers est la somme vectorielle de ceux des dislocations initiales. Une autre possibilité consiste à immobiliser les segments de dislocation qui se recouvrent le long de la direction de jonction. Ces deux solutions sont strictement équivalentes en élasticité linéaire.
- La dernière étape est associée à la génération de *crans* et de *décrochements* le long des lignes de dislocations, après que celle-ci se soit croisées. La modélisation de ces défauts de dimension atomique ne peut être que phénoménologique à l'échelle mésoscopique. Leur contribution à l'écoulement plastique peut varier d'un matériau à l'autre et doit être traitée avec discernement. C'est pourquoi des solutions très divergentes existent. Dans certaines travaux, la présence de ces défauts est simplement négligée [103]. Cette solution semble correspondre à une réalité expérimentale, au moins dans les matériaux CFC et CC et pour des conditions de déformation normales. Dans la simulation de Zbib et col., [26], les crans sont décrits comme des points d'ancrage forts et avec une force de traînage proportionnelle à l'énergie de formation et de migration des défauts ponctuels (lacunes et interstitiels). Cela pourrait correspondre à une situation rencontrée lors de déformations à grande vitesse. Dans la plupart des publications, cette question difficile est passée sous silence !

Il faut noter qu'à aucun moment il n'est utile de définir un critère de destruction des jonctions[2]. Comme le montrent les résultats de l'article reproduit à la suite de ce paragraphe, c'est le déplacement sous contrainte des bras des dislocations parentes qui fixent la stabilité d'une jonction en augmentant ou réduisant sa longueur. Dans le language imagé des simulations, on dit que la jonction se 'zippe' ou se 'dézippe'. La contrainte de destruction d'une jonction peut donc être calculée précisément dans le cadre de l'élasticité linéaire, sans aucun paramètre ajustable.

[1] Les simulations de DD ont montré que le critère de Frank souvent utilisé lors de calculs analytiques est tout à fait insuffisant. Il faut en pratique utiliser conjointement des expressions de l'énergie de ligne et des forces d'interactions qui prennent en compte le caractère des dislocations en contact [45, 101, 102].

[2] Dans les premières simulations de DD, une contrainte moyenne de destruction des jonctions était définie. Comme l'ont montré de nombreux travaux publiés ces dernières années, il était en fait inutile d'introduire ce paramètre empirique.

Connecting atomistic and mesoscale simulations of crystal plasticity

Vasily Bulatov*, Farid F. Abraham†, Ladislas Kubin‡, Benoit Devincre‡ & Sidney Yip*

* Massachusetts Institute of Technology, Cambridge, Massachusetts 02139, USA
† IBM Research Division, Almaden Research Center, San Jose, California 95120, USA
‡ Laboratoire d'Etude des Microstructures (CNRS-ONERA), 29 Av. de la Division Leclerc, BP72, 92322 Chatillon Cedex, France

A quantitative description of plastic deformation in crystalline solids requires a knowledge of how an assembly of dislocations—the defects responsible for crystal plasticity—evolves under stress[1]. In this context, molecular-dynamics simulations have been used to elucidate interatomic processes on microscopic ($\sim 10^{-10}$ m) scales[2], whereas 'dislocation-dynamics' simulations have explored the long-range elastic interactions between dislocations on mesoscopic ($\sim 10^{-6}$ m) scales[3]. But a quantitative connection between interatomic processes and behaviour on mesoscopic scales has hitherto been lacking. Here we show how such a connection can be made using large-scale (100 million atoms) molecular-dynamics simulations to establish the local rules for mesoscopic simulations of interacting dislocations. In our molecular-dynamics simulations, we observe directly the formation and subsequent destruction of a junction (a Lomer–Cottrell lock) between two dislocations in the plastic zone near a crack tip: the formation of such junctions is an essential process in plastic deformation, as they act as an obstacle to dislocation motion. The force required to destroy this junction is then used to formulate the critical condition for junction destruction in a dislocation-dynamics simulation, the results of which compare well with previous deformation experiments[4].

Recent molecular-dynamics (MD) studies of dynamic crack propagation using 100 million atoms have produced massive amounts of atomic-level details on the spontaneous emission of dislocation loops from the crack tip which result in shielding, blunting and crack arrest[2,5]. A Lennard–Jones potential is used to simulate the response of a face-centred cubic (f.c.c.) structure characterized by a low stacking-fault energy. Figure 1 shows the evolution of a 'flower' of dislocation loops emitted from a crack tip advancing under the action of a transverse applied strain. We shall focus on the evolution of three particular dislocation loops shown in Fig. 1, labelled 1, 2 and 3. In this sequence one sees explicitly, for the first time to our knowledge, how a dislocation junction is first formed (Fig. 1b) and then partially destroyed in a cooperative process which involves the formation of a second junction while the first junction is being unzipped (Fig. 1c). The atomic configuration of the core of the first junction, known as a Lomer–Cottrell lock, is shown in Fig. 2. Dislocation configurations of this kind are believed to be one of the principal mechanisms of strain hardening in f.c.c. metals with low stacking-fault energy.

The process of dislocation junction formation which we have identified in the MD simulation has been discussed only in schematic terms in classical textbooks[1,6,7], but no explicit details produced by quantitative calculations in three dimensions have (to our knowledge) been given before. The rather intricate exchange between the two junctions, apparently unforeseen and unknown, is driven by the balance between the crack-tip stress, dislocation interaction forces, the line tension forces on the mobile dislocation segments, and the constraint forces from the sessile (immobile) junctions. The destruction of Lomer–Cottrell locks has been

thought to involve rather large stresses, because the junction segment is sessile and the whole configuration is fully extended. As shown by the above sequence (Fig. 1), junction destruction is likely to proceed via 'unzipping', that is, motion of the dislocation node along the junction line, as was anticipated by the Friedel–Saada model[1]. If this were indeed the case, then the fate of a given junction should be governed primarily by the force driving nodal displacement, while junction extension, as determined by the stacking-fault energy, should be of secondary importance. Another implication of the observed sequence is that a quantitative physical theory of strain hardening and dynamic recovery behaviour may need to include three-body and higher-order dislocation reactions.

The present example illustrates how large-scale atomistic simulations can provide new insights into possible mechanisms of close-

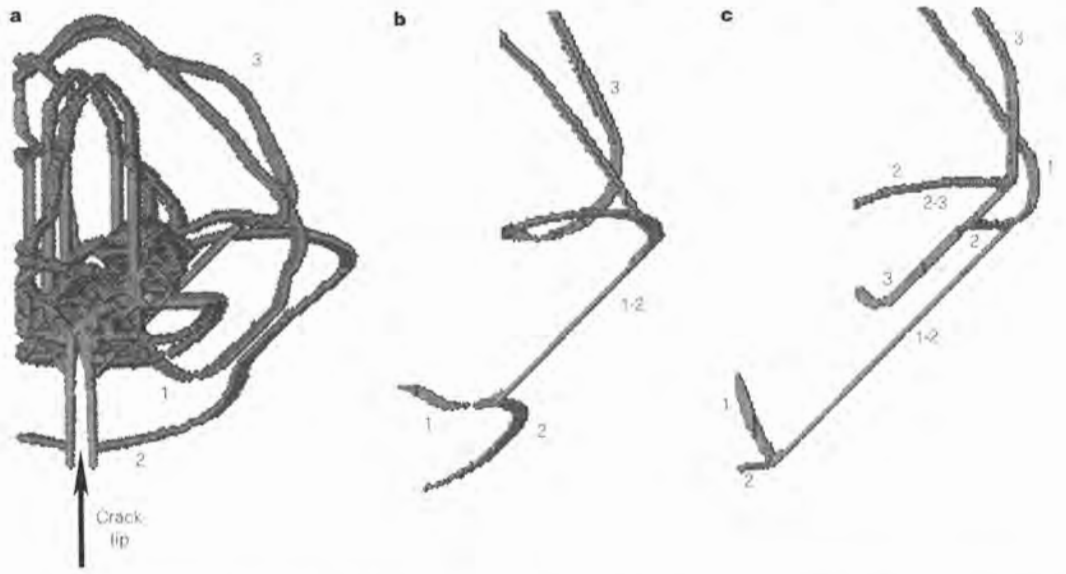

Figure 1 Evolution sequence of dislocation loops emitted spontaneously from an advancing crack tip which is suddenly arrested. In displaying the MD results, only atoms with energies exceeding the ideal bulk value by ≥3% are shown. **a**, The expansion (spreading) of a number of dislocation loops, with loops 1 and 3 gliding in parallel (111) planes and loop 2 gliding in an intersecting ($1\bar{1}1$) plane. As loops 1 and 2 approach each other, their leading segments are seen to attract each other and line up in parallel. These dislocations, on analysis, are found to be Shockley partial (imperfect) dislocations, with co-planar loops having the same Burgers vector, $a/6[11\bar{2}]$ where a is the lattice parameter, while that of loop 2 is $a/6[\bar{2}\bar{1}1]$. In **b**, the leading segments of 1 and 2 have merged, forming a junction dislocation 1–2, or 'zipper', stretching along $[10\bar{1}]$ direction, with Burgers vector equal to the vector sum of the Burgers vectors of the two parent dislocations: $a/6[11\bar{2}] + a/6[\bar{2}\bar{1}1] = a/6[\bar{1}0\bar{1}]$. This reaction product, an imperfect dislocation known as a stair-rod, is sessile (immobile) because its slip plane, defined as the plane containing the line direction and Burgers vector, is not a glide plane in the f.c.c. structure. In **c**, loop 3 now glides in a plane parallel to loop 1. The elastic interaction between loop 3 and junction 1–2 is repulsive, causing loop 3 to line up along the junction. As a part of loop 3 touches the free end of the intersecting loop 2 (on the right), another junction 2–3 of the same Lomer–Cottrell type forms along the stretched segment of loop 3, while simultaneously unzipping the first junction 1–2. (Further details of fracture simulations are available at http://www.almaden.ibm.com/st/Simulate/Fracture)

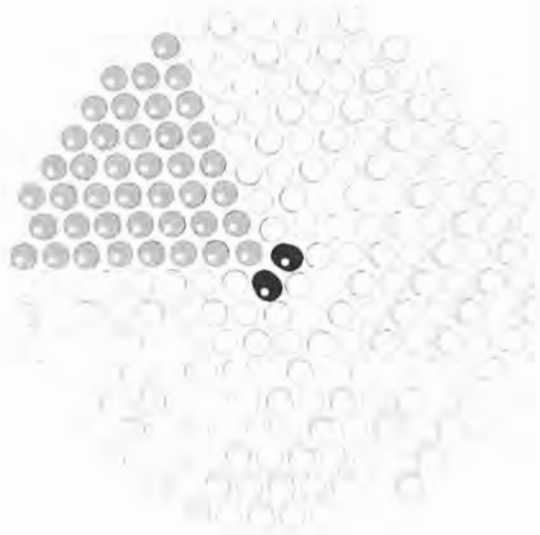

Figure 2 Atomic core structure of the junction dislocation viewed along $[10\bar{1}]$ junction line. The junction (black atoms) appears at the intersection of two stacking faults resulting from two intersecting partial dislocations, each of a mixed, 30° character with respect to the junction line direction. In terms of atomic displacement, the combination of the two partials is equivalent to carving out a triangular wedge (grey atoms) and displacing the wedge matter away from the junction by $a/6[\bar{1}0\bar{1}]$ and along the junction line by $a/4[10\bar{1}]$. The product dislocation is a sessile stair-rod whose core is narrow and energy is low, as indicated by the fact that only two rows of atoms (black) have energies in excess of the 3% threshold. This stair-rod is a part of the so-called Lomer–Cottrell lock[9] which has been observed in experiments[3].

range dislocation interactions. On the other hand, dislocation behaviour is also governed by long-range elastic interactions; a natural length scale for the collective response of dislocation microstructures is in the micrometre range. The appropriate method to treat the elastic interactions is a mesoscopic approach known as dislocation-dynamics. In this method, dislocations are represented by piecewise straight segments connecting the nodes of a regular three-dimensional mesh whose symmetries are those of the underlying crystal structure. Dislocation-dynamics simulations are currently used to examine collective dislocation behaviour on much larger scales, (typically 15 μm) for f.c.c. crystals, and longer time intervals (50 μs) than is feasible with MD. Dislocation-dynamics studies have the potential to probe the macroscopic mechanical response of single crystals controlled by the collective behaviour of dislocations at high densities: such behaviours include the formation and evolution of dislocation microstructures under stress (Fig. 3) which ultimately determine the constitutive behaviour of single crystals in various stages of plastic deformation[8]. Of particular interest is the nature of the reciprocal scaling relationship between yield stress and the length scale of dislocation patterns, postulated to date as a universal empirical 'principle of similitude'.

In dislocation-dynamics simulations, computational efficiency is achieved through a less detailed description of dislocations in which atomic degrees of freedom are replaced by piecewise straight lines, and a mesh spacing (a few nanometres) is used that is larger than the crystal lattice parameter. This means dislocation mobility and close-range interactions are not determined as atomic-level processes, but are specified by external parameters known as 'local rules'[3]. For this approach to be predictive, atomistic behaviour of dislocation cores has to be integrated into meso-scale dislocation-dynamics simulations. We therefore propose to establish a micro-to-meso connection in which the local rules are derived from the physically occurring dislocation core processes in an atomistic simulation. Figure 3c shows the formation, in a meso-scale simulation, of an attractive junction under conditions close to the MD simulation described above. The behaviour of this mesoscopic junction needs to be matched to the behaviour of its atomistic analogue, such as the one shown in Fig. 1b.

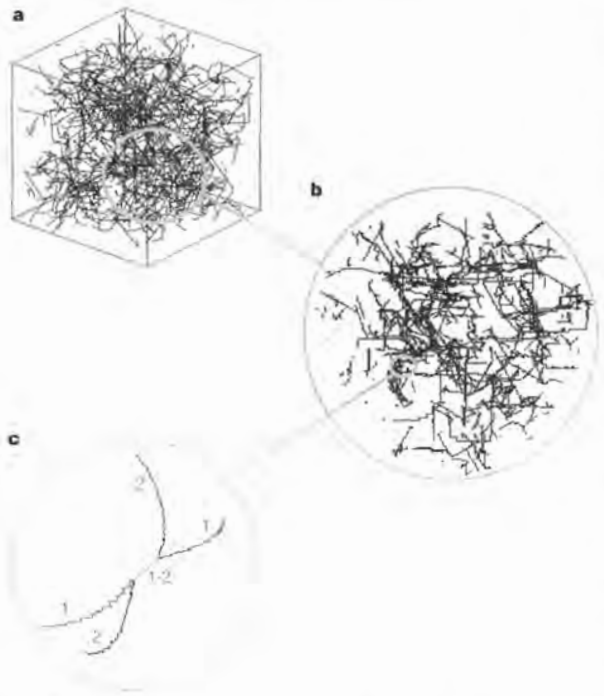

Figure 3 A composite of dislocation-dynamics simulation results. **a**, Snapshot of a dislocation-dynamics simulation where dislocations, at an initial density 2×10^{7} cm^{-2} and placed in the simulation box at random, move in response to external and interaction stresses. **b**, A magnified interior cross-section of thickness 1 μm extracted from the simulation box of **a**; it can be seen that the dislocations are beginning to organize into a cell pattern. **c**, Further magnification showing two dislocation lines 1 and 2 tied together by a junction 1–2. The junction, formed by two perfect dislocations with Burgers vectors $a/2[10\bar{1}]$ and $a/2[\bar{1}10]$ moving under applied stress on two intersecting slip planes, (111) and $(\bar{1}11)$, respectively, is a perfect $a/2[011]$ dislocation. The parent dislocations mutually knit with each other until an equilibrium configuration is reached. The junction formation is mimicked by locking conditionally the knitted portions. (Further details of dislocation-dynamics simulations are available at http://zig.onera.fr/lem/DisGallery).

Evolution of the junction, zipping further or unzipping, will depend on the forces acting on the two mobile segments connected to each node at the junction's end (nodal segments). It is the junction strength that governs the strain-hardening properties of f.c.c. crystals (so-called stage II hardening). We now analyse the junction strength in terms of the minimum force required to drive the unzipping process. In general, the force F acting to separate the junction is the Peach–Koehler force, τb, where τ is the stress on the mobile nodal segment and b is the magnitude of its Burgers vector, times the effective arm-length of the segment l. The critical condition for unzipping is that F should be equal to the energy spent on separating a unit length of the junction and moving the resulting partials apart by a distance l. This energy is the sum of core W_c and elastic W_{el} contributions. Practically, for mesoscopic simulations, junction strength is treated through an effective junction stress $\tau_j = (W_c + W_{el})/bl$, which is then combined with the local stress τ acting on every segment connected to a junction node. Although τ_j is not a material parameter itself, as it depends on the length of the unzipping arm, the local rule for mobility of the nodal segments is nevertheless fully specified, once W_c and W_{el} are known. Whereas W_{el} can be calculated from elasticity theory, the core contribution W_c can only be determined atomistically.

We have carried out an explicit atomistic calculation to obtain the core contribution W_c. To avoid the complications of dealing with non-uniform stress distributions near a crack tip, we analyse the energetics of junction unzipping in the same crystal without the crack and under zero stress. The energy cost of junction unzipping was obtained by comparing the energy of a sufficiently large cylindrical slab (559.6 Å in diameter) centred around lock 1–2 (Fig. 1b) with the energy of the same slab for a configuration where partials 1 and 2 are lined up parallel at a distance d, similar to that shown in Fig. 1a. Presenting our result in a form scaled to the length l of the mobile segment, the effective junction stress is given by the above equation with $W_c(b) = -0.0542\,\text{eV Å}^{-1}$ and $W_{el}(l/b) = 0.106 \ln(l/b)\,\text{eV Å}^{-1}$, $b = 1.65$ Å. These numerical values were obtained for Lennard–Jones potential with well depth $\epsilon = 0.15$ eV and length parameter $\sigma = 2.556$ Å, nominally representing Cu. For the arm length of 0.5 μm, the effective junction stress is 15.5 MPa, which compares very well with the junction strength parameter previously obtained by fitting mesoscopic simulation data to deformation experiments[4].

The overlap of atomistic and continuum length scales, demonstrated in this work for the case of dislocation junctions, points to the feasibility of a critical connection between two different modelling methodologies. It should lead to significantly improved understanding of dislocation behaviour which up to now has been investigated mostly within the framework of linear elasticity. As well as the properties of dislocation locks and junctions, a host of other essential mechanisms could be elucidated, including the cross-slip properties of screw dislocations, the dynamics of the formation and motion of kink pairs, and the annihilation properties of closely spaced edge-dislocation dipoles. □

Received 1 October; accepted 30 December 1997.

1. Friedel, J. *Dislocations* (Pergamon, Oxford, 1964).
2. Abraham, F. F. *et al.* Instability dynamics in three-dimensional fracture: an atomistic approach. *J. Mech. Phys. Solids* **43,** 1461–1473 (1997).
3. Devincre, B. & Kubin, L. P. Mesoscopic simulations of dislocations and plasticity. *Mater. Sci. Eng.* **A234–236,** 8–14 (1997).
4. Devincre, B. & Kubin, L. Simulations of forest interactions and strain hardening in FCC crystals. *Modelling Simul. Mater. Sci. Eng.* **2,** 559–570 (1994).
5. Abraham, F. F. On the transition from brittle to plastic failure in breaking a nanocrystal under tension. *Europhys. Lett.* **38,** 103–106 (1997).
6. Hirth, J. P. & Lothe, J. *Theory of Dislocations* 2nd edn 792–806 (Wiley, New York, 1982).
7. Nabarro, F. R. N. *Theory of Crystal Dislocations* (Oxford Univ. Press, London, 1967).
8. Pranz, I. & Argon, A. S. Dislocation cell formation during plastic deformation of copper single crystals. *Phys. Status Solidi A* **57,** 741–753 (1980).
9. Korner, A. & Karnthaler, H. P. Weak-beam studies of composite dislocations gliding on (001) planes in Si. *Phil. Mag.* **44,** 275–284 (1981).

Acknowledgements. This work originated at a collaborative workshop on materials modelling held at the Institute for Theoretical Physics, UCSB, during March 1997. E.F.A. acknowledges the use of the Cornell Theory Center, which receives funding from the NSF and New York State; B.D. and L.K. acknowledge the support of CNRS through the GdR programme on mesoscopic simulations and modelling in metallurgy; V.B. and S.Y. acknowledge support from LLNL; and V.B. acknowledges support from the Alcoa Foundation.

Correspondence and requests for materials should be addressed to V.B. (e-mail: vasily@mit.edu).

3.2. Le glissement dévié

Une dislocation vis se déplaçant dans son plan de glissement *primaire* peut sous certaines conditions changer de plan et partir dans un plan de *déviation* contenant son vecteur de Burgers. Souvent, après avoir glissé d'une distance qui dépend des contraintes locales dans le solide, cette dislocation vis dévie à nouveau pour revenir dans son plan primaire où la contrainte projetée est en moyenne la plus forte. C'est le mécanisme de double glissement dévié.

Pour des dislocations parfaites dans un milieu continu, le glissement dévié (GD) se produit facilement dès que la contrainte dans le plan de déviation, τ_d, est supérieure à la contrainte dans le plan primaire, τ_p. Dans un cristal réel, les dislocations sont le plus souvent dissociées, et les mécanismes mis en jeu sont plus complexes. La dissociation des dislocations vis en partielles impose préalablement à toute déviation une constriction du coeur étendu et le franchissement d'une barrière d'énergie. Le GD fait alors intervenir des mécanismes fondamentalement tridimensionnels et qui dépendent de la structure de coeur des dislocations. Les modèles théoriques décrivant ce phénomène sont relativement anciens et presque exclusivement issus de la théorie élastique.

Le GD mettant en jeu une restructuration de la structure de coeur des dislocations, la barrière d'énergie correspondante est du bon ordre de grandeur pour que ce mécanisme soir thermiquement activé. L'activité et l'importance du GD varie donc d'un matériau à l'autre suivant la structure de coeur. Dans les cristaux CFC, la largeur de dissociation et l'énergie de ligne étant la même dans tous les plans de glissement compacts {111}, le GD est indépendant du choix du plan d'origine et d'arrivée. Ce cas est le plus simple et aussi le plus étudié dans la littérature. Il faut cependant garder à l'esprit qu'il n'est pas le cas le plus commun. Dans beaucoup de matériaux, le GD implique des déviations entre plans de glissement de natures cristallographiques différentes ou entre plans ayant des énergies de faute ou des frictions de réseau différentes. Ces déviations *non compactes* sont observés par exemple entre plans {111} et {100} dans les cristaux CFC aux moyennes et hautes températures, ou entre plans basal et prismatique dans les cristaux HC. Pour une revue des différents modèles de GD et de leur domaine d'application, on se reportera à [104, 105]. Ici, seul le modèle dit de Friedel-Escaig est rappelé.

3.2.1. Le modèle de Friedel-Escaig

Le GD dans les cristaux CFC est généralement modélisé dans le cadre de l'élasticité isotrope à l'aide des calculs d'Escaig [106, 107] basés sur un chemin de réaction proposé par Friedel [108]. Ce chemin se décompose en deux étapes. Tout d'abord, il faut effectuer un pincement ponctuel, appelé constriction, de la dislocation dissociée dans le plan primaire [3]. Ensuite, la constriction se dissocie en deux demi-constrictions limitant un segment de dislocation parfaite qui se dissocie immédiatement dans le plan de déviation. La position de col de cette transition est atteinte pour une longueur critique du segment dévié, tel qu'il devient énergétiquement favorable d'accroître le ruban de faute dans le plan dévié. Le point essentiel de ce modèle est que l'énergie de déviation dépend uniquement des contraintes sur les dislocations partielles.

Les principales causes d'incertitude du modèle de Friedel-Escaig viennent de l'approximation de la tension de ligne pour le calcul des forces et d'une définition arbitraire de la largeur de dissociation critique en dessous de laquelle une dislocation est supposée recombinée et parfaite. Cela introduit dans l'énergie des constrictions, donnée par une formule de Stroh, un facteur non contôlé. Ces points faibles ont été discutés par Saada [109], Duesbery [110] et Püschl [104].

[3] Ces constrictions pré-existent probablement le long des lignes de dislocation et leur nombre croît avec la déformation. Elles peuvent être formées lors de l'intersection des dislocations et sont alors associées à des crans et décrochements. Elles se trouvent naturellement aux noeuds triples bordant les jonctions. Chaque fois qu'une dislocation dévie ou s'annihile avec une dislocation de signe opposé, des constrictions sont également formées sans possibilité d'être éliminées.

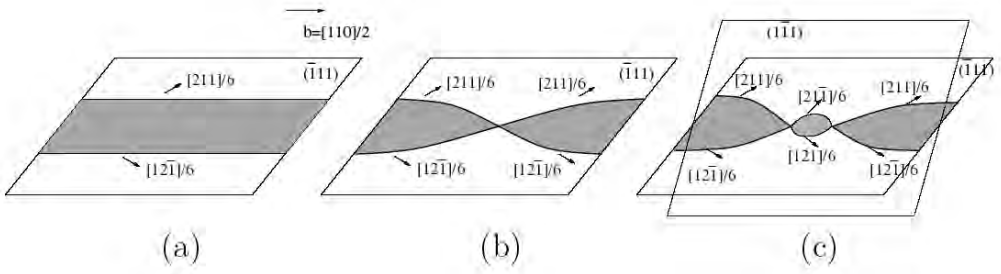

FIG. 3.1.: Chemin réactionnel en trois étapes du glissement dévié dans les métaux CFC d'après Friedel-Escaig.

Un résultat important de ce modèle, qui n'est pas pris en compte dans les simulations de DD, est ce qu'on appelle *l'effet Escaig*. Pour un état de contrainte donné, les forces de Peach-Koehler sur les dislocations partielles ne sont pas en général identiques. Dans les cristaux CFC, les dislocations se décomposent en deux Schokley avec des vecteurs de Burgers à $\pm 30°$ de la direction vis. Pour une contrainte uniaxiale donnée, il est facile de vérifier que la contrainte projetée impose sur les composantes vis des partielles une translation uniforme, alors que les forces sur les composantes coins sont différentes et peuvent induire une élargissement ou un rétrécissement du ruban de faute. Ainsi, l'énergie d'activation du GD est sensible à l'orientation de la contrainte appliquée [111].

3.2.2. Rôle du glissement dévié en plasticité

Dans une certaine mesure, le glissement dévié et la montée jouent un rôle similaire en plasticité. Ces deux mécanismes confèrent aux dislocations des degrés de liberté supplémentaires en leur donnant la possibilité de quitter leur plan de glissement. La principale différence entre ces deux mécanismes est que le GD peut être activé mécaniquement et intervient même aux basses températures si la contrainte locale est suffisamment forte. Le GD affecte de nombreuses manières le comportement collectif des dislocations et la déformation plastique. Dans les métaux CFC, les contributions les plus importantes dans les cristaux CFC sont :

- Le glissement dévié facilite l'annihilation entre dislocations vis d'un même système de glissement. Il faut différentier les annihilations favorisées mécaniquement et intervenant entre dislocations trés proches l'une de l'autre et les annihilations thermiquement assistées pouvant intervenir entre dislocations plus éloignées lors de la *restauration dynamique*. La *distance critique d'annihilation* entre deux dislocations vis de vecteurs de Burgers opposés, y_s, est un paramètre clé des lois d'évolutions des densités de dislocations pour les modèles de déformation monotone ou cyclique. En bon accord avec la théorie, il a été vérifié expérimentalement que y_s est fonction de la contrainte, de la température et de l'énergie de faute. Dans le cuivre à température ambiante, $y_s = 50 - 60\,\text{nm}$ [112]. Des résultats récents de simulations atomiques confirment qu'à cette distance le GD est vraisemblablement activé thermiquement [113, 114].
- Dans les monocristaux CFC, la formation de cellules de dislocations n'intervient qu'au début du stade III de la courbe de déformation, en raison de l'apparition de la restauration dynamique associée au GD. On sait, en effet, depuis longtemps que la formation d'une structure de dislocations organisée en 3-d suppose la contribution d'un mécanisme permettant une délocalisation des dislocations en dehors de leur plan de glissement comme le GD ou la montée.
- Le double GD permet aux dislocations vis de contourner des obstacles comme les dislocations répulsives ou les précipités. Ce mécanisme favorise aussi la multiplication des dislocations en

formant des sources de Frank-Read, si les super-crans dans le plan de déviation sont peu mobiles. De même le double GD favorise une homogénéisation de la déformation plastique en propageant des dislocations dans les régions du cristal non déformées.
- Le GD relaxe les contraintes internes en permettant la formation de débris, boucles dipolaires, fragments déviés, supercrans etc. Ces défauts stabilisent les configurations planaires de dislocations en leur permettant d'abaisser leur énergie élastique. Inversement, ils contribuent à l'écrouissage plastique en formant une forêt d'obstacles stables pour le mouvement des dislocations mobiles.
- Expérimentalement, les observations en topographie X et au MET montrent que des dislocations peuvent être nucléées par GD près des surfaces libres. Ce phénomène a été interprété par Hazzledine [69] et confirmé plus récemment par simulations atomiques [115]. L'effet conjugué d'un chargement et de la force image, favorise sur certains système de glissement un *effet Escaig* qui permet le déclenchement du GD et une bifurcation des dislocations glissant en direction de la surface, vers l'intérieur du cristal. Dans les nanomatériaux, le fort rapport surface sur volume favorise ce mécanisme.

On voit donc dans ce cas précis qu'une simulation de DD qui s'en tiendrait à la description de la théorie élastique des dislocations n'aurait guère de sens. C'est pourquoi des règles locales spécifiques au GD doivent être défini dans la DD.

3.2.3. Le glissement dévié dans la DD

Le mécanisme de GD est un phénomène local lié à la structure du coeur des dislocations (§ 3.2.1). L'échelle mésoscopique n'est donc pas, à priori, adaptée à sa modélisation. La quasi-totalité des simulations de DD utilise un jeu de règles locales proposé initialement par Kubin et col. [32, 47, 103]. Cette modélisation mesoscopique s'inspire directement du modèle de Friedel-Escaig[4]. Par exemple, l'énergie d'activation dépend de l'énergie de faute du matériau considéré, des contraintes locales et de la température. Le fait de prendre en compte le GD dans une simulation des CFC permet aussi indirectement de définir une température de simulation.

Le mécanisme de GD est phénoménologiquement décomposé en trois étapes, géométrique, mécanique et stochastique.

1. Il faut tout d'abord identifier les segments qui peuvent potentiellement dévier car ils sont proches de la direction vis. Le caractère des dislocations étant discrétisé, un segment a une très faible probabilité de se trouver exactement dans la direction vis. C'est pourquoi il faut introduire dans les simulations une tolérance angulaire sur les directions de ligne pouvant dévier. Celle-ci est choisie, un peu arbitrairement, de l'ordre de $\pm 5°$. De même, il faut calculer la vraie longueur effective, l, dans la direction vis et fixer un plan de déviation unique lorsque la section de dislocation approximativement vis considéré est décrite à partir de plusieurs segments.
2. Il faut ensuite vérifier qu'il existe une force motrice pour la déviation. Le modèle de Friedel-Escaig ne met en jeu que les contraintes sur les partielles. Via les facteurs de Schmid, ces contraintes, sont transformées en contraintes équivalentes sur les plans de glissement et de déviation. On vérifie donc que le rapport des contraintes projetées dans le plan dévié, τ_{GD}, et dans le plan de glissement primaire, τ_{G}, est supérieur à une valeur critique :

$$\frac{\tau_{\mathrm{GD}}}{\tau_{\mathrm{G}}} > \chi \tag{3.1}$$

L'amplitude de χ est une estimation des efforts s'exerçant sur une dislocation pour effectuer une constriction. Cette quantité varie avec l'énergie de faute du matériau simulé. Pour l'aluminium,

[4] Les simulations de DD ne considèrent la plupart du temps que des dislocations parfaites. Cependant la modélisation mésosocopique du glissement dévié permet de reproduire des propriétés spécifiquement liées à la dissociation des dislocations.

$\chi \approx 1,1$ car le coeur des dislocations est compact. Pour le cuivre, les forces nécessaires pour pincer le ruban de faute sont plus importantes. Une estimation sommaire conduit à $\chi \approx 1,6$ [32].

3. Enfin, la cinétique de déviation est modélisée à l'aide d'une loi d'Arrhénius représentant la *probabilité de déviation* :

$$P(l) = \beta \frac{l}{l_0} \frac{\Delta t}{\Delta t_0} \exp(\frac{|\tau_{\mathrm{G}}| - \tau_{\mathrm{III}}}{S}) \tag{3.2}$$

Cette expression définit la probabilité pour un segment vis de dislocation de longueur l de changer de plan de glissement pendant un intervalle de temps, Δt, sous une contrainte interne locale τ_{GD}. β est une constante de normalisation et Δt_0, un temps de référence. La longueur l_0 représente la longueur critique de l'arc dévié. D'une part, aucun segment de longeur $l < l_0$ ne peut dévier et, d'autre part, la probabilité de déviation est proportionnelle au nombre de sites en compétition, l/l_0. τ_{III} est la cission critique qui marque le début du stade III sur la courbe de traction des monocristaux, c'est-à-dire le début de la restauration dynamique. Cette contrainte est représentative des états de chargement interne ou le glissement dévié devient facile. $S = kT/V$ est la sensibilité à la vitesse et V le volume d'activation du GD. Cette quantité peut être déterminée expérimentalement. Dans le cas du cuivre, $V \approx 300\, b^3$ [116]. Le paramètre $\beta \Delta t_0 / l_0$ est sont ajusté pour que la probabilité d'annihilation par GD de deux dislocations vis distantes de la distance critique d'annihilation y_s soit égale à 1 pendant un intervalle de temps de simulation de quelques Δt. Lors des simulations, la probabilité de GD sur un segment est testée avec un schéma de Monte-Carlo classique.

Cet ensemble de règles peut être considéré comme une vision impressioniste du mécanisme de glissement dévié. Il reflète, en fait l'état actuel des connnaissances car, même si des simulations atomiques récentes ont confirmé les bases du modèle de Friedel-Escaig, il subsite de fortes incertitudes même dans les CFC sur les valeurs des énergies d'activation, du volume d'activation et des paramètres numériques du modèle. C'est la raison pour laquelle il est souvent fait appel à des valeurs expérimentales ou à des estimations d'ordre de grandeur pour calibrer les règles locales du GD.

3.2.4. Glissement dévié et plasticité des alliages intermétalliques

Dans le précédent paragraphe nous avons vu un exemple de règles locales utilisées en DD pour décrire le GD à l'échelle mésoscopique. Cet exemple est important, car il est bien justifié théoriquement dans les métaux CFC. Malheureusement, il n'en va pas de même pour des matériaux plus complexes sur le plan chimique, où la mise en œuvre des règles du glissement dévié devient compliquée et incertaine. Le GD est donc en pratique un mécanisme qui sélectionne les matériaux pouvant ou ne pouvant pas encore être simulés en fonction des informations disponibles.

Un article sur l'étude de l'anomalie de comportement plastique dans Ni_3Al conclut cette partie. Cette étude réalisée en collaboration avec P. Veyssière et G. Saada s'inscrit dans la continuité des études expérimentales conduites au LEM sur les alliages intermétalliques. Notre principal objectif était d'identifier les propriétés élémentaires des dislocations à l'origine des anomalies du comportement plastique, limite élastique et durcissement d'écrouissage, dans Ni_3Al. Ce travail a permis de tester les modèles théoriques existants et de discuter leur réalisme en comparant d'une part les microstructures simulées à celles observées au MET et, d'autre part, la réponse mécanique simulée à l'expérience. Les résultats montrent bien que lorsque les mécanismes élémentaires sont relativement bien caractérisés aux échelles fines, des simulations de DD peuvent apporter des informations originales et difficiles à obtenir par d'autres moyens d'investigation.

Le résultat le plus marquant est la mise en évidence de la compétition entre deux mécanismes qui compensent l'épuisement de la densité de dislocations vis mobiles induit par la formation de nombreux verrous de Kear-Wilsdorf (KW). Aux plus basses températures (c'est-à-dire au pied de l'anomalie de la limite élastique), le mouvement des dislocations dans les plans octaédriques est entretenu par l'expansion de grands décrochements présents dans la microstructure. En glissant, ces décrochements détruisent (dézippent) les verrous de KW et créent de nouvelles longueurs de ligne glissiles. Aux plus fortes températures, la fréquence de formation des verrous de KW augmente et les décrochements, dont la hauteur a substantiellement diminué, ne peuvent plus se déplacer. La contrainte d'écoulement doit alors augmenter jusqu'au niveau requis pour la destruction locale des verrous de KW. On observe dans ce cas un mode de déplacement différent des dislocations dans la direction vis, par propagation de doubles décrochements formés au cours du désancrage et de l'ancrage des verrous de KW.

PHILOSOPHICAL MAGAZINE A, 1999, VOL. 79, NO. 7, 1609–1627

Simulation of the plastic flow in Ni_3Al: work hardening and strain-rate sensitivity

B. DEVINCRE, P. VEYSSIÈRE and G. SAADA

Laboratoire d'Etude des Microstructures, CNRS–ONERA, 92322 Chatillon, France

[*Received 2 July 1998 and accepted 9 September 1998*]

ABSTRACT

The origin of the anomalous temperature dependence of the giant work-hardening rate and of the modest strain-rate sensitivity observed in many $L1_2$ alloys is investigated by means of an 'end-on' simulation of dislocation dynamics in Ni_3Al. The present model reproduces most of the atypical mechanical properties observed experimentally. The study of the evolution of the distribution of the Kear–Wilsdorf locks during plastic deformation indicates that the order of magnitude of the work-hardening rate stems from a preferred exhaustion of the weakest locks. In addition, the low strain-rate sensitivity measured is found to rely on the absence of a correlation between the dislocation properties which provide the plastic strain and those which determine the flow stress level.

§1. INTRODUCTION

A variety of well identified, atypical mechanical properties take place in $L1_2$ alloys of which the peak of yield stress is by far the most documented. The various attempts at designing an analytical model which would account for the overall mechanical responses of these alloys have not yet converged towards a unique point of view. This is essentially because the models are partly inadequate to reproduce the several intricate microstructural processes that take place during deformation (for reviews, see Hirsch (1993), Caillard and Couret (1996) and Veyssière and Saada (1996)). It is commonly accepted that the anomalous mechanical behaviour of these alloys is to a large extent determined by specific transformations taking place within the core of ⟨110⟩ dislocations. The dissociated core of a screw dislocation can switch from the primary {111} octahedral (O) slip plane to the cross-slip {100} cube (C) plane in which, however, lattice resistance to dislocation motion is much more substantial than in the former (§2.2). This configuration is referred to as an incomplete or a complete Kear–Wilsdorf lock (KWL) depending upon whether dissociation occurs partly or fully respectively in C planes (Bontemps and Veyssière 1990). The transformed configuration is sessile with respect to glide in the primary O plane. It can give rise to a fairly efficient dislocation immobilization under an applied stress (Molénat *et al.* 1993, Saada and Veyssière 1994). As a result, the deformation microstructure consists of long straight screw locks.

Following the work of Mills and Chrzan (1992), we have recently addressed the question of the flow stress anomaly in a model Ni_3Al alloy, by means of a dislocation dynamics simulation (Devincre *et al.* 1997). For this purpose, we incorporated

Philosophical Magazine A ISSN 0141–8610 print/ISSN 1460-6992 on line
http://www.tandf.co.uk/JNLS/phm.htm
http://www.taylorandfrancis.com/JNLS/phm.htm

selected documented properties of dislocation cores, including the above locking mechanism and its thermally activated nature, into a pre-existing three-dimensional (3D) simulation code designed to model dislocation dynamics at a mesoscopic scale (Devincre and Kubin 1997a). In particular and for simplicity, we ascribed the motion of dislocations to remain in plane, for example the finite motion on the cube cross-slip plane was not accounted for explicitly. With the specific properties of KWLs being included, the simulations yield dislocation microstructures naturally stretched in the screw direction. Futhermore, because the locking is treated as a thermally activated process, the preference of dislocations for the screw orientation spontaneously soars as the temperature increases. Simultaneously, the mean length of the kinks joining successive KWLs in the O planes decreases monotonically. An important feature suggested by the simulation is that plastic strain proceeds mostly from the sliding of kinks along the screw direction. The mobility of a given kink is controlled by its length as well as by the friction stress which acts on the jogs that interconnects a kink to a KWL (see figure 1 in the paper by Devincre *et al.* (1997)). In order to reproduce the flow stress anomaly as well as realistic microstructures, it was determined that kink sliding ought to be somewhat hindered, which in turn implies that a substantial friction stress be exerted on the geometrically necessary jogs.

The flow stress anomaly was found to consist of two regimes, each corresponding to a specific dislocation mechanism. At low temperatures, the longest kinks operate as dislocation sources, much as a Frank–Read source at least in its first stages but, as the temperature is raised, the kinks decrease in length and tend to slide over increasingly long distances in the screw direction. Strain then proceeds essentially by the motion of the kink pairs which are nucleated upon KWL destruction. However, the 'in-plane' simulation could not help us to investigate the origin of the atypical work-hardening rate (WHR) and of the modest strain-rate sensitivity (SRS) which are part of the signatures of the anomalous deformation regime of Ni_3Al:

(i) The WHR is indeed astonishingly large, exhibiting in addition a peak at a temperature systematically lower than that of the flow stress. The physical origin of the microscopical mechanism responsible for the work hardening remains uncertain (Veyssière and Saada 1996).
(ii) The SRS of Ni_3Al is very small, comparable with that of pure fcc metals. It shows a minimum within the temperature domain of the flow stress anomaly (Thornton *et al.* 1970, Ezz and Hirsch 1994).

In this paper we report the results of an alternative two-dimensional (2D) computer simulation which we have designed to investigate the above two properties. This method, in which dislocations are viewed and treated end on, is capable of handling a large density of dislocations over relatively large strains. By this means we can account for variations in the density of mobile dislocations, include interactions between non-coplanar dislocations and allow for cross-slip. A detailed description on the computational technique and of its main outcome is presented in §§2 and 3. The discussion of the simulation results including a comparison with experiments is addressed in §4.

§2. THE TWO-DIMENSIONAL 'END-ON' SIMULATION MODEL

Inasmuch as one's interest is restricted to properties that take place in the limits of small strains, such as yielding, the simplification that dislocations cannot glide

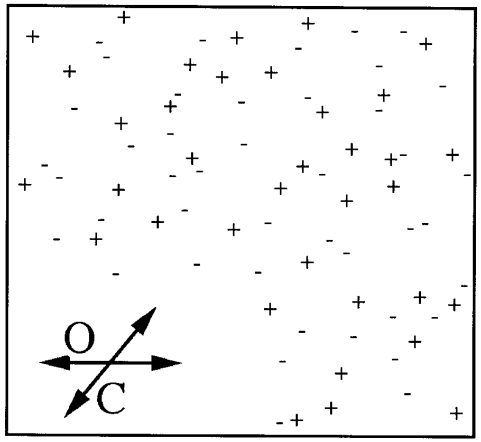

Figure 1. Schematic representation of the 2D 'end-on' simulation system. The plane frame, 25 μm × 25 μm large, is normal to the screw direction. The dislocations of either sign, are assumed to be straight. They are allowed to glide in either one of O and C planes and to cross-slip on these.

in C planes has little influence on the modelling of plasticity by means of the 'in-plane' simulation. By contrast, in addressing the WHR and the SRS, out-of-slip-plane dislocation interactions and recovery can no longer be ignored. Unfortunately a full 3D simulation is at present out of reach in terms of computing time. The substantial length of dislocation line which needs to be taken into account is indeed incompatible with the necessarily large number of segments required to discretize the curvature of the kinks, which are inherently numerous. The alternative 2D 'end-on' computer model which we have designed consists essentially in considering a cross-section perpendicular to the screw direction (figure 1) and in incorporating several rules adequate to mimic the features ignored in the previous simplified 2D in-plane geometry. As a counterpart, features such as kinks and their multiple properties (Devincre *et al.* 1997) cannot be accounted for explicitly.

2.1. *Discretization of time and space*

The present end-on simulation bears many similarities to molecular dynamics. It is actually inspired from a technique of simulation first designed by Amadeo and Ghoniem (1989) to study dislocation patterning. Because the dislocation lines in Ni_3Al is predominantly straight and of screw character (§1), we chose to represent a dislocation by its intersection with a plane frame xOy normal to the (110) direction (figure 1). In this frame Ox is taken along the slip direction in the O plane. The microstructure is thus approximated to a distribution of parallel and antiparallel screw $\pm\langle 110\rangle$ dislocations.

The effective shear stress τ^* on the dislocations resolved on the O plane, originates from three different contributions.

(1) The internal elastic stress field τ_{int}, is computed for a dislocation i by superimposing the stress field of each surrounding dislocation j, calculated in the frame of linear anisotropic elasticity:

$$\tau_{int} = \sum_{j \neq i} \frac{c_{44} b}{2\pi A^{1/2}} \frac{X}{X^2 + AY^2}, \tag{1}$$

where c_{44} is an elastic constant and A the Zener ratio which in Ni_3Al are 128 GPa and 3.28 respectively. The dislocation Burgers vector b is 5×10^{-10} m and (X, Y) are the coordinates of the vector joining dislocation i to j. Given a reasonable dislocation density of about 10^{12} m^{-2}, we have determined that, beyond 2 μm, the contribution of dislocation interactions becomes negligible relative to the other contributions to the effective stress. Accordingly, a cut-off distance for the dislocation self-stress field is set to 5 μm.

(2) The frictional stress τ_f is ascribed a value of 10 MPa in the O plane. Since τ_f is then always smaller than the applied stress, it does not influence dislocation dynamics substantially. In the same vein, there is little interest in considering that τ_f is temperature dependent.

(3) The applied stress, τ_{app}, is adjusted so as to maintain a given constant plastic strain rate $\dot{\gamma}_{app}$. After each time step Δt, τ_{app} is corrected for the quantity: $M(\dot{\gamma}_{app} - \dot{\gamma}_{true})\Delta t$ (see appendix B in the paper by Devincre *et al.* (1997)) where M is a stiffness constant set to μ in order to represent a stiff testing device. As the temperature is raised from 200 to 600 K, Δt must be changed from 10^{-9} to 10^{-10} s in order to take the increase in the dislocation free flight velocity into account. The instantaneous strain rate $\dot{\gamma}_{true}$, is calculated at each step of the simulation, based on the Orowan equation

$$\dot{\gamma}_{true} = \frac{1}{L^2} \sum_{i=1}^{n} \frac{b_i \Delta x_i}{\Delta t}, \tag{2}$$

where n is the number of dislocations contained in the frame of surface L^2 and Δx_i is the displacement of dislocation i during Δt.

We ignore the possible effects of acceleration. The mean free glide velocity v as well as the free flight distance Δx are determined within each simulation step from

$$v(t) = \frac{\tau^*(t) b}{B} \tag{3}$$

and

$$x(t + \Delta t) = x(t) + v(t)\Delta t, \tag{4}$$

where B is a drag coefficient representing the dissipation which accompanies dislocation glide. Mills and Chrzan (1992) have estimated B to about 2×10^{-3} Pa s in Ni_3Al.

The simulation procedure begins with a random distribution of 100 dislocations, that is a dislocation density of 1.6×10^{11} m^{-2} in a frame of 25 μm × 25 μm (we also tried 1.6×10^{13} m^{-2} in a smaller frame of 2.5 μm × 2.5μm; see §3.3). To avoid difficulties at boundaries, the calculation of the forces includes image replica of the main simulation frame and, every time that a dislocation disappears at a boundary of the main frame, its image is allowed to cross through the opposite boundary in the same slip plane.

2.2. *The local simulation rules*

For the sake of practicality, we do not account explicitly for dislocation dissociation in the simulation. On the other hand and by construction, line tension cannot be included in the end-on simulation. These two components are nonetheless essential and they must be incorporated in the model via constitutive rules. What these local rules have to reproduce in practice are firstly the conditions of cross-slip immobilization by formation of a KWL and secondly the subsequent strength of the KWLs.

Unlocking occurs when the effective stress becomes locally larger than the KWL unlocking stress τ_u, which itself depends on the extent $l_c(T)$ of the configuration in the C plane, (Molénat *et al.* 1993, Saada and Veyssière 1994). In view of the 3D nature of a KWL, unlocking implies an overall double cross-slip process which must be also included in the end-on simulation. The procedure which we have employed to account for these rules and which is largely inspired from our previous work is as follows.

(i) To model the formation of KWLs, the number of cross-slip events (from O to C) for a length l of screw dislocation during the incremental time Δt of the simulation, is represented by means of the expression

$$P(T) = f \exp\left(-\frac{W_{o\text{-}c}}{kT}\right) l \Delta t, \tag{5}$$

where kT has its usual thermodynamical meaning, f, the attempt frequency for cross-slip per unit length, is set to $3.26 \times 10^{19}\,m^{-1}\,s^{-1}$, while $W_{o\text{-}c}$ the stress-independent activation energy, is 7×10^{-20} J. Both quantities together with equation (5) compare with those previously employed by Paidar *et al.* (1984), Mills and Chrzan (1992), Ezz and Hirsch (1994), Caillard and Paidar (1996), Devincre *et al.* (1997) and Louchet (1997). At each step, the expression of $P(T)$ is tested for every mobile screw dislocation by means of a Monte Carlo scheme.

(ii) Yet in the end-on simulation the characteristic screw length l, which appears in equation (5), is not immediately accessible since no characters other than the screw dislocation are explicitly considered. One way to circumvent this difficulty is first to consider that, when submitted to an effective stress τ^*, mobile dislocations assume a certain curvature whose radius R is, in the approximation of line tension, given by

$$R = \frac{\mu b}{\tau^*}. \tag{6}$$

Then, we equate the hypothetical line segment which is liable to cross-slip to the chord of length l in the screw direction located at a distance $R - w$ from the centre of curvature (Veyssière and Saada 1996). In order for the chord to represent a given dislocation character (here the screw character), the adjustable parameter w must remain modest, say of the order of the size of the dislocation core (about $2b$ where b is the Burgers vector of the perfect dislocation). In these conditions, the dependence of l upon the local effective stress is given by

$$l = (8Rw)^{1/2} = 4b\left(\frac{\mu}{\tau^*}\right)^{1/2} \tag{7}$$

It should be emphasized that this approach corresponds to a quasistatic approximation of the dislocation curvature which tends to underestimate the length of the mobile screw portion. Under dynamical conditions, the actual radius of curvature becomes necessarily larger than R for expanding configurations tend to evolve out of mechanical equilibrium. As a consequence, the simulation is actually expected to underestimate the probability of KWL formation. In addition, one must realize that, in the anomalous domain of temperature, τ^* is close to τ_{app}. Then, the relative fluctuations in l due to fluctuations in τ^* are small and the main results of the simulation would not be affected by taking a constant length $l \approx b(\mu/\tau_{app})^{1/2}$.

(iii) We make use of the same rules for the KWL unlocking stress τ_u, as those which we had designed for the in-plane simulation. In view of figure 8 of the paper by Saada and Veyssière (1994), the KWL unlocking stress follows approximately

$$\tau_u(l_c) = 16.5\,\frac{l_c}{b} + 50, \tag{8}$$

where τ_u is expressed in megapascals and l_c, the antiphase-boundary extent of the KWL in the C plane, ranges between b and $10b$ ($10b$ compares with spreading height of the complete KWLs).

In addition, l_c is assumed to follow a normal distribution centred on a temperature-dependent mean value $\bar{l}_c(T)$:

$$P(l_c) = \frac{1}{\pi^{1/2}} \exp\left[-\left(\frac{l_c - \bar{l}_c(T)}{b}\right)^2\right]. \tag{9}$$

In an attempt to reflect the gradual decrease in lattice friction in the C plane with increasing temperature (suggested in particular by several experimental studies such as Hemker's (1990) creep experiments and transmission electron microscopy observations (Veyssière and Saada 1996)), the quantity $\bar{l}_c(T)$ is ascribed the following Arrhenius form:

$$\bar{l}_c(T) = d_c \exp\left(-\frac{W_c}{kT}\right), \tag{10}$$

where d_c and W_c are set to $40b$ and 1.52×10^{-20} J respectively in order to model a monotonic increase in the mean KWL height from b at 300 K to 10b at 800 K. It should be noted that we have incorporated no provision for a possible ageing of the KWLs, that is for a time dependence of $\bar{l}_c(T)$ once the KWL is formed (see the appendix of the paper by Devincre *et al.* (1997)).

At each step of the computation and for every KWL present, the effective stress τ^*, resolved in the O plane is calculated and compared with the unlocking stress τ_u (equation (8)). When the ratio τ^*/τ_u exceeds unity, the KWL is declared unlocked and the dislocation ascribed the second stage of an overall double cross-slip process. In practice, the newly freed dislocation is first translated in the direction determined by the sign of $\tau^* b$, over the distance l_c in the C plane (i.e. over the height of the KWL in the C plane). Subsequently, the dislocation resumes slip in a O plane which is distinct from the O plane where it was slipping before it became locked. This local rule is one of the major differences between the in-plane and the end-on simulations. It should be noted that, since the cross-slip frequency

and the mobility of dislocations in the C plane both increase with increasing temperature, the tendency towards slip planarity is decreased as temperature is raised.

(iv) When two dislocations approach each other, elastic interactions can either further stabilize or help to destroy KWLs, depending on how the local effective stress is perturbed (§3.1). Attractive interactions between close dislocations can for instance favour repeated cross-slip events and promote dislocation annihilation (Veyssière 1997). This latter process is accounted for by means of a cross-section $Y_s(T)$ for spontaneous annihilation. On the other hand, since annihilation involves cross-slip, $Y_s(T)$ should be temperature dependent. We have thus chosen to describe $Y_s(T)$ by the following expression:

$$Y_s(T) = Y_0 \exp\left(-\frac{W_c}{kT}\right). \tag{11}$$

This expression, similar to that for the KWL height l_c (equation (9)), accounts for the idea that cube slip constitutes one probable component of the wholesale annihilation event and thus reminds us of the temperature-dependence of friction in this plane. Y_0 is a fitting parameter representing the ease of cross-slip annihilation and which we have tested in the range from 40b to 4000b (see §4.3).

(v) In the absence of sufficient information on multiplication in Ni_3Al, we have allowed no provision for multiplication. Introduction of the multiplication is indeed necessarily crude in end-on simulation. Instead and in order to test the sensitivity of the model to variations in the dislocation density as deformation proceeds, we have preferred to conduct simulations with various initial dislocation densities and cross-sections for annihilation.

Finally, it should be mentioned that, as a result of the above rules, computations become excessively time consuming above 600 K. Beyond this temperature, what occurs indeed is that, on the one hand, the slip velocity is far too high for acceleration to be ignored while, on the other hand, the number of locking and unlocking events increases exponentially with increasing temperature.

§3. Results

As made clear by figures 2 and 3, the critical resolved shear stress (CRSS) determined within the end-on model, increases continuously with increasing temperature in the temperature range explored.

The contribution of unlocking to the flow stress is essential (figure 3). From the combination of equations (8) and (10), one can indeed define a mean unlocking stress† $\tau_u(\bar{l}_c)$. The closeness between the variations in $\tau_u(\bar{l}_c)$ and those of the CRSS provided by the simulations is striking. We have checked in addition that the unlocking events always correspond to those KWLs characterized by the smallest

† It should be realized that, for the notion of an unlocking stress to be physically sound, the distribution of KWL height must be essentially that determined by equation (9), that is when the distribution is not yet substantially affected by the dynamical feature discussed in §4.2.

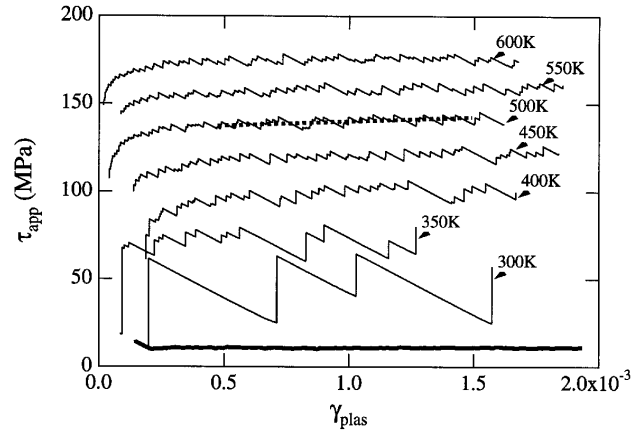

Figure 2. Stress–strain curves at different temperatures under a pre-set strain rate $\dot{\gamma} = 10^{-2}\ s^{-1}$. The size of the simulation frame is 25 μm × 25 μm, with an initial dislocation density of $1.6 \times 10^{11}\ m^{-2}$. The plastic instabilities visible on the stress–strain curves illustrate the jerky nature of dislocation motion during simulations. For instance, the large serrations at low temperatures stem from avalanches of unlocking events and from large mean free-glide distances (§3.1). The thick line, which exhibits neither work hardening nor serrations, represents the response of the system when no cross-slip onto the C planes is permitted. Note the increase in flow stress and the decrease in the amplitude of serrations with increasing temperature. The dotted straight line embodies the WHR at 500 K, that is the slope of the stress–strain curve averaged over $\Delta\gamma = 10^{-3}$.

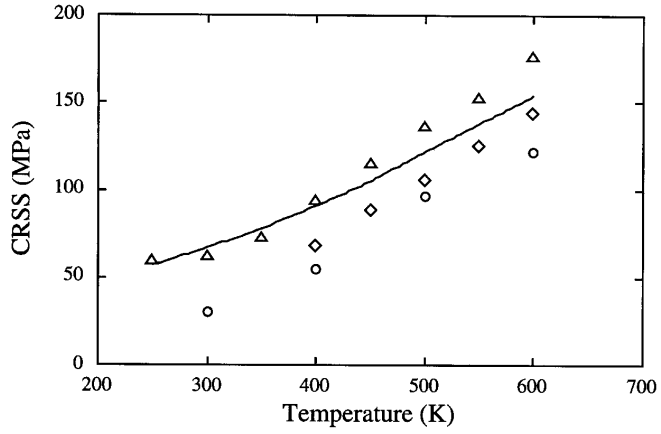

Figure 3. Dependences of the simulated CRSS with test temperature for initial dislocation densities of $1.6 \times 10^{11}\ m^{-2}$ (△) and $1.6 \times 10^{13}\ m^{-2}$ (◇): (——), temperature dependence of $\tau_u(\bar{l}_c)$ (see equations (8) and (10)); (○), 'in-plane' simulation (Devincre *et al.* 1997).

l_c, of which the most unstable are of course those whose destruction can be further assisted locally by internal stresses.

Up to a density of the order of 10^{12} m^{-2}, the stress–strain curves are insensitive to variations in the dislocation density. Beyond that value, the CRSS becomes systematically decreased (figure 3) and, when deformation proceeds, the dislocation density remains homogeneously distributed in the simulation frame. While the formation of KWLs is determined by the stochastic operation of cross-slip, their destruction is controlled by the local, effective stress. Accordingly, deformation proceeds to a large extent from individual behaviour. We have actually determined that it is only at the highest dislocation densities tested, the elastic interactions can be locally as high as τ_u. Under these circumstances, the internal stress, especially the contribution from the first-neighbour dislocations, increases with increasing dislocation density, which in turn promotes the destruction of certain weak KWLs.

3.1. *Plastic instabilities*

As shown in figure 2, the deformation under a constant strain rate proceeds by bursts (note in particular that the reference thick curve, which corresponds to the case where KWL formation is forbidden, shows no instabilities). The same behaviour was observed in the in-plane simulation where discontinuous dislocation motion takes place in the two temperature regimes. There are finite periods of time during which no dislocation is moving. Meanwhile, the stress is accordingly increased (the vertical section on the stress–strain curves in figure 4) until the stress is locally enough to unlock a KWL. Then, during its free flight the newly freed dislocation experiences interactions with the surrounding dislocations and the stress

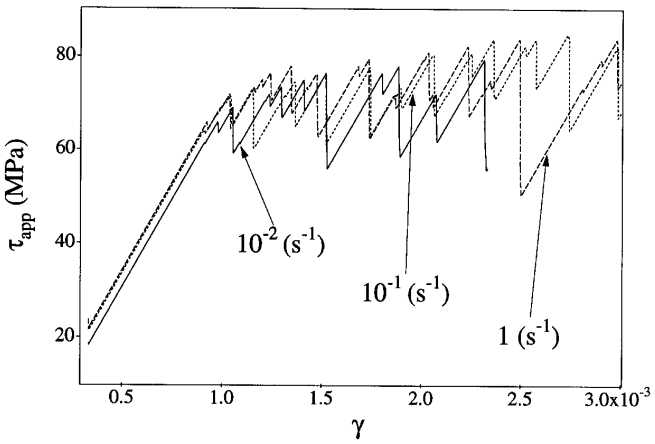

Figure 4. Comparison between the instabilities found on simulated stress–strain curves at 350 K over three orders of magnitude in strain rate $\dot{\gamma}_{app} = 1$, 10^{-1} and 10^{-2} s^{-1}. The stress is plotted against the total strain so as to display the ascending part of the serrations, which by comparison with figure 2, appears to be purely elastic in nature. The upper flow stresses, which correspond to the destruction of the weakest KWL(s) at that particular instant, are reasonable well aligned within the same stress–strain curve. The simulations indicate a modest positive SRS, if any.

distribution is accordingly perturbed. This is in turn liable to provide the stress increment required to unlock one or, step by step, several KWLs. Given the test temperature, the serrated aspect of the stress–strain curves originates from the operation of a stress-assisted unlocking process which is capable of creating avalanches of strain. Plastic instabilities are particularly prominent at low temperatures. This is because the dislocation mean free-flight distance is large while the mean KWL height is modest and the resulting unlocking stress moderate and thus more sensitive to interactions. On the other hand, we have found that the amplitude of the plastic instabilities increases with increasing stiffness constant, a behaviour fully consistent with the fact that the applied stress then decreases more rapidly during the avalanches. As the test temperature is increased, serrations tend to vanish. Deformation then proceeds in a more continuous manner for it results from the compensating contribution of a number of small free-flight jumps (see the following section on the SRS). To the present authors' knowledge, no incompatibility seems to exist between the present results and the experimental evidence of instabilities. Several workers have indeed reported that plastic instabilities do take place in Ni_3Al-based alloys, especially at low temperatures within the domain of flow stress anomaly, in particular in the course of reversibility experiments (Veyssière and Saada 1996). However, the experimental conditions from which instabilities are likely to result are not yet clearly established except for the recently reported correlation between serrations and strain-rate jumps (Demura and Hirano 1997), which we have not explored yet.

3.2. *Strain-rate sensitivity*

When cross-slip locking is not accounted for, dislocations are ascribed to remain in the O slip plane where they were sitting before the deformation test was started. When the dislocation density becomes large enough for the elastic interactions to be of the order of magnitude of the friction stress, the work hardening vanishes and deformation proceeds smoothly. All the dislocations are moving simultaneously and at a moderate velocity directly monitored by the applied strain rate (figure 2). The SRS is Newtonian in nature (Devincre and Kubin 1997b), showing a linear dependence of τ_{app} upon $\dot{\gamma}$ which takes place over three decades of strain rate. In other words, the plastic flow is controlled only by the viscous nature of dislocation glide via the adjusted drag coefficient B (§2). The strain rate obeys

$$\tau_{app} \approx \frac{\dot{\gamma} B}{\rho b^2}, \tag{12}$$

which is a variant of equation (3) reformulated to include the Orowan expression. When, on the other hand, the KWLs are incorporated in the hypotheses of the simulation to represent a model Ni_3Al crystal, then no significant variation in the flow stress can be observed over two decades of strain rate (between $\dot{\gamma} = 10^{-2}$ s^{-1} and $\dot{\gamma} = 1$ s^{-1}). This lack of a sensitivity to the strain rate is accompanied by a drastic change in the dislocation dynamics. Only a very small fraction of dislocations are mobile during plastic bursts and the dislocation free-flight time is small compared with the waiting time in the KWL configuration (figure 5). Figure 6 reproduces the dependence of the mean free-flight time upon temperature. The rapid decrease stems from the fact that the probability of forming KWLs, that is of immobilizing a dislocation gliding in an O plane, increases exponentially with increasing temperature.

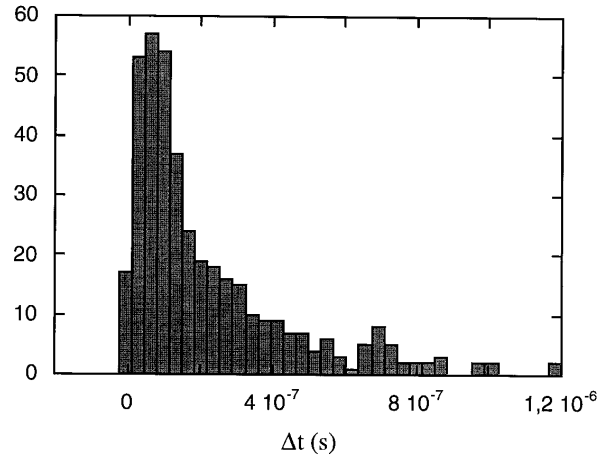

Figure 5. Statistical distribution of the dislocation free-flight time between the destruction of a KWL and the formation of the next KWL on the same line. The simulation test is conducted at 400 K; the strain rate is equal $10^{-1}\,s^{-1}$ and the dislocation density to $1.6\times10^{11}\,m^{-2}$.

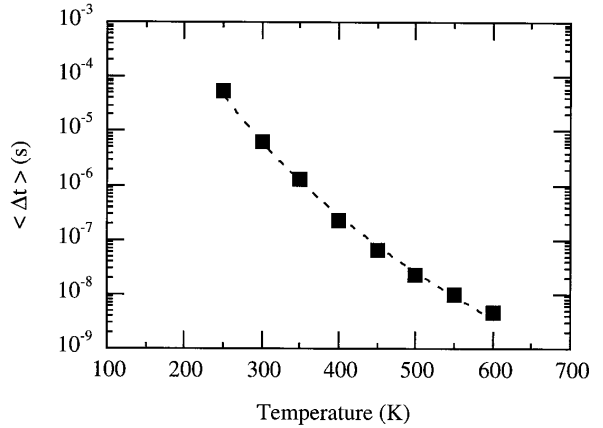

Figure 6. Temperature dependence of the mean free-flight time between two consecutive KWLs. The strain rate and the dislocation density are equal to $10^{-1}\,s^{-1}$ and about $1.6\times10^{11}\,m^{-2}$ respectively.

The dislocation velocities measured in the course of the simulations which incorporate KWL formation are much larger than those found in the absence of a cross-slip locking process (figure 7). Indeed, with the simulation conditions used in figure 7 the dislocation mean velocity is about $20\,ms^{-1}$, while it is about $10^{-3}\,ms^{-1}$ in the absence of locking. As discussed in the previous section, this drastic change in the

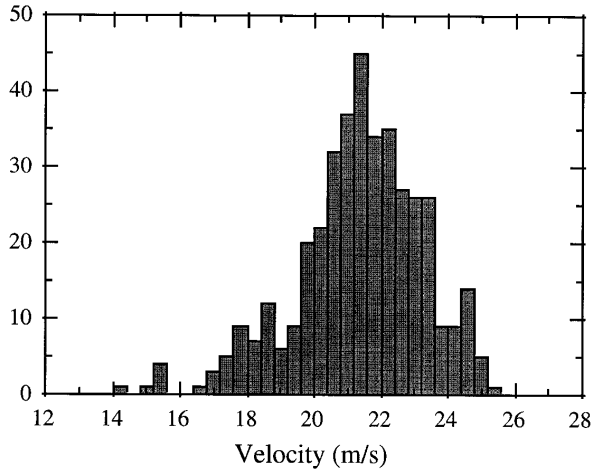

Figure 7. Distribution of the velocity of a dislocation in between two consecutive locked configurations. The simulation conditions are identical with those used in figure 5.

dislocation dynamics comes from the fact that in Ni_3Al the fraction of mobile dislocation is extremely low and the flow stress large.

Figure 8 shows a distribution of free-flight distances in the O plane between the destruction of a given KWL and the formation of the next KWL on the same dislocation (the simulation temperature is 400 K). Since this distribution is rather spread out, dislocation dynamics in the O plane are difficult to anticipate

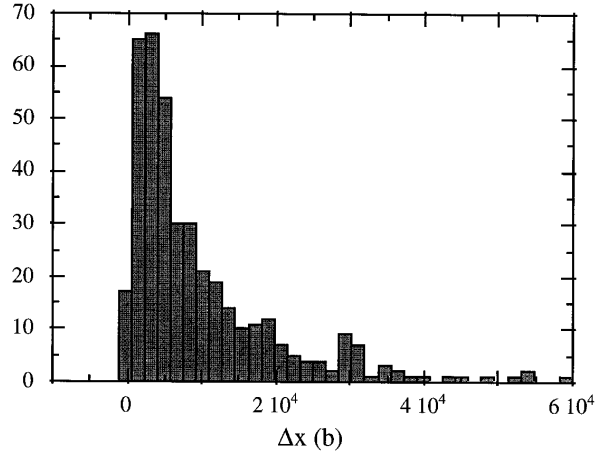

Figure 8. Free-flight distances between two sequential KWLs at 400 K. The simulation conditions are identical with those of figure 5.

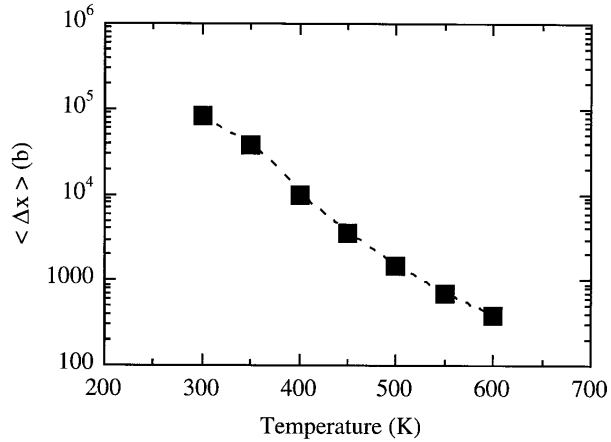

Figure 9. Temperature dependence of the free-flight distance between two sequential KWLs. The simulation conditions are identical with those used in figure 6.

from these data. Nevertheless, the large free-flight distances observed at low temperatures would correspond to large dislocation kinks (§4), as previously observed in the in-plane simulation. When the test temperature is increased, since the probability of forming KWLs increases exponentially, the mean free-flight distances decrease rapidly (figure 9) and kinks are expected to be gradually shorter.

3.3. *Work-hardening rate*

By contrast with the in-plane simulation, the range of plastic strains that one has access to by means of the end-on model is large enough to help to measure meaningful increases in the flow stress. Figure 10 reproduces the temperature dependence of the WHR θ thus measured on the simulated stress–strain curves with two different initial dislocation densities. It should be noted that the WHR is found to decrease continuously with increasing temperature (figure 10). It is clear from these results that the ingredients incorporated in the end-on simulation are sufficient to reproduce very high values of θ (in fact up to $\mu/10$ at 400 K). Also, the WHR is found to be poorly sensitive to the initial dislocation density. In those respects, the agreement with experiments is satisfactory.

In order to determine whether the above results are affected by variations in the dislocation density when deformation proceeds, simulations with larger value of the cross-section, Y_0 for the dislocation annihilation, have been performed. We have found that the dislocation density then decreases rapidly with increasing strain. On the other hand, the recovery increases with increasing temperature since numerous cross-slip annihilations of large amplitude take place in the C plane. Nevertheless, these modifications of the simulation conditions were found not to affect the value of the WHR significantly.

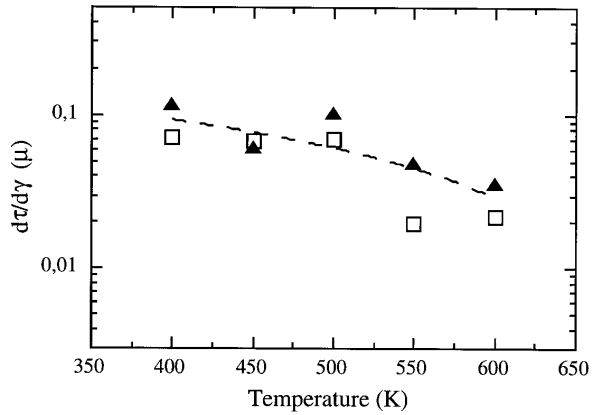

Figure 10. Temperature dependence of the WHR θ which is determined as the slope of a linear interpolation made, over a large deformation domain ($\Delta\gamma = 10^{-3}$), on each stress–strain curve, where the strain rate conforms to the ascribed value ($\dot{\gamma} = 0.1\,s^{-1}$). (□), taken from the stress–strain curves in figure 2, with $Y_{0s} = 40b$; (▲) simulations carried out under a larger annihilation distance ($Y_{0s} = 4000b$), which causes the rapid decrease in the initial dislocation density.

§4. Discussion

Compared with the in-plane approach, the present end-on model permits us to account for interactions between dislocations as well as for the motion of these in the C plane, including double cross-slip. It enables us in addition to check that incorporating elastic anisotropy, which is another difference between our present and previous work, has only a little impact on the overall mechanical behaviour. On the other hand, computing workability implied that several simplifying assumptions be made in the end-on case, of which presumably the most instrumental is concerned with the curvature of dislocations in the O plane.

The in-plane simulation suggests that the flow stress anomaly should be decomposed into two temperature domains, each controlled by a specific dislocation freeing mechanism: firstly the bypassing of KWLs by expanding kinks and secondly the KWL destruction, which operate at low and high temperatures respectively (Devincre *et al.* 1997). When, as observed in the course of the simulations, the mobile dislocations become completely exhausted, the stress to unfreeze a kinked KWL depends upon whether this occurs via the operation of kinks as sources or else by the unlocking of the KWL branches. In the former case of kink sources, the stress is approximately fixed by the kink length, which itself scales with the free-flight distance of the screw dislocation between two consecutive locking events. In the latter case where KWLs are directly destroyed, the stress is determined by the KWL height l_c in the cube plane. As a result, the two temperature regimes rely on two independent critical lengths.

4.1. *The flow stress*

Since, by construction, the end-on simulation cannot account for the bypassing of KWLs by expanding kinks, it is in the high-temperature domain that this model is

expected to reproduce the flow stress anomaly most appropriately. Nevertheless, in the domain of low temperatures, we have found that the CRSSs determined within the end-on simulation (KWL destruction) are only moderately larger than those provided by the in-plane approach (KWL bypassing; figure 3). Hence, while the origins of the two controlling mechanisms are physically independent, distinguishing between the low- and high-temperature modes is not critical in practice. In fact, the two processes of KWL unlocking and kink bypassing are formally equivalent and this can be justified by considering that the former is founded on equation (8), which determines the strength of an incomplete KWL, while the latter is based on the critical stress for kink expansion:

$$\tau_{app} \approx \frac{\mu b}{h_k}, \tag{13}$$

which defines the approximate stress to operate a kink with height h_k as a source. There is a formal analogy between these two mechanisms which originates from the temperature dependence of the mean KWL height $\bar{l}_c(T)$ (equation (10)), which is reciprocal to that of the mean kink length in the KWL bypassing mechanism (Mills *et al.* 1989, Hirsch and Sun 1993, Louchet 1997):

$$\bar{h}_k(T) \approx \frac{V_0}{f \exp\left[-(W_{o\text{-}c})/(kT)\right]}, \tag{14}$$

where V_0 is a constant which can be adjusted to experimental distributions of kink heights. Hence, the fact that the end-on approach reproduces the flow stress anomaly at low temperature results from the fact that the basic equations and most of the parameters employed here are formally the same as those which we had originally set up for the in-plane simulation (Devincre *et al.* 1997). In addition, the operation of kink widening at low temperatures is consistent with the present end-on approach where significantly large free-flight distances then suggest the formation of a noticeable fraction of large kinks.

4.2. *The strain-rate sensitivity and plastic instabilities*

We have seen that deformation proceeds by bursts of dislocation displacements spaced out by waiting times during which dislocations are all immobile. Strain bursts generate softening instabilities on the simulated stress–strain curves (figure 4). When all the dislocations become locked, the applied stress must be increased until locks are destroyed. Interestingly, plastic instabilities are independent of the freeing process considered, that is kink widening or KWL unlocking. We now examine how these instabilities can be made consistent with the atypical property of a low SRS.

When the stress is large enough locally to unlock the weakest KWL, the freshly freed line moves at a velocity imposed by the level of stress itself. Then, the free-flight time is determined by the locking probability and the resulting strain is the product of these two quantities (modulated of course by the elastic stiffness). Thus the decreasing part of a serration must be strain rate independent. By contrast, the ascending part is purely elastic (dislocations are all locked), thus exhibiting a stress–time slope that increases with increasing strain rate. Since the upper stress level is determined by the strength of the weakest KWL, the flow stress is strain rate insensitive and the waiting time in the immobilized state is conversely proportional to the strain rate. Consequently, the low SRS observed in the present computer model relies on the same idea as that expressed by Saada and Veyssière (1993)

and developped by Sun (1997) within the kink widening process, that is there is no correlation between the dislocation properties which control the plastic strain (dislocations are arrested by their self-transformation into KWLs) and the flow stress level (determined by the stability of the KWLs). Two additional points are worth considering.

(1) The jerky nature of flow is smeared out gradually as the temperature is raised since then the plastic strain originates from the superimposition of numerous uncorrelated short slip events.
(2) There is a possibility that plastic flow becomes localized at large strains which would in turn yield spatial instabilities (i.e. shear bands). This is indeed suggested by figure 3 which shows a softening as the dislocation density is increased. However the property remains to be checked under multiple slip conditions.

4.3. *The work-hardening rate*

We have shown in § 3.3 that the end-on simulation is capable of reproducing giant levels of the WHR. The simulation indicates in addition that, since the flow stress decreases as the dislocation density is increased, the hardening mechanism involved should be neither of the forest nor of the Taylor type. In order to gain a better insight into the origin of this property, we have investigated the sensitivity of the distribution of KWL height to temperature and strain. Figure 11 shows histograms of this height at $\epsilon_{plas} = 5 \times 10^{-4}$, as a function of test temperature. As the temperature is raised, the distribution is gradually shifted towards increasing values of l_c and this accounts fairly well for the increase in flow stress (figure 2). Note also that the distribution of KWL height becomes sharper as the temperature is increased. A similar trend is observed in the strain dependence of the KWL height (figure 12). At the beginning of the stress–strain curve, a Gaussian distribution of l_c tends to take place, but KWLs ought to be destroyed for deformation to carry on.

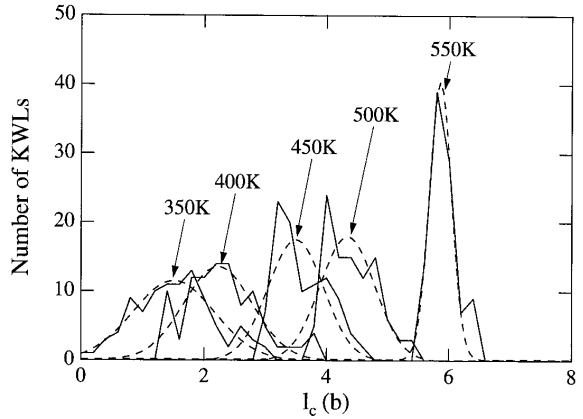

Figure 11. Dependence of the distribution of KWL height l_c (——) at $\epsilon_{plas} = 0.05\%$ upon temperature: (– – –), simulated distributions fitted to a Gaussian distribution.

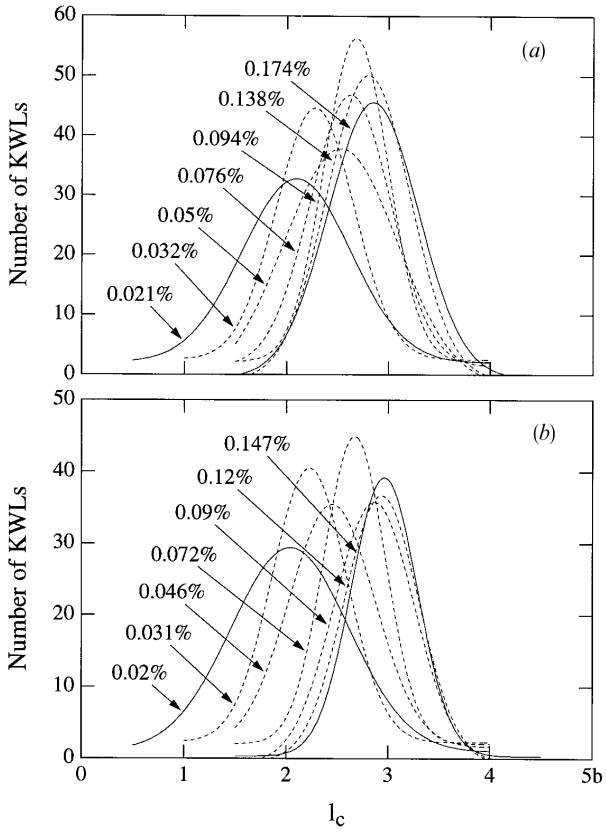

Figure 12. Evolution of the distribution of KWL height during plastic deformation at 400 K (——). For simplicity, each histogram is fitted to a gaussian distribution as in figure 11 (- - - - -). As the strain is increased, the distributions are shifted towards large values of l_c. Two significantly distinct annihilation cross-sections are compared: (*a*) $Y_0 = 40b$; (*b*) $Y_0 = 4000b$.

This causes a preferential depletion of the histogram whereby the weakest KWLs, that is those with smallest heights, are destroyed first. As dislocations continue to become locked, the histogram incorporates a distribution of fresh KWLs which conforms the imposed statistics (figure 12) but which obviously cannot compensate for the selective continuous depletion of the left-hand part of the distribution.

In the light of the above microstructural analysis, the giant WHRs exhibited by $L1_2$ alloys deformed in the domain of flow stress anomaly appear to originate from the preferential exhaustion of the weakest locks and to some extent from the shape of their distribution. What occurs is that the generation of fresh locks cannot counterbalance the systematic destruction of the weakest. For deformation to proceed from γ to $\gamma + \Delta\gamma$, the system does not contain enough locks that can be freed under $\tau(\gamma)$

and it has thus to make use of further available locks, which all are of a higher strength (larger l_c). Accordingly, the applied stress must be raised on an average so as to maintain a constant strain rate. As the strain increases, an increasing fraction of the tail of the distribution is depleted which maintains a high WHR.

It should be noted that the above reasoning can well apply to a regime controlled by a distribution of kinks similar to that of the KWL height, thus explaining the large WHRs measured experimentally in the low-temperature regime. Why the WHR increases with increasing temperature in the low-temperature regime while it decreases at high temperatures is, however, beyond reach within the present approach. The reasons for that may be that we have not taken the possible ageing of the KWL height subsequent to the formation and that we cannot incorporate multiplication realistically. We may nevertheless suggest the following scenario which bears some similarities to the recent phenomenological 'E.L.U.' model proposed by Louchet (1995, 1997).

(i) At low temperatures, coinciding with the beginning of the WHR anomaly, the exhaustion rate of the mobile dislocations is low. Cross-slip is not very efficient and the formation of few KWLs does not restrict dislocation glide. Then, the WHR is inherently modest.
(ii) The WHR takes large values when the generation of fresh locks cannot statistically counterbalance exhaustion (whether this occurs via the systematic destruction of the largest kinks or of the weakest KWLs).
(iii) At the highest temperatures, the decrease in WHR (figure 11) comes in the simulation from the fact that the number of dislocation locking–unlocking events becomes extremely high, thus preventing any preferential depletion of the weak KWL from taking place.

§5. Conclusions

The present 2D end-on simulation reproduces a large amount of the set of mechanical anomalies of $L1_2$ alloys.

(1) The flow stress increases with increasing temperature, here as a result of the exhaustion of mobile dislocations by the formation of KWLs. We nevertheless believe that the controlling mechanism at low temperatures is related to the widening of kinks and is not directly accessible with the present technique.
(2) The very low SRSs originate from the jerky motion of dislocations in the O plane. Changing the strain rate just modifies the waiting times between dislocation-free glide sequences.
(3) Because the free-flight distances are large and the dislocation velocities high, and since dislocation interactions help the freeing processes (at least at the lowest temperatures explored), plasticity proceeds by avalanches of strain manifested by serrations on the stress–strain curves. These serrations result from a process which is entirely intrinsic to the core of dislocations.
(4) Giant WHRs are satisfactorily accounted for by the end-on simulation although their temperature dependence is beyond reach. Irrespective of the freeing process involved (kink widening or KWL unlocking), hardening stems from a preferred exhaustion of the weakest obstacles.

References

Amadeo, R. J., and Ghoniem, N. M., 1989, *Phys. Rev.* B, **41**, 6968.

Bontemps, C., and Veyssière, P., 1990, *Phil. Mag. Lett.*, **61**, 259.

Caillard, D., and Couret, A., 1996, *Dislocations in Solids*, Vol. 10, edited by F. R. Nabarro (Amsterdam: North-Holland), p. 69.

Caillard, D., and Paidar, V., 1996, *Acta mater.*, **44**, 2759.

Demura, M., and Hirano, T., 1997, *Phil. Mag. Lett.*, **75**, 143.

Devincre, B., and Kubin, L. P., 1997a, *Mater. Sci. Engng*, **A234–236**, 8; 1997b, *Phil. Trans. R. Soc.* A, **355**, 2003.

Devincre, B., Veyssière, P., Kubin, L. P., and Saada, G., 1997, *Phil. Mag.* A, **75**, 1263.

Ezz, S. S., and Hirsch, P. B., 1994, *Phil. Mag.* A, **69**, 105.

Hemker, K. J., 1990, PhD Thesis, Stanford University, Stanford, California.

Hirsch, P. B., 1993, *Mater. Res. Soc. Symp. Proc.*, **288**, 33.

Hirsch, P. B., and Sun, Y. Q., 1993, *Mater. Sci. Engng*, 395.

Louchet, F., 1995, *J. Phys. III*, **5**, 1803; 1997, *Mater. Sci. Engng*, 275.

Mills, M. J., Baluc, N., and Karnthaler, P., 1989, *Mater. Res. Soc. Symp. Proc.*, **133**, 203.

Mills, M. J., and Chrzan, D. C., 1992, *Acta metall.*, **40**, 3051.

Molénat, G., Caillard, D., and Couret, A., 1993, *Mater. Res. Soc. Symp. Proc.*, **298**, 281.

Paidar, V., Pope, D. P., and Vitek, V., 1984, *Acta metall.*, **32**, 435.

Saada, G., and Veyssière, P., 1993, *Structural Intermetallics*, edited by R. Darolia *et al.* (Warrendale, Pennsylvania: Metallurgical Society of AIME), pp. 379; 1994, *Phil. Mag.* A, **70**, 925.

Sun, Y. Q., 1997, *Acta mater.*, **45**, 3527.

Thornton, P. H., Davies, R. G., and Johnston, T. L., 1970, *Metall. Trans.*, **1**, 207.

Veyssière, P., 1997, *Mater. Res. Soc. Symp. Proc.*, **460**, 54.

Veyssière, P., and Saada, G., 1996, *Dislocations in Solids*, Vol. 10, edited by F. R. Nabarro (Amsterdam: North-Holland), p. 253.

3.3. Autres propriétés locales

Ce dernière partie traite de quelques propriétés élémentaires des dislocations qui, à ce jour, on reçu encore peu d'attention.

Dans le cas des matériaux à faible énergie de faute, la largeur de dissociation entre partielles est grande et l'existence d'effets de dissociation sur la stabilité des jonctions, la mobilité des lignes de dislocation, la multiplication, etc, pourrait être examinée. Dans les alliages à très faible énergie de faute, ou sous très forte contrainte dans beaucoup de matériaux, les dislocations partielles bougent individuellement en trainant un défaut d'empilement. La contrainte critique pour le mouvement d'une partielle isolée s'écrit simplement $\tau_c = \gamma/b_p$, où γ est l'énergie de défaut d'empilement et b_p la norme du vecteur de Burgers des partielles. Une dynamique de dislocations dissociées ou de dislocations partielles individuelles est relativement simple à reproduire sur le plan conceptuel. Cependant, la prise en compte des dissociations dans une DD entraîne des surcoûts de calculs importants qui ne pourraient se justifier que pour des applications bien spécifiques [100, 117, 118]. A ce jour, il n'est pas certain qu'il existe une réelle motivation scientifique pour ce genre d'étude.

Le mécanisme de *montée* des dislocations non-vis est non conservatif. Il repose sur un transport de matière assuré par la diffusion de défauts ponctuels et ne peut donc intervenir qu'à relativement haute température. La vitesse de montée est généralement beaucoup plus lente que celle du glissement, c'est pourquoi il est difficile dans une même simulation de considérer simultanément les deux modes de déplacement. Il n'existe à ce jour que très peu de modélisation mésoscopiques incluant l'effet de la montée (que des simulations 2-d). Néanmoins, les solutions pour réaliser de telles modélisation, sans être simples, sont évidentes. Il n'est naturellement pas possible de traiter ce mécanisme au niveau atomique, mais le flux de défauts ponctuels sur une dislocation et la vitesse de montée qui en résulte peuvent être modélisés dans le continu. Afin de calculer cette vitesse de montée, avec ou sans prise en compte des effets de la contrainte sur la diffusion, il est possible d'utiliser un schéma similaire à celui proposé par Chateau et al. [119] pour étudier la diffusion de l'hydrogène au coeur des dislocations. De même, pourvu que l'on néglige la dynamique des crans formés le long des lignes de dislocations, la description du mouvement des dislocations en dehors de leur plan de glissement est simple à reproduire avec les modèles continus de discrétisation des lignes [120]. Il y aurait plusieurs objectifs possibles pour une étude de la montée des dislocations à l'échelle mésoscopique : - la cinétique de franchissement d'obstacles localisés stables, c'est-à-dire des précipités plutôt que des petits amas de défauts ponctuels, - la détermination de la forme de la loi de vitesses mésosocopique, en particulier son exposant de contrainte - la compétition entre glissement dévié et montée aux températures moyennes.

A l'heure actuelle, le mécanisme élémentaire le plus important qui reste à éclaircir concerne la nucléation des dislocations, plus précisément leur nucléation hétérogène. Des dislocations peuvent être nucléées en surface de couches minces épitaxiées ou de cristaux exempts de dislocations [121], sur des défauts d'interfaces ou de joints de grains [122], en fond de fissure ou sous un nanoindenteur [123]. Les deux principaux domaines d'étude sont donc la transition ductile-fragile, et surtout la génération des dislocations dans les matériaux nanostructurés. Ce type de problème a fait l'objet de nombreuses études récentes à l'échelle atomique, mais on est encore assez loin de pouvoir en tirer une règle locale systématique à l'échelle mésoscopique.

CHAPITRE 4

Mobilité des dislocations et plasticité

4.1. Vitesse des Dislocations

La mobilité d'une dislocation isolée est modélisée de différentes manières en fonction de l'amplitude de la contrainte appliquée sur la ligne de dislocation et de la nature de ses interactions avec le réseau cristallin ou divers défauts, y compris d'autres dislocations. Une première approche consiste à examiner le déplacement d'une ligne de dislocation isolée, rectiligne et infinie, dans un continuum élastique. Pour une dislocation vis, en l'absence de dissipation et dans le cadre de l'élasticité isotrope, les conditions d'équilibre dynamique sur la ligne se réduisent à une équation de la forme [21, 41] :

$$\Delta \mathbf{u} = \frac{1}{{c_t}^2} \frac{\partial^2 \mathbf{u}}{\partial t^2}, \tag{4.1}$$

où $c_t = (\mu/\rho_o)^{1/2}$ est la vitesse d'une onde de cisaillement transverse, qui est égale à la vitesse du son dans un cristal élastique isotrope, et ρ_o est la densité du milieu. Pour une vitesse uniforme, v, les solutions de l'équation 4.1 ont un comportement de type relativiste et l'énergie élastique totale diverge comme $(1 - v^2/c_t^2)$ lorsque $v = c_t$. On peut alors attribuer aux dislocations une masse effective, $m_o = W/c_t^2 \approx \rho_o b^2$ par unité de longueur. En fait, les dislocations ont une faible inertie, car cette masse au repos est approximativement égale à la masse d'une rangée d'atomes de même longueur.

Au cours de son déplacement, une dislocation dissipe de l'énergie via différents mécanismes, dont l'importance relative et la nature varient suivant que v est proche ou non de la vitesse limite c_t. Classiquement, on différencie les régimes plastiques dits "dynamiques" des régimes "quasi-statiques", la frontière entre les deux se situant approximativement à $v \approx c_t/2 \approx 10^3$ ms^{-1}. Pour une dislocation qui se déplace dans le régime dynamique, il faut tenir compte des effets intertiels et il existe deux principaux modes de dissipation. Le premier a pour origine le rayonnement de modes de phonons par les dislocations qui accélèrent ou oscillent. Le second est lié aux interactions entre le champ de déplacement de la dislocation et les modes de phonons du cristal. On trouve une discussion détaillée de ces mécanismes dans les ouvrages de Weertman et Weertman [124], Alshits et Indenbom [91] et Hirth et Lothe [21]. Ces régimes dynamiques sont observés lors d'essais de déformation par chocs ou à de très grande fréquences d'oscillation, près d'une fissure qui se propage en mode fragile, ou encore localement lorsque deux dislocations s'attirent fortement à courte distance, pour s'annihiler ou former une jonction.

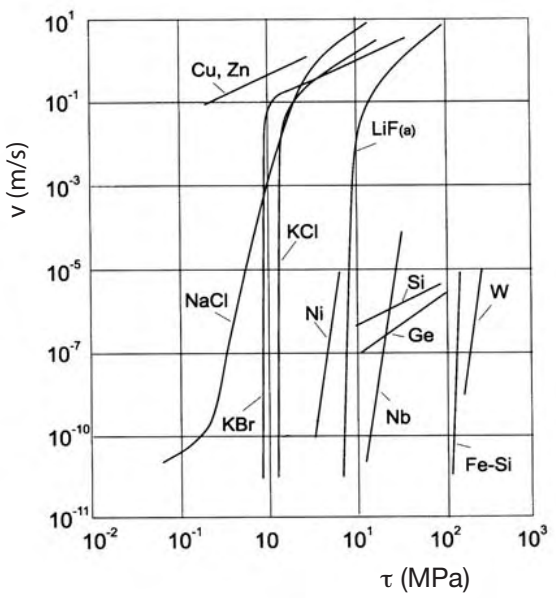

FIG. 4.1.: Mesures expérimentales de la mobilité des dislocations dans différents matériaux et à la température ambiante (excepté pour Ge (450°C) et Si (850°C)) (d'après [125]). Ces mesures ont été effectuées par attaque chimique de la surface de monocristaux, entre deux applications d'une contrainte contrôlée pendant un très court intervalle de temps.

Pour les dislocations qui se déplacent à $v < c_t/2$, les effets d'inertie et de rayonnement deviennent négligeable. En l'absence d'obstacle forts (ou entre deux obstacles forts), ce sont les mécanismes de frottement visqueux induits par les phonons, ('phonon drag'), qui deviennent prépondérants. Comme cela a déjà été mentionné plutôt, une vitesse de $c_t/2$ correspond à une distance de 10 nm parcourue en 10^{-11} s. Les échelles de longueurs et de temps des simulations de DD entrent donc en majorité dans cette classe de problème.

Par opposition avec les hypothèses simplificatrices utilisées ci-dessus, les vraies dislocations ne sont pas de longueur infinie, ne sont pas isolées et interagissent avec différents types d'obstacles. D'un matériau à l'autre, on mesure une grande diversité de relations contrainte-vitesse, comme illustré par la figure 4.1. Aux très faibles vitesses, un rapport constant entre vitesse et contrainte imposée (cf. la courbe de NaCl) est la manifestation d'interactions entre dislocations et obstacles au voisinage de la limite élastique. Pour les matériaux à faible limite d'élasticité, l'interaction avec les phonons ne se manifeste qu'au-delà de $v = 10^{-3}c_t \approx 1$ ms^{-1}. Pour les matériaux où il existe une forte friction de réseau, comme Si, les métaux CC et Fe-Si sur la figure 4.1, cette transition est décalée vers les plus grandes vitesses et surtout les plus fortes contraintes. Ces comportements sont fréquemment décrits de manière phénoménologique sous la forme de lois puissance. Dans le cadre d'une approche plus physique, il est utile de distinguer trois régimes de vitesse :

1. En l'absence de friction de réseau et pendant qu'une dislocation se déplace librement entre deux obstacles, sa vitesse est essentiellement contrôlée par ses interactions avec les modes de phonons. En présence d'une 'forêt' de dislocations, ou d'autres obstacles localisés, le mouvement des dislocations est saccadé et consiste en une alternance de temps d'arrêt devant les obstacles et de temps de vols entre ces mêmes obstacles. Le rapport temps d'attente sur temps de vol peut varier très sensiblement suivant la vitesse imposée aux dislocations. Dans le régime quasi-

statique, il est très grand et la vitesse instantanée d'une dislocation mobile peut être notablement supérieure à sa vitesse moyenne. Le temps d'attente qui gouverne la vitesse moyenne est de nature thermiquement activée si les obstacles sont suffisamment forts et localisés (amas de défauts ponctuels, petits précipités cohérents ...), ou de nature purement mécanique dans le cas contraire. Les matériaux généralement choisis pour étudier ce régime sont les métaux CFC purs (cf. Chapitre 5).

2. En présence d'une forte friction de réseau, le déplacement des dislocations est essentiellement contrôlé par des mécanismes élémentaires thermiquement activés, qui favorisent le franchissement des vallées de Peierls. En l'absence de mécanisme additionnel d'ancrage des dislocations, le mouvement des dislocations est en apparence régulier à toute échelle supérieure à l'échelle atomique. Il n'existe pratiquement pas de différence entre vitesses instantanée et moyenne des dislocations. Les métaux entrant dans cette catégorie sont typiquement de structure CC ou HC. L'exemple du zirconium est présenté en détail dans la suite de ce Chapitre (cf. Section 4.2.2).
3. Finalement, les matériaux réels peuvent contenir une grande diversité d'obstacles extrinsèques limitant la mobilité des dislocations de différentes manières. Le durcissement associé à ces obstacles a favorisé le développement de nombreux modèles dans le cadre de la théorie élastique (ces modèles peuvent donc tous être testés par DD). Les modèles les plus importants sont relatifs aux effets d'alliage [126, 127, 128] et de durcissement structural par précipitation [129, 130, 131]. Le problème de l'interaction entre dislocations et joints de grains ou de phases entre aussi dans cette catégorie ; c'est sans doute le moins bien connu [122]. Une discussion sur ce dernier point, consacrée au cas des matériaux nanostructurés, est donnée en fin de ce mémoire, dans mon Projet de Recherche (Chapitre 7).

4.2. Matériaux à forte friction de réseau

Dans certains matériaux, la moilité des dislocations est très faible en raison de leur forte interaction avec le réseau cristallin. Celle-ci gouverne alors le comportement plastique. Ces situations se rencontrent dans le cas de liaisons non-métalliques directionnelles ou, dans certains métaux, lorsque la structure de coeur est étalée de manière tridimensionnelle. On observe dans ces conditions des propriétés mécaniques spécifiques, très différentes de celles qui sont rencontrées dans les métaux CFC. Comme les interactions entre dislocations et réseau cristallin prédominent vis-à-vis des interactions entre dislocations, aucune formation de structures de dislocations organisées n'est observée dans une large gamme de températures, de vitesses de déformation et de déformation.

4.2.1. Plasticité des métaux CC à froid

En dessous d'une température de l'ordre de $0,10 - 0,15\ T_F$, où T_F est la température de fusion, la déformation plastique des métaux CC est gouvernée par la structure de cœur des dislocations vis. Il faut de fortes contraintes pour rendre glissiles les cœurs de ces dislocations qui sont étalés, faiblement mais de manière simultanée, sur plusieurs plans de glissement.

Débutées en 1997, à l'initiative de G. Canova, mes recherches sur ces matériaux se sont focalisées sur le problème du durcissement de la forêt, c'est-à-dire la relation entre contrainte et densité de dislocations. Le résultat le plus marquant est que la relation usuelle entre contrainte et racine carrée de la densité (équation 5.1), n'est plus valable dans les métaux CC à basse température. En accord avec l'expérience, la relation trouvée est plus complexe et met en jeu deux termes. Le premier est linéaire et lié aux effets de tension de ligne, le second est logarithmique et trouve son origine dans la mobilité des segments de dislocation vis, qui est proportionnelle à leur longueur. Un article résumant

les principaux résultats des simulations et la modélisation du mécanisme de la forêt est reproduit en annexe de ce mémoire (cf. Annexe B4).

4.2.2. Déformation plastique du zirconium monocristallin

Dans le cadre du stage post-doctoral de G. Monnet, j'ai entrepris en 2001 la modélisation des mécanismes de déformation plastique des matériaux hexagonaux de transition qui ont pour plan de glissement préférentiel le plan prismatique, notamment le titane et le zirconium. Dans ces métaux, comme dans les cristaux CC, la structure de coeur particulière des dislocations vis induit une force de friction de réseau [132]. On dispose d'observations expérimentales sur les microstructures de dislocations et les propriétés mécaniques, certaines assez anciennes et d'autres plus récentes. Cependant, les mécanismes de dislocations sont assez mal connus (durcissement de la forêt pour les différents systèmes de glissement actifs, effet des impuretés interstitielles sur la mobilité des dislocations, etc). L'objectif de ce travail est 'd'éduquer' une simulation mésoscopique de manière à reproduire à la fois les microstructures et le comportement mécanique du zirconium, qui est choisi comme matériau modèle.

Les premiers résultats de cette étude ont porté sur la force des interactions entre dislocations. De façon inattendue, la simulation de DD, qui capture suffisamment d'ingrédients physiques pour reproduire des microstructures de dislocations réalistes, ne conduit qu'à un durcissement d'écrouissage quasiment nul. Une étude systématique a montré, en effet, que la nature des interactions entre systèmes de glissement prismatique-prismatique, pyramidal-pyramidal et prismatique-pyramidal, ne suffit pas pour expliquer directement les comportements mécaniques observés expérimentalement. Cette étude s'oriente aujourd'hui vers l'étude de mécanismes alternatifs de durcissement, basés sur la formation de crans sur les dislocations. D'autres domaines abordés sont les effets d'alliage (passage du zirconium au Zircaloy) et la prise en compte à l'échelle mésoscopique de défauts d'irradiation.

Available online at www.sciencedirect.com
SCIENCE DIRECT®
Acta Materialia 52 (2004) 4317–4328
Acta MATERIALIA
www.actamat-journals.com

Dislocation study of prismatic slip systems and their interactions in hexagonal close packed metals: application to zirconium

G. Monnet *, B. Devincre, L.P. Kubin

Laboratoire d'Etude des Microstructures, CNRS-ONERA, 29 av. de la Division leclerc, BP72, 92322 Châtillon Cedex, France

Received 4 July 2003; received in revised form 27 May 2004; accepted 28 May 2004
Available online 19 June 2004

Abstract

Simulations of dislocation dynamics in single crystals of hcp zirconium are presented with emphasis on the hardening associated with prismatic slip at low temperature. Two original aspects of the simulation method are discussed, the treatment of the hcp lattice by an orthorhombic representation and the use of periodic boundary conditions. The mobility of screw and non-screw segments are defined in a phenomenological manner. Different investigations on the interactions between dislocations gliding in different prismatic planes show that no junction is formed between intersecting screw dislocations, which results in a rather small forest hardening at low temperature. This explains experimental observations of an initial deformation stage with a low strain hardening coefficient in zirconium or titanium crystals at low temperature.

Keywords: Dislocation dynamics; Strain hardening; Prismatic slip; Simulation; Zirconium

1. Introduction

The present paper is devoted to a simulation study of forest and strain hardening in zirconium crystals deforming by prismatic slip. The plastic deformation of Zr single crystals has been the object of many early studies. Whatever the temperature, prismatic slip is the dominant deformation mode [1]. Secondary deformation modes are mechanical twinning at low temperature [2], and basal and $\langle c+a\rangle$ slip at high temperature [3]. In addition, pyramidal slip is sometimes observed and its activity increases with increasing temperature [6]. The conditions for the operation of these hard slip modes are poorly known, especially at low temperatures, as illustrated by continuum models for polycrystal plasticity and texture simulations (see e.g. [4,5]). In the present study, we exclusively consider dislocation glide in the prismatic planes.

In zirconium, as well as in titanium, which behaves in quite a similar manner, the flow stress is strongly temperature dependent [7–9] and the microstructures of deformed specimens mainly contain long and straight screw segments [6] (see also [10] and references therein for *in situ* studies of prismatic slip in several hcp metals by transmission electron microscopy). Atomistic simulations showing a three-dimensional spread of the screw dislocation cores [11,12], also confirm the presence of a significant lattice friction on screw dislocations. At the mesoscale, the mobility of screw dislocations and its temperature and strain rate dependencies can be modeled in terms of the kink-pair mechanism [13], embedded into the framework of thermally activated deformation [14]. Another contribution to dislocation mobilities stems from a rather strong sensitivity to trace amounts of interstitial impurities, the origin of which has not yet been clarified [7–9,15].

These aspects cannot be investigated at the mesoscopic scale and will be considered in what follows as input properties. On the other hand, strain hardening properties are related to dislocation interactions, which can be treated within an elastic framework and are, therefore, suited for mesoscale analyses.

In the absence of experimental data on pure material, dislocation dynamics (DD) simulations specifically designed for Zr single crystals can be used to check several aspects of the mechanical response. A first step in this direction is presented here. The first three-dimensional DD simulation specifically devoted to crystals with hexagonal symmetry and its application to Zr single crystals is presented in Section 2. As discussed in Section 3, the mobility laws for screw and non-screw segments are implemented by combining current phenomenology and the available experimental data. The interactions between prismatic slip planes and the resulting forest and strain hardening properties are then investigated in Section 4 and discussed in Section 5.

* Corresponding author. Present address: EDF – MMC, Avenue des Renardières, 77818 Moretsur Loing, France. Tel.: +33-1-46-73-44-49; fax: +33-1-46-73-41-55/60-73-68-89.

1359-6454/$30.00 © 2004 Acta Materialia Inc. Published by Elsevier Ltd. All rights reserved.
doi:10.1016/j.actamat.2004.05.048

2. Dislocation dynamics simulations

The DD simulation used in the present study is described in several publications [16,17]. For this reason, only features that are specific to the present work are recalled in this section. Two important aspects are detailed, namely the treatment of the hexagonal symmetry and the monitoring of the mean free-path of dislocations using periodic boundary conditions (PBCs).

2.1. The discrete model

Line discretization and the definition of a three-dimensional lattice tiling an elastic continuum constitute the two essential features of the present DD simulation. Like in other existing simulations [18–20], dislocation lines are decomposed in a piecewise manner but, in the present case, the segments considered are constrained to lie on a lattice that discretizes the simulated volumes. Then, by construction, the dislocation segments can only take a finite number of characters. In practice, only the $[0\,0\,0\,1]$ edge, $\langle 2\,-1\,-1\,0\rangle$ screw and two mixed line directions are taken into account in each slip system. The two mixed directions are needed in order to further treat reactions between prismatic slip and another slip system [21], for instance the pyramidal one. Line discretization decreases the number of degrees of freedom to be accounted for during the displacement of the dislocation lines; it results in a better computing efficiency without loss of accuracy [17,21].

The incremental time steps of the simulation are divided into two parts. Firstly, dislocations are treated as purely elastic defects. The effective force on each segment is computed at its midpoint as a superposition of several contributions. The latter include the Peach–Koehler forces derived from the applied stress, the stress fields of other dislocation segments [22] and a local line tension term taken from the classical work by Foreman [23]. To estimate the resulting displacement of the segments, a mobility law is required. The definition of mobility laws is an important input of DD simulations, especially in the presence of lattice friction. This particular aspect deserves a specific discussion, which is given in Section 3.

Secondly, the positions of the dislocation segments are updated using a procedure that accounts for possible local events occurring during their displacement. These events include direct annihilation with other dislocations, junction formation with non-coplanar dislocations [24] and cross-slip, for which specific local rules are implemented [16]. Therefore, although this is not relevant to the present study, the DD simulation can treat cross-slip from prismatic planes to a secondary slip system and the mutual interaction of these two slip systems.

Finally, well-known limitation of DD simulation originates in the small value of the maximum plastic strain that can be reached, typically a few 10^{-3}. This is due to the fast increase of the number of interacting dislocation segments during plastic straining.

2.2. Hexagonal symmetry

The crystallography of the hcp lattice traditionally makes use of the four Miller–Bravais indices, *hkil*, attached to the four-axis system $\{\vec{a_1},\vec{a_2},\vec{a_3},\vec{c}\}$, where $\vec{c}$ is the axis of six-fold symmetry and the three others axes are lying in the basal plane. This representation is unfortunately not appropriate for DD simulations. It implies handling one additional index with respect to cubic notations and abandoning all the advantages of orthogonality for arithmetic computations. Alternatively, one can use a set of cubic axes and three real indexes, but these coordinate axes do not coincide with those used to discretize the dislocation segments, which makes them fully inconvenient. An alternative solution, which is compatible with our lattice-based approach, has been adopted. It makes use of the orthorhombic description of the hexagonal cell [25,26], which is widely used for numerical calculations in hexagonal lattices. The basal plane is indexed as a $(1\,1\,1)$ plane and the $\vec{a}$ directions become $\langle 1\,1\,0\rangle$ directions, like in the fcc structure. The transformation matrix from the 4D-space generated by the classical Miller–Bravais indices to this new 3D coordinate system is written:

$$M = 22\begin{pmatrix} 0 & 3 & \bar{3} & 4 \\ 3 & \bar{3} & 0 & 4 \\ \bar{3} & 0 & 3 & 4 \end{pmatrix}. \tag{1}$$

The scaling factor of 22 is introduced here to ensure that all the elementary vectors of the simulation have integer value in the orthorhombic set of axes. For example, the matrix M allows transforming the Burgers vectors $\vec{a_1} = 1/3\,[2\,\bar{1}\,\bar{1}\,0]$ and $\vec{a_2} = 1/3\,[\bar{1}\,2\,\bar{1}\,0]$ and the direction $\vec{c} = [0\,0\,0\,1]$, into the new vectors: $\vec{t_1} = 66\,[0\,1\,\bar{1}]$, $\vec{t_2} = 66\,[1\,\bar{1}\,0]$, and $\vec{t_3} = 88\,[1\,1\,1]$. In this new set of coordinates, the discretization length of the screw segments, i.e., their minimum length, L_s, is set to

$L_s = |\langle 1\,1\,0\rangle| = 2$ nm. For edge segments, the corresponding value is $L_e = 3.26$ nm. These small segment's lengths allow treating in an accurate manner the curvature radii of non-screw segments under stress. The above transformation of axes assumes an ideal hexagonal cell ($c/a = \sqrt{8/3}$). In the case of Zr or Ti, where this ratio is about 1.59, the transformation involves a small distortion of the elastic continuum of about 2.7% along the $\vec{c}$ axis. The resulting error, for instance in the Peach–Koehler force, is at most of same order and can be neglected.

2.3. Periodic boundary conditions

The implementation of PBCs in DD simulation was proposed and discussed by Bulatov et al. [27]. These conditions make use of a simulation cell and a set of replicas. Every time a dislocation segment crosses a boundary between two cells, a replica of it emerges in all cells at the equivalent position in the opposite boundary (cf. Fig. 1). There is, however, a known problem associated with PBCs, specifically that of the self-reactions of portions of dislocation loops with their replicas after a certain glide path over the extended simulation volume. This distance is a complex function of the dimensions of the simulation cell, of the slip geometry and of the shape, isotropic or anisotropic, of the expanding dislocation loops. A general solution has been developed to control this artifact and prescribe a minimum value for the self-reaction distance of the order of the relevant

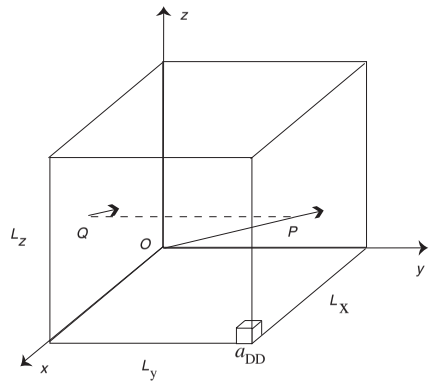

Fig. 1. When a small edge segment propagating along OP crosses the boundary of a simulation cell to enter another cell, a replica of it is reintroduced at a position defined by a translation, here $PQ = -L_y$, in order to balance the dislocation flux. The dimensions of the cell are L_x, L_y, L_z and a_{DD} is the parameter of the underlying lattice, which governs the length scale of the simulation.

mean-free path. It is based on an adequate choice of the dimensions of the primary cell, which is no longer cubic but orthorhombic [28]. Only the particular case of Zr at low temperature, i.e., of strongly anisotropic dislocation loops, is examined here.

At low temperature in Zr, screw dislocations have a low mobility in the prismatic planes, as compared to the non-screw segments that experience a comparatively much smaller lattice friction. Hence, the non-screw segments can travel long distances and the dislocation loops are elongated along the direction of their Burgers vector. The self-interaction distance, λ, to be controlled is then that of non-screw segments propagating along the screw direction in the prismatic planes.

The dimensions of the orthorhombic simulation cell, (L_x, L_y, L_z), are integer multiples of the dimensions of the simulation lattice $a_{DD} : L_x = N_x a_{DD}, L_y = N_y a_{DD}$ and $L_z = N_z a_{DD}$ (cf. Fig. 1). The unit glide direction of the short edge segments is $\vec{d} = (d_x, d_y, d_z)$ and the corresponding glide path is represented by a vector $\overrightarrow{OP}$, starting from the origin O and of increasing magnitude $l : \overrightarrow{OP} = l\vec{d}$. With increasing time, the small portion of dislocation line represented by P repeatedly crosses the periodic boundaries. Every time this happens, a new replica of P starts gliding into a new slip plane, as a result of translations along the three Cartesian axes, like the one shown in Fig. 1. Eventually, after a number (u, v, w) of boundary crossings and translations along the three Cartesian directions, P returns to its original position or a replica of it. Thus, the condition for self-reaction, is written:

$$\begin{cases} ld_x - uN_x = 0, \\ ld_y - vN_y = 0, \\ ld_z - wN_z = 0. \end{cases} \tag{2}$$

By eliminating l, one obtains two independent relations:

$$\begin{cases} u = \frac{N_x d_x}{N_z d_z} v, \\ v = \frac{N_z d_z}{N_y d_y} w. \end{cases} \tag{3}$$

This set of equations has an infinite number of solutions for integer values of (u, v, w). The first self-reaction event is the physically meaningful one; it corresponds to the smallest non-zero integer solution (u_0, v_0, w_0) of the set of Eqs. (3). One then has:

$$\lambda = \sqrt{(u_0 L_x)^2 + (v_0 L_y)^2 + (w_0 L_z)^2}. \tag{4}$$

For an elongated loop expanding in two opposite directions, Eq. (4) represents the total self-annihilation diameter, i.e., twice the self-interaction path of each extremity. From this simple result, we see that the lengths $u_0 L_x$, $v_0 L_y$ and $w_0 L_z$ define the dimensions of a virtual extended crystal such that a dislocation loop expanding from its center gets annihilated when reaching its boundaries. As a result, the dimensions of this virtual crystal can be adjusted by selecting adequate cell dimensions for a given slip system in order to impose any prescribed self-annihilation distance.

Due to the high Peierls stress, it is not possible to simultaneously activate the three prismatic slip systems in single crystals. Then, it is sufficient to control only two mean-free paths. For instance, with an orthorhombic simulation cell of reduced dimensions $N_x = N_y = 3/2N_z = 3564$, and with $a_{DD} = 0.343 \times 10^{-8}$ m, the solutions of Eq. (4) are $(u = 0,\ v = -2,\ w = 3)$ and $(u = -2,\ v = 0,\ w = 3)$, for short non-screw segments propagating along the screw direction in the two prismatic planes $P_I = (0\bar{1}10)[2\bar{1}\bar{1}0]$ and $P_{III} = (\bar{1}100)[\bar{1}\bar{1}20]$, respectively. The mean free-path has then the same value in the two systems, $\lambda = 2\sqrt{2}N_x a_{DD} \approx 34$ μm. These values are the ones adopted in this work for the study of duplex slip in prismatic planes (cf. Section 3.2).

3. Mobility laws

3.1. Screw dislocations

A typical Arrhenius form suited for representing dislocation motion by a kink-pair mechanism is written [14]:

$$v(\tau^*, T) = v_0 \frac{l}{l_0} \exp\left(-\frac{\Delta G(\tau^*)}{kT}\right), \tag{5}$$

where, v is the velocity of a straight screw dislocation segment of length l between strong obstacles to kink motion, $\Delta G(\tau^*)$ is the activation free-energy under the effective shear stress τ^* at the absolute temperature T and k is the Boltzmann's constant. The velocity v_0 is a constant, which includes a Debye frequency and other terms [30], and l_0 is a scaling length. The proportionality of the velocity to the segment's length accounts for the number of potential nucleation sites in competition for each kink-pair nucleation event. The prefactor is not strictly speaking a constant, but its variations are negligible as compared to those of the exponential term.

Following a method previously developed for the simulation of Dislocation dynamics in bcc metals [29,30], use was made of a phenomenological form for the activation free energy associated with dislocation–obstacle interactions [31]:

$$\Delta G(\tau^*) = \Delta G_0 \left(1 - \left(\frac{\tau^*}{\tau_0}\right)^p\right)^q, \tag{6}$$

ΔG_0 is the total activation free energy, τ_0 the Peierls stress at 0 K and p and q are free parameters. The unknown parameters in Eqs. (5) and (6) were fitted to experimental data on single crystals obtained by Mills and Craig [8]. We obtained: $v_0 = 1600$ m/s, $l_0 = 5$ μm, $p = 0.757$ and $q = 1.075$. $\tau_0 = 262$ MPa $= 5.8 \times 10^{-3}\mu$ (where $\mu = 45$ GPa is the shear modulus of zirconium extrapolated at the absolute zero of temperature). The total activation energy is $\Delta G_0 = 1.06$ eV, or $0.12\mu b^3$ (with a basal Burgers vector $b = 0.323$ nm). These values are in agreement with experimental determinations [7,8] and the reduced values are of same order of magnitude as those found in bcc metals [29,30].

In the present work, we assumed that the effect of interstitial impurities present in the material tested by Mills and Craig [8], which is about 1200 wt. ppm, is incorporated into the above stress vs. velocity law for screw dislocations. In Ti or Zr, it was shown by Tyson [33] (see also [9]) that there is no net elastic interaction energy between a perfect screw dislocation and a solute atom inducing a tetragonal distortion. It has been suggested that the interaction between screw dislocations and interstitial solutes is chemical in nature and induces a modification of the core structure of screw dislocations and of the resulting energetic of kink-pair nucleation rate, whereas propagating kinks probably also interact with solute atoms. These hypotheses, which have not yet been confirmed by atomistic simulations, are implicit in the present treatment of the screw dislocation velocities.

3.2. Non-screw segments

The non-screw segments have a much larger mobility than the screw ones, as experimentally attested by the highly anisotropic shapes of expanding dislocation loops (cf. Section 4.2 and Fig. 3(c)). This indicates that their interaction with interstitial solutes has a weaker effect on their mobility than the Peierls force has on the mobility of screw dislocations. Their dynamics involves two unknown quantities: their mean free-flight distance, λ, and their velocity, which depends in principle on stress and temperature. A range of plausible values for these two parameters was obtained by considering their coupled influence on the simulated microstructures and the stress–strain curves.

Non-screw dislocations are responsible for the occurrence of a small pre-yield deformation at stress levels below the critical resolved shear stress (CRSS), i.e., before the onset of screw dislocation motion (cf. Fig. 2). In the DD simulation and below the macroscopic yield stress, the non-screw segments are mobile and are seen to trail long dipoles of sessile screw segments. This effect is well documented in pure bcc crystals [30], much less in Ti or Zr crystals, due to usually high impurity contents. No estimate is available for the related mean-free path but it seems reasonable to assume that it is governed by strong obstacles like sub-grain boundaries, other dislocations, or simply the free surfaces of the specimen. Assuming too great value for the mean free-path λ would result in an unrealistically large amount of pre-

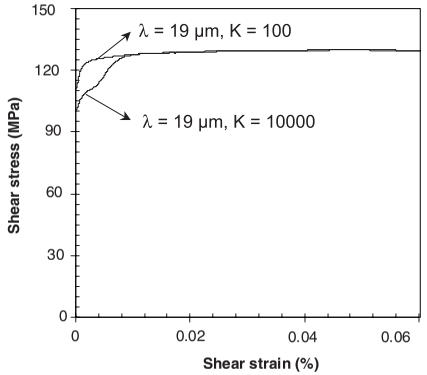

Fig. 2. Influence of K, the ratio of non-screw to screw velocities, on the simulated stress–strain response. The temperature is 300 K and the constant imposed strain rate is 10^{-3} s^{-1}. λ is the mean free-path of the non-screw dislocations.

yield deformation given by non-screw segments. With too short a value, long screw segments would no longer be obtained. In the absence of any numerical data, it was assumed that λ is at least one order of magnitude larger than the average distance between dislocations. As this last distance is in the μm range, an appropriate value of λ is typically a few tens of micrometers. This value was implemented into the DD simulation via the PBCs (cf. Section 2.3).

Several types of stress vs. velocity laws were tested for the mobility of the non-screw segments. They were found not to affect the flow stress as long as the mobility of non-screw segments was substantially larger than that of screw segments. For the sake of simplicity, the mobilities of the two types of segments were assumed to be proportional to each other, with a proportionality constant K.

Fig. 2 shows simulated stress–strain curves at 300 K for two different values of K, $K = 100$ and $K = 10,000$ and with a mean free-path of 19 μm for the non-screw segments. One can see that a substantial change in the value of K does not alter the yield stress, which confirms that the latter is governed by the onset of screw dislocation motion. However, such a change affects the pre-yield stage: as expected, the pre-yield deformation increases with increasing non-screw mobility. With very high values of K, however, the time step of the simulation has to be reduced, due to the increase in the velocity of non-screw segments, which results in a loss of computing efficiency. With values of K smaller than 100, dislocation loops tend to become less anisotropic than experimentally observed [6]. All these dependencies are not significantly affected if the value of λ is modified within the previously defined range. As a result of this preliminary study, all the simulations of plastic deformation were carried out with $K = 1000$ and $\lambda = 34$ μm.

4. Simulation results

4.1. Initial configurations

The initial configurations used in DD simulation attempt to mimic those of annealed specimens. The orthorhombic reference cell has linear dimensions of about 10 μm. It initially contains a random distribution of Frank–Read sources on the three prismatic slip systems. All the sources are of edge character and their total density is about 10^{-3} m^{-2}. The simulations reported here were carried out with a tensile axis parallel to $\vec{a_2}$, which activates duplex slip on the two prismatic systems P_{I} and P_{III} with a Schmid factor of 0.433. These symmetrical conditions are the simplest ones that allow characterizing the forest interactions between two prismatic slip systems.

4.2. Simulated microstructures

An example of a simulated microstructure at $T = 300$ K is shown in Fig. 3(a). After a plastic strain $\epsilon_{\mathrm{p}} = 0.2\%$, obtained by imposing a constant total strain rate of $\dot{\gamma} = 10^{-4}$ s^{-1}, a uniform dislocation density of 1.5×10^{12} m^{-2} is obtained. As expected from the loading conditions, this microstructure is mostly composed of dislocations belonging to the systems P_{I} and P_{III}.

More detail can be seen in a thin foil extracted from the simulation and parallel to the basal plane (cf. Fig. 3(b)). The prismatic planes are normal to the foil and their projections are parallel to the Burgers vectors. The microstructure consists of a random array of long screw dislocation segments on the two active slip systems. Close inspection of the simulated microstructures reveals that very few junctions are formed between the two active slip systems, and none between screw dislocations. Similar dislocation configurations were found all through the low temperature range. They are a direct consequence of the low mobility of the screw dislocations. For comparison, Fig. 3(c) reproduces a transmission electron micrograph from a Zr polycrystal plastically deformed at 300 K (after [6]). (Fig. 3(d)) shows a high-temperature microstructure obtained by attributing to both screw and non-screw segments a Newtonian stress vs. velocity relationship typical of metals where the dislocation velocity is governed by phonon damping [16,17]. In such conditions, the microstructure presents many similarities with those observed in fcc crystals: the screw dislocations are no longer straight; they bow-out under stress and the dislocation loops exhibit isotropic shapes. In addition,

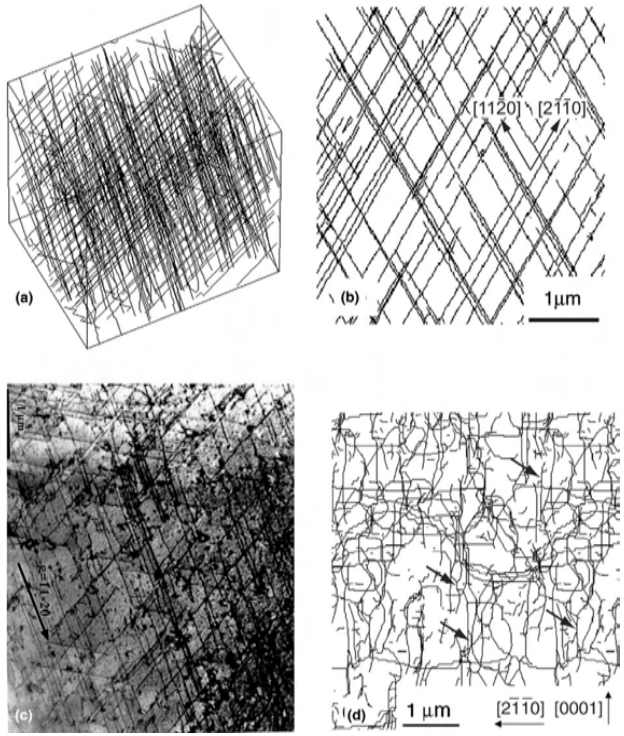

Fig. 3. (a) Simulated dislocation microstructure after a tensile test in duplex slip conditions with a constant imposed strain rate of 10^{-4} s^{-1} ($T = 300$ K, $\epsilon_{\mathrm{p}} = 0.2\%$). (b) A thin foil of thickness 1 μm cut from the simulation cell (a) along the basal plane. The microstructure essentially consists of elongated screw segments developed on the two activated prismatic slip systems. (c) Transmission electron micrograph showing a similar microstructure in a zirconium polycrystal after 2% plastic strain at 300 K with a constant applied strain rate of 5×10^{-5} s^{-1} [6]. (d) A simulated high-temperature microstructure with isotropic velocities for screw and non-screw dislocations. The thin foil, of thickness 1 μm, is parallel to one of the active prismatic slip planes. The arrows point at junction configurations.

junction formation is observed to occur, principally between non-screw segments.

4.3. Thermally activated properties

The evolution of the CRSS with temperature under a constant applied strain rate of 10^{-3} s^{-1} is shown in Fig. 4 and compared with the experimental data that served to calibrate the mobility rule for screw dislocations (cf. Section 3.1). An athermal alloy friction of 20 MPa was added to the glide resistance in order to match the experimental value of the CRSS at high temperature. The excellent coincidence confirms, indeed, that the Arrhenius form describing the mobility law of the screw dislocations fully reproduces the low temperature dependence of the macroscopic CRSS in Zr.

For temperature above 470 K, however, the simulation results start departing from the experimental data (this can be seen from the data points at 520 K in Fig. 4). Close to the so-called athermal temperature of 580 K, where the lattice friction is no longer significant, the mobility of screw dislocations becomes comparable to that of non-screw dislocations [8]. To account for this transition domain, the constant velocity ratio K should be made temperature-dependent. For instance, taking smaller K-values (typically less than 10) in this temperature range, one obtains as expected, rather different dislocation microstructures, similar to the one shown in

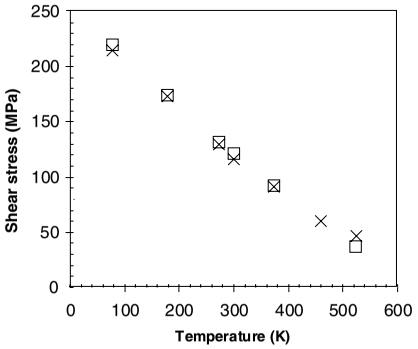

Fig. 4. Temperature dependence of the CRSS under a constant imposed strain rate of 10^{-3} s^{-1}. The simulation results (×) are compared to the experimental values [8] used to calibrate the velocity of screw dislocation segments (□).

Fig. 3(d). Hence, a transition is obtained from the low temperature regime to a high temperature regime governed by dislocation intersections and characterized by primarily athermal processes.

The influence of strain rate on the mechanical response was also tested. Simulation results obtained at $T = 300$ K and with three different imposed strain rates are shown in Fig. 5. The strain rate sensitivity of the yield stress is, as expected, fully consistent with the sensitivity of the screw dislocation velocities to the effective stress, as deduced from the imposed velocity rule (cf. Section 3.1). For instance, the value of the activation volume, V, can be deduced from Fig. 5, by measuring the stress difference associated with a change in strain rate by a factor of 10, in conditions of constant dislocation density (i.e., at the stress maxima). One finds $V \approx 22b^3$, whereas the input value deduced from Eq. (6) is $V = -\mathrm{d}\Delta G(\tau^*)/\mathrm{d}\tau^* = 19b^3$.

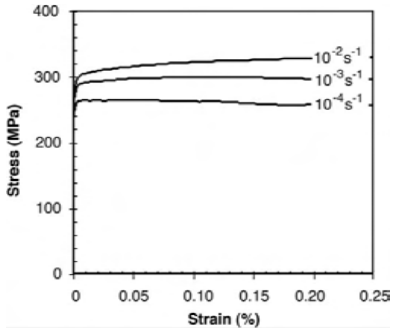

Fig. 5. Simulated stress–strain curves obtained at $T = 300$ K and with three different imposed strain rates. The simulation conditions are the same as in Fig. 4.

The two checks presented above, and others that are not reported here, simply show that, just like in the case of bcc metals [32], the thermally activated properties of the simulated mechanical response are the same as those implemented in the velocity law for screw dislocations (Eqs. (5) and (6)). In the absence of any theoretical prediction of the screw dislocation mobilities, a fitting procedure such as the one utilized here is unavoidable. It allows, nevertheless, performing a study of the mesoscopic response related to the forest and strain hardening properties.

4.4. Forest hardening

Beyond the yield stress, the dislocation density increases continuously and dislocation intersections and reactions become more frequent. Quite generally, the corresponding increase in glide resistance is thought to be responsible for strain hardening. However, no measurable work hardening was yielded by the present DD simulations in the low temperature range, as can be checked from Fig. 5. In contrast, a smooth yield point was systematically recorded, inducing some softening either just after the yield stress or after a variable amount of strain. This feature is associated with a continuous multiplication of the screw dislocations and an absence of storage, leading to a plastic strain rate that slightly increases above the nominal value. This seems to indicate that the interaction between prismatic slip systems does not harden the crystal. To understand this unexpected result, the strength of the prismatic forest was examined by two different methods. An interaction mapping was constructed, which describes the domain of junction formation for different possible geometrical configurations. It is emphasized that, owing to the purely elastic nature of the processes investigated, these simulations are parameter-free. Further, model simulations of latent hardening were performed to quantify the contribution of the forest density to the flow stress.

4.4.1. Interaction mapping

The orientation dependence of the interaction between two initially straight, non-coplanar, segments gliding in two different prismatic planes has been simulated. For more detail on the procedure used, the reader is refereed to a recent systematic study performed on bcc and fcc metals [34]. Fig. 6(a) shows the mapping obtained for the interaction of two segments of initial length 10 μm and with variable orientations, in a graphical representation similar to the one used by Wickham et al. [35] for bcc metals and Madec et al. [36] for fcc metals. The orientation of the lines are defined by their angles φ_1 and φ_2 with respect to [0001], the

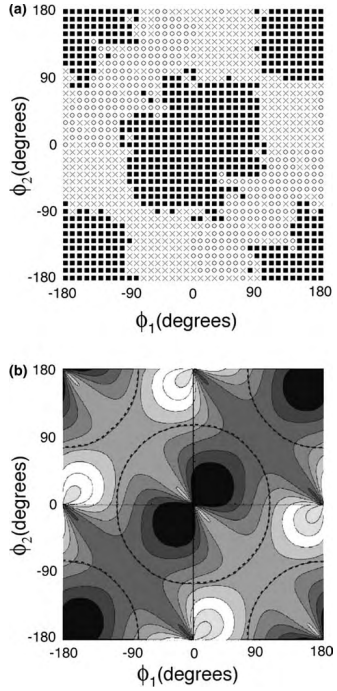

Fig. 6. Interaction mapping for two dislocation segments of length 10 μm in two intersecting prismatic planes. The angles φ_1 and φ_2 define the orientation of the lines with respect to the intersection of the two slip planes. (a) Simulation results (filled rectangles, crosses and open circles refer to junction formation, crossed-state and repulsive crossing, respectively). (b) Elastic prediction for the interaction force of two infinite and straight dislocations (see text for detail).

direction at the intersection of the two slip planes. After relaxation of the initial configuration, three types of configurations are obtained: (i) when the elastic interactions are strong and attractive, junction formation occurs. (ii) Repulsive configurations are observed in some other regions of the mapping, and (iii) when the interaction is weak, either local pinning occurs or the nature of the interaction, attractive or repulsive, cannot be defined. These last states are called cross-states [35,36]. Each final configuration is in equilibrium under zero applied stress and does not depend on kinetics. In other terms, the equilibrium states are independent of the lattice friction and correspond to the configuration formed in a real crystal at high temperature.

In Fig. 6(b), two predictions obtained using simplified elastic models [36,34], are shown. They aim at providing a check from elastic solutions less sophisticated than those yielded by the simulation. The dashed, approximately circular domains enclose areas where junction formation induces a reduction of the elastic line energy of the whole configuration. This condition is calculated for straight segments, in isotropic elasticity and with an orientation-dependent line tension that does not include a logarithmic term (this last term is, indeed, accounted for in the simulations). The set of contour levels in gray shades represent iso-interaction forces (white corresponds to strong repulsion and black to strong attraction) along the shortest approach distance of two rigid, infinite dislocations. This last calculation was performed using a simple solution given by Kroupa [37].

The comparison between Fig. 6(a) and (b) shows that, like in other crystal structures, junction formation can be qualitatively predicted by an energetic criterion. This criterion is, however, slightly in defect when the two segments are initially repulsive, which clearly shows the limits of too simple elastic models [34]. Junctions between prismatic systems are always formed when the dislocation lines are the most attractive and make a small angle with respect to the intersection of the slip planes and with each other. This maximizes their interaction, which results in junction formation inside a closed domain centered on the origin and its periodic duplicates. The edge direction [0001] is located at the center of these domains, where the junction strength is maximum. On the other hand, one can note that the regions corresponding to the intersection of two screw lines, $\varphi_1 = \pm 90°$ and $\varphi_2 = \pm 90°$, are always outside the domain of junction formation.

During the plastic deformation of Zr crystals at low temperature, the dominant component of the dislocation density is of screw character. It is, therefore, not likely to form junctions through forest interactions, irrespective of the kinetics of the process. The short and highly mobile non-screw segments have a quite small probability of mutual interaction, whereas the intersections of screw and non-screw segments are found at the periphery of the domain of junction formation, which means that they constitute a weak obstacle. Hence, very little forest hardening is expected to occur at low temperature, in agreement with the results reported in Fig. 5 and the absence of junctions in the simulated microstructures (Fig. 3(b)).

At high temperature, in contrast, the hardening due to the prismatic forest should not be much different from the typical stage II behavior of fcc crystals, since the mapping shown in Fig. 6(a) is not much different from the one found for e.g., Lomer locks [36].

4.4.2. Model simulations of forest hardening

In order to substantiate the information provided by the interaction mapping, model simulations of forest hardening were performed. The aim of those

computations is to investigate, in dynamic conditions involving an applied stress and the effect of the lattice friction, the contribution from several types of intersections to the glide resistance. Fig. 7(a) and (b) shows the configurations adopted by long dislocation lines of initially edge or screw character upon moving across a density of intersecting dislocations. These simulations were carried out by imposing a constant strain rate of 10^{-5} s^{-1}. The forest density was set to 10^{12} m^{-2} and it only contained screw dislocations, since the majority of dislocations in the microstructure have that character. The applied resolved stress on the forest slip system was set to zero in order to prevent the forest density from multiplying under stress.

A mobile line of initially edge character acquires a distinct roughness during its motion, which shows that it is, indeed, strongly pinned by junctions formed with forest obstacles. These junctions induce local bowed-out configurations that tend to align themselves along the screw direction (cf. Fig. 7(a)). According to the results of Fig. 6, the interaction between screw and edge dislocation is located at the periphery of the junction lobe and results in a weak junction. However, when the lines that bow out during the unzipping process reach the screw orientation, they form small segments of screw orientation (cf. arrows in Fig. 7(a)). Since these screw segments have a low mobility, they delay the destruction of the junction and increase the effective junction strength with respect to its value at high temperature.

The length of the junctions, reduced by the average distance between forest obstacles, is shorter than predicted by simplified energetic arguments. This is due to the effect of the applied stress, which reduces the equilibrium length of junctions and also to a kinetic effect. The forest dislocations of screw character have a low mobility and the junctions are unzipped under stress before having reached their maximum extension.

Gliding screw dislocations do not exhibit any marked roughness (Fig. 7(b)) and do not form stable junctions with the forest dislocations, as expected. Only a few superkinks are observed to form on the screw lines as a result of the strong local elastic interactions occurring when lines are crossing each other. Hence, the propagation of screw dislocation lines in prismatic slip planes is mostly insensitive to prismatic forest obstacles, except in the occasional cases where the latter are of non-screw character.

Fig. 8 synthesizes these results by showing the stress–strain responses associated with the model simulations shown in Fig. 7(a) and (b) (curves 1 and 3), to which are added two curves obtained in the absence of forest dislocations, for mobiles lines of screw and edge character (curves 2 and 4, respectively). After a transient stage, the stress saturates at a level that is sensitive to the presence

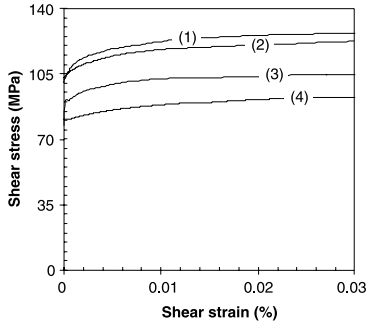

Fig. 8. Simulations of forest hardening: influence of the prismatic forest on the stress–strain curve for edge and screw dislocations at $T = 300$ K and with an imposed strain rate of 10^{-5} s^{-1}. (1) Screw dislocation line interacting with a prismatic forest. (2) Screw dislocation line in the absence of forest. (3) Edge dislocation line interacting with a prismatic forest. (4) Edge dislocation line in the absence of forest.

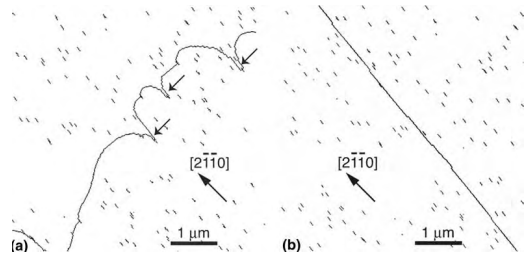

Fig. 7. Simulations of forest hardening. Thin foils of thickness 0.2 μm extracted from the simulation cell. The forest dislocations of screw character intersect the slip plane with an average spacing of 1 μm. The initial character of the mobile line is edge (a) or screw (b). Notice in (a) the short screw segments formed near the junctions (arrows).

or absence of a forest density. The stress levels reached with edge dislocations depend on their mobility. Thus, they depend on the constitutive assumptions made in Section 3.2. What matters, however, is the difference recorded in the presence or absence of a forest density.

With an initially edge dislocation line, a significant hardening is obtained. A moderate forest density of $\rho_f = 10^{12}$ m^{-2} induces in the present case a stress increase of 12 MPa at 300 K. In comparison, the hardening recorded for screw lines does not exceed 3 MPa. This simple example confirms that the motion of screw dislocations is weakly sensitive to the presence of a prismatic forest. In the absence of junctions, the increase in flow stress recorded for screw dislocations does not result from line tension effects. It arises from a local decrease in dislocation mobility due to superkink formation upon elastic interactions with obstacles at small approach distances (Fig. 7(b)). Under a constant imposed dislocation mobility, the corresponding reduction in the free-length of the screw segments results in a rather small hardening according to Eq. (5). Indeed, a small stress increase in the exponential term is sufficient to compensate for the decrease of the prefactor.

5. Discussion

As was shown in Figs. 4 and 5, the sensitivity of the flow stress to temperature and strain rate can be properly reproduced provided that the stress vs. velocity law for screw dislocations is known and that the screw mobility is low compared to that of edges. Thus, prismatic slip of dislocations in pure Zr at low temperature is entirely determined by the strong lattice friction on screw dislocations. Since the physical origin of solute hardening is still a matter of debate (see [6,9]), it is accounted for by lumping it into the velocity rule for screw dislocations. There is also an interaction between non-screw segments and impurities, which can be accounted for by the mobility law for non-screw dislocations. However, this interaction is not strong enough to prevent the formation of long screw segments at low temperature.

The strain hardening produced by the interaction of prismatic slip systems at low temperature is unexpectedly small. The two approaches used here, namely the mapping of equilibrium configurations of interacting dislocations and the simulations of forest hardening, provide results that are consistent with the simulated microstructures. While edge dislocations form junctions with forest dislocations of all characters, the interaction between screw dislocations never results in junction formation. As a consequence, the low temperature hardening is rather moderate, since it only involves non-contact interactions. One may note that it was not estimated here using a Taylor-type relationship between flow stress and the square root of forest density. Indeed, as was shown experimentally by Keh and Weissmann in the case of alpha-iron [38] and further checked in a simulation study of bcc crystals at low temperature [32], the Taylor relation does not apply to forest hardening in the presence of strong Peierls forces. This relation is in fact only valid for dislocations that bow out under stress and take equilibrium shapes between forest obstacles. In contrast, screw dislocation still move as straight lines in the same conditions (compare Fig. 7(a) and (b)).

The simulated stress–strain curves actually exhibit a hardening that is smaller than the one predicted by model simulations of forest hardening, or even a small softening (Fig. 5). This is due to the multiplication of screw dislocations in the absence of obstacles that can significantly reduce their mobility with increasing strain. Thus, single crystals of Ti or Zr deformed in conditions of single or duplex slip on prismatic planes are expected to show a rather flat initial deformation stage as long as other slip systems are not activated. Experimental evidences obtained in such conditions are available for both Ti [9] and Zr crystals (Fig. 9). This figure shows the stress–strain curve of a Zr single crystal containing 400 wt. ppm of oxygen at 300 K. The orientation of the stress axis is close to the one investigated here, but such that a single prismatic slip plane is activated with a Schmid factor of 0.46 (J. Crepin, unpublished work). A kind of easy glide behavior is obtained, with practically no measurable strain hardening. At larger strains, a stage with stronger hardening is observed, which is associated with the onset of first-order pyramidal slip and the observation of cross-slipped traces at the surface of the deformed crystals. In spite of the analogy that is often made between the low temperature properties of bcc metals and hcp metals deforming by prismatic slip, the stress–strain responses appear, thus, to be quite

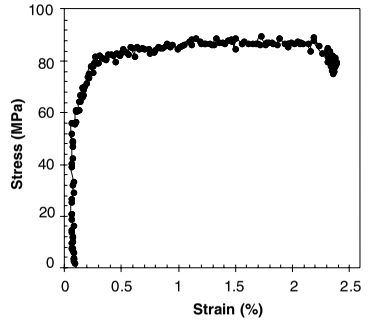

Fig. 9. Stress–strain curve of a Zr crystal in easy glide conditions at $T = 300$ K and with an imposed strain rate of 2×10^{-4} s^{-1}. After J. Crépin (unpublished work), by courtesy.

different. No well-defined stages are found in bcc crystals, due to stronger forest interactions and the continuous production of forest density by the easy motion of non-screw segments in many slip planes. Therefore, the low temperature stress–strain curves associated with prismatic slip in hcp metals are unique and combine features typical of both bcc and fcc crystals.

The present results suggest two directions for future developments. As far as prismatic hardening is concerned, the absence of forest hardening may lead to the consideration of less efficient hardening mechanisms that are usually neglected. The formation of jogs upon dislocation intersections is not accounted for in the present simulations and could be implemented. Perhaps more relevant to the present study is another jog hardening mechanism that is typically associated with lattice friction. The jogs are mobile in the $\{0001\}$ basal plane and are dragged by the screw dislocations. They can also block kinks moving along the dislocation lines, which contributes to a further reduction of the free-length of the screw segments by a mechanism similar to the one described in Section 4.4.2. A strong pinning effect is, nevertheless, not expected since this would contradict the experimental observation of long straight screw segments.

Finally, the activation of first-order $\langle a \rangle$ pyramidal slip results in the occurrence of a hardening stage akin to stage II behavior in fcc single crystals. DD simulations, using the methods developed in the present study, can perform an investigation of the resulting forest interactions. The main difficulty resides in the extreme scarcity of the experimental or theoretical results on dislocation glide in secondary slip systems.

6. Conclusion

This paper presents the first simulation of DD in single crystals of hcp transition metals, like Zr or Ti, which preferentially deform by prismatic slip. The crystallographic structure was reproduced using an orthorhombic representation of the hexagonal lattice. This allowed transposing without major modifications existing DD simulations developed for cubic materials. The emphasis being on low temperature properties, a methodology was developed to control the mean-free path of the highly mobile non-screw dislocations. As the available models provide guidelines but no numerical predictions, the mobilities of screw and non-screw segments were defined in a phenomenological manner. Several investigations were performed on the hardening that results from the interactions of dislocations gliding in different prismatic slip planes. The net result is that no junctions can be formed between intersecting screw dislocations, so that the work hardening coefficient drops to rather small values when temperature decreases and the microstructure increasingly consists of long screw segments. This explains experimental observations of an initial deformation stage with a low strain hardening coefficient during the low temperature deformation of Ti or Zr. Thus, the thermally activated mobility of screw dislocations in zirconium does not influence only the arrangement of the dislocation microstructures but also the strain hardening properties. Finally, this work shows that in spite of the lack of predictive models for dislocation mobilities, it is still possible to carry out controlled simulations of hardening properties and obtain from them some meaningful physical insight.

Acknowledgements

The authors are grateful to Dr. J. Crépin for providing his experimental results prior to publication.

References

[1] Rapperport EJ, Hartley CS. Trans Metall Soc AIME 1960;218:869.
[2] Reed-Hill RE. In: Reed-Hill RE, Hirth JP, Rogers HC, editors. Deformation Twinning, vol. 25. Warrendale (PA, USA): TMS; 1964. p. 295.
[3] Akhtar A. Met Trans A 1975;6:1217.
[4] Tomé CN, Lebensohn RA, Kocks UF. Acta Metall Mater 1991;39:2667.
[5] Fundenberger JJ, Philippe MJ, Wagner F, Esling C. Acta Mater 1997;45:4041.
[6] Ferrer F. PhD thesis, Ecole Polytechnique, Palaiseau, France 2000.
[7] Soo P, Higgins GT. Acta Met 1968;16:177.
[8] Mills D, Craig GB. Trans Metal Soc AIME 1968;242:1881.
[9] Naka S, Lasalmonie A, Costa P, Kubin LP. Phil Mag A 1988;57:717.
[10] Caillard D, Couret A. Mater Sci Eng A 2002;322:108.
[11] Legrand B. Phil Mag A 1984;52:83.
[12] Bacon DJ, Vitek V. Metall Mater Trans A 2002;33:721.
[13] Seeger A, Schiller P. Acta Met 1962;10:348.
[14] Schoeck G. Phys Stat Sol 1965;8:499.
[15] Levine ED. Trans JIM 1968;9:832.
[16] Devincre B. In: Kirchner HO, Pontikis V, Kubin LP, editors. Computer Simulation in Materials Science. Amsterdam, North-Holland: Kluwer Academic Publishers; 1996. p. 309.
[17] Devincre B, Kubin LP, Lemarchand C, Madec R. Mater Sci Eng A 2001;309–310:211–9.
[18] Schwarz KW. J Appl Phys 1999;85:108–19.
[19] Zbib HM, Rhee M, Hirth JP. Int J Mech Sci 1998;40:113–27.
[20] Ghoniem NM, Tong SH, Sun LZ. Phys Rev B 2000;139(2):913–27.
[21] Madec R, Devincre B, Kubin LP. In: Kubin LP, Selinger RL, Bassani JL, Cho K, editors. Multiscale modeling of materials – 2000, Symp Proc vol 653. Warrendale (PA, USA): Materials Research Society; 2001. p. Z1.8.1.
[22] Devincre B, Condat M. Acta Metall Mater 1992;40:2629.
[23] Foreman AJE. Phil Mag 1967;15:1011–21.
[24] Madec R, Devincre B, Kubin LP. Phys Rev Lett 2002;89(25):255508.
[25] Otte HM, Crooker AG. Phys Stat Sol 1965;9:441.

[26] Henry NFM, Lonsdale K. International tables for X-ray crystallography. Birmingham: The Kynoch Press; 1969. p. 19.
[27] Bulatov VV, Rhee M, Cai W. In: Kubin LP, Selinger RL, Bassani JL, Cho K, editors. Multiscale modeling of materials – 2000, Symp Proc vol 653. Warrendale (PA, USA): Materials Research Society; 2001. p. Z1.3.1.
[28] Madec R, Devincre B, Kubin LP. In: Proceedings of IUTAM Symposium on Mesoscopic Dynamics in Fracture Process and Strength of Materials. Amsterdam, North-Holland: Kluwer Academic Publishers, in press.
[29] Devincre B, Roberts S. Acta Metall 1996;74:2891.
[30] Tang M, Kubin LP, Canova GR. Acta Mater 1998;46:3221.
[31] Kocks UF, Argon AS, Ashby MF. Thermodynamics and kinetics of slip. Prog Mater Sci 1975;19:1.
[32] Tang M, Devincre B, Kubin LP. Modelling Simul Mater Sci Eng 1999;7:893–908.
[33] Tyson WR. Canad Met Quart 1968;6:301.
[34] Kubin LP, Madec R, Devincre B. In: Zbib HM, Lassila DH, Levine LE, Hemker KJ, editors. Multiscale Phenomena in Materials, Symp Proc vol 779. Warrendale (PA, USA): Materials Research Society; 2001. p. 25.
[35] Wickham LK, Schwarz KW, Stölken JS. Phys Rev Lett 1999;83:4574–7.
[36] Madec R, Devincre B, Kubin LP. Computat Mater Sci 2002;23:219–24.
[37] Kroupa F. Czech J Phys B 1961;11:847.
[38] Keh AS, Weissmann S. In: Thomas G, Washburn J, editors. Microscopy and strength of crystals. New York: Interscience; 1963. p. 231.

CHAPITRE 5

Plasticité du monocristal CFC

Le travail présenté dans ce chapitre a deux objectifs principaux. D'une part, il s'agit d"élaborer des modèles prédictifs de la plasticité des CFC, basés sur des lois d'évolution des densités de dislocations et pouvant être utilisés dans des modèles continus. D'autre part, les simulations de DD sont utilisées en vue d'identifier les mécanismes physiques contrôlant les propriétés mécaniques des CFC, la formation et l'évolution des microstructures organisées de dislocations et, à plus long terme, leur impact sur les propriétés mécaniques. Sous l'angle de la mécanique des milieux continus, l'existence d'une microstructure auto-organisée est difficile à prendre en compte car elle introduit une hétérogénéité spatiale en constante évolution.

5.1. Durcissement de la forêt

Cette étude entreprise il y a maintenant une dizaine d'année et qui incorpore le travail de thèse de R. Madec est aujourd'hui en voie d'achèvement. Les simulations de DD ont permis une étude complète du durcissement des métaux CFC, depuis les événements élémentaires d'intersection entre dislocations jusqu'à un formalisme continu (collaboration avec T. Hoc, Ecole Centrale Paris). Ces intersections, notamment la formation et la destruction des jonctions, ont dans un premier temps été examinées en détail (§ 3.1). Dans la simulation, tous ces mécanismes sont traités de manière purement élastique et sans aucun paramètre ajustable. Les résultats de cette première étape de notre étude ont permis l'établissement de cartographies des différents types d'intersections, des longueurs des jonctions et de leurs contraintes critiques de destruction (cf. Annexe B3).

A ce stade, il faut souligner que seule une simulation mésoscopique permet d'intégrer sur un volume suffisant les propriétés mécaniques résultant du spectre très large de configurations élémentaires formées en cours de déformation. C'est pourquoi, dans une seconde étape, nous avons pour la première fois simulé le passage des propriétés élémentaires des interactions entre dislocations au durcissement de la forêt dans le monocristal massif. Ces simulations ont été effectuées sur des monocristaux de cuivre d'orientation [001], déformés en vitesse de déformation imposée. La relation classique entre contrainte d'écoulement, τ, et racine carrée de la densité de dislocations, ρ, s'écrit :

$$\tau = \alpha \mu b \sqrt{\rho}, \tag{5.1}$$

où b est la norme du vecteur de Burgers et μ module de cisaillement. Le coefficient α représente l'effet durcissant moyen des intersections entre dislocations. α n'est pas une constante, comme montré dans l'article reproduit ci-dessous, et varie de $\approx 0,5$ aux faibles densités à $\approx 0,2$ aux fortes densités.

La DD conduit à des résultats en excellent accord avec les résultats expérimentaux sur le cuivre, l'argent et l'aluminium, toujours sans paramètre ajustable. On peut en tirer plusieurs enseignements. La loi d'échelle en $\sqrt{\rho}$ peut être améliorée en relaxant une approximation faite sur la tension de ligne des dislocations, où un terme logarithmique est négligé. Cela permet d'éliminer les incertitudes sur la valeur du coefficient α. On aboutit ainsi à une relation extrêmement robuste, valable quelles que soient l'énergie de défaut d'empilement du matériau, la déformation ou l'état d'organisation de la microstructure. Ces aspects, qui ont fait l'objet de nombreuses discussions, sont expliqués à partir de la notion d'un mécanisme purement élastique et mettant principalement en jeu des mécanismes pouvant être décrits en grande partie dans une approximation de tension de ligne.

From Dislocation Junctions to Forest Hardening

R. Madec, B. Devincre, and L. P. Kubin

Laboratoire d'Etude des Microstructures, CNRS-ONERA, BP72, 92322 Châtillon Cedex, France

(Received 14 March 2002; revised manuscript received 18 June 2002; published 4 December 2002)

The mechanisms of dislocation intersection and strain hardening in fcc crystals are examined with emphasis on the process of junction formation and destruction. Large-scale 3D simulations of dislocation dynamics were performed yielding access for the first time to statistically averaged quantities. These simulations provide a parameter-free estimate of the dislocation microstructure strength and of its scaling law. It is shown that forest hardening is dominated by short-range elastic processes and is insensitive to the detail of the dislocation core structure.

DOI: 10.1103/PhysRevLett.89.255508 PACS numbers: 61.72.Lk, 62.20.Fe, 82.20.Wt

The more a crystal is deformed plastically, the larger is the stress needed to further deform it. This property, which ensures the stability of plastic flow, is called strain hardening. Its physical origin is understood in terms of dislocations, the linear defects that carry plastic flow in crystals. When two attractive dislocations gliding in different slip planes cross each other, they can reduce their total energy by reacting to form a third dislocation segment called a junction. This junction lies at the intersection of the two dislocation slip planes. It is usually not mobile and therefore represents a barrier to further dislocation motion, until the local stress is raised to a critical value such that the junction is destroyed and dislocation crossing occurs. During plastic deformation, the dislocation density increases and, as a result, the number of such events continuously increases, thus leading to strain hardening through a mechanism called forest hardening.

The objective of the present study is to establish a rigorous connection between the individual configurations of dislocation intersections and their macroscopic average strength in fcc crystals and therefore to improve the physical content of current models for strain hardening. For this purpose, use is made of a mesoscale simulation of dislocation dynamics (DD). The elementary configurations of two intersecting dislocations have been systematically studied in order to check that their individual contributions to hardening are properly accounted for in the present numerical model. Large-scale 3D simulations of forest hardening in fcc crystals are then presented, leading for the first time to a parameter-free computation of the relation between flow stress and dislocation density. The obtained scaling relation is compared to experimental data and its consequences are discussed.

The calculation of the energy of isolated junction configurations is a very complex problem [1]. In early studies it was performed using elasticity theory with strong simplifications [2,3]. More recently, a few junction configurations have been studied more precisely by atomistic [4,5] and mesoscopic simulations [6,7]. It was confirmed that the contribution of the dislocation core regions to junction stability is negligible compared to the elastic contribution from regions outside the core. For instance, it was shown that the perfect Lomer lock and the Lomer-Cottrell lock, where the core energy is reduced by dissociation and reaction of partial dislocations, have practically the same critical stress for destruction [8].

Within the forest model [2], the critical resolved stress τ to destroy a junction and remobilize the dislocation lines is proportional to $\mu b/l$, where μ is the shear modulus, b is the modulus of the Burgers vector of the mobile dislocations, and l is the distance between the intersecting obstacles along the dislocation line. The average value of this distance scales as $1/\sqrt{\rho_f}$, where ρ_f is the density of forest obstacles. This leads to a well-known relationship:

$$\tau/\mu = \alpha b\sqrt{\rho_f}, \tag{1}$$

where the constant α is an average value of the junctions strength over all existing configurations.

A major difficulty arises when performing this average, because of the wide spectrum of possible dislocation reactions [3]. Nevertheless, Eq. (1) is commonly verified by experiment. In fcc crystals, both theoretical [2,3] and experimental estimates [9,10] exist and they suggest $\alpha \approx 0.35 \pm 0.15$ (cf. the review [11]).

The constitutive rules of three-dimensional DD simulations have been discussed in several papers [12–14] (see also [15] for full details on the present simulation). Thus, for the present purpose, only a few relevant methodological aspects require a specific discussion. In each slip system, the continuous shapes of the dislocation lines are discretized into a finite number of segment directions: screw, edge, or mixed (i.e., making angles of $\pm\pi/3$ and $\pm 2\pi/3$ with the direction of the Burgers vector). This allows us to simplify the treatment of all junction segments, whose line directions at the intersection of two (111) glide planes are of either mixed or edge character. Only $a/2\langle 110\rangle\{111\}$ slip systems are explicitly accounted for (a is the lattice parameter). Additional Burgers vectors of perfect dislocations are obtained by linear combination. For instance, a particular junction, the Hirth lock,

is reproduced by superimposing segments with different Burgers vectors according to the reaction $a/2[\bar{1}10] + a/2[110] = a[010]$. As mentioned above, the dissociation of the dislocations is a core effect that needs not to be considered here. The same holds for the atomic jogs formed at the lines' intersection, as they induce a negligible resistance to dislocation motion [16]. The cross slip of screw dislocations is another important core mechanism that depends sensitively on the dissociation width of dislocations. As will be discussed below, cross slip does not appear, however, to significantly affect the intersection mechanisms. Thus, we focus here on the results obtained in conditions such that cross slip is deactivated in the simulations. The forest model is then investigated in a linear elastic and athermal (i.e., strain-rate independent) framework that does not involve any adjustable parameter.

The resolved effective force per unit length on a segment is the sum of the Peach-Koehler force and of a local line tension term balancing effects of the dislocation discretization [1]. The Peach-Koehler term accounts for the effect of the external loading and of the field of the embedding dislocation microstructure. The steady state dislocation velocity is governed by viscous drag on electron and phonons. It is of the form $v = \tau^{\star} b/B$, where $\tau^{\star} b$ is the effective force and $\tau^{\star}$ is the corresponding effective stress. B is a viscous drag constant ($B \approx 5 \times 10^{-5}$ Pa s in copper at room temperature). The model material investigated here is copper, with isotropic elastic constants $\mu = 42$ GPa, $\nu = 0.33$, and $a = 0.361$ nm. The present results can be extended to any other fcc crystal by appropriately modifying these three material constants.

Before going to large-scale simulations, one must verify that the properties of elementary configurations are well reproduced by the simulations. This is why the three possible types of junctions, namely, the Lomer, Hirth, and glissile junctions, have been examined in detail. We focus here on the Lomer lock, as some of its configurations have already been examined [5,7,8]. The two interacting slip systems are $a/2[10\bar{1}](111)$ and $a/2[011](11\bar{1})$. The tested configurations consist of two initially straight lines, pinned at their ends, of length $l_o = 30$ μm, which intersect at their midpoint. The lines initially make two angles ϕ_1 and ϕ_2, respectively, with the direction of the incipient junction. They are allowed to relax, in the absence of applied forces and under the influence of their interaction forces, until they reach a stable configuration. Three situations can occur. If the lines are attractive, they either zip a junction or, when junction formation is energetically unfavorable, they mutually pin each other at their intersection point. This last configuration is called a crossed state [6]. If the lines are repulsive, they move apart from each other.

Figure 1 shows a three-dimensional plot of the length of the Lomer lock as a function of the initial orientation of the interacting lines denoted by the angles ϕ_1 and ϕ_2.

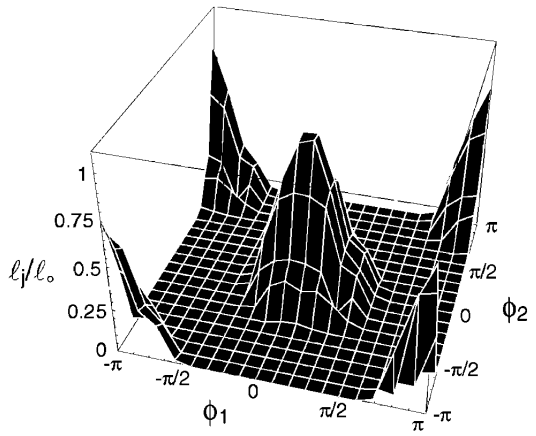

FIG. 1. Three-dimensional plot of the reduced length of the Lomer locks l_j/l_o obtained at the intersection of the two slip systems $a/2[10\bar{1}](111)$ and $a/2[011](11\bar{1})$. ϕ_1 and ϕ_2 are the initial directions of the lines with respect to the intersection of the two slip planes. Each node corresponds to a simulation result. The domain of junction formation consists of a periodic array of closed domains, with maximum junction length ($l_j/l_o = 1$) when the attractive lines are parallel. The regions where $l_j = 0$ correspond to either repulsive interactions or crossed states.

Junction formation is obtained in a periodic array of closed domains. Outside these domains, one finds another attractive region with crossed states and a region of repulsive states. The boundaries between these different types of final configurations were calculated using simplified elastic models, similar to those used in previous studies [2,3,6]. These calculations are not detailed here for the sake of brevity.

As illustrated by Fig. 1, the strength of junctions, which is inversely proportional to their length and to the lengths of the initial dislocations, critically depends on the angles ϕ_1 and ϕ_2. For the Lomer lock, it was verified that the simulated junction lengths and critical destruction stresses are the same as those previously found by other authors in the particular case $\phi_1 = \phi_2$ [5,7]. Even with the simplified geometry used here, averaging the junction strength for all values of the angles (ϕ_1, ϕ_2) involves many uncertainties. Indeed, under stress, the weakest junctions are destroyed in such a way as to provide the crystal with a sufficient density of mobile dislocations [17]. The remaining junctions have a spectrum of strengths and each strength has its own probability of occurrence. This is why only large-scale simulations can effectively integrate the contributions to the flow stress resulting from all the possible configurations of intersecting dislocations.

Large-scale simulations were carried out with several initial dislocation densities, ρ_i, in the range from 10^{10} to 10^{14} m^{-2}. These densities consisted of dislocation sources distributed at random over the 12 possible slip systems of the fcc structure. After full discretization and

relaxation, an initial microstructure with a density smaller than ρ_i was obtained. A constant total strain rate was imposed along a high symmetry [001] axis. For each density, the dimension of the simulated volume, the average length of the source segments, and the strain rate were chosen according to simple scaling laws. To fix ideas, with an initial dislocation density $\rho_i = 1.5 \times 10^{11}$ m^{-2}, a simulation cell of $26.9 \times 31.6 \times 38.9$ μm^3 was used, with a strain rate $\dot{\epsilon} = 2$ s^{-1}. Following the work of Bulatov [18], periodic boundary conditions were used in order to ensure that the dislocation densities are not affected by image forces or dislocation flux unbalance at the boundaries of the simulation cell. These conditions, although extremely useful, have to be handled with care. For instance, the incommensurate dimensions of the simulated volume are intended to limit spurious spatial correlations between the active slip planes [15].

The simulations were stopped once stable plastic flow was reached after the yield stress, which corresponded to plastic strains in the range of 10^{-4}–2.0×10^{-3}. At this point of the stress-strain curve, the average distance between dislocations, $\rho_t^{-1/2}$, where ρ_t is the total dislocation density, is at least 15 times smaller than the initial source length. This ensures that plasticity is governed by forest interactions and not by dislocation multiplication, as should be the case in typical laboratory tests. Figure 2 shows a typical dislocation microstructure obtained in such conditions for an initial density of 10^{12} m^{-2}. More detail about the stress-strain curve, dislocation microstructure, and internal stresses can be found in [17]. With a [001] stress axis, four slip systems have zero Schmid factors and are inactive, whereas eight slip systems are active with the same Schmid factor. To obtain the effective density of forest dislocations in each active slip system, ρ_f, one has to subtract from ρ_t the density of the system considered and those of its two coplanar systems. In the present case, symmetry imposes $\rho_f = 3\rho_t/4$. For each simulation, the flow stress and the final dislocation densities were measured at the maximum strain reached by the simulation.

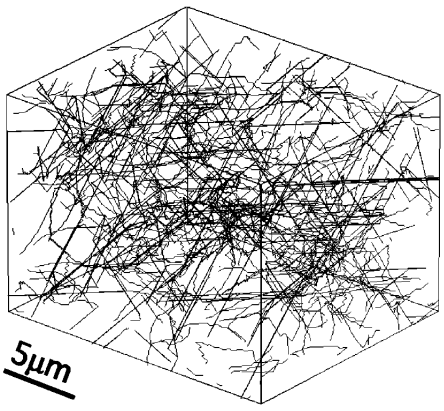

FIG. 2. The cell of the DD simulation and a dislocation microstructure at a plastic strain of 2.0×10^{-3}.

The simulation results are shown in Fig. 3. These results are subject to two causes of uncertainty. One arises from fluctuations on the simulated stress-strain curves, which are inherent to the small volumes investigated and the other from the statistical influence of the initial configurations. The resulting relative error is always within $\pm 5\%$. For comparison, we reproduce in Fig. 3 a compilation of experimental data on Cu and Ag [9] and more recent experimental results on pure Al [19].

For densities in the range of 10^{12} m^{-2}, where many measurements have been performed, the simulation yields the currently quoted value $\alpha \approx 0.35$. Considering, however, the whole range of numerical data, one can see from Fig. 3 that the average slope is not fully consistent with the square root relationship predicted by Eq. (1). In fact, α substantially decreases with increasing forest density, from about 0.5 to about 0.2. This discrepancy has already been mentioned by Basinski and Basinski [9]. Indeed, Eq. (1) makes use of a simplified form for the line tension, which omits a logarithmic term including an inner core radius ($\approx b$) and an outer cutoff radius ($\approx 1/\sqrt{\rho_f}$) taking into account self-screening due to line curvature [9,11]. Upon reintroducing this contribution, which is accounted for in the simulations, Eq. (1) becomes

$$\tau/\mu = k \ln(\rho_f^{-1/2}/b) b \sqrt{\rho_f}, \qquad (2)$$

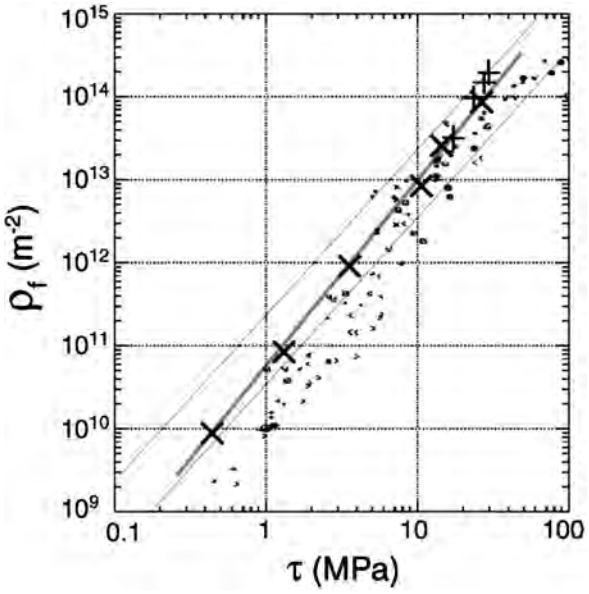

FIG. 3. Logarithmic plot of the forest dislocation density, ρ_f, vs the corresponding flow stress τ. $\times$: simulation results, regression line in grey. $+$: rescaled experimental results on aluminum after [19]. Small symbols: experimental results on Cu and Ag, after [9]. The two thin lines are plots of Eq. (1) with $\alpha = 0.2$ and 0.5.

where k is a constant that again represents the average strength of the forest. Equation (2), with $k = 0.1$, perfectly fits the present numerical data. The simulated results globally fall in the left region of the cloud of earlier data, which corresponds to the cleanest experiments. Equation (2) is also fully consistent with the more recent experimental results at high densities [10,19]. This gives confidence that no contribution to forest hardening that is accessible to experiment is missing in the simulation.

The present results apply to all pure fcc crystals, as illustrated by Fig. 3 in the cases of Cu, Al, and Ag. For instance, it was noticed long ago [9] that in all pure fcc crystals, the athermal deformation stage (stage II), which is governed by forest intersections, exhibits an almost constant strain hardening coefficient of about $\mu/250$.

In multislip conditions, such as the ones used in the present study, dislocation cross slip and dynamic recovery come into play. The scaling law of the forest mechanism [Eq. (2)] nevertheless holds all through the range of dislocation densities, stresses, and strains which has been experimentally investigated. As a matter of fact, at large stresses, Fig. 3 includes both results from poorly organized simulated microstructures and experimental data obtained in conditions where well-formed dislocations cells are necessarily present. The fact that dislocation patterning does not influence notably the value of α has puzzled many authors (see, e.g., [9,10]). Cross slip influences the dislocation density evolution and is responsible for the formation of dislocation patterns. Thus, simulations were carried out in the same conditions as above but taking cross slip into account. In agreement with expectation, heterogeneous microstructures are then formed [17], but the forest constant increases from $k = 0.1$ to $k = 0.109$ only. A tentative explanation for this paradoxical behavior was proposed by Neuhaus and Schwink [10]. Self-organized dislocation microstructures are arranged according to scaling laws such that their flow stress is almost independent of the degree of heterogeneity. It appears now that simulation methods may be of some help in clarifying this question.

Finally, one must notice that the flow stress given by Eq. (2) contains a specific signature of local line curvatures, the logarithmic term. Indeed, the Peach-Koehler forces/stresses induced on the intersecting lines by other loops do not include logarithmic terms whatever the spatial arrangement of the microstructure. Thus, the flow stress of fcc crystals deformed in the multislip condition is dominated by short-range interactions and contact reactions.

In summary, the forest mechanism has been reproduced numerically within an elastic framework that involves no adjustable parameter. The present results consistently show that no core effects appear for fcc crystals when cross slip and climb are suppressed. These results clearly show that DD simulations provide an efficient solution to the problem of averaging the extended spectrum of dislocation interactions during plastic deformation. Thus, a robust connection is established for the first time between the local properties of junction configurations and the resulting flow stress of the bulk material. In parallel, this approach allows one to examine microstructural evolutions under stress. This opens the way for novel types of studies in which, for instance, the global material hardening could be decomposed into a set of contributions stemming from pair interactions between the various slip systems.

[1] J. P. Hirth and J. Lothe, *Theory of Dislocations* (McGraw-Hill, New York, 1982).
[2] G. Saada, Acta Metall. **8**, 841 (1960).
[3] G. Schoeck and R. Frydman, Phys. Status Solidi (b) **53**, 661 (1972).
[4] V.V. Bulatov, F. F. Abraham, L. P. Kubin, B. Devincre, and S. Yip, Nature (London) **391**, 669 (1998).
[5] D. Rodney and R. Phillips, Phys. Rev. Lett. **82**, 1704 (1999).
[6] L. K. Wickham, K.W. Schwarz, and J. S. Stölken, Phys. Rev. Lett. **83**, 4574 (1999).
[7] V. B. Shenoy, R.V. Kukta, and R. Phillips, Phys. Rev. Lett. **84**, 1491 (2000).
[8] C. Shin, M. Fivel, D. Rodney, R. Phillips, V. B. Shenoy, and L. Dupuy, J. Phys. IV (France) **11**, 19 (2001).
[9] S. J. Basinski and Z. S. Basinski, *Dislocations in Solids* (North-Holland, Amsterdam, 1979), Vol. 4, pp. 261–362.
[10] R. Neuhaus and C. Schwink, Philos. Mag. A **65**, 1463 (1992).
[11] J. G. Sevillano, in *Materials Science and Technology*, edited by H. Mughrabi (VCH, Weinheim, 1993), Vol. 6, p. 19.
[12] B. Devincre, in *Computer Simulation in Materials Science: Nano/Meso/Macroscopic Space & Time Scales*, edited by H. O. Kirchner, L. P. Kubin, and V. Pontikis (Kluwer Academic Publishers, Dordrecht, Boston, 1996), pp. 309–323.
[13] H. M. Zbib, M. Rhee, and J. P. Hirth, Int. J. Mech. Sci. **40**, 113 (1998).
[14] K.W. Schwarz, J. Appl. Phys. **85**, 108 (1999).
[15] R. Madec, Ph.D. thesis, University of Orsay, 2001.
[16] J. Friedel, *Dislocations* (Pergamon Press, Oxford, 1964).
[17] R. Madec, B. Devincre, and L. P. Kubin, Scr. Metall. **47**, 689 (2002).
[18] V.V. Bulatov, M. Rhee, and W. Cai, in *Multiscale Modeling of Materials–2000*, edited by L. Kubin *et al.* (Materials Research Society, Warrendale, PA, 2001), Vol. 653, p. Z1.3.1.
[19] N. Hansen and X. Huang, Acta Mater. **46**, 1827 (1998).

5.2. Matrice des interactions entre systèmes de glissement

Dans un modèle continu du monocristal, ou pour un grain d'un polycristal, il faut pouvoir estimer l'activité des différents systèmes de glissement en cours de déformation et, par conséquent, connaître les lois d'interaction entre ces systèmes pris deux à deux. La loi de composition entre divers obstacles de la forêt est bien établie ; elle revient à décomposer sous la racine la densité totale d'obstacles en une densité par systèmes, affectés d'un coefficient qui représente la 'force' de leur interaction avec le système considéré :

$$\tau_c^i = \mu b \sqrt{\sum_j a^{ij} \rho^j} \tag{5.2}$$

Dans cette expression, τ_c^i représente la contrainte critique pour l'activation du système (i). Cette contrainte critique dépend des densités de dislocations sur tous les systèmes (j), y compris pour $i = j$. Les coefficients de matrice a^{ij} tiennent compte des différents types d'interactions entre systèmes. Afin d'aboutir à un modèle complet du durcissement d'écrouissage, cette loi d'écoulement doit être complétée par des lois d'évolutions couplées pour les densités de dislocations. La sensibilité à la vitesse des métaux CFC étant faible dans le domaine du glissement, elle ne réclame pas un effort de modélisation particulier.

Nous avons tout d'abord mesuré par simulations les coefficients de la matrice d'interaction, a^{ij}, et cet exercice a conduit à un résultat tout à fait inattendu. Cette matrice est symétrique et contient six coefficients distincts relatifs à six différents types d'interactions[1]. Deux des coefficients sont faibles car ils correspondent à des interactions élastiques dipôlaires, c'est-à-dire sans formation de jonctions entre dislocations. Trois autres correspondent à des interactions plus fortes car des jonctions sont formées (jonctions de Lomer, de Hirth et jonction dite glissile). Nous mettons à part l'interaction dite *colinéaire* qui intervient entre dislocations de même vecteur de Burgers glissant sur deux plans sécants (ces deux plans sont mutuellement des plans de glissement dévié l'un pour l'autre). Cette interaction était considérée avant notre travail comme de force moyenne ou faible, mais n'avait jamais fait l'objet d'une étude spécifique, contrairement aux trois types de jonctions mentionnés ci-dessus.

Les valeurs des différents coefficients de la matrice a^{ij} ont été obtenus à partir de simulations "modèles" où la nature des arbres de la forêt pour un système de glissement actif donné était contrôlée. Les valeurs obtenues ont été vérifiées en reconstruisant une courbe de déformation en glissement multiple suivant [100] et en la comparant à une courbe simulée dans les mêmes conditions. Les résultats obtenus (toujours sans paramètre ajustable) confirment pour une part les estimations données dans la littérature, mais font apparaître que l'interaction colinéaire a été sévèrement sous-estimée. Elle est de loin la plus forte de toutes et conduit à un durcissement considérable car elle annihile des densités en interaction, ne laissant que des débris seulement mobiles sous forte contrainte.

Ce résultat est maintenant bien vérifié, y compris à l'aide de simulations atomiques. Il peut avoir beaucoup de conséquences sur la modélisation du durcissement des monocristaux en glissement multiple ou celui des polycristaux, ou encore sur l'interprétation des expériences de durcissement latent. Il s'applique en toute généralité et pas seulement aux métaux CFC. La publication qui suit résume ce travail.

[1] Une description systématique des réactions observé dans les cfc lors de l'intersection entre lignes de dislocation est donné dans l'article reproduit en Annexe B 3

The Role of Collinear Interaction in Dislocation-Induced Hardening

R. Madec,[1]* B. Devincre,[1] L. Kubin,[1]† T. Hoc,[2] D. Rodney[3]

We connected dislocation-based atomic-scale and continuum models of plasticity in crystalline solids through numerical simulations of dislocation intersections in face-centered cubic crystals. The results contradict the traditional assumption that strain hardening is governed by the formation of sessile junctions between dislocations. The interaction between two dislocations with collinear Burgers vectors gliding in intersecting slip planes was found to be by far the strongest of all reactions. Its properties were investigated and discussed using a multiscale approach.

Plastic flow in crystalline materials is intimately related to the generation, motion, and storage of linear defects, known as dislocations. These defects connect two areas of the crystal that are sheared with respect to each other by an atomic translation called the Burgers vector. They locally disrupt the ordering of the atoms in a crystal and induce long-range stress and strain fields. Under an externally applied stress, dislocations interact and multiply in crystallographic slip planes, producing plastic deformation through the accumulation of atomic shears. In all crystalline materials, including alloys and compounds, strain hardening occurs because of the increased number of interacting dislocations that trap each other in minimum energy configurations (*1*). In face-centered cubic (fcc) crystals, these interactions occur between 12 slip systems that involve {111} slip planes and 1/2 ξ Burgers vectors. The prevailing view has been that reactions between intersecting dislocations leading to the formation of stable barriers, notably the Lomer-Cottrell lock, govern the flow stress in multislip conditions (*2*). The present investigation, which combines simulations at different scales, shows that this belief is partly incorrect, in that the strongest reaction has thus far been neglected.

Theoretical and experimental investigations agree that the flow stress of pure fcc crystals is inversely proportional to the average distance between obstacles in the slip planes and is therefore proportional to the square root of the dislocation density (*2*–*5*). However, in this global relation, the strengths of all interactions are lumped into a single proportionality coefficient. To predict the number and nature of active slip systems, a more sophisticated relation must be employed, where the dislocation density is decomposed into densities per slip system. With ρ^s denoting the density on slip system (s) and τ_c^s the critical resolved shear stress for dislocation motion in this system, we have (*6*)

$$\tau_c^s/\mu = b\sqrt{\sum_u a^{su}\rho^u} \qquad (1)$$

where the summation is carried out over all slip systems (u). b is the modulus of the Burgers vector, and μ is the shear modulus. For elastically anisotropic crystals, the effect of anisotropy is averaged out in large dislocation densities and μ is an isotropic average shear modulus. $[a^{su}]$ is a dimensionless interaction matrix expressing the average strength of the interactions and reactions between slip systems.

By reason of symmetry, the interaction matrix $[a^{su}]$ has only six independent coefficients. Two of them involve only elastic interactions between dislocations gliding in parallel slip planes. Because these interactions are weak (*3*, *4*), their properties are not reported here. Three intersections form stable junctions; namely, the Hirth lock, the glissile junction, and the Lomer-Cottrell lock, which is thought to be the strongest. The corresponding configuration formed with perfect nondissociated dislocations is called the Lomer lock. Lomer and Lomer-Cotrell locks have been the subject of several recent investigations (*5*, *7*–*9*) by atomistic and dislocation dynamics simulations (DDSs) at the mesoscale, which showed that they have practically the same strength. The reason is that the contribution of the dislocation core to the self energy of a dislocation line is small enough to be neglected (*1*). Owing to the very large self energy of a dislocation, typically μb^3 per atomic length of line, thermal fluctuations do not contribute significantly to junction destruction. This justifies estimating "forest" hardening within an elastic athermal framework and with perfect dislocations, as in earlier calculations (*1*, *2*).

The sixth interaction coefficient corresponds to the so-called collinear interaction between dislocations of parallel Burgers vectors gliding in intersecting slip planes, each plane being the cross-slip plane of the other. This interaction has not been studied in detail and is assumed to be of weak or intermediate strength (*3*, *4*, *6*, *10*). Two experimental observations are available. One is concerned with strained SiGe/Si epitaxial layers (*11*), where dislocations of same Burgers vectors tend to accumulate at the film/substrate interface, thus increasing the visibility of the collinear interaction. The other (*12*) was obtained by deforming an Al-Mg alloy in situ in a transmission electron microscope (fig. S1).

The average strength of the various dislocation interactions is difficult to estimate from theory or extract from experiments (*3*, *6*, *10*), but can be evaluated by DDS. We employ a three-dimensional DDS (*13*), in which connected segments describing perfect dislocation lines are embedded into an elastic continuum. These segments move by discrete crystallographic steps, and the level of discretization is adjusted to the scale of the investigated configuration (*5*). The interaction coefficients of Eq. 1 were evaluated from model simulations in which the interacting dislocations were chosen so that only one type of reaction occurred at a time. The simulated fcc crystal contained a few long mobile dislocation lines on one system and a random distribution of forest segments on other slip systems, producing a specific type of reaction with the mobile dislocations. A constant strain rate was applied, which induced a resolved shear stress on the mobile dislocations, whereas the forest systems were not activated. The model material had the isotropic elastic constants and Burgers vector of copper. The interaction coefficients were deduced from Eq. 1 by the simultaneous measurement of the resolved applied stress and the forest density.

Figure 1A shows the traditional picture of a dislocation moving through a forest, by the formation and destruction of junctions. By way of contrast, in the case of the collinear interaction shown in Fig. 1B, the

[1]Laboratoire d'Etude des Microstructures, UMR 104 CNRS, CNRS-ONERA, 20 Avenue de la Division Leclerc, BP 72, 92322 Chatillon Cedex, France. [2]Laboratoire Mécanique des Sols, Structures et Matériaux, UMR 8579 CNRS, Ecole Centrale Paris, Grande Voie des Vignes, 92295 Chatenay-Malabry Cedex, France. [3]Génie Physique et Mécanique des Matériaux, UMR 5010 CNRS, ENSPG, Domaine Universitaire, 38402 St. Martin d'Hères Cedex, France.

*Present address: Département de Physique Théorique et Appliquée, Commissariat à l'Energie Atomique, BP 12, 91680 Bruyères-le-Châtel, France.
†To whom correspondence should be addressed. E-mail: kubin@onera.fr

moving line undergoes successive partial annihilations with the attractive "trees," resulting in the formation of many small residual segments (Fig. 2, A and E). To accommodate the imposed strain rate, these segments have to be remobilized, which requires an activation stress that is inversely proportional to their length. Thus, in qualitative terms, the exhaustion of the mobile density and the need to generate mobile segments result in a much higher applied stress, as compared to all other junction-forming interactions. Values of the dimensionless coefficients of the interaction matrix for the four reactions mentioned above are given in Table 1. They are rather insensitive to the degree of organization of the dislocation microstructure, as shown in (*5*). These values slightly depend on the density of forest obstacles, as discussed below (Eq. 2), and are given here for a density of 10^{12} m^{-2}.

The values of the measured interaction coefficients corresponding to the three junctions agree with the hierarchy of strengths deduced from latent hardening experiments (*3*, *6*, *10*). Moreover, in agreement with the qualitative arguments given above, the coefficient of the collinear interaction appears to surpass all the other coefficients.

To ascertain that dislocation dissociation does not result in atomic-scale configurations that affect the properties of the collinear annihilation, we investigated the evolution of two straight segments cutting each other at their midpoint, using both DDS and molecular static simulations (MSSs); that is, atomic-scale simulations where equilibrium configurations of minimum energy are obtained between increments of applied shear strain (*13*). Elastic anisotropy may influence the properties of individual configurations. For that reason and to help comparisons between MSS, which includes anisotropy, and DDS, which uses isotropic elasticity, the simulations were performed on aluminum, which is almost isotropic. In both simulations, a shear stress was applied along the same orientation. The common initial configuration consisted of two straight dislocation lines 27 nm in length, shown as dotted lines in Fig. 2E. In the MSS, a semi-empirical embedded atom method was employed as in earlier studies of junctions (*8*). The two simulations differed only in the boundary conditions (*13*). Rigid conditions were used in the MSS in order to pin the dislocation lines at their extremities and measure their remobilization stress. In the DDS, the segments were also pinned at their ends, and remote periodic conditions were used.

Partial annihilation of the lines produces composite dislocations made of two segments, one in each slip plane, connected by a

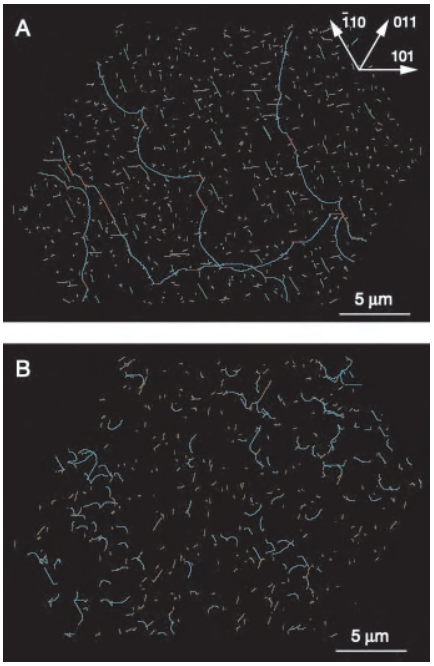

Fig. 1. Non-coplanar interactions between slip systems. Dislocations (blue lines) of Burgers vector 1/2[011] glide in (11$\bar{1}$) slip planes and interact with randomly distributed forest segments 2 μm in length. The figures show (11$\bar{1}$) thin films of thickness 0.1 μm extracted from the simulations. (**A**) Formation of Lomer locks (straight red segments) through the interaction with a forest of 1/2[110]($\bar{1}$11) and 1/2[$\bar{1}$01](111) dislocations. (**B**) Collinear interaction with a forest of 1/2[011] dislocations gliding in the (1$\bar{1}$1) cross-slip plane of the mobile dislocation.

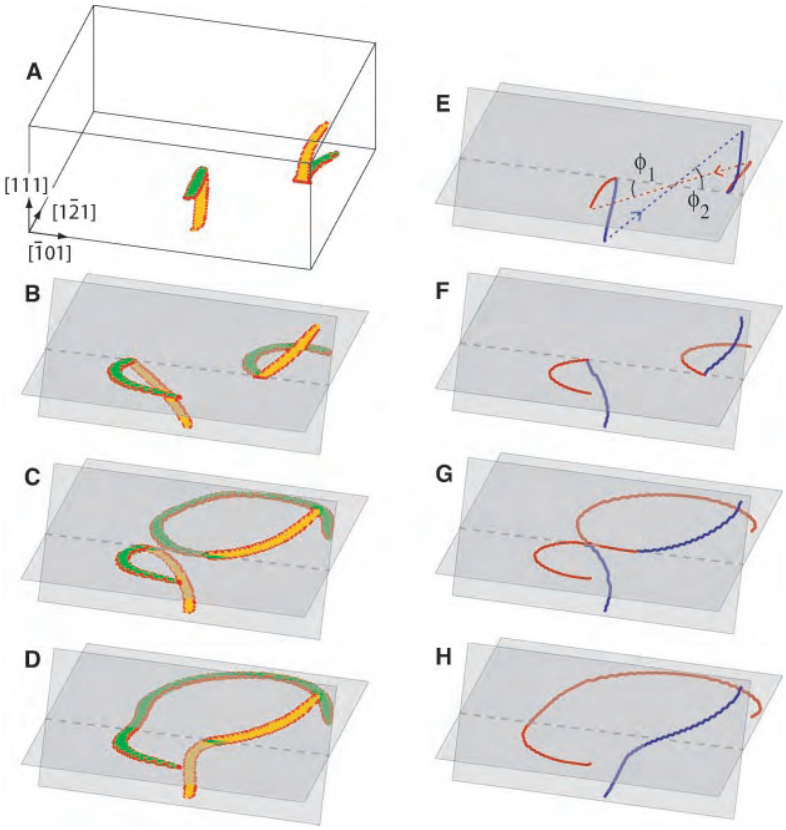

Fig. 2. Simulations of the collinear interaction in aluminum. Two segments [dotted lines in (E); the arrows show the positive sense on the lines] with collinear Burgers vectors 1/2[$\bar{1}$01](111) and 1/2[$\bar{1}$01](1$\bar{1}$1) make angles of $\phi_1 = \phi_2 = \pi/4$ with the [$\bar{1}$01] intersection of the two slip planes (dashed lines). An increasing strain (from top to bottom), is applied in the (111) plane, parallel to the common Burgers vector. Left column: MSS. The dislocation stacking faults are visualized by showing only the atoms with a non-fcc local environment. Right column: DDS. The two initial segments are shown with different colors. (**A** and **E**) Initial configuration after annihilation and without applied loading. (**B** and **F**) Critical configurations under stress. (**C**, **G**, **D**, and **H**) Recombination and remobilization of the two initial segments.

Table 1. Dimensionless coefficients of the interaction matrix for fcc crystals.

Type of interaction	Hirth lock	Glissile junction	Lomer lock	Collinear interaction
Value	0.051 ± 0.012	0.075 ± 0.014	0.084 ± 0.012	1.265 ± 0.125

node along the intersection line between the slip planes (Fig. 2, A and E). As mentioned, reaction decreases the mobile dislocation length, as seen when comparing the initial and final lengths of the dislocation segments. However, the collinear annihilation can also be viewed as forming a junction of zero Burgers vector and therefore zero elastic energy, implying that it is the most stable possible reaction. Figure 2 shows excellent agreement between the dislocation configurations obtained from MSS and DDS. Moreover, for the configurations of Fig. 2, B and F, which correspond to the critical remobilization stress, the reduced stress values are $\tau_c/\mu = 1.85 \times 10^{-2}$ for the MSS and $\tau_c/\mu = 1.67 \times 10^{-2}$ for the DDS. The small difference is attributed to the use of different boundary conditions in the two simulations. These agreements confirm the absence of any atomic-scale configuration to be accounted for at an upper scale.

The critical remobilization stress of a dislocation segment of length l is written in the dimensionless form (*1*, *4*, *14*)

$$\tau_c = K\frac{\mu b}{l}\, ln(\frac{l}{b}) \qquad (2)$$

where the logarithmic term includes inner and outer cut-off radii for the elastic field and K is a constant. Because the length l of the segments produced by a collinear annihilation is geometrically related to the initial length l_0 of the interacting segments, this expression allows one to rescale the critical stresses for any value of l_0 or of the forest density, $\rho \propto l_0^{-2}$. Thus, the coefficients of the interaction matrix given in Table 1 depend in a logarithmic manner on the forest density.

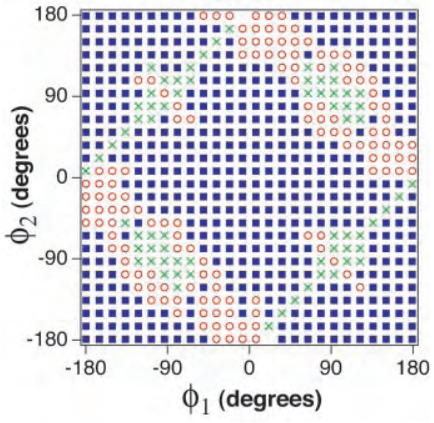

Fig. 3. Mapping of the collinear interaction in fcc crystals. The two interacting segments have opposite Burgers vector $b_1 = -b_2 = 1/2[011]$ and make variable angles, ϕ_1 in $(1\bar{1}\bar{1})$ and ϕ_2 in $(11\bar{1})$, with respect to the intersection of their slip planes (Fig. 2). The initially straight segments are pinned at their ends, and their length is $l_0 = 1$ μm. The model material is copper. The symbols indicate the nature of the final configuration: squares, collinear annihilation; circles, repulsive interaction; crosses, crossed state.

To complete this study, the dependence of the collinear annihilation on the orientation of the dislocation lines was investigated and compared to similar investigations on the Lomer lock (*5*). We carried out DDS on pairs of interacting segments like those of Fig. 2, 1 μm in length, initially making variable angles ϕ_1 and ϕ_2 with respect to the direction of their common Burgers vector. The result is plotted in Fig. 3 in the form of a mapping, where the symbols represent the final result of the interaction. Although half of the initial configurations correspond to segments that elastically repel each other, collinear annihilations appear in a vast majority in the relaxed configurations. The reason is that the flexibility of the lines allows them, through bending and twisting, to reach the minimum energy configuration corresponding to mutual annihilation. One also finds repulsive configurations and crossed states (*15*), where dislocation segments weakly interact (*14*). A graph similar to that of Fig. 3, drawn for the Lomer lock (*5*), shows that junction formation is restricted to only about 25% of the configurations. Thus, the high strength of the collinear reaction is due not only to its intrinsic stability, but also to its very high probability of occurrence.

Several consequences can be deduced from the present study, which we believe apply to all crystalline structures, although only fcc crystals are discussed here. The collinear interaction is expected to strongly influence the mechanical properties of crystals stressed along high-symmetry orientations, where slip and cross-slip systems have same resolved shear stresses, such as [100] or [111]. Figure 4 shows the stress-strain curve obtained from the DDS for a copper crystal deformed along a [100] orientation (*13*). It was found that with increasing strain, four out of the eight initially active slip systems became inactive, which were the cross-slip systems of the four other systems. Dislocation densities and strains were recorded for all the slip systems. Inserting their values into Eq. 1 and making use of the interaction coefficients of Table 1, the strain dependencies of the critical activation stresses of the slip systems were reconstructed. From the reconstructed curves shown in Fig. 4, one can see that the stress-strain curves cannot be reproduced in the absence of the collinear interaction. In addition, in the presence of the collinear interaction, the simultaneous activation of both the slip and cross-slip systems is predicted to be unstable. Indeed, the critical resolved shear stress, as given by Eq. 1, favors the activation of those slip systems that experience the weakest global interaction with the microstructure. The same holds for grains of polycrystals, which can be thought of as a composition of single-crystal properties in multislip conditions (*16*). Thus, the collinear interaction affects plastic flow in multislip conditions by selecting one combination of slip systems among all possible ones.

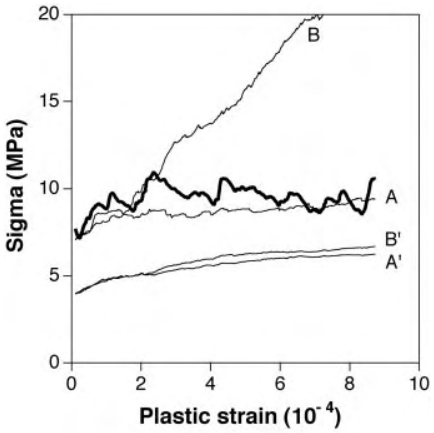

Fig. 4. Bold curve: [100] stress-strain curve obtained from the DDS for a copper crystal of size $(10\ \mu m)^3$, using periodic boundary conditions. Curve A shows the reconstructed strain dependency of the critical stress for one of the four active slip systems. This curve matches the result of the "mass" simulation, confirming that this system should be active. Curve B is for one of the cross-slip systems that becomes inactive. As expected, the critical stress increases above the applied stress. Curves A′ and B′ refer to the same slip systems as A and B but were obtained by omitting the collinear interaction. The predicted critical stresses are far below the applied stress.

The collinear interaction, which promotes local rearrangements, annihilations, and blocking effects, also affects the recovery and relaxation properties of dislocation microstructures, in static conditions or under stress. This was suggested in different contexts by Jackson (*17*) and Stach *et al.* (*18*), who discussed mechanisms involving collinear annihilation under the name of exchange interaction and reactive blocking, respectively.

Therefore, owing to its considerable contribution to multislip hardening and its influence on the selection of active slip systems, the collinear interaction appears to deserve much more attention than it has been given up to now and provides a reason to revisit the traditional picture of strain hardening entirely governed by junction properties (*1*–*4*, *14*). Moreover, the interaction matrix of Table 1, which is evaluated from parameter-free DDS, is valid for all fcc crystals and is a fundamental constituent of physically based predictive models of plastic deformation at the macroscale.

References and Notes

1. J. Friedel, *Dislocations* (Pergamon, Oxford, 1967).
2. G. Saada, *Acta Metall.* **8**, 441 (1960).
3. S. J. Basinski, Z. S. Basinski, in *Dislocations in Solids*,

F. R. N. Nabarro, Ed. (North Holland, Amsterdam, 1979), vol. 4, pp. 261–362.
4. J. Gil Sevillano, in *Materials Science and Technology*, H. Mughrabi, Ed. (VCH, Weinheim, Germany, 1993), vol. 6, pp. 19–88.
5. R. Madec, B. Devincre, L. P. Kubin, *Phys. Rev. Lett.* **89**, 255508 (2002).
6. P. Franciosi, M. Berveiller, A. Zaoui, *Acta Metall.* **28**, 273 (1980).
7. V. V. Bulatov, F. F. Abraham, L. P. Kubin, B. Devincre, S. Yip, *Nature* **391**, 669 (1998).
8. D. Rodney, R. Phillips, *Phys. Rev. Lett.* **82**, 1704 (1999).
9. V. B. Shenoy, R. V. Kukta, R. Phillips, *Phys. Rev. Lett.* **84**, 1491 (2000).
10. J. L. Bassani, T. Y. Wu, *Proc. R. Soc. London Ser. A* **435**, 21 (1991).
11. E. A. Stach *et al.*, *Philos. Mag. A* **80**, 2159 (2000).
12. M. J. Mills, unpublished data.
13. Methods are available as supporting material on *Science* Online.
14. G. Schoeck, R. Frydman, *Phys. Stat. Sol. B* **53**, 661 (1972)
15. L. K. Wickham, K. W. Schwarz, J. S. Stölken, *Phys. Rev. Lett.* **83**, 4574 (1999).
16. S. Hansen, X. Huang, *Acta Mater.* **46**, 1827 (1998).
17. P. J. Jackson, *Progr. Mat. Sci.* **29**, 139 (1985).
18. E. A. Stach, K. W. Schwarz, R. Hull, F. M. Ross, R. M. Tromp, *Phys. Rev. Lett.* **84**, 947 (2000).

Supporting Online Material

www.sciencemag.org/cgi/content/full/301/5641/1879/DC1
Methods
Fig. S1
References

9 April 2003; accepted 14 August 2003

5.3. Modèle cristallin méso-macro

5.3.1. État de l'art

Dans la dernière étape de la modélisation, maintenant en voie d'achèvement, les courbes de déformation des monocristaux CFC sont reconstruites avec l'aide d'un modèle cristallin ne contenant qu'un seul paramètre ajustable. Nous avons testé ce modèle dans le cas du cuivre à la température ambiante, c'est-à-dire dans une situation permettant la comparaison avec de nombreuses données expérimentales [133, 134]. Il n'y a pas de difficulté réelle pour étendre ces résultats à tous les métaux CFC purs et à toutes les températures dans le domaine du glissement. Le passage qui suit synthétise plusieurs articles en cours de rédaction (T. Hoc, B. Devincre et L. Kubin).

Il est connu depuis les années 1950 que les courbes de déformation des monocristaux CFC présentent soit une succession de stades bien définis, soit des formes pseudo-paraboliques lorsque la contrainte est appliquée suivant des orientations de haute symétrie comme $\langle 001 \rangle$, $\langle 111 \rangle$ et $\langle 112 \rangle$. La dépendance du durcissement d'écrouissage en fonction de l'orientation est bien caractérisée expérimentalement et peut servir de test pour les lois de comportement du polycristal. Sa prédiction constitue, en effet, un des premiers objectifs que s'était initialement fixée la théorie des dislocations. Paradoxalement, même si les causes du durcissement sont bien comprises, il n'existe pas encore de modèle du monocristal ayant un caractère prédictif. La tendance actuelle consiste à utiliser des lois constitutives écrites en termes de densités de dislocations, qui dérivent d'un modèle phénoménologique de Kocks [135], largement développé par Kocks et Mecking [136]. En substance, le durcissement résulte d'une compétition entre le stockage de dislocations par interaction des dislocations mobiles avec la 'forêt' et la restauration dynamique par un mécanisme souvent non spécifié, qui conduit à des réarrangements et à des annihilations. Seule compte donc la densité de forêt, qui détermine la contrainte d'écoulement, et son évolution avec le temps et la déformation. Teodosiu et col. [137] on généralisé le modèle scalaire de Kocks pour introduire les densités de dislocations par plans de glissement. Cela leur a permis, et à beaucoup d'autres après eux, de tirer parti de l'existence de codes d'éléments finis dits de plasticité cristalline, qui tiennent compte de la nature cristallographique du glissement et calculent les rotations des grains associées au glissement des dislocations ainsi que les conditions d'équilibre mécanique. Ces modèles mettent en jeu un nombre variable de paramètres (au moins douze) qui sont toujours ajustés ('validés'). Ils ne peuvent en aucun cas reproduire la complexité de comportement du monocristal. Nous pouvons maintenant prouver que, désormais, ces procédures de validation ne sont plus inéluctables et qu'il est possible de construire grâce à la DD de véritables modèles physiques où chaque paramètre a été déterminé par la simulation.

5.3.2. Les lois constitutives du modèle

Notre modèle est semblable dans sont principe à celui utilisé par beaucoup d'autres auteurs. Il est juste aussi de rappeler que ces travaux s'inscrivent dans la continuité d'une étude exploratoire réalisée par Fivel durant sa thèse [138]. Les simulations mésoscopiques décrites dans les parties précédentes nous ont néanmoins suggéré des modifications importantes vis a vis des modèles existant. L'ensemble des lois constitutives est basé sur trois équations, dont les deux premières sont les plus importantes. La première est l'équation de Taylor généralisée (equation 5.2), que nous récrivons sous la forme :

$$\tau_c^i = \mu b \sqrt{\sum_{j=d} a_{ij} \rho_f^j + \sum_{j=r} a_{ij}^* \rho_f^j} \tag{5.3}$$

Les densités de dislocations portent l'indice f pour forêt, la forêt étant considérée comme majoritairement constituée des dislocations stockées dans le cristal. Il y a deux différences majeures par rapport à l'équation 5.2. La sommation sur les systèmes distingue les interactions à distance (indice $j = d$ pour 'dipolaire'), ne formant pas de jonctions, et les interactions de contact entre dislocations

glissant sur des plans non parallèles (indice $j = r$ pour 'réaction'). Dans ce dernier cas, l'astérisque indique que les effets de courbure sont pris en compte correctement en incluant le terme logarithmique de la tension de ligne. Une seconde modification vise à inclure le glissement simple dans ce type de modèle qui ne décrit que les situations de glissement multiple. Cette question est traitée dans un article récent [139], où nous tirons les conséquences d'une idée proposée par des auteurs comme Hirsch, Argon, et Nabarro dans la littérature des années 1950-1970. En substance, le glissement facile est caractérisé par la formation de dipôles de dislocations, principalement de caractère coin. Cependant les modèles de dipôles ne conduisent pas à un auto-durcissement suffisant pour permettre le passage du stade I de glissement simple au stade II de glissement double. L'autre caractéristique du stade I est l'absence quasi-totale de dislocations vis sur les micrographies électroniques. Ces dislocations qui ont un très grand libre parcours moyen (≈ 1 mm), finissent toujours par s'annihiler de manière purement mécanique avec des dislocations vis de signe opposé glissant sur des plans très proches. Ces annihilations produisent des supercrans dans le plan de glissement, qui interagissent avec les dislocations primaires via l'interaction colinéaire. L'apport de la DD consiste ici en la mise en évidence du très fort caractère durcissant de l'interaction colinéaire. Nous suposons donc que c'est la forêt colinéaire qui induit la transition vers le stade II. Pour en tenir compte, nous avons montré [139] qu'il suffisait d'ajouter au coefficient d'interaction dipôlaire une contribution colinéaire effective qui peut s'estimer exactement dans le cas du cuivre.

La seconde équation permet d'estimer l'évolution des densités de dislocations de la forêt dans chaque système. Nous l'écrivons d'abord sous sa forme complète, pour la commenter ensuite :

$$\frac{d\rho_f^i}{d\gamma_i} = \frac{1}{b}\left(\sqrt{\frac{1}{K_d^2}\sum_{j=d} a_{ij}\rho_f^j + \frac{1}{K_r^2}\sum_{j=r} a_{ij}^*\rho_f^j} - y_c\rho_f^i\right) \tag{5.4}$$

Le terme sous la racine carrée est une forme modifiée de la contrainte critique (équation 5.3), qui tient compte du stockage des dislocations mobiles sur des obstacles de la forêt, par exemple par formation de jonctions fortes ou de débris produits lors d'interactions collinéaires. Pour le discuter, on peut se référer à la forme scalaire proposée par Kocks [135] :

$$\frac{d\rho_f}{d\gamma} = \frac{1}{b\Lambda} \tag{5.5}$$

Le stockage des dislocations est gouverné par un libre parcours moyen, Λ, qui est inversement proportionnel à la distance entre dislocations de la forêt, et donc à la contrainte via la relation de Taylor (équation 5.1). Dans la version généralisée, Λ doit être également inversement proportionnel à la force moyenne des obstacles. En d'autres termes, le libre parcours moyen est inversement proportionnel à la contrainte critique telle que donnée par l'équation 5.3. On l'écrit donc sous la forme sans dimensions $\Lambda = K\mu b/\tau_c^i$. La distinction entre interactions dipôlaires et interactions de contact s'avère ici de nouveau nécessaire. En effet, dans les deux cas, le libre parcours moyen correspond à des interactions ayant une topologie diférente et à des distances entre obstacles qui ne sont pas définies géométriquement de la même manière. C'est la raison pour laquelle on trouve dans l'équation 5.5 deux libres parcours moyens, l'un, K_d, caractérisant les interactions dipolaires et l'autre, K_r, caractérisant les interactions de contact.

Le terme scalaire, à droite de la loi d'évolution décrit la restauration dynamique. Nous interprétons ce dernier mécanisme comme résultant de l'annihilation par glissement dévié des dislocation vis de la forêt par les dislocations mobiles du même sytème, en densité ρ_m. La densité mobile est présente dans l'incrément de déformation $d\gamma_i$, via la loi d'Orowan ($d\gamma = \rho_m bvdt$ avec les notations usuelles) et, comme attendu, ce terme est quadratique en termes de densités de dislocations ($\rho_m\rho_f$) lors d'une évolution en fonction du temps. Le paramètre y_c, qui est une longueur catactéristique de la restauration dynamique, est fonction de la distance d'annihilation des dislocations vis par glissement dévié. Il

contient cependant un facteur inconnu, car le modèle ne distingue pas les caractères des dislocations. En fait, il n'existe à l'heure actuelle aucune donnée, théorique ou expérimentale, sur la fraction de dislocations à caractère vis dans la microstructure. Néanmoins, la dépendance de y_c en fonction de l'énergie de faute et de la température peut être estimée semi-quantitativement à partir des modèles du glissement dévié.

Enfin, la loi d'évolution donnée par l'équation 5.4, $d\rho_f^i/d\gamma_i$, est celle qu'intègrent les modèles courants, mais elle pose problème. L'ajustement des paramètres ne permet pas de se rendre compte du problème, mais les solutions du modèle mettent clairement en évidence que les taux de durcissement doivent, pour chaque orientation, être corrigés d'un facteur proportionnel au nombre de systèmes actifs. Des expériences numériques menées par la DD montrent que l'origine de cette correction est de nature microstructurale. Elle est liée aux conditions de formation des jonctions en glissement multiple.

D'après la loi de Schmid, un système n'est activé que si la contrainte d'écoulement projetée, τ^i, est supérieure à sa contrainte critique, τ_c^i. La vitesse de déformation, $\dot{\gamma}^i$, est alors fonction du rapport de ces deux contraintes. Pour exprimer ce caractère visco-plastique de la déformation, nous utilisons une formulation traditionelle en mécanique des milieux continus, adaptée pour des matériaux à faible sensibilité à la vitesse :

$$\dot{\gamma}_i = \dot{\gamma}_o \left| \frac{\tau^i}{\tau_c^i} \right|^n sign(\tau^i) \;\; si \; |\tau^i| \geq \tau_c^i; \;\; sinon \; \dot{\gamma}_i = 0 \tag{5.6}$$

Cette expression complète la partie constitutive du modèle. Les valeurs des coefficients $\dot{\gamma}_o$ et n sont celles typiquement utilisées pour les cristaux CFC, $n = 100$ et $\dot{\gamma}_o = 10^{-3}$ s^{-1}. Dans ces conditions, la contrainte d'écoulement est toujours très proche de la contrainte critique, quelles que soient les valeurs exactes de ces deux paramètres.

Dans une formulation généralisée, le durcissement d'écrouissage s'exprime sous forme matricielle :

$$\tau_c^i = \sum_j h^{ij} \gamma^i; \quad h^{ij} = \frac{d\tau_c^i}{d\rho_f^j} \frac{d\rho_f^j}{d\gamma^j} \tag{5.7}$$

Les coefficients de cette matrice d'écrouissage se déduisent directement de la loi d'évolution 5.4 et de la contrainte critique 5.3, dont il faut prendre la dérivée.

5.3.3. Paramètres et mise en oeuvre du modèle

Les six coefficients d'interaction entre systèmes de glissement qui apparaissent dans les équations 5.3 et 5.4 ont été mesurés par la DD comme indiqué dans l'article reproduit à la fin de la partie précédente (5.2). Ces valeurs sont communes à tous les métaux CFC. La valeur de la constante K_r décrivant les libres parcours moyens pour les interactions de contact a été déterminée de deux manières différentes : d'une part, par Ambrosi et Schwink [140] qui ont mesuré les longueurs de fines traces de glissement sur des monocristaux [001] et [111], et d'autre part à partir de simulations de DD en masse sur des monocristaux d'orientation [001], [111] et [112]. On obtient exactement le même résultat dans les deux cas ($K_r = 5,75$). Le libre parcours moyen pour les interactions dipolaires est trop grand pour être calculé par DD et déterminé d'après une compilation de résultats expérimentaux de Basinski et Basinski [141] : $K_d = 100$. La correction à apporter au terme dipolaire pour tenir compte des annihilations non activées entre dislocations vis a été obtenu à partir de la mesure expérimentales des densités de dislocations à la fin du stade I [139]. Comme mentionné ci-dessus, la longueur de restauration y_c est le seul paramètre inconnu ; on peut seulement estimer son ordre de grandeur à $y_c \approx 1$ nm. Sa valeur est fixée par ajustement du début du stade III sur une courbe de déformation d'un monocristal d'orientation [$\bar{1}$23], soit y_c=0.7 nm. Une discussion plus détaillée de ces valeurs devrait mentionner le

cas très intéressant de l'orientation ⟨111⟩, pour laquelle le glissement dévié est pratiquement interdit (W. Pantleon, communication privée). La raison est que la contrainte projetée dans le plan de déviation favorise le glissement dévié dans le sens opposé à celui habituellement considéré.

Les valeurs des paramètres sont identiques pour toutes les simulations effectuées sur le cuivre. Une densité initiale de dislocations représentative d'un monocristal bien recuit, $\rho = 1,2 \times 10^9\ m^{-2}$ est également distribuée sur les douze systèmes potentiellement actifs. Le code d'éléments finis utilisé est le code de plasticité cristalline développé par Hoc et col. [142]. Une éprouvette modèle est définie, dont le corps contient $6 \times 14 = 84$ éléments identiques, auxquels une dimension linéaire de 0.5 mm est attribuée par convention. Cette éprouvette est soumise à une vitesse d'allongement constante, comme dans un essai en laboratoire, correspondant à une vitesse initiale de déformation de $10^{-4}\ s^{-1}$. Plusieurs types de courbes contrainte-déformation peuvent être extraites des simulations : une courbe théorique prise sur un élément central de l'éprouvette, une courbe moyenne déterminée sur le corps de l'éprouvette et une courbe moyenne recalculée à partir de la force appliquée et de l'élongation. Comme le montre la figure 5.1, ces trois courbes sont en fait confondues jusqu'au l'apparition de la striction. Cela prouve la bonne homogénéité de la déformation dans l'éprouvette virtuelle et la cohérence interne des résultats du modèle.

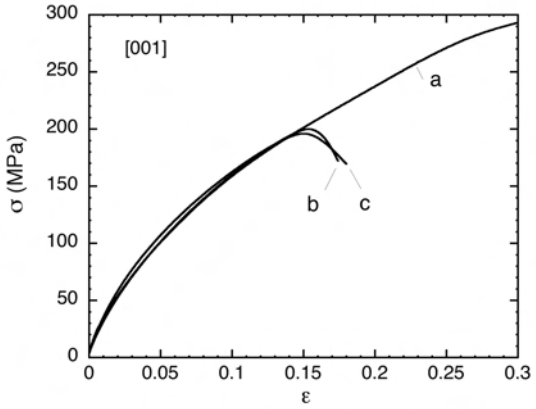

FIG. 5.1.: Trois différentes courbes contrainte axiale - déformation axiale (σ - ε), obtenues pour une orientation [001] à partir des données de sortie du modèle. a) Réponse d'un élément central de l'éprouvette. b) Réponse moyenne du corps de l'éprouvette. c) Réponse calculée à partir de la force appliquée et de l'élongation. La divergence entre la courbe a) et les deux autres courbes marque le début de la striction (instabilité de Considère). À plus faible déformation, les courbes sont pratiquement superposées.

5.3.4. Premiers résultats

Pour illustration j'extrais des nombreux résultats obtenus à ce jour, et qui n'ont pas été encore tous analysés, quelques courbes de déformation en stade I, montrant le début de l'activation du stade II. La transition stade I - stade II, c'est-à-dire l'apparition du glissement double, n'a jamais été modélisée, même pour une orientation unique. La figure 5.2 montre une comparaison de ces résultats avec les courbes expérimentales de Diehl [133]. Les courbes contrainte projetée - déformation projetée sont celles obtenues sur l'élément central de l'éprouvette modèle. En principe, elles diffèrent légèrement des courbes expérimentales, qui n'ont pas été encore reconstruites, dès l'activation du système secondaire. Malgré les différences d'échelle, on peut voir que la pente initiale du stade I ($\mu/3000$) est bien reproduite. L'activation du système secondaire, qui se traduit par une augmentation du durcissement, dépend fortement de l'orientation. La déformation correspondante est faible près des

orientations [001] et [$\bar{1}$11] et maximale au centre du triangle stéréographique standard et vers [011]. Le modèle rend bien compte de cette dépendance. Les pentes de durcissement pour les orientations [$\bar{1}$25] et [$\bar{1}$23] sont affectées par l'activation transitoire d'un système coplanaire, qui n'est pas prise en compte dans les courbes de Diehl.

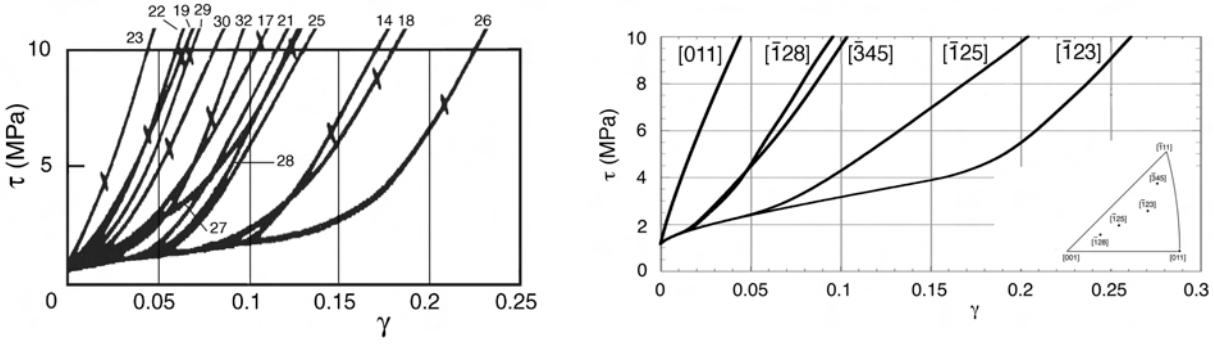

FIG. 5.2.: Le stade I de glissement facile et l'activation du système secondaire dans le cuivre à la température ambiante. γ est la projection de la déformation axiale totale sur le système primaire. a) À gauche, un agrandissement des courbes expérimentales de Diehl [133]. b) À droite, les courbes issues du modèle pour différentes orientations. Les orientations [$\bar{3}$45] (proche de [$\bar{1}$11]) et [$\bar{1}$28] (proche de [001]) correspondent respectivement aux orientations 22-19 et 29 de Diehl. Les orientations au centre du triangle standard, [$\bar{1}$25] et [$\bar{1}$23], correspondent approximativement aux orientations 32 et 18-21.

La figure 5.3 montre une comparaison des résultats obtenus pour diverses orientations avec les courbes de déformation expérimentales de Takeuchi [134]. Dans les deux cas, la déformation γ est la déformation axiale totale projetée sur le plan de glissement primaire. On peut noter la bonne concordance des pentes de durcissement en stade II et de leur évolution avec l'orientation jusqu'à d'assez fortes déformations. L'examen détaillé montre que des divergences apparaissent entre courbes simulées et courbes expérimentales lors de l'apparition du stade IV, c'est-à-dire pour de très grandes déformations correspondant à l'apparition de désorientations locales importantes dans le cristal. Clairement, le modèle, en son état actuel ne rend pas compte du stade IV.

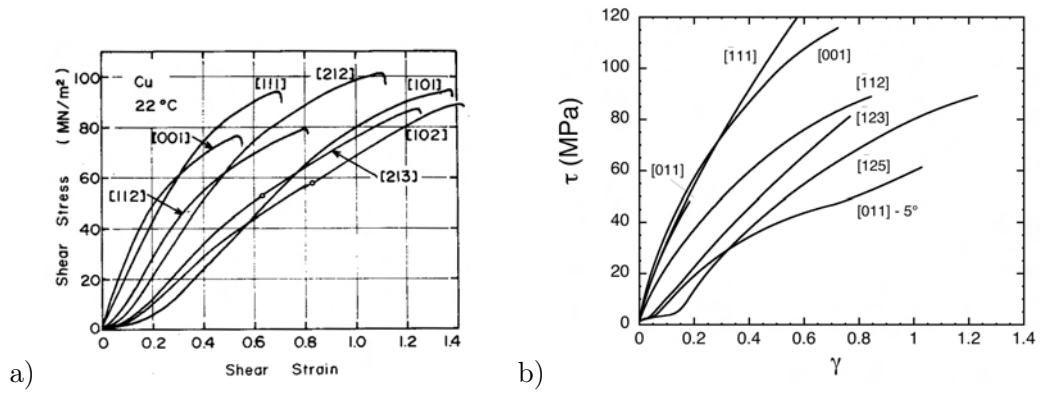

a) b)

FIG. 5.3.: Courbes de déformation du cuivre à la température ambiante pour différentes orientations de haute et basse symétrie. La contrainte et la déformation totale sont projetées sur le système primaire. a) Les courbes expérimentales de Takeuchi [134]. b) Les courbes théoriques (sur un élément) issues du modèle. La courbe [011] -5° est désorientée de 5° par rapport à l'orientation idéale.

Il y a beaucoup d'informations à tirer de cette comparaison avec l'expérience. On peut par exemple observer l'instabilité inhérente à l'orientation [011] qui est tracée pour l'orientation idéale et pour une

orientation décalée de 5°. Dans ce dernier cas, un stade I apparaît, comme sur la courbe de Takeuchi. Pour les deux orientations de haute symétrie, [001] et [$\bar{1}$11], le nombre de systèmes actifs est de quatre (au lieu de huit) et de trois (au lieu de six). Cette particularité est connue expérimentalement et elle est également reproduite par la DD. Elle s'explique par la très forte interaction entre systèmes colinéaires, qui rend leur activation simultanée instable. En conséquence, un système et son dévié ne sont jamais activés simultanément, comme Franciosi et Zaoui [143] l'avaient observé par analyse des lignes de glissement sur un monocristal d'orientation [$\bar{1}$11]. Il est également intéressant de noter que le modèle reproduit bien le croisement des courbes de déformation pour [001] et [$\bar{1}$11], qui est attesté par plusieurs exemples dans la littérature.

Quelques remarques concluent cette partie qui est encore en pleine évolution. Avec un seul paramètre ajustable, nous montrons qu'il est possible de reproduire les courbes contrainte-déformation des monocristaux de cuivre à la température ambiante jusqu'à la fin du stade III. L'apport de la DD est ici considérable, puisqu'il permet d'estimer tous les paramètres relevant de la théorie élastique des dislocations, c'est-à-dire les coefficients d'interaction entre systèmes et le libre parcours moyen entre systèmes non-coplanaires. Les développements en cours concernent l'obtention de courbes de déformation encore plus réalistes, reconstruites suivant les conventions des expérimentateurs, l'application au polycristal, vraisemblablement en collaboration avec un groupe du Risoe National Lab. et l'extension aux autres métaux CFC et aux dépendances en température. Ces deux derniers aspects sont, en effet, couplés via l'énergie de défaut d'empilement et la dépendance en température du glissement dévié intervenant dans la longueur de restauration dynamique, y_c. Un effort expérimental et théorique permettra peut-être d'obtenir à l'avenir des informations plus précises pour cette dernière quantité.

Finalement, on peut se demander pourquoi un modèle basé sur des densités de dislocations uniformes peut reproduire le comportement plastique jusqu'à de très fortes déformations, pour lesquelles la microstructure est fortement organisée. Cette question est abordée de manière spéculative dans la partie suivante. Il est certain, en tout cas, que le présent modèle ne s'applique plus dès lors que les désorientations entre sous-grains ou sous-joints sont telles qu'ils se comportent comme des joints de grains impénétrables aux dislocations. De même, le modèle ne s'applique pas non plus dans le cas d'un chargement de trajet, car il faudrait pouvoir alors distinguer entre les composantes réversibles et irréversibles de la microstructure donnant lieu à un durcissement cinématique ou isotrope.

5.4. Microstructures organisées

Un ensemble d'études a été consacré aussi aux mécanismes physiques à l'origine de la formation des microstructures organisées de dislocations, en pratique des cellules de déformation en déformation uniaxiale, et de leur évolution en cours de déformation. Nos simulations sont, à ce jour, les seules permettant d'obtenir l'émergence de telles structures (cf. figure 5.4). Un premier objectif a été de découpler les différents mécanismes élémentaires mis en jeu afin de définir ceux qui sont essentiels pour la modélisation. L'ensemble de ces résultats sont rassemblé dans une publication reproduite en Annexe B 5. On trouvera dans cette publication les références les plus importante concernant ce sujet d'étude.

Une question à laquelle il est désormais possible de répondre est celle de l'importance relative des interactions de contact (jonctions attractives), ou à courte distance, et des interactions élastiques à longue distance. Nous avons montré que les interactions à longue distance ne jouent pas un rôle fondamental dans la formation de ces structures, contrairement à une croyance largement répandue et aux modèles actuellement en vogue, car leur contribution à la contrainte locale n'est pas prépondérante. Ceci est en bon accord avec les simulations de la contrainte d'écoulement discutées plus haut. Nos calculs confirment également que les microstructures simulées sont sensibles au glissement dévié

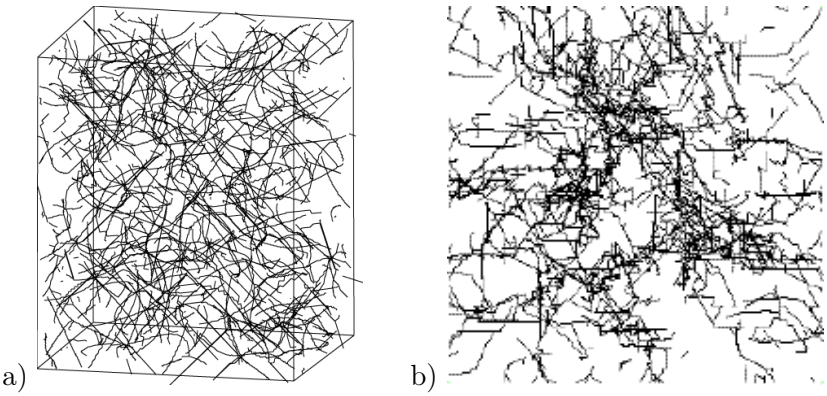

FIG. 5.4.: Simulation 3-d de la dynamique des dislocation dans un échantillon de cuivre de dimension $(10\mu m)^3$, sollicité en tension uniaxiale. a) La cellule élémentaire de simulation (sans ses répliques via les conditions aux limites périodiques) après une faible déformation. b) Lame mince (100) d'épaisseur $2\mu m$, extraite de la 'boite' de simulation après une déformation plastique de $0,3\%$. Noter le début d'organisation de la microstructure.

et que les processus d'auto-organisation sont très sensiblement réduits en son absence. Les microstructures émergentes reproduites par les simulations conduisent à une structuration des contraintes internes qualitativement conforme au modèle composite de Mughrabi : contrainte interne négative dans les zones peu denses, qui sont très déformables, et positive dans les zones denses qui sont peu déformables. Ces contraintes internes ont simplement pour origine les interactions à longue distance entre dislocations, mais peuvent être interprétées comme assurant la compatibilité de la déformation entre les "phases" riches et pauvres en dislocations. En fait, la contrainte d'écoulement plastique est, pour sa part, sensiblement la même en présence et en l'absence du glissement dévié, c'est-à-dire pour des microstructures plutôt uniformes ou plutôt organisées. Ce dernier résultat est important, car il confirme la relative insensibilité de l'écoulement plastique au degré d'organisation des microstructures de dislocations. Il s'agit là d'une simplification considérable pour la modélisation, mais la question se pose désormais de comprendre son origine aussi bien que ses limites. Il est possible qu'il s'agisse d'une question de composition de mécanismes. En effet, l'addition sous la racine carrée des densités des phases riche et pauvre en dislocations $(\rho_1,\ \rho_2)$, affectées de leurs fractions volumiques $(f_1,\ f_2)$, redonne automatiquement la valeur moyenne $(f_1\rho_1 + f_2\rho_2 \equiv \bar{\rho})$

À l'aide de la simulation, il est maintenant possible de proposer un scénario expliquant la séquence de formation des microstructures de dislocations organisées. Par exemple, il est clair que le glissement dévié facilite l'émergence de structures organisées par un processus de rétroaction positive. Là où des jonctions fortes bloquent le mouvement des dislocations mobiles, il permet à la structure de relaxer vers des configurations stables (annihilations partielles, formation de débris tridimensionnels et d'écheveaux de dislocations), ce qui accroît la stabilité des obstacles locaux au mouvement des dislocations mobiles. En cours de déformation, ces zones se densifient progressivement et se connectent, tandis que le glissement dévié est de plus en plus actif dans ces régions de fortes contraintes internes. La formation de microstructures de dislocations fortement organisées réclame cependant des temps de simulation très longs en 3-d. Pour cette raison, j'ai développé (avec D. Gomez-Garcia, Université de Séville) une simulation en '2,5-d', c'est-à-dire une simulation 2-d incorporant aussi fidèlement que possible les mécanismes et cinétiques du 3-d, mais avec un moindre coût de calcul. Les microstructures obtenues reproduisent pour la première fois le principe dit 'de similitude' (figure 5.5), qui a fait l'objet de nombreuses études expérimentales et de controverses non moins nombreuses. Grâce à ce type de simulation simplifiée et à l'accélération des simulation 3-d, il sera possible à court terme d'aboutir à une meilleure compréhension des périodicités caractéristiques des microstructures de dislocations et

a) 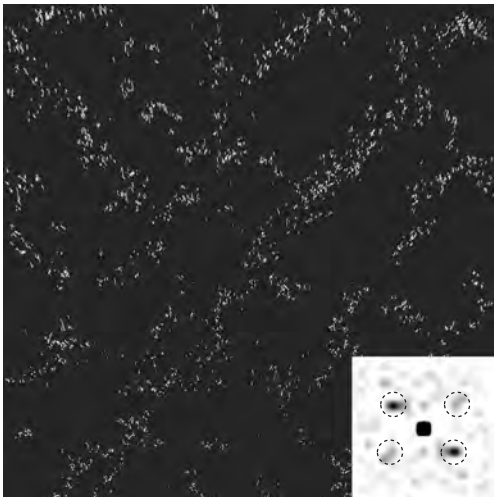

b) 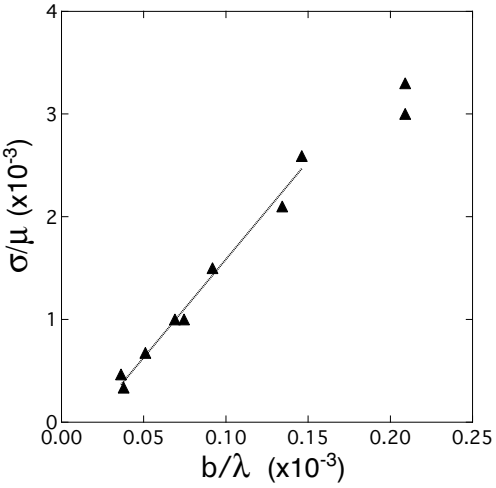

FIG. 5.5.: Simulation "2,5-d" de la formation d'une microstructure de dislocations organisée dans le cuivre en glissement double. a) Si le glissement dévié est activé, il apparaît une microstructure de dislocations de type "labyrinthe" avec une longueur caractéristique bien définie, λ, comme le montre la transformée de Fourier insérée en bas à gauche. b) Variation linéaire de l'inverse de λ avec la contrainte non projetée. La pente, $\sigma\lambda/\mu b \approx 20$, est conforme à l'expérience [144]. On retrouve ainsi le principe dit de "similitude".

des paramètres physiques qui les gouvernent. Cette étape étant franchie, il sera possible d'étudier la question complexe du durcissement latent induit par une microstructure de dislocations [145].

CHAPITRE 6

Déformation plastique dans les matériaux complexes

Ce chapitre est consacré aux travaux réalisés à l'aide du couplage numérique entre le code de dynamique des dislocations et un code éléments finis ("modèle discret-continu" ou MDC). L'objectif est cette fois d'incorporer à la fois les aspects dislocationnels et un traitement rigoureux de la contrainte locale dans une même simulation hybride. Cet exercice un peu complexe a néanmoins une importance à la fois fondamentale et pratique. Il donne, en effet, accès aux propriétés des matériaux réels, par opposition aux matériaux modèles, et permet de juger des forces et faiblesses des approches "mécaniques" et "métallurgiques". Après une longue phase d'incubation liée à des difficultés aussi bien conceptuelles que techniques [25], trois études ont débuté au cours de l'année 2000. Elles ont porté sur : - l'étude de la déformation plastique dans les canaux de superalliages base nickel (stage post-doctoral de C. Lemarchand), - l'étude de la déformation plastique dans les composites à matrice métallique (Thèse de S. Groh), - et l'étude de la relaxation plastique dans une couche mince épitaxiée (Thèse de S. Groh). A ce jour, les simulations sur les composites ont donné des résultats spectaculaires, notamment sur les effets de taille, mais qui ne sont pas encore en forme finale. Un article extrait de cette étude est reproduit en annexe B. Dans la suite de ce texte un résumé des principaux résultats de cette étude est fait. Il illustre les apports significatifs du modèle MDC sur le problème de l'équilibre mécanique aux limites des simulations de DD. Cette étude est directement lié à la question des effets de taille sur les quelles nous reviendrons au § 7. L'étude de la relaxation plastique des couches minces a donné des résultats originaux et bien compris. C'est pourquoi, après un bref rappel, un article détaillant cette étude est reproduit ci-dessous intégralement.

6.1. Plasticité des composites à matrice métallique

Cette étude s'intéresse aux propriétés mécaniques des composites à matrice métallique et plus généralement à la question des effets de confinement rencontré également dans beaucoup d'autre matériaux tel que les superalliages ou les aciers bainitique. Ce travail est réalisé en collaboration avec F. Feyel, A. Roos, et J.L Chaboche à l'ONERA et à bénéficier de discussions avec A. Mortensen à l'Ecole Polytechnique de Lausanne. Elle peut être regardé comme une première tentative d'étude de matériaux très fortement structurés. Plus précisément cette étude s'intéresse à un composite à fibres longues, le modèle étant Al_2O_3/Al, pour lequel des données expérimentales précises existe et ou il est possible de détailler les différentes composantes du durcissement et les effets de taille sous l'angle du comportement des dislocations et des états de contrainte locaux.

Cette étude réalisé dans le cadre de la thèse de S. Groh a permis de mettre en évidence, en

comparant les résultats de différents types de simulations, les mécanismes importants qui contrôlent la plasticité d'un composite à matrice métallique. Il faut noter, un durcissement de la matrice idem à celui présent dans une phase monocristalline, un transfert de charge entre fibres et matrice, des contraintes internes induites par la microstructure de dislocations et enfin des effets de confinement liées aux faibles dimensions microstructurales du matériau simulé. Les résultats obtenus lors de sollicitations longitudinales et transversales ont montré la présence d'effets de taille, à la limite élastique et en cours de déformation. Ces effets sont liés à l'accumulation de dislocation aux interfaces fibre/matrice ou au franchissement des canaux entre fibres. La compréhension fine de ces effets est essentielle pour prédire précisément les propriétés mécaniques exceptionnelles de ces matériaux.

Size effects in metal matrix composites

S. Groh [a,1,*] B. Devincre [a] L.P. Kubin [a] A. Roos [b] F. Feyel [b] J.-L. Chaboche [b]

[a] *LEM, CNRS-ONERA, 29 Avenue de la Division Leclerc, BP 72, 92322 Chatillon Cedex, FRANCE*

[b] *DMSE, ONERA, 29 Avenue de la Division Leclerc, BP 72, 92322 Chatillon Cedex, FRANCE*

Abstract

The mechanical properties of Al/Al_2O_3 metal matrix composites are investigated using a 3D discrete-continuum simulation of dislocations and plasticity. The variations of the yield stress as a function of fibre volume fraction can be predicted from Orowan's law. The dependence of internal stresses on fibre volume fraction leads to a size effect resulting from a virtual decrease of the channel width between fibres.

Key words: Metal matrix composite, Size effect, Dislocation dynamics, Finite elements, Simulation
PACS:

1. Introduction

The yield stress of metal matrix composites (MMC) reinforced by long fibres results from a composition of the properties of both phases. Under longitudinal loading, parallel to the fibre axis, the yield stress is mainly controlled by the properties of the fibres because stress and strain are (i) relatively uniform and (ii) far higher along the fibres than in any other direction. On the other hand, the yield stress is mainly controlled by the matrix properties when the MMC is loaded in the transverse direction, because the matrix deforms plastically while the fibres remain elastic.

Within a classical continuum mechanical framework, the yield stress only depends on the volume fraction of fibres and the possible effect of microstructural parameters such as the distance between fibres is not accounted for. Size effects may, however, manifest themselves when the characteristic dimensions of a composite are decreased. They may not be revealed by such type of modelling.

The mechanical properties of a MMC, with a typical distance d between fibres, depends on how this geometrical parameter interferes with other characteristic distance such as the mean-free path of dislocations.

The present study examines the behaviour of a MMC when the characteristic length, $d \approx 0.5$ μ m, is smaller than the mean-free path of the dislocations. The objective is to simulate and model a size effect which can happen in structural materials. Use is made of a hybrid simulation called the discrete-continuum model (DCM), which incorporates both discrete dislocation properties and the relevant length scales, as well as continuum aspects. The output of this study is compared to that of a simple continuum mechanical model and the evolution of the yield stress for different geometrical configurations shows clear evidence for a size effect. The DCM is shortly presented in section 2. Section 3 is dedicated to a presentation and a discussion of the simulation results and section 4 to concluding remarks.

* corresponding author
Email address: groh@daisy.engin.brown.edu (S. Groh).
[1] Present address : Brown University, Department of Engineering, Providence, RI 02912, USA

2. Simulation method

Coupled simulations combining a Dislocation Dynamics (DD) code and a Finite Element (FE) code allow treating simultaneously the discrete and continuum aspects of plasticity. Their use is for the moment restricted to relatively simple configurations, [1,2]. In essence, the DCM is made up of a FE code, in which the constitutive law is replaced by a DD simulation. The main advantage of this method is that the elastic and plastic fields can be determined numerically in a rigorous manner, taking into account the presence of dislocations in a small volume element and with a variety of possible boundary conditions [3]. By lack of space, the DD simulation is not presented here [4].

The initial geometry of the model composite is presented in Fig. 1. Three volume fractions of fibres, from 5% to 45%, have been tested. The minimum distance between fibres ranges between 0.27 μm and 0.82 μm. Periodic boundary conditions are applied and the primary cell of the periodic MMC is shown in Fig. 1. The FE mesh is built with quadratic elements, so that the fibres have a square cross section. To avoid stress concentrations, all fibre corners are rounded. The z axis of the fibers is parallel to the [001] direction of the matrix. Thus, longitudinal and transverse loading are in z and y directions, respectively.

Al/Al_2O_3 was selected as a model material because its mechanical properties are well documented in the literature [5,6]. To be consistent with the dislocation microstructure generated during processing, the initial dislocation density was set, in all investigated cases, to a rather large value, $\rho_0 \approx 0.7\ 10^{14}$ m^{-2}. The Young's moduli and Poisson's ratios for the two phases are respectively, $E_{Al} = 71.3$ GPa, $E_{Al_2O_3} = 373$ GPa, $\nu_{Al} = 0.347$, $\nu_{Al_2O_3} = 0.235$. For reasons of simplicity, no residual stresses are introduced.

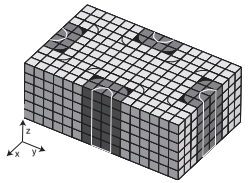

Fig. 1. Geometry of the investigated metal matrix composites for three volume fractions of fibres, f_v. White lines : $f_v = 5\%$, dark grey lines : $f_v = 20\%$, black lines : 45%

3. Results and discussion

In a first step, the simulation results are compared to those of a simple FE computation, in which the constitutive behaviour of the matrix is described by a power law. This law is fitted to the stress-strain curve computed by the DCM for an aluminium crystal in the same conditions as in the MMC material, that is same dislocation density, loading and boundary conditions. The critical stress is defined by a von Mises criterion and the work hardening rate, R, is defined by :

$$R(\varepsilon) = R_0 + K(\varepsilon_0 + <\varepsilon>)^n, \quad (1)$$

where $R_0 = 0.1$ MPa, $K = 55$ MPa, $\varepsilon_0 = 10^{-9}$ s^{-1} and $n = 0.16$.

The value of the work hardening exponent, n, obtained from the DCM is in good agreement with the experimentally obtained one [5].

3.1. *MDC versus plastic continuum modelling*

Figure 2 represents the transverse stress-strain curves obtained for three volume fractions of fibres. With respect to the FE calculation, the yield stress is increased by 50% and 95% for the smallest and highest volume fraction of fibres, respectively. These results illustrate the weakness of a simple continuum model which contains no length scale.

Two main types of size effects are found in the literature. The first one is represented by the well-known Hall-Petch relationship for polycrystals, in

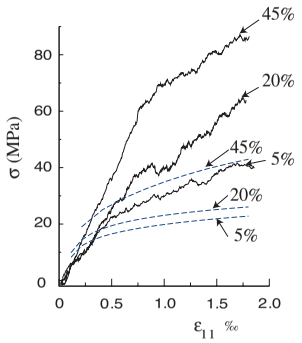

Fig. 2. Transverse stress-strain curves for Al_2O_3/Al composites with different fibre volume fractions, in a simulation cell of constant size and with a constant initial dislocation density. The volume fraction of fibres are 5%, 20% and 45%. The dashed lines refer to the continuum predictions. Solid lines represent the output of the discrete-continuum model.

which the stress is inversely proportional to the square root of the grain size. This size effect is described in terms of dislocations through the properties of dislocation pile-ups blocked at grain boundaries. The second effect arises from confinement and line tension properties, which induce a critical stress inversely proportional to a characteristic length. A typical examples is the Orowan stress for dislocation bowing out between precipitates.

As the size effect is already present at small plastic strains and no pile-ups appear at the interfaces (see Fig. 3), the Hall-Petch relationship may be considered irrelevant in the present case. A generic confinement law in $1/d$ is, therefore, tested in the form :

$$\sigma_t = \frac{2\Phi\Gamma}{bd} \text{ with } \Gamma = \frac{\mu b^2(1-\nu cos^2\alpha)}{4\pi(1-\nu)} log\frac{d}{b} \qquad (2)$$

where Γ is the line tension and Φ an orientation factor.

The evolution of the yield stress simulated with the DCM is in good agreement with such a simple line tension model (see Fig. 4). This confirms that for a transverse loading, the contribution of the fibres to the mechanical response is negligible. However, this result disagrees with the one obtained in 2D by Cleveringa *et al.* [1], where the size effect is attributed to pile-up formation.

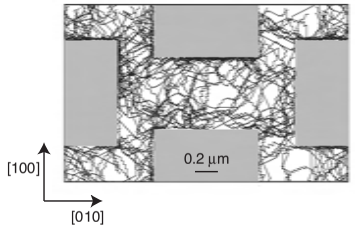

Fig. 3. Dislocation microstructure projected into a (001) plane simulated with the DCM for the highest volume fraction of fibres at $\varepsilon = 1.6 \times 10^{-3}$. Note the accumulation of dislocations at the interfaces and in the channels of smallest widths.

A *source-shortening* mechanism was proposed by Mortensen *et al.* [7] to explain the very large work-hardening rate in MMCs. Due to the accumulation of dislocations at interfaces, the segments that bow-out between fibres have decreasing lengths with increasing strain. In a similar manner, a *structural* source-shortening can be considered to explain the increase of yield stress with decreasing spacing between fibres experimentally observed and numerically reproduced by the DCM.

3.2. *Source-shortening effect*

Another important feature to be noticed in Fig. 2 is the very high work hardening rate ($\delta\sigma_{11}/\delta\varepsilon_{11} \approx \mu_{Al}$). To explain this high value, which is also observed experimentally, Mortensen *et al.* [7] proposed a mechanism of dynamic source-shortening between fibres. To investigate this hypothesis, Fig. 5 shows a resolved stress profile calculated in a matrix channel confined between two fibres. The dashed line shows raw stress data at the Gauss points and the solid line represents the corresponding regression profile.

The resolved stresses are computed on the most active slip system, $[\bar{1}01](111)$. The stress profile shown in Fig. 5 is obtained for a plastic strain of about 1.6×10^{-3}. The distance between two fibres is d and dislocations of the preferred glide system can bow out along all this width and trail segments

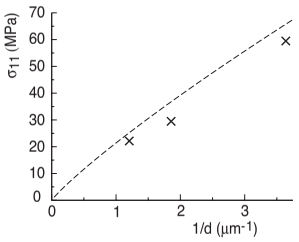

Fig. 4. Evolution of the yield stress as a function of the inverse of the distance between fibres. Dashed line: prediction of a generic confinement law in $1/d$. Crosses: prediction of the DCM. When $1/d$ increases, the volume fraction of fibres in the composite increases.

deposited at the interfaces. An analysis of this profile shows that the sign of the resolved stress is not the same between the interfaces and in the middle of the channel. This inversion of sign can be explained by a polarization of each interface due to the accumulation of dislocations of same sign. Thus, for the plastic strain considered here, dislocations glide in channels of effective width, d^{eff} smaller than d (see Fig. 5).

Using such resolved stress profiles, we observe that the matrix channels progressively close up during the plastic strain. In parallel, the stress level increases up to very high values along the interface. This increase of internal stress can be responsible for crack nucleation and propagation at the interface.

4. Concluding remarks

The present work illustrates the strong influence of the characteristic microstructural dimensions on the mechanical properties of structural materials. Due to small dimensions, dislocations are forced to bow out with small curvature radii and their motion requires an applied stress that depends on a microstructural parameter, specifically the spacing between fibres. The same conclusions were obtained experimentally by Kouzeli *et al.* [8] for a particle-reinforced aluminium material.

In contrast to the 2D results by Cleveringa *et al.* [1], no pile-up is formed in the present simulations.

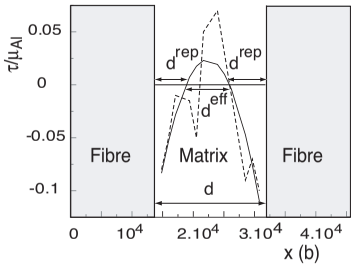

Fig. 5. Resolved stress profile across the MMC with highest volume fraction of fibres and smallest spacing between fibres for the most active slip system. The dashed line is a raw profile extracted from the simulation data and the solid line is the corresponding regression profile. The dislocations accumulated at the interface create an internal stress larger than the resolved applied stress and of opposite sign up to a distance d^{rep}. As a consequence, the initial width of the channel, d, is effectively reduced to d^{eff}.

The yield stress is, in first approximation, governed by an Orowan mechanism. A source-shortening effect is observed, which confirms the hypothesis made by Mortensen *et al.* [7]. This effect is attributed to dislocation accumulation at the interfaces; it is present for all the volume fractions of fibres tested in the present study.

References

[1] H.H.M. Cleveringa, E. van der Giessen, A. Needleman, Acta. Mater. 45 (1997) 3156-3179

[2] S. Groh, B. Devincre, L. P. Kubin, A. Roos, F. Feyel, J.-L. Chaboche, Phil. Mag. Lett. 83 (2003) 303-313

[3] C. Lemarchand, B. Devincre, L.P. Kubin, J.-L. Chaboche, Mat. Res. Soc. Symp. Proc. 538 (1999) 63-68

[4] S. Groh, B. Devincre, F. Feyel, L.P. Kubin, A. Roos, J.-L. Chaboche, IUTAM 2003, edited by Y. Shibutani, H. Kitagawa, 235-244, Kluwer, NL-Dordrecht, 2003

[5] P. Bystricky, H. Bjerregard, A. Mortensen, Metall. Mater. Trans. A 30A (1999) 1843-1866

[6] A. Rossoll, B. Moser, A. Mortensen, Mech. of Mater. (2004) in press

[7] A. Mortensen, O.B. Pedersen, H. Lilholt, Scripta Mater. 38 (1998) 1109-1115

[8] M. Kouzeli, A. Mortensen, Acta. Mater. 50 (2002) 39-51

6.2. Relaxation des couches minces hétéroépitaxiées

Ce travail traite de la relaxation des contraintes internes par le mouvement des dislocations traversantes ("threading dislocations") dans les couches minces épitaxiées et a également été réalisé dans le cadre de la thèse de S. Groh. Lors de la croissance des couches épitaxiées, le désaccord paramétrique entre le substrat et le film, ε_0, induit un état de contraintes biaxial dans les plans parallèles à l'interface, avec des contraintes et des déformations élastiques qui croissent avec l'épaisseur. Au-delà d'une certaine valeur critique de l'épaisseur, l'énergie élastique stockée est relaxée par l'introduction de dislocations d'interface. Dans les métaux, ces dislocations sont initialement présentes ; elles participent au processus de croissance de la couche mince et leur direction est selon l'axe de croissance du film. Sous l'effet des contraintes d'épitaxie, elles se courbent et deviennent mobiles, déposant des dislocations à l'interface. L'épaisseur critique, h_c, est donnée par un modèle très connu de Matthews et Blakeslee [146], en élasticité isotrope :

$$\varepsilon_0 h_c/b = F[\ln(h_c/r_0) + 1], \tag{6.1}$$

où b est le vecteur de Burgers des dislocations traversantes, F regroupe différentes constantes et r_0 est un rayon de coupure inférieur. Pour des écarts paramétriques de l'ordre du pourcent, les épaisseurs critiques sont de l'ordre de quelques dizaines de nanomètres. L'expérience montre que cette prédiction est toujours en défaut dans les métaux, l'épaisseur critique étant environ deux fois plus forte que prévu (ce n'est pas le cas dans les semi-conducteurs). Plusieurs hypothèses ont été proposées pour expliquer cette différence, notamment l'interaction entre dislocations traversantes sur différents systèmes de glissement. La simulation hybride nous a permis de tester une autre hypothèse, suivant laquelle c'est le modèle de Matthews et Blakeslee qui est imparfait, car il ne tient pas compte d'une éventuelle anisotropie élastique. En effet, la plupart des mesures expérimentales ont été obtenues sur des films de cuivre (coefficient d'anisotropie élastique $A = 3,21$). J'ai donc examiné l'influence de l'anisotropie élastique - sur le chargement du fil mince, - sur la tension de ligne des dislocations, - sur les interactions des dislocations avec la surface libre et l'interface film-substrat (forces images).

Les résultats les plus significatifs de cette étude sont reproduits dans l'article ci-après. Le système étudié est constitué d'un film de cuivre sur différents substrats, avec une interface de type (001), une dislocation traversante et des conditions aux limites transversales périodiques. Pour une épaisseur donnée du film variant entre $10b$ et $1000b$, l'écart paramétrique est augmenté artificiellement en appliquant une élévation de température et en introduisant ainsi des dilatations différentielles fictives entre le film et le substrat. Les conditions critiques sont obtenues lorsque la dislocation traversante devient mobile et commence à déposer une dislocation d'interface.

Ces simulations montrent que le simple fait de tenir compte de l'anisotropie élastique du film double en moyenne la valeur critique de l'écart paramétrique pour une valeur donnée de l'épaisseur du film. La nature du substrat module ce résultat à travers l'énergie élastique que la dislocation y stocke. De même, si on tient compte de l'anisotropie élastique dans la tension de ligne des dislocation, il apparaît une augmentation supplémentaire de l'épaisseur critique. Un effet similaire est obtenu pour une orientation (111) de l'interface, mais dans ce cas, le film est plus "dur" que suivant (100), alors que le modèle de Matthews et Blakeslee prédit le contraire. Des expériences menées sur des films minces texturés par le groupe du MPI-Stuttgart [147] ont conduit à des conclusions semblables aux nôtres.

PHILOSOPHICAL MAGAZINE LETTERS, 2003
VOL. 83, NO. 5, 303–313

Taylor & Francis
Taylor & Francis Group

Dislocations and elastic anisotropy in heteroepitaxial metallic thin films

S. GROH, B. DEVINCRE†, L. P. KUBIN

LEM, CNRS–ONERA, 29 Avenue de la Division Leclerc, BP 72, 92322 Chatillon Cedex, France

A. ROOS, F. FEYEL and J.-L. CHABOCHE

DMSE, ONERA, 29 avenue de la Division Leclerc, BP 72, 92322 Chatillon Cedex, France

[*Received in final form 11 December 2002 and accepted 22 January 2003*]

ABSTRACT

The influence of elastic anisotropy on the critical thickness for the plastic relaxation of epitaxial layers is examined with the help of a coupled discrete–continuum simulation. The latter incorporates a rigorous treatment of the boundary conditions and of mismatch stresses, as well as the elastic properties of a single threading dislocation. Numerical experiments conducted on model Cu/Cu, Cu/Au and Cu/Ni systems with a (001) interface show that, through several distinct effects, elastic anisotropy induces a significant increase in the critical thickness with respect to the values predicted by Matthews *et al*. The isotropic model of a comparison of the anisotropic critical thicknesses for (001) and (111) interfaces shows that Cu-(111) films on Ni substrates are about 50% 'harder' than (001) films. This feature is discussed in relation to the strength of thin metallic films.

§ 1. INTRODUCTION

The growth of a thin epitaxial film on a substrate with a different chemical nature induces stresses in the film. These stresses are uniform and depend on the mismatch strain ε_0 between the two lattices. Beyond a critical film thickness h_c, the elastic energy of the film is relaxed by misfit dislocations that appear at the film–substrate interface. These dislocations are formed by the glide of pre-existing segments, the so-called threading dislocations. The present work is concerned with the critical stress for the motion of threading dislocations, which governs plastic relaxation in metallic systems (Arzt *et al.* 2001). Processes involving the heterogeneous nucleation of dislocations in dislocation-free films or the possible influence of a passivating layer are not considered here.

When the film thickness h is larger than the critical value h_c, a threading dislocation with suitable Burgers vector magnitude b bows out critically and glides, depositing a misfit dislocation at the interface. The first prediction of the critical thickness value was proposed by Matthews *et al.* (1970), within the framework of isotropic

† Author for correspondence. Email: benoit.devincre@onera.fr.

Philosophical Magazine Letters ISSN 0950–0839 print/ISSN 1362–3036 online © 2003 Taylor & Francis Ltd
http://www.tandf.co.uk/journals
DOI: 10.1080/0950083032000069249

linear elasticity. The Matthews *et al.* criterion expresses a minimum-energy condition for an epitaxial layer containing a single threading dislocation. It is written

$$\frac{\varepsilon_0 h_c}{b} = FK\left[\ln\left(\frac{h_c}{r_0}\right) + 1\right]. \tag{1}$$

The term on the right-hand side arises from the dislocation line tension; it contains an outer cut-off radius taken as the film thickness and an inner core radius r_0 of the order of b. The factor K accounts for the dependence of the line tension on dislocation character and the factor F for the orientation of the dislocation glide plane. In semiconductor/semiconductor systems with small misfit strains (typically below 2%), the prediction of the Matthews *et al.* criterion is relatively well verified by experiment (Matthews and Blakeslee 1974). However, with larger misfit values, such as those found in metal/metal systems, the observed critical thicknesses can be substantially larger than predicted by equation (1).

For this reason, Freund (1990) and Nix (1998) extended the Matthews *et al.* model to account for the elastic interactions between dislocations with different Burgers vectors. Indeed, the larger the misfit, the larger is the amount of plastic relaxation in the film and, therefore, the higher is the density of misfit dislocations deposited at the interface. The interactions between these dislocations may cause strain hardening and increase the effective value of the critical strain (see figure 2). These models and several variants have been reviewed by Fitzgerald (1991). A similar problem is encountered with the strength of thin polycrystalline metallic films on substrates, which is significantly higher than that of the corresponding bulk material. This strengthening cannot be rationalized by combining Hall–Petch hardening with a critical thickness model (Arzt *et al.* 2001).

Some aspects of the mutual interactions of dislocations have been analysed with the help of dislocation dynamics (DD) simulations (Schwarz and Tersoff 1996, Gomez-Garcia *et al.* 1999, Pant *et al.* 2001, von Blanckenhagen *et al.* 2001). In the present work, we show that the critical thickness depends sensitively on elastic anisotropy, a feature that is not considered in the currently available models. To estimate the influence of anisotropy, use is made of a hybrid simulation method, the discrete-continuum model (DCM). In the DCM, a DD simulation is coupled to a finite-element (FE) code, which solves boundary value problems. This allows one to obtain the state of stress in the film and in the substrate, in the presence of a threading dislocation and within the framework of isotropic or anisotropic linear elasticity. A few basic features of the DCM and the conditions in which the computations were carried out are described in §2. In §3, a validation test for equation (1) is performed on a model Cu/Cu system. Then, the influence of elastic anisotropy on the critical thickness is examined and discussed by considering a Cu film on several substrates with different elastic properties, namely Cu, Ni and Au. Finally, the influence of the interface orientation, (111) or (100), is examined in the case of the Cu/Ni system. The concluding §4 emphasizes that a rigorous description of the stress fields may account for a large part of the differences observed between predicted and observed values of the critical thickness in epitaxial layers. The same conclusion is thought to apply as well to thin polycrystalline metallic films on substrates.

§ 2. Simulation method

Coupled simulations combining a DD code and an FE code allow the discrete and continuum aspects of plasticity to be treated simultaneously. Their use is for the moment restricted to relatively simple configurations (van der Giessen and Needleman 1995, Fivel and Canova 1999, Lemarchand *et al.* 2001). In essence, the numerical model used here, the DCM, is made up of an FE code, in which the constitutive law is replaced by a DD simulation. The main advantage of this method resides in the fact that the elastic and plastic fields can be determined numerically in a rigorous manner, taking into account the presence of dislocations in a small volume element and with a variety of possible boundary conditions (Lemarchand *et al.* 1999).

2.1. *The threading dislocation: dislocation dynamics simulations*

DD simulations are performed using the 'edge–screw' model, in which the continuous shape of perfect dislocation lines is decomposed into a succession of edge and screw segments moving by crystallographic translations in an underlying fcc lattice of parameter a^*. This parameter is not necessarily of atomic dimension. Its value is defined according to the characteristic scale of the problem to be treated, as discussed below. The effective stress on each segment is the sum of the stresses arising from the boundary conditions, of dislocation self-stresses, both of which are computed by the FE code, and of a local, character-dependent line tension T, which is incorporated into the DD simulation. In isotropic elasticity, use is made of an expression developed by Foreman (1967) and modified by Gomez-Garcia *et al.* (1999) to account for the geometrical specificities of the 'edge–screw' model. Within this formulation, only three quantities have to be defined: the magnitude b of the Burgers vector of the threading dislocation, the shear modulus μ which is taken as the Reuss average (for copper films, $b = 0.256$ nm and $\mu_R = 42$ GPa) and r_0, the inner cut-off radius in the dislocation line energy.

In anisotropic elasticity, the line tension takes a more complex form, which is generally not analytical. Its values were directly computed with the help of the DisDi code (Douin *et al.* 1986) and tabulated in the DD simulation.

The output of the simulation, and in particular the implementation of the line tension, has been tested in several ways. For instance, we find that, for a dislocation line emerging at a free surface, the computation of the line tension requires a specific procedure. The latter accounts for the local character and curvature of the line and is similar to that used by Schwarz (1999). In isotropic elasticity, the critical stress for the motion of a threading dislocation in a capped layer was compared with results from Schwarz and Tersoff (1996) and Gomez-Garcia *et al.* (1996). This preliminary work lead to a definition of the core radius, $r_0 = 2b$. Finally, the velocity of a dislocation segment is related to the effective stress τ^*, calculated in its centre, through $v = \tau^* b/B$, where B is a drag constant ($B_{Cu} = 5 \times 10^{-5}$ Pa s^{-1}).

The geometry of the initial configuration is shown in figure 1. In order to obtain an accurate description of the dislocation shapes irrespective of the film thickness, the underlying lattice parameter of the DD code was selected in such a way as always to satisfy $h = 2700a^*$. Two different crystallographic configurations have been studied. For (001) films, the slip system with highest Schmid factor is $[\bar{1}01](111)$, and the direction of motion of the treading dislocation is $[\bar{1}10]$. For (111) films, the active slip system is $[101](11\bar{1})$ and the direction of motion is also $[\bar{1}10]$. For both orientations, the initial and final configurations of the threading dislocation are

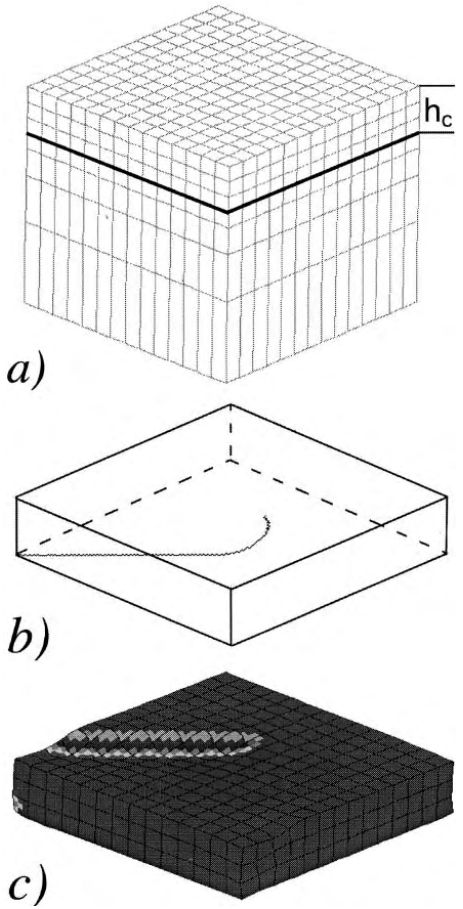

Figure 1. (*a*) Mesh geometry of the MDC simulation for the (001) interface. (*b*) A critically bowed-out shape of the threading dislocation. The latter is initially introduced by a Volterra process. It is made up of a discrete line deposited at the film–substrate interface and a straight threading segment which ends up at the surface of the film. (*c*) The resolved plastic shear strain corresponding to (*b*), $6^{1/2}(\varepsilon^p_{11} - \varepsilon^p_{33} + \varepsilon^p_{12} - \varepsilon^p_{23})$, magnified by a factor of 350.

almost crystallographically equivalent. Thus, its elastic, isotropic and anisotropic properties are nearly the same. The only difference stems from the different angles between the slip plane and the surface plane.

The (111) interface requires a specific treatment. In figure 1 (*a*) the elements of the FE mesh and of the DD lattice are oriented in the same manner, with horizontal and vertical faces parallel to {100} directions. Thus, a (001) interface is effectively flat in

the DCM. However, a (111) interface would be corrugated, which does not allow reliable computations to be performed. To bypass this problem, the procedure used is as follows. A set of coordinate axes based on the three directions [111], $[\bar{1}01]$ and $[1\bar{2}1]$ is defined. Then, without modifying the geometry in figure 1 (*a*), the material's properties, namely the crystallographic directions and the associated matrix of elastic constants, are rotated in such a way to bring the [111] direction normal to the interface. Then, a flat interface can be used in the computation with suitable values for the dislocation and thin film properties. In all the simulations, the film–substrate interfaces are supposed to be impenetrable barriers to dislocation glide and the latter are not allowed to propagate into the substrate.

2.2. *The boundary value problem*

The boundary value problem is treated by the FE code. All the results presented here were obtained with mirror boundary conditions at the side surfaces of the FE meshing (the normal displacement on the side surfaces is set to zero). One advantage of these conditions is to minimize the interactions between the threading dislocation and its periodic images. By reason of symmetry these interactions are negligible in the central area of the simulated film. Therefore, the displacements of the dislocations are restricted to that region. The top surface of the film is treated as a free surface and all the displacements on the lower surface of the substrate are set to zero. Numerical values for the elastic constants of the film and substrate are taken from Hosford (1993).

In the DCM, a FE mesh is superimposed on the DD lattice. In the present work the mesh is made up of $14 \times 4 \times 3 = 588$ cubic elements in the film and $14 \times 14 \times 4 = 784$ parallelepipedic elements in the substrate (see figure 1). It was verified that the simulation results are not affected by the use of a more refined meshing for the film ($20 \times 20 \times 3$). All elements have 20 nodes and 27 Gauss points. The ratio of the substrate thickness h_s to that of the film is set to $h_s/h = 3.5$ (larger values would necessitate too many elements to mesh the substrate). The threading dislocation is introduced by a Volterra process and moved into place from one side of the simulation box (figures 1 (*b*) and (*c*)). This displacement produces a plastic shear which is treated by the FE code as part of the boundary value problem. As this shear is localized in one slip plane of the DD simulation, it has to be homogenized over some height compatible with the FE mesh (Lemarchand *et al.* 2001). In the present case, the homogenization height is set to $3L/2$, where L is the linear dimension of the mesh elements in the film.

The mismatch strain between the film and the substrate is introduced by imposing a differential thermal strain between the two materials. Specifically, the substrate is assumed to have no thermal dilatation and the mismatch strain ε_0 is obtained by applying a temperature change ΔT to a film with a thermal expansion coefficient α_f such that $\varepsilon_0 = -\alpha_f \Delta T$. As a result, the film is elastically deformed in plane-stress conditions and there is no deformation in the substrate. Thus, the loading imposed on a threading dislocation is identical with that obtained when $h_s/h \gg 1$.

§ 3. Isotropic and anisotropic critical thicknesses

The critical thicknesses are computed as follows. Five values of the film thickness, ranging from $10b$ to $10^3 b$, are selected, thus defining the dimension of the FE mesh and of the DD lattice. For each thickness, the mismatch strain is progressively incremented and the plastic strain produced by the threading dislocation as well as

the resolved stresses on it is monitored. For a critical value of the mismatch strain, the threading dislocation starts to glide forwards, which defines a couple of critical values for the mismatch strain and the film thickness. In such conditions, h_c is measured within an accuracy of 3%.

In a first step, results of the simulation in isotropic elasticity are validated with respect to the Matthews *et al.* criterion. Figure 2 shows the critical thickness for a (001) interface in the Cu/Cu system, as yielded by the MDC. These results perfectly agree with the values predicted by equation (1). One can notice that, as mentioned above, the core radius used in the simulations is $r_0 = 2b$, whereas $r_0 = b$ in equation (1). This factor of two is attributed to differences in the cut-off procedures for the elastic energy.

In a second step, the influence of elastic anisotropy is investigated. It is split into two contributions. The anisotropic elastic stresses in the film, keeping the local line tension of the dislocation isotropic, are considered first. Then, the additional effect of an anisotropic line tension is introduced. As expected from plane-stress conditions, the mismatch stress in a dislocation-free film is uniform but depends on the orientation (*hkl*) of the interface. The two non-zero components of the stress tensor are of the form

$$\sigma^a = Y^{hkl} \varepsilon_0, \tag{2}$$

where Y^{hkl} is a biaxial modulus which reduces to $E/(1-\nu)$ in isotropic elasticity. For Cu at room temperature, $Y^{001} = 115$ GPa, $Y^{111} = 261$ GPa and $E = 112$ GPa.

The strong influence of an anisotropic treatment of the stresses is illustrated in figure 3 for a Cu film on different substrates and a (001) interface. The prediction of

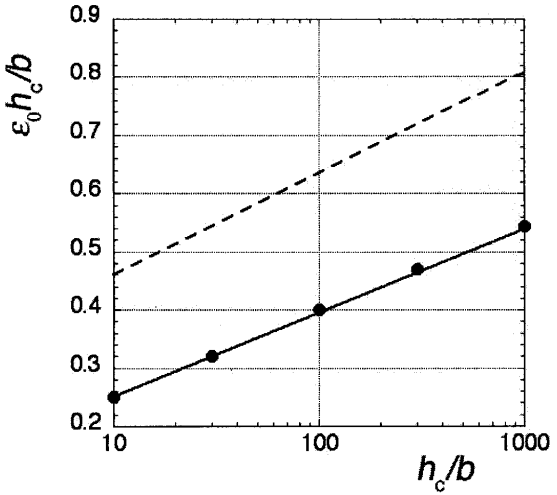

Figure 2. Semilogarithmic plot of the reduced misfit $\varepsilon_0 h_c/b$ as a function of the reduced critical film thickness h_c/b for the Cu/Cu system in isotropic elasticity and with a (001) interface: (——), prediction of the Matthews *et al.* criterion; (- - - -), prediction of the modified model by Freund (1990); (●), simulation results.

the Matthews *et al.* criterion (see figure 2) is also shown for comparison. Considering first the two sets of results obtained for the Cu/Cu system, the two curves are approximatively parallel but, for a given thickness, the critical misfit strain is increased by a factor ranging between 2.3 for $h_c/b = 10$ and 1.7 for $h_c/b = 10^3$. This relative hardening can be compared with the value of 1.6 yielded by the isotropic model given by Freund (1990), which considers the interactions of threading and misfit dislocations (see figure 2).

The small dependence of the above results on the film thickness is thought to originate in the increasing influence of the image forces from the free surface when the film thickness decreases. Unfortunately, this feature cannot be investigated directly with the MDC since the latter does not allow one to differentiate between the different stress contributions.

The influence of the elastic properties of the substrate is shown in figure 3, where results are plotted for two materials other than Cu: Au ($Y^{001} = 78\,\text{GPa}$, $Y^{111} = 189\,\text{GPa}$ and $E = 64\,\text{GPa}$) and Ni ($Y^{001} = 210\,\text{GPa}$, $Y^{111} = 394\,\text{GPa}$ and $E = 202\,\text{GPa}$). Note that Au is on average substantially more compliant than Cu and that Ni is substantially stiffer.

Changing the nature of the substrate slightly modifies the critical conditions for the motion of the threading dislocations. The influence of the anisotropy of the Cu film discussed above is thus predominant. Nevertheless, second-order effects manifest themselves in figure 3, in the form of small shifts between the results obtained for different systems. It was checked that, as expected, the substrate is not deformed by the mismatch stresses. However, some local deformation should be induced in it by the self-stress field of the dislocation. In other terms, the threading dislocation sees

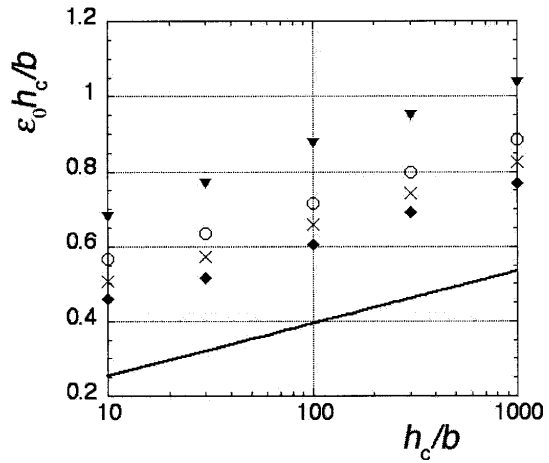

Figure 3. Influence of elastic anisotropy on the critical thickness for a Cu film on various substrates and with a (001) interface. (——), for comparison the prediction of the Matthews *et al.* criterion for the isotropic Cu/Cu system; (×), (◆), (○), the results for anisotropic mismatch stresses and isotropic line tension for the threading dislocation for Cu/Cu (×), Cu/Au (◆) and Cu/Ni (○); (▼) the additional effect of an anisotropic line tension in the case of the Cu/Ni system.

an image force from the substrate that is attractive for compliant substrates and repulsive for stiff substrates. The present results indicate that this effect cannot be simply rationalized, as is sometimes done, by considering an average modulus (Fitzgerald 1991).

Another result is shown in figure 3, still for a (001) interface. It is concerned with a full anisotropic calculation for the Cu/Ni system, that is including the anisotropic local line tension. The critical mismatch strain is then further increased by about 20%. This additional effect is explained as follows. The critical stress is mainly governed by the dragging effect of the misfit dislocation through its line tension. This effect is accounted for in the simulation through the anisotropic long-range interactions between segments. The additional effect of the anisotropic local line tension is therefore restricted to the bowed-out part of the line. The anisotropic line tension of Cu is a maximum for the screw orientation and a minimum near the edge orientation. The ratio of the maximum to minimum values is about 3, twice the corresponding value in isotropic elasticity: $1/(1-\nu) = 3/2$. In the geometry of a [001] interface, a threading dislocation bows out towards the screw direction. Thus, the enhancement in line tension near the screw orientation in the anisotropic case is partly translated into an increase in critical stress to move the dislocation or, equivalently, into an increase in the critical thickness. Similar qualitative considerations would apply for other interface orientations and character dependencies of the line tension.

Figure 4 shows the results obtained for the Cu/Ni system with a (111) interface. For a given thickness, the critical misfit strain increases by a factor of between two

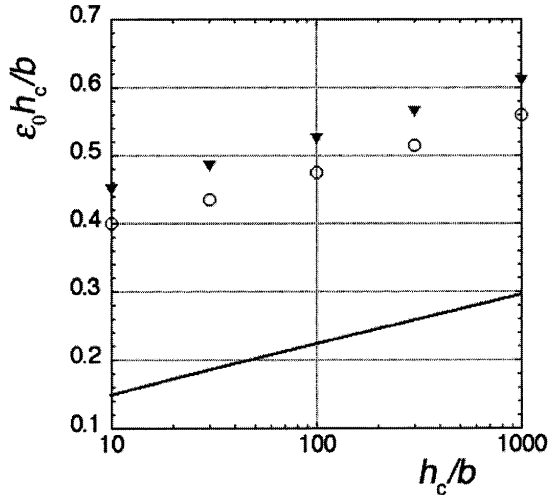

Figure 4. Influence of the elastic anisotropy on the critical thickness for the Cu/Ni system with a (111) interface: (——), the prediction of the Matthews criterion for the isotropic Cu/Cu system, as applied to a (111) interface; (○), (▼), the results for anisotropic mismatch stresses and isotropic line tension for the threading dislocation (○) and for the full anisotropic calculation (▼).

Table 1. Ratios of the critical properties of Cu/Ni films for (001) and (111) interfaces and two different thicknesses in anisotropic elasticity: mismatch strains from figures 3 and 4, stresses, resolved stresses and resolved stresses per unit line length.

Thickness	$\varepsilon_0^{111}/\varepsilon_0^{001}$	$\sigma_c^{111}/\sigma_c^{001}$	$\tau_c^{111}/\tau_c^{001}$	$\tau_c^{111}l^{001}/\tau_c^{001}l^{111}$
10*b*	0.661	1.500	0.922	1.065
1000*b*	0.588	1.335	0.821	0.948

and three when going from the isotropic prediction to the fully anisotropic calculation. When the line tension of the dislocation is isotropic, this increase is slightly smaller, a factor of between 1.85 and 2.65.

Within the framework of anisotropic elasticity, the quantitative influence of the interface orientation can be rationalized as follows. For a given value of the misfit strain ε_0, σ_c denotes the critical stress to move an isolated threading dislocation on a slip system with Schmid factor S and τ_c is the corresponding resolved shear stress. Then, making use of equation (2), we have

$$\tau_c = S^{hkl}\sigma_c^{hkl} = S^{hkl}Y^{hkl}\varepsilon_0. \tag{3}$$

Table 1 shows the ratios of the critical mismatch stresses and strains for (111) and (100) interfaces in Cu/Ni, for the smallest and largest thicknesses investigated. From figures 3 and 4, it appears that the critical mismatch strain is always smaller for the (111) interface than for the (100) interface. There is a compensating effect of the Schmid factors ($S^{001} = 0.408$ and $S^{111} = 0.251$; hence $S^{111}/S^{001} = 0.615$) and of the biaxial moduli ($Y^{111}/Y^{001} = 2.270$), so that the critical resolved stresses are not very different for the two orientations (cf. equation (3) and table 1). Taking into account the difference in initial dislocation length between the two orientations ($l^{111}/l^{001} = 3^{1/2}/2$), the two critical resolved stresses per unit length become almost identical. This simply results from the crystallographic similarity between the two configurations mentioned in §2.1. Regarding the critical non-resolved stresses (equations (2) and (3)), the effect of the biaxial moduli reverses the trend observed on the mismatch strains, so that the (111) interface is the 'hardest' (table 1). This non-trivial result cannot be simply guessed from figures 3 and 4.

Thus, the dependence of the critical stress on interface orientation is sensitive to elastic anisotropy. In fact, the Matthews *et al.* isotropic criterion leads to a prediction opposite to the present criterion. This can be checked from figures 3 and 4, where the critical mismatch strain (or stress) is the largest for the (100) orientation.

§ 4. Concluding remarks

The influence of elastic anisotropy on the critical conditions for plastic relaxation was investigated numerically for Cu films deposited on various substrates with two interface orientations. With respect to the isotropic prediction of Matthews *et al.*, the critical thickness is found to be substantially larger. This hardening effect is mainly due to the influence of anisotropic elasticity on mismatch stresses. To a smaller extent it depends on other factors such as the anisotropy of dislocation line tension and the elastic properties of the substrate.

Models including dislocation–dislocation hardening effects have been proposed to improve the predictions yielded by the Matthews *et al.* criterion, which are too

small in comparison with experiments. However, the present results show that the influence of interface orientation is opposite to the predictions of these models.

A similar question is met in thin polycrystalline metallic films. Their surprisingly large plastic strength is thought to result from a combination of several contributions to dislocation glide:

(i) line tension forces;
(ii) image forces arising from the condition of strain continuity at the film–substrate interface and at the free surface of the film;
(iii) interactions between dislocations with same Burgers vector;
(iv) interactions of threading dislocations with other dislocations intersecting their glide plane.

Recent experimental investigations on metallic systems suggest that the last two contributions may be the most important ones in a grain of given orientation (Baker *et al.* 2001, Kobrinsky *et al.* 2001, Weihnacht and Bruckner 2001). There are, however, marked orientation effects in Cu films, where the texture is made up of columnar (001) and (111) grains. For instance, Hommel and Kraft (2001) found that the flow stress of (111) grains at 0.1 and 0.5% strain is about twice that of (001) grains. As illustrated above, the present numerical model qualitatively reproduces this important experimental fact. The ratio $\sigma_c^{111}/\sigma_c^{001}$ reproduced by the simulation goes from 1.5 to 1.35 when the film thickness is increased. It is suggested that the difference between simulation and experiment can be explained by the absence of strain hardening in the present simulations.

In conclusion, elastic anisotropy appears to affect dislocation behaviour significantly in confined systems. The results presented here deal only with a few model situations. A wealth of types of behaviour is expected to arise from the consideration of a wider spectrum of materials and textures.

References

Arzt, E., Dehm, G., Gumbsch, P., Kraft, O., and Weiss, D., 2001, *Prog. Mater. Sci.,* **46**, 283.

Baker, S. P., Kretschmann, A., and Arzt, E., 2001, *Acta mater.,* **49**, 2145.

Douin, J., Veyssière, P., and Beauchamp, P., 1986, *Phil. Mag.* A, **54**, 375.

Fitzgerald, E. A., 1991, *Mater. Sci. Rep.* **7**, 87.

Fivel, M., and Canova, G. R., 1999, *Modelling Simulation Mater. Sci. Engng,* **7**, 753.

Foreman, A. J. E., 1967, *Phil. Mag.,* **15**, 1011.

Freund, L. B., 1990, *J. appl. Phys.,* **68**, 2073.

Gomez-Garcia, D., Devincre, B., and Kubin, L. P., 1999, *J. Comput. Aided Mater. Des.,* **6**, 157.

Hommel, M., and Kraft, O., 2001, *Acta mater.,* **49**, 3935.

Hosford, W. F., 1993, *The Mechanics of Crystals and Textured Polycrystals* (Oxford University Press).

Kobrinsky, M. J., Dehm, G., Thompson, C. V., and Arzt, E., 2001, *Acta mater.,* **49**, 3597.

Lemarchand, C., Devincre, B., Kubin, L. P., and Chaboche, J. L., 1999, *Multiscale Modelling of Materials*, Materials Research Society Symposium Proceeding, Vol. 538, edited by V. V. Bulatov, T. D. de la Rubia, R. Phillips, E. Kaxiras and N. Ghoniem (Warrendale, Pennsylvania: Materials Research Society), pp. 63–68.

Lemarchand, C., Devincre, B., and Kubin, L. P., 2001, *J. Mech. Phys. Solids,* **49**, 1969.

Matthews, J. W., and Blakeslee, A. E., 1974, *J. Cryst. Growth,* **27**, 118.

Matthews, J. W., Mader, S., and Light, T. B., 1970, *J. appl. Phys.,* **41**, 3800.

Nix, W. D., 1998, *Scripta mater.* **39**, 545.

PANT, P., SCHWARZ, K. W., and BAKER, S. P., 2001, *Dislocations and Deformation Mechanisms in Thin Films and Small Structures,* Materials Research Society Symposium Proceedings, Vol. 673, edited by K. Schwarz, O. Kraft, S. P. Baker, B. Freund and R. Hull (Warrendale, Pennsylvania: Materials Research Society), pp. 2.2.1–2.2.6.

SCHWARZ, K. W., 1999, *J. appl. Phys.,* **85**, 108.

SCHWARZ, K. W., and TERSOFF, J., 1996, *Appl. Phys. Lett.,* **69**, 1220.

VAN DER GIESSEN, E., and NEEDLEMAN, A., 1995, *Modelling Simulation Mater. Sci. Engng,* **3**, 689.

VON BLANCKENHAGEN, B., GUMBSCH, P., and ARZT, E., 2001, *Modelling Simulation Mater. Sci. Engng,* **9**, 157.

WEILNACHT, V., and BRUCKNER, W., 2001, *Acta mater.,* **49**, 2365

CHAPITRE 7

Projet de recherche.

Les simulations mésoscopiques de Dynamique des Dislocations (DD) ont constitué mon principal outil de travail au cours de ces dix dernière années. Il me parait donc utile de débuter ce projet de recherche par une brève discussion des perspectives de cette méthode. Une analogie simple entre les progrès réalisés par la DD et l'évolution d'autres méthodes de simulations, comme la Dynamique Moléculaire, suggère que les études à venir vont progressivement prendre de la distance par rapport aux aspects techniques et se mettre au service de problématiques de plus en plus variées. Le nombre sans cesse croissant d'équipes dans le monde qui investissent dans la DD, avec souvent des ressources humaines et informatiques considérables, est sans doute un gage de pérennité de la méthode. On notera que la recherche française, avec le soutien du CNRS, a joué au cours des années passées un rôle de pionnier dans le développement de ces simulations depuis l'apparition de la première simulation de DD tridimensionnelle au début des années 1990. De même, la décision prise il y a deux ans de continuer à développer notre simulation dans le cadre d'une licence publique et de distribuer les sources de notre code sans restriction devrait favoriser la dissémination de ces simulations.

Aujourd'hui, de vastes domaines d'applications me paraissent ouverts à l'utilisation des outils numériques que j'ai développés. Deux grandes orientations peuvent être envisagées pour les recherches à venir. D'une part, le caractère prédictif de la DD et le fait qu'elle autorise une comparaison simple avec l'expérience va susciter de plus en plus d'études à caractère appliqué. De nombreuses demandes s'expriment d'ores et déjà dans ce sens. La difficulté consiste alors à déterminer quels sont les problèmes qui peuvent effectivement faire l'objet d'une approche physique et ne comportent pas trop de paramètres d'entrée mal connus. D'autre part, la DD est un formidable outil de recherche fondamentale permettant d'une part de réviser et clarifier des problèmes encore mal élucidés par la théorie des dislocations et, d'autre part, d'établir le lien entre approches continue et discrète de la plasticité.

C'est dans cette seconde voie que je souhaite m'investir. La déformation plastique est un phénomène non linéaire faisant intervenir des interactions à longue distance, des réactions locales et des mécanismes opérant à différentes échelles. C'est donc typiquement un phénomène complexe. Depuis le milieu des années 1980 de nombreux modèles analytiques, statistiques ou déterministes, ont vu le jour avec pour objectif de capturer cette complexité. De leur côté, les simulations de DD tridimensionnelles permettent de reproduire de manière réaliste la déformation plastique à l'échelle mésoscopique. La conjonction de ces différentes approches, qui n'est pas encore réalisée, devrait aboutir à la mise au point d'un formalisme théorique ayant un réel caractère prédictif.

Plus précisément, je souhaite organiser mes futurs travaux autour de trois grands axes de recherche.

7.1. Modéliser la déformation plastique

La possibilité de simuler, à l'échelle des dislocations, des éléments de volume de plus en plus grands et des déformations de plus en plus importantes va favoriser dans les années à venir un rapprochement entre les études sur la physique des défauts cristallins et les études issues de la mécanique des milieux continus. Dans la continuité des travaux en cours sur les monocristaux métalliques de structure CFC, des recherches seront entreprises pour valider, corriger ou développer de nouvelles lois de comportement, qui seront couplées à des codes de plasticité cristalline. En effet, il est maintenant prouvé que les simulations mésoscopiques sont en mesure de calculer un certain nombre de données ou de paramètres mis en jeu dans les modèles analytiques de la plasticité et de vérifier ou de corriger un certain nombre d'hypothèses (cf. Chapitre 5 de ce mémoire). L'apport des simulations dans ce domaine est essentiel car bien souvent ces données ne peuvent pas être mesurées expérimentalement avec une bonne précision (par exemple la matrice d'interaction entre systèmes de glissement, le libre parcours moyen des dislocations ou l'évolution des densités de dislocations).

Mes travaux devraient ensuite progressivement s'orienter vers des structures cristallines autres que la structure CFC, c'est-à-dire où les dislocations interagissent fortement avec le réseau via leur structure de cœur. Avec l'aide des simulations atomiques ou *ab initio*, nos connaissances dans ce domaine progressent rapidement. Par exemple, la description de la structure des dislocations dans les métaux CC et de ses conséquences a notablement progressé ces dernières années [148, 149] et il sera bientôt possible de modéliser rigoureusement la friction de réseau dans ces métaux. Ainsi, les progrès enregistrés à l'échelle atomique apporteront les données d'entrée nécessaires pour une modélisation réaliste de la déformation plastique dans des matériaux stratégiques comme le molybdène, le tantale, le fer α, etc , ainsi que certains métaux hexagonaux de transition comme le zirconium et le titane. Dans le même ordre d'idées, mais à plus long terme, les résultats de simulations à l'échelle atomique sur les effets d'alliage et d'impuretés pourraient permettre l'étude des problématiques où des effets chimiques se mêlent aux propriétés mécaniques.

Un autre sujet que je souhaite aborder se situe à la frontière entre la mécanique et la physique. C'est la question de l'irréversibilité de l'écrouissage plastique dans les métaux en fonction des chemins de sollicitation et des microstructures correspondantes. Ce problème, d'une importance pratique considérable, est rattaché pour les mécaniciens aux concepts de durcissement isotrope, indépendant du sens de la vitesse de déformation, et de durcissement cinématique, qui en dépend. Le cas modèle pour l'étude de ces phénomènes est celui de l'asymétrie de la contrainte d'écoulement lorsqu'on inverse le sens du chargement, par exemple lorsqu'on passe de traction en compression. C'est l'effet Bauschinger, dont la compréhension passe par une modélisation des microstructures organisées de dislocations, des contraintes internes qui en résultent et de leur évolution lors de cet essai de déformation. Enfin, l'étude des réponses plastiques à des états de chargement de plus en plus complexes (torsion, flexion ...) pourra être entreprise grâce aux méthodes numériques couplant DD et simulation par éléments finis (tel que le modèle *mdc* développé au LEM). On passera ainsi progressivement de l'étude de matériaux modèles à l'étude des métaux et alliages ayant une microstructure de plus en plus proche de la réalité industrielle. Ce dernier aspect me permet d'introduire le second axe de recherche.

7.2. Prédire les propriétés mécaniques

L'étude des propriétés des dislocations et de la déformation plastique qu'elles engendrent est généralement réalisée dans le cadre d'hypothèses simplificatrices. Par exemple, l'objet étudié est souvent exempt de surfaces libres ou d'interfaces internes et ses dimensions sont suffisamment grandes pour qu'on puisse l'assimiler à un milieu infini, soumis à un état de chargement homogène. Or, les propriétés mécaniques des matériaux réels sont souvent modifiées ou contrôlées par la présence de défauts cristallins autre que les dislocations (joints de grains ou de phases, précipités ..). La présence de ces défauts suppose que l'on soit capable de prendre en compte des hétérogénéités de contraintes de diverses origines. La liste des problèmes restant à résoudre pour modéliser les propriétés plastiques des matériaux complexes est longue et va bien au delà du présent projet de recherche. Dans les années à venir, ma contribution dans ce domaine sera focalisée sur deux points ayant de nombreuses implications théoriques et pratiques.

Le premier problème concerne l'étude des mécanismes de déformation dans les bicristaux. Ce sujet me semble intéressant car il peut dès maintenant être approché de manière rigoureuse et en parallèle par notre simulation *mdc* et par un code de plasticité cristalline traitant de façon continue la contribution des systèmes de glissement présents dans le matériau. La simulation *mdc* est ici nécessaire, à l'échelle des dislocations pour traiter la question difficile de l'état des contraintes dans le matériau, qui est lié à la compatibilité des déformations de part et d'autre du joint de grain. D'un point de vue théorique, l'étude d'un tel système débouche sur la question critique des gradients de déformation dans un matériau et sur la manière dont ils affectent les mécanismes d'écrouissage. Cet travail peut être considéré comme un premier pas conduisant à plus long terme vers la modélisation des propriétés mécaniques des matériaux polycristallins. Les résultats de cette étude pourraient donner à la communauté de la mécanique des solides l'occasion de tester les formalismes liés aux méthodes d'homogénéisation ainsi que les modèles de plasticité avec gradients. De même, cette étude sera très instructive car elle permettra une comparaison directe entre simulations et mesures expérimentales de la déformation, de l'orientation et des densités accumulées au voisinage des grains, actuellement réalisées par les méthodes de diffraction X ou les méthodes d'imagerie d'orientation (orientation imaging method ou OIM).

Le second thème porte sur la question de la rupture des matériaux et plus particulièrement sur la transition fragile-ductile dans les métaux et alliages. Cette étude sera certainement réalisée en collaboration avec le groupe de S. Roberts de l'Université d'Oxford et dans le cadre de projets Européens traitant de cette question (par exemple le projet PERFECT pour la prédiction des propriétés mécaniques des aciers de cuves débuté en 2004). Il s'agit là d'un problème encore largement non résolu et qui, une fois encore, se situe clairement à la frontière entre physique et mécanique. Si les modèles existants sont essentiellement qualitatifs, c'est parce que l'on ne sait pas calculer précisément la dissipation plastique autour d'une fissure. Les progrès importants réalisés ces dernières années par nos simulations laissent entrevoir qu'il est maintenant possible d'aborder ce problème, que j'avais approché un peu prématurément lors de mon séjour post-doctoral à l'Université d'Oxford. Pour s'avérer suffisamment réaliste, cette étude devra être centrée sur des matériaux dont les propriétés élémentaires des dislocations sont bien documentées expérimentalement ou précisément décrites par des modélisations à l'échelle atomique. De même, l'accent sera mis sur des matériaux contenant avant déformation une grande densité de dislocations afin de ne pas avoir à traiter la question, encore mal comprise à l'échelle atomique, de la nucléation des dislocations en fond de fissure.

7.3. Etudier les matériaux micro ou nano-structurés

Finalement, une part de mes travaux va s'orienter vers des études se situant entre l'échelle submicronique et celle de la dizaine de nanomètres, c'est-à-dire jusqu'à la limite où le glissement des dislocations est remplacé par d'autres mécanismes de déformation. En effet, une nouvelle problèmatique a émergé ces dernières années avec le développement des nano-technologies (nanomatériaux, matériaux nanostructurés, films, couches minces et multicouches, MEMS ...). Les problèmes liés à la réduction des dimensions et à l'augmentation du rapport surface sur volume font intervenir de nouveaux mécanismes très intéressants, mais qui doivent être abordés sous un angle multidisciplinaire (physique des surfaces, élasticité anisotrope, chimie, micromécanique, ...). De plus, la nature fortement hétérogène de la déformation plastique à ces échelles souligne clairement la limite des formalismes continus, qui devront être remplacés par de nouvelles approches (par exemple des modèles statistiques).

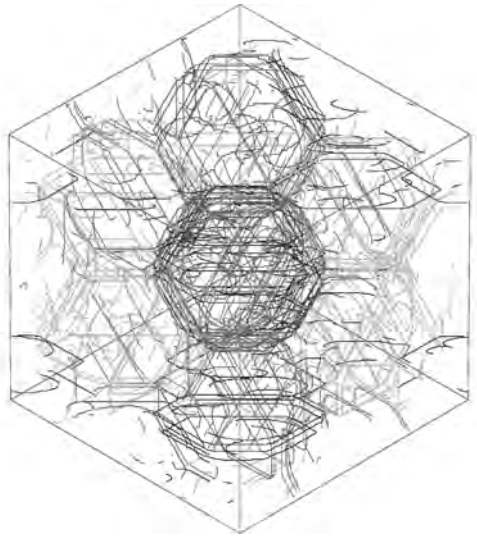

FIG. 7.1.: Exemple de simulation 3-d d'un polycristal de cuivre avec une microstructure périodique de petits grains de taille $d = 0.5\mu$m. Cette figure illustre les simulations en cours de développement pour l'étude de matériaux micro ou nano-structurés (thèse de C. de Sansal).

Comme, j'ai pu le vérifier au cours de mes travaux sur la relaxation plastique des couches minces épitaxiées, il s'agit là de sujets relativement faciles à aborder sur le plan numérique (petits volumes, peu de dislocations, donc calculs rapides). D'un point de vue théorique, ils font appel à une nouvelle physique mettant en jeu, outre les effets de confinement des dislocations : loi d'échelle en $1/L$, où L est une dimension géométrique imposant la courbure des dislocations, en $1/\sqrt{d}$ pour les effets de taille de grains, des effets de surface, d'interface et de gradients de déformation.

À ces échelles, le principal obstacle à la mise en oeuvre de simulations mésoscopiques est la question de la génération des dislocations dans de petits volumes de cristal parfait. Une rugosité, un défaut de surface ou d'interface peuvent modifier le comportement et, surtout, induire une nucléation hétérogène de dislocations. Ce mécanisme relève de l'échelle atomique et ces études seront donc conditionnées par l'apport de simulations à plus fine échelle, visant à déterminer des critères de nucléation utilisables à l'échelle mésoscopique.

Fin 2003, dans le cadre de deux sujets de thèses que je co-dirige (S. Lefèbvre à l' Ecole Centrale Paris et C. de Sansal au LEM), j'ai commencé une étude sur la question de l'écrouissage des métaux

polycristallins avec une taille de grains submicronique (typiquement un pont de connection dans les microprocesseurs). La relation de Hall-Petch qui prédit un durcissement proportionnel à l'inverse de la racine carrée de la taille de grains est généralement bien vérifiée jusqu'à de toutes petites tailles de grains (une dizaine de nm pour des matériaux élaborés avec grand soin). Cependant, les modèles existants pour la loi de Hall-Petch ne sont pas mutuellement consistants et doivent être réévalués pour définir un description unifiée du comportement de ces matériaux allant de leur limite élastique jusqu'aux grandes déformations. Il existe un très grand nombre de résultats expérimentaux dans ce domaine. Même s'ils sont assez confus, ils suggèrent qu'au fur et à mesure que la taille de grain décroît, il apparaît des transitions entre différents mécanismes faisant intervenir (i) la génération de dislocation parfaites puis partielles, (ii) la multiplication des dislocations en volume puis aux joints de grains et (iii) une compétition entre déformation par glissement des dislocations et par maclage. Par ailleurs, les simulations de dynamique moléculaire atteignent maintenant des tailles de grains de plusieurs dizaines de nanomètres dans des nano-polycristaux modèles. Elles confirment les points précédents, mais n'ont pu jusqu'ici confirmer ou infirmer la loi de Hall-Petch à cette échelle de dimensions.

Le seul point acquis au départ, et qui fait l'unanimité des experts, est que les dislocations ne traversent pas les joints de grains, sauf sous de très fortes contraintes, à haute température ou pour des temps longs. L'activation du glissement d'un joint à l'autre se fait donc sous l'effet des contraintes locales et il n'est pas nécessaire de connaître, à cette échelle, la structure fine des joints de grains. Cette étude sera traitée en allant du plus simple au plus compliqué, c'est-à-dire à partir de simulations de DD (en 2-d et 3-d) dans un premier temps, puis avec l'aide d'un code EF de plasticité cristalline utilisant une forme modifiée de la loi de comportement du monocristal présentée en § 5.3.2. Ce travail se prolongera sans doute sur plusieurs années et devrait concerner dans le moyen terme les propriétés mécaniques de matériaux nanostructurés où interviennent les interactions entre dislocations et surfaces ou interfaces.

En conclusion, il existe à ce jour une théorie des dislocations, mais pas encore de théorie bien établie de la plasticité. Les questions ouvertes sont nombreuses et se situent à différentes échelles. Mon ambition, pour les années à venir, sera de contribuer à résoudre quelques unes de ces difficultés à l'aide de simulations numériques, mises au service de l'élaboration de modèles analytiques simples aussi souvent que possible. Ces travaux pourront être accompagnés, lorsque cela s'avèrera nécessaire, d'études expérimentales, réalisées par d'autres groupes, afin de valider ou infirmer les prédictions des modèles.

Deuxième partie .

Annexes

ANNEXE A

Liste de publications

A.1. Publications dans des revues à comité de lecture

1. B. Devincre and M. Condat, *Model validation of a 3D simulation of dislocation dynamics : Discretization and line tension effects*, Acta. metall., **40**, p. 2629, 1992.
2. L.P. Kubin, G. Canova, M. Condat, B. Devincre, V. Pontikis and Y. Bréchet, *Dislocation structures and plastic flow : a 3D simulation*, Solid State Phenomena, **23-24**, pp. 455-472, 1992.
3. B. Devincre and L.P. Kubin, *Simulations of forest interactions and strain hardening in FCC crystals*, Modell. Simul. Mat. Sci. Eng., **2**, p. 559, 1994.
4. B. Devincre, *Three dimensional stress field expressions for straight dislocation segments*, Solid State Communications, **93**, p. 875, 1995.
5. B. Devincre and S. G. Roberts, *3-D simulation of dislocations-crack interactions in BCC metals at the mesoscopic scale*, Acta. metall., **74**, p. 2891, 1996.
6. B. Devincre, P. Veyssière, L.P. Kubin et G. Saada, *A simulation of dislocation dynamics and of the flow stress anomaly in $L1_2$ alloys*, Phil. Mag. A, **75**, p. 1263, 1997.
7. J. Kratochvil, M. Saxlova, B. Devincre and L.P. Kubin, *On the sweeping of dipolar loops by gliding dislocations*, Mat. Sci. Eng. A **234-236**, pp.
318-321, 1997.
8. B. Devincre and L.P. Kubin, *Mesoscopic simulations of dislocations and plasticity*, Mat. Sci. Eng. A **234-236**, pp. 8-14, 1997.
9. V. Bulatov, F. Abraham, L. Kubin, B. Devincre and S. Yip, *Dislocation junction and crystal plasticity : linking atomistic and mesoscale simulations*, Nature, **391**, p. 669, 12 Février 1998.
10. L.P. Kubin, B. Devincre and M. Tang, *Mesoscopic modeling and simulation of plasticity in FCC and BCC crystals : Dislocations intersections and mobility*, J. of Computer-Aided Materials Design, **5**, pp. 31-54, 1998.
11. M. Tang, B. Devincre and L.P. Kubin, *Simulation and modeling of forest hardening in BCC crystals at low temperature*, Model. Simul. in Mat. Sci. Eng., **7**, p. 893, 1999.
12. B. Devincre, P. Veyssière and G. Saada, *Simulation of the plastic flow in Ni_3Al : work hardening and strain rate sensitivity*, Phil. Mag. A, **79**, pp. 1609-1627, 1999.
13. C. Lemarchand, B. Devincre and L.P. Kubin, *Homogenization method for a discrete-continuum simulation of dislocation dynamics*, J. Mech. Phys. of Solids, **49**, pp. 1969-1982, 2001.
14. R. Madec, B. Devincre and L.P. Kubin, *Simulation of dislocation patterns in multislip*, Scripta Mater., **47**, pp. 689-695, 2002.

15. R. Madec, B. Devincre and L.P. Kubin, *From dislocation junctions to forest hardening*, Phys. Rev. Let., **89**, 255508, 2002.
16. S. Groh, B. Devincre , L.P. Kubin, A. Roos, F. Feyel and J-L Chaboche, *Dislocations and elastic anisotropy in heteroepitaxial metallic thin films*, Phil. Mag. Letters, **Vol. 83**, N. 5, pp. 303-313, 2003.
17. R. Madec, B. Devincre, L.P. Kubin, T. Hoc and D. Rodney, *The role of collinear interaction in dislocation-induced hardening*, Science, **Vol 301**, 26 septembre 2003, pp. 1879-1882, 2003.
18. G. Monnet, B. Devincre, L.P. Kubin, *Dislocation study of prismatic slip systems and their interactions in hexagonal close-packed metals : Application to zirconium* Acta Mater. **52**, pp. 4217-4328, 2004.

A.2. Livres, chapitres de livres et activités d'édition

Edition

- Co-éditeur du volume n°578 des MRS Proceedings, "Multiscale Phenomena in Materials Experiments and modeling". Editeurs : I.M. Robertson, D.H. Lassila, B. Devincre et R. Phillips, 2000.

En cours

- En collaboration avec L. Kubin, rédaction d'un ouvrage intitulé "Mesoscale Simulations of Dislocations and Plasticity", Oxford University Press, Oxford Series on Materials Modelling (A.P Sutton and R.E. Rudd, Eds.). A paraître début 2006.
- *Dislocations 2004 : Fundamentals of Plastic Deformation*, B. Devincre, D. Rodney, P. Veyssière and G. Kostorz (Eds.), Special Issue of Materials Science and Engineering (Elsevier), à paraître en 2005.
- *Dislocation-Dislocation Reactions and Plastic Flow in FCC Single Crystals*, B. Devincre, T. Hoc and L. Kubin, Chapitre à paraître dans le volume 14 de la série "Dislocations In Solids", F.R.N. Nabarro and J. Hirth (Eds.), Elsevier B.V., Amsterdam, the Netherlands, 2006.

A.3. Publications dans des actes de colloques à comité de lecture

(Les communications plénières ou invitées sont soulignées)

1. B. Devincre, V. Pontikis, Y. Bréchet, G. Canova, M. Condat and L.P. Kubin, *Three-dimensional simulations of plastic flow in crystals*, dans "Microscopic Simulations of Complex Hydrodynamic Phenomena", M. Mareshal and B.L. Holian (Eds.), Plenum Pess, pp. 413-423, 1992.
2. B. Devincre and V. Pontikis, *Computer modelling of dynamically-induced dislocation patterning*, dans "Materials Theory and Modelling", Mat. Res. Soc. Symp. Proc. **Vol. 291**, p. 555, 1993.
3. G. Canova, Y. Bréchet, L.P. Kubin, B. Devincre, V. Pontikis and M. Condat, *3D Simulation of dislocation motion on a lattice : Application to the yield surface of single crystals*, dans "Dislocation 93", J. Rabier et al. (Eds.), Solid State phenomena, **35-36**, p. 101, 1994.
4. B. Devincre and L.P. Kubin, *Three dimensional simulations of plasticity*, dans "Strength of Materials", H. Oikawa et al. (Eds.), Japan Inst. of Metals, p. 179, 1994.
5. L.P. Kubin, B. Devincre, G. Canova and Y. Bréchet, *3-D simulations of dislocations and plasticity*, dans "Non-Linear Phenomena in Materials Science III", Solid State Phenomena, **42-43**, p. 217, 1995.
6. B. Devincre and S. G. Roberts, *3-D simulation of dislocations-crack interactions at the mesoscopic scale*, dans "Plastic and Fracture Instabilities in Materials", AMD-Vol. 200 / MD-Vol. 57, ASME, p. 47, 1995.
7. B. Devincre, *Mesco-Scale simulation of the dislocation dynamics*, dans "Computer simulation in Materials Science", H.O. Kirchner et al. (Ed.), NATO ASI Series, Series E **Vol. 308**, p. 309, 1996.
8. B. Devincre, P. Veyssière, L. Kubin and G. Saada, *Modelling of dislocation dynamics in Ni_3Al and of the flow stress anomaly*, Mat. Res. Soc. Symp. Proc., **Vol. 460**, p. 535, 1997.
9. G. Saada, B. Devincre and P. Veyssière, *Mechanical properties of LI_2 alloys*, dans "Microstructures and Functions of Materials", N. Igata et al. (Ed.), p. 213, 1997.
10. B. Devincre and L.P. Kubin, *The modelling of dislocation dynamics : elastic versus core properties*, Phil. Trans. Roy. Soc. Lond. A, **355**, p. 2003, 1997.

11. L.P. Kubin and B. Devincre, *Mesoscopic simulation of dislocations*, JFMSS-5, Sapporo (Japon), Annales de Physique, **Vol 22**, C2, p. 109, 1997.
12. C. Lemarchand, B. Devincre, L.P. Kubin and J. L. Chaboche, *Coupled meso-macro simulations of plasticity : validation tests*, MRS Symposium Proceedings, **Vol. 538**, V.V. Bulatov et al. (Eds.), pp. 63-68, 1999.
13. C. Lemarchand, J.L. Chaboche, B. Devincre and L.P. Kubin, *Multiscale modelling of plastic deformation*, Euromech-Mecamat Conference on Mechanics and Multi-Physics Processes in Solids, J. de Physique IV **Vol. 9**, pp. 271-277, 1999.
14. L.P. Kubin and B. Devincre, *From dislocation mechanisms to dislocation microstructures and strain hardening*, dans "Deformation-Induced Microstructures : Analysis and Relation to Properties" (20th Risoe Symposium), J.B. Bilde Soerensen et al. (Eds.), Risoe natl. Lab., Roskilde, Denmark, pp. 61-83, 1999.
15. D. Gomez-Garcia, B. Devincre and L.P. Kubin, *Dislocation dynamics in confined geometry*, J. Comp. Aided Design of Mats., **6**, pp. 157-164, 1999.
16. B. Devincre, *Atypical plastic properties of Ni_3Al alloys studied by dislocation dynamics simulations*, dans "Multiscale phenomena in plasticity", J. Lepinoux et al. (Eds.), Kluwer Academic Publishers, Netherlands, pp. 319-328, 2000.
17. C. Lemarchand, B. Devincre, L.P. Kubin and J.L. Chaboche, *Dislocations and internal stresses in thin films : a discrete-continuum simulation*, dans "Multiscale Phenomena in Materials", I.M. Robertson et al. (Eds.), Mat. Res. Soc. Symp. Proc. **Vol. 578**, p. 87, 2000.
18. D. Gomez-Garcia, B. Devincre and L.P. Kubin, *Forest hardening and boundary conditions in 2-D simulations of dislocation dynamics*. Multiscale Phenomena in Materials, I.M. Robertson et al. (Eds.), Mat. Res. Soc. Symp. Proc. **Vol. 578**, p. 131, 2000.
19. B. Devincre, L. Kubin, C. Lemarchand and R. Madec, *Mesoscopic simulations of plastic deformation*, Mat. Sci. and Eng. A **309-310**, pp. 211-219, 2001.
20. R. Madec, B. Devincre and L.P. Kubin, *New line model for optimized dislocation dynamics simulations*, dans "Multiscale Modeling of Materials-2000", L. Kubin et al. (Eds.), Mat. Res. Soc. Symp. Proc. **Vol. 653**, p. Z1.8.1, 2001.
21. D. Gomez-Garcia, A. Dominguez-Rodriguez, B. Devincre and L.P. Kubin, *Recientes avances en simulacion mesoscopica de la dinamica de dislocations*, Rev. Metl. Madrid, **37**, pp. 273-276, 2001.
22. R. Madec, B. Devincre and L.P. Kubin, *On the nature of attractive dislocation crossed states*, Computational Materials Sciences, **23**, pp. 219-224, 2002.
23. L. Kubin, R. Madec and B. Devincre, *Dislocation intersections and reactions in FCC and BCC crystals*, dans "Multiscale Phenomena in Materials-Experiments and Modeling Related to Mechanical Behavior", H. Zbib et al. (Eds.), Mat. Res. Soc. Symp. Proc. **Vol. 779**, p. W1.6, 2003.
24. B. Devincre, A. Roos and S. Groh, *Boundary problems in DD simulations*, dans "Thermodynamics, Microstructures and Plasticity", A. Finel et al., NATO Science Series : II : Mathematics, Physics and Chemistry, **Vol. 108**, p. 275, Eds. (Kluwer, NL-Dordrecht) 2003.
25. S. Groh, B. Devincre, F. Feyel, L. Kubin, A. Roos and J.-L. Chaboche, *Discrete-continuum modeling of metal-matrix composites plasticity*, dans "Mesoscopic Dynamics in Fracture Process and Strength of Materials", Y Shibutani, H. Kitagawa (Eds.), Kluwer Academic Publishers, NL-Dordrecht, pp. 235-244, 2004.
26. R. Madec, B. Devincre and L. Kubin, *On the use of periodic boundary conditions in dislocation dynamics simulation*, IUTAM Symposium on Mesoscopic Dynamics of Fracture Process and Materials Strength, H. Kitagawa and Y Shibutani (Eds.), Kluwer Academic Publishers, NL-Dordrecht, pp. 35-44, 2004.
27. T. Hoc, B. Devincre and L. Kubin *Deformation stage I of FCC crystals : Constitutive modelling*, dans Evolution of Deformation Microstructures in 3D, Proceedings of the 25th Risoe International symposium on Materials Science, Gundlach et al. (Eds.), pp. 43-59, 2004.
28. S. Groh, B. Devincre, L. Kubin, A. Roos, F. Feyel, and J.-L. Chaboche *Size effects in metal matrix composites*, Mat. Sci. and Eng. A, 'Dislocations 2004 special issue', à paraître en 2005.
29. B. Devincre, T. Hoc and L. Kubin *Collinear interactions of dislocations and slip systems*, Mat. Sci. and Eng. A, 'Dislocations 2004 special issue', à paraître en 2005.

30. P. Carrez, P. Cordier, B. Devincre, L. Kubin *Dislocations reactions and junctions in MgO*, Mat. Sci. and Eng. A, 'Dislocations 2004 special issue', à paraître en 2005.
31. S. Lefebvre, B. Devincre, T. Hoc *Simulation of the Hall-Petch effect in ultra-fine grained copper*, Mat. Sci. and Eng. A, 'Dislocations 2004 special issue', à paraître en 2005.

A.4. Autres publications et communications

(Les communications plénières ou invitées sont soulignées)

1. G. Canova, L. Kubin, M. Condat, B. Devincre and V. Pontikis, *Simulation of dislocation microstructures during plastic flow*, Workshop "Dynamics of Microstructures", Los Alamos Natl. Lab., 1991.
2. G. Canova, M. Condat, B. Devincre, L. Kubin and V. Pontikis, *Simulation de l'écoulement plastique et des microstructures de dislocations*, Colloque SFP, 1991.
3. L. Kubin, G. Canova, M. Condat, V. Pontikis, B. Devincre, Y. Bréchet, *Micro-macro en plasticité : une simulation 3-D à l'échelle mésoscopique*, "Comportement des Superalliages Monocristallins", ONERA-ETCA, 1991.
4. L.P. Kubin, G. Canova, Y. Bréchet, B. Devincre, V. Pontikis et M. Condat *Simulations mésoscopiques des microstructures de dislocations et de la plasticité*, Journées d'Automne de la SF2M, 1992.
5. B. Devincre and L.P. Kubin, *Simulations of forest interactions and strain hardening in FCC metals*, Third Workshop on Computational Modelling of the Mechanical Behaviour of Materials, MPI Stuttgart GERMANY 1993.
6. B. Devincre, L.P. Kubin and V. Pontikis, *Simulation de la dynamique des dislocations à une échelle mésoscopique* Colloque SFP, 1994.
7. B. Devincre *The modelling of dislocation microstructure and plasticity*, Condensed Matter and Material Physics Conference 19-21 Dec. 1994, Organised by University of Cambridge at Warwick, UK, 1994.
8. B. Devincre, *Simulation of the dislocation dynamics*, ASME, Joint Applied Mechanics and Materials, Crète, 6-11 sept 1995.
9. B. Devincre and S.G. Roberts *Transition ductile-fragile : modélisation et simulation à l'échelle mésoscopique*, Journées d'automne 1996, Paris, 15-17 Oct 1996.
10. B. Devincre et L. P. Kubin, *Simulations 3D de la plasticité des métaux CFC purs aux faibles déformations*, Colloque Plasticité, Lans-en Vercors, 11-13 Mars 1996.
11. B. Devincre *Simulation de la dynamique des dislocations dans les alliages LI_2, Journées Simulation Numérique, Matière Condensée et Désordre, Paris, 5-6 Juin 1997.*
12. B. Devincre, *The Modeling of 3-D Dislocation Structures*, CECAM Discussion Meeting on "Multiscale Modeling and Grand challenge Problems in Materials Research", October 23-25, Lyon, 1997.
13. B. Devincre and P. Veyssière, *Mesoscopic simulation of the complex dislocation dynamics in Ni_3Al alloys*, CECAM/PSIK Workshop on "Ab Initio Calculation in Relation to Modelling Constitutive Relations and Fracture Toughness of Metals". Lyon, 20-22 October 1997.
14. L.P. Kubin, B. Devincre, V. Bulatov, F.F. Abraham and S. Yip, *Un exemple de relation entre propriétés atomiques et mésoscopiques des dislocations*, Colloque Plasticité, Poitiers, Mars 1998.
15. V. Bulatov, F.F. Abraham, L.P. Kubin, B. Devincre and S. Yip *Connecting atomistic and mesoscale simulations of crystal plasticity*, European Research Conference on Plasticity of Materials, E-Granada, Avril 1998.
16. L.P. Kubin, B. Devincre, Ch. Lemarchand, A. Moulin, M. Condat and M. Tang *Multiscale modelling of plasticity : the mesoscopic view*, Multi-Scale Modelling of Mechanical Properties of Materials, G. Canova's Memorial Symposium, Autrans 13-15 Juin 1998.
17. B. Devincre, *Contributions of dislocation cross-slip to plasticity*, Séminaire au MIT, Boston USA, 5 Juin 1998.
18. B. Devincre, *3-D simulation of dislocation dynamics at the mesoscopic scale*, The Tri-Lab Short Course on Dislocation in Materials, Lawrence Livermore National Laboratory USA, 8-10 June 1998.

19. L.P. Kubin and B. Devincre, *Coupling of mesoscopic and macroscopic simulations of plastic deformation*, NIST-LLNL Workshop on : Work hardening & dislocation patterning in metals, Pleasanton CA USA, 11-12 June 1998.
20. L.P. Kubin and B. Devincre *Limitations and difficulties in the dislocation dynamics approach*, Dislocation Dynamics Day, Boston, 4 Dec. 1998.
21. B. Devincre *Simulation mésoscopique de la déformation plastique*, Séminaire à l'Ecole Polytéchnique, Palaiseau France, 17 Nov. 1998.
22. D. Gomez-Garcia, B. Devincre and L. P. Kubin, *On the critical stress for dislocation motion in thin films*, Colloque Plasticité, Nancy, Mars 1999.
23. B. Devincre, C. Lemarchand and L. Kubin, *Simulation of dislocation motion in confined geometries*, IUMRS-ICAM'99, Beijing, Chine, June 1999.
24. B. Devincre, *Three-dimensional simulation of dislocation dynamics at a mesoscopic scale*, Séminaire au Department of Materials Science and Engineering, University of Illinois USA, 7 Dec. 1999.
25. B. Devincre, *Simulations mésoscopiques de la déformation plastique*, à l'Ecole des Mines de Nancy, 16 Dec. 1999.
26. B. Devincre, *Simulations mesoscopiques de la déformation plastique : durcissement d'écrouissage dans le monocristaux CFC*, Séminaire à l'Ecole Centrale Paris, 16 Mai 2000
27. B. Devincre, *Simulations multi-échelles de la déformation plastique : de la dynamique des dislocations a un modèle discret continu*, Institut pour la Promotion des Sciences de l'Ingénieur, 15 juin 2000
28. B. Devincre, D. Gomez-Garcia and L.P. Kubin, *Simulation of dislocation wall and cell structures*, MRS Fall Meeting 2000, Symposium Z, Boston 27 Nov. - 2 Dec. 2000.
29. B. Devincre, L. Kubin, C. Lemarchand and R. Madec, *Mesoscopic simulations of plastic deformation*, Plenary talk at "Dislocation 2000", NIST, 21 June 2000.
30. B. Devincre, *New development in the simulation methods for dislocation dynamics*, LLNL Workshop on Dislocation Dynamics Simulations. 12-14 November 2000.
31. C. Lemarchand, B. Devincre, L.P. Kubin and J.L. Chaboche, *Discrete and discrete-continuum simulations of plasticity*, 5th European Mechanics of Materials Conference (EMMC5), Delft, 5-8 March 2001.
32. B. Devincre, R. Madec and LP. Kubin, *Simulations of dislocation patterning and strain hardening in metals*, MRS 2001 Spring Meeting, 19 April 2001.
33. B. Devincre, C. Lemarchand, L.P. Kubin and J.L. Chaboche, *Modeling plastic deformation in confined media*, MRS 2001 Spring Meeting, 19 April 2001.
34. B. Devincre, *Recent progress in dislocation dynamics simulations*, CECAM / SIMU Workshop on "Multiscale Modelling of Materials : Methods, Algorithms and Unsolved Problems", Heraklion, Crète, July 2-6, 2001.
35. B. Devincre, *Dislocation microstructures and mechanical properties*, CECAM Workshop on "Modelling Materials : From Atoms to Microstructures", 18-21 Septembre 2001, Lyon.
36. B. Devincre, *Plasticity by 3D dislocation dynamics*, International Workshop on Multiscale Modeling of Materials, Strength and Failure, Bodega Bay (CA, USA), Oct. 7-10, 2001.
37. R. Madec, B. Devincre, L.P. Kubin, *Strain hardening in fcc crystals : from discrete to continuum models*, 1st. Int. Conf. on Multiscale Materials Modelling, 17-20 June 2002, London.
38. B. Devincre, *From dislocation intersections to plastic flow : DD simulations*, Research workshop on Statistical Mechanics of Plastic Deformation, Trieste, Italy, 4-7 March 2002.
39. B. Devincre, *Modelling plasticity at mesoscale with dislocation dnamics and finite elements coupling*, Thermodynamics, Microstructures and Plasticity, NATO Advanced Study Institute, Fréjus, 2-13 Sept. 2002.
40. G. Monnet and B. Devincre, *A study of plastic hardening in Zr by dislocation dynamics simulations*, 2nd IEA Meeting on Modeling and Experimental Validation, Les Diablerets, Suisse, 30 Septembre - 4 Octobre 2002.
41. B. Devincre, *Boundary conditions in dislocation dynamics simulations*, Colloque Franco-Italien sur la Micromécanique des Matériaux, Todi (Italy), 9-12 Octobre 2002.

42. B. Devincre, *Simulation de la dynamique des dislocations : Techniques et enjeux*, Colloque Plasticité 2003, Lille, Mars 24-26, 2003.
43. B. Devincre, *Modelling plasticity at mesoscale with dislocation dynamics and finite elements coupling*, IUTAM Symposium on Mesoscopic Dynamics in Fracture Process and Materials Strength, Osaka, Japan, July 6-11, 2003.
44. B. Devincre, *Dynamique des dislocations discrètes*, Ecole Thématique du CNRS, 'Homogénisation en Mécanique et Physique des Matériaux', La Londe les Maures, 18-29 Août 2003.
45. B. Devincre, *Influence of alloy friction on dislocation dynamics*, Workshop on Prediction of Radiation Damage in Ferritic Alloys, Mol, Belgium, 23-24 October 2003.
46. B. Devincre, *Periodic Boundary Conditions in Dislocation Dynamics Simulations*, Second ITEM workshop Franco-Italien, Dijon, 27 November 2003.
47. B. Devincre, *Dislocation patterning studied with 2D/3D DD simulations*, 'Multiscale Modeling of Strength and Fracture : Linking Through the Mesoscale', 2nd International Workshop, Berkeley, CA, USA, 7-9 Jan. 2004.
48. B. Devincre, *Strain hardening and dislocation patterning studied by DD simulations*, Linking Processing, Microstructure and Property Modeling, Breitnau/Freiburg, Germany, May 2nd-5th, 2004.
49. B. Devincre, *Dislocations Patterns versus mechanical properties in crystalline plasticity*, XIX Sitges Conference, Jamming, Yielding and Irreversible Deformation in Condensed Matter, Sitges, Barcelona, Espagne, 14-18 Juin 2004.
50. B. Devincre, *Recent progress on 3D discrete dislocation dynamics simulations*, "Discussion Meeting on Discrete Dislocation Plasticity", Cambridge, UK, 1-2 Juillet 2004.
51. L. Kubin, B. Devincre and T. Hoc *The long march to strain hardening in FCC crystals*, "Second International Conference on Multiscale Materials Modeling", UCLA, USA, October 11 - 15, 2004.
52. B. Devincre, D. Gomez-Garcia *The similitude principle in plasticity : Long vs. short-range interactions*, "Second International Conference on Multiscale Materials Modeling", UCLA, USA, October 11 - 15, 2004.
53. G. Monnet and B. Devincre *Influence of lattice friction on junctions in HCP and BCC metals : dislocation dynamics simulations*, 'Dislocations 2004' An International Conference on the Fundamentals of Plastic Deformation, "La Colle-sur-Loup", France, September 13-17, 2004.

ANNEXE B

Articles complémentaires

La présente annexe rassemble un ensemble d'articles techniques ou scientifiques significatifs qui ne sont pas développés en détail dans le présent mémoire. Dans l'ordre, ces documents donnent des informations complémentaires sur :

1. Le champ de contrainte d'une dislocation dans un milieu élastique isotrope infini [30].
2. L'influence des conditions aux limites périodiques sur les simulations de DD [60].
3. La nature diverse des réactions entre dislocations non-coplanaires dans les métaux CFC et les CC [150].
4. Le durcissement de la forêt dans les métaux CC et sa dépendance en température [151].
5. Les propriétés élémentaires intervenant dans la formation de microstructure de dislocation organisées [152].
6. La modélisation de la déformation d'un composite à matrice métallique avec le MDC (modèle discret-continu) [37].

Pergamon

Solid State Communications, Vol. 93, No. 11, pp. 875–878, 1995

0038-1098/95 $9.50+.00

0038-1098(94)00894-9

THREE DIMENSIONAL STRESS FIELD EXPRESSIONS FOR STRAIGHT DISLOCATION SEGMENTS

B. Devincre

SESI, CEA-CEREM, Ecole Polytechnique, 91128 Palaiseau Cedex, France
Now at: LEM, CNRS / ONERA, 29 av. de la division Leclerc, BP 72, 92322 Châtillon Cedex, France

(*Received* 20 *October* 1994; *accepted in revised form* 28 *November* 1994 *by J. Joffrin*)

New expressions for the stress field of straight dislocation segments are derived from the de Wit's expressions for an infinite straight dislocation. Restricted to linear isotropic elasticity, these compact formulae are given in tensor and vector notation expressed in an arbitrary Cartesian reference frame. This solution, allows to compute the internal stress fields or the dislocation-dislocation interactions involved in three-dimensional simulations of plastic strain at spatial scales involving large numbers of dislocations.

Keywords: D. elasticity, mechanical properties

1. Introduction

It is widely recognised that the connection between mechanical properties at the microscopic and macroscopic scale involves the knowledge of the spatial variations of the internal stress stemming from crystal defects. More particularly, the existence of a dislocation microstructure influences the static and dynamic mechanical properties. For this reason, during the last few years, theoretical investigation of the dislocation collective properties at an intermediate scale appeared [1-4].

The direct calculation of this plastic properties based on a three-dimensional simulation has been thought for a long time to be impossible since the dislocation stress fields are additive and long ranged (they decrease as the inverse of the distance). To date, the increase of computing power combined with a few decades of experience in physical modelling authorise such calculations provided that special attention is paid to express the elementary dislocation stress fields in the simplest possible way. Thus, these fields appear to play in the case of plasticity a role comparable to that of interaction potentials in atomistic models.

The aim of the present note is to derive such optimised expressions adapted to the three-dimensional numerical modelling of static or dynamic properties of large discretized dislocation densities. It is emphasised that in such simulations or calculations, most of the computing time (about 80%) is devoted to the computation of the pair interactions of dislocations segments. Therefore, it is essential to significantly reduce this time by adopting formulations more efficient than those presently available (e.g. [5]).

2. Expression for Straight Dislocation Segment Stress Field

The computation of the stress field due to an array of curved dislocations approximated by a succession of straight segments is now a standard technique [5-6]. Such discretization has been successfully used to compute, for instance, the elastic energy or the strain field of simple dislocation configurations [7-8].

According to de Wit [9] the stress tensor elements $\sigma_{ij}(\mathbf{r})$, generated at a point $\mathbf{r}$ by an infinite straight dislocation of Burgers vector $\mathbf{b'}$ and line direction $\mathbf{t'}$ are given, within the frame of isotropic elasticity by

$$\sigma_{ij}(\mathbf{r}) = \frac{\mu b'_n}{8\pi}\left[\begin{array}{l} q_{,mqq}\left(\epsilon_{jmn}\, t'_i + \epsilon_{imn}\, t'_j\right) \\ +\dfrac{2}{(1-\nu)}\epsilon_{kmn}\left(q_{,mij} - q_{,mqq}\,\delta_{ij}\right)t'_k \end{array}\right] \quad (1)$$

Repeated indices are summed, and the symbols following the primes refer to spatial derivatives. μ and ν are the shear modulus and the Poisson's ratio, respectively, δ_{ij}

is the Kronecker symbol and ϵ_{ijk} is the permutation operator whose non-zero elements are:

$$\epsilon_{123}=\epsilon_{231}=\epsilon_{312}=1 \qquad \epsilon_{132}=\epsilon_{321}=\epsilon_{213}=-1 \quad (2)$$

Vectors and scalars entering in the definition of the stress tensor are represented on figure 1. We have

$$\mathbf{r'} = \mathbf{a'} + l'\mathbf{t'} \quad (3)$$
$$\mathbf{R} = \mathbf{r} - \mathbf{r'} \quad (4)$$
$$L' = \mathbf{R}.\mathbf{t'} \quad (5)$$
$$\boldsymbol{\rho} = \mathbf{R} - L'\mathbf{t'} \quad (6)$$

q is the indefinite integral along the dislocation line defined by de Wit [9] as

$$q = \int R\, dl' = -\frac{1}{2}\left\{\rho^2\left(\ln(L'+R) - \frac{1}{2}\right) + L'R\right\} \quad (7)$$

This solution can easily be checked by differentiating q with respect to l', noticing that

$$\frac{dL'}{dl'} = -1 \quad (8)$$
$$\frac{dR}{dl'} = -\frac{L'}{R} \quad (9)$$

To differentiate q with respect to $\mathbf{r}$, one needs

$$L'_{,i} = t'_i \quad (10)$$
$$R_{,i} = \frac{R_i}{R} \quad (11)$$
$$\left(\rho^2\right)_{,i} = 2\rho_i \quad (12)$$
$$\rho_{i,j} = \left(\delta_{ij} - t'_i t'_j\right) \quad (13)$$

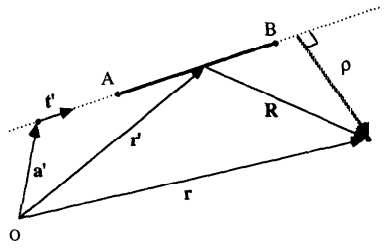

Fig. 1. Vectors and scalars appearing in the definition of the stress tensor generated by a dislocation segment AB. The unit vector $\mathbf{t'}$ is parallel to the dislocation line, $\mathbf{R}$ is the vectorial distance between a point $\mathbf{r'}$ of the dislocation line and an arbitrary point $\mathbf{r}$ at which the stress produced by the segment AB is calculated. $\boldsymbol{\rho}$ is the component of $\mathbf{R}$ normal to $\mathbf{t'}$.

and it is useful to define the vector $\mathbf{Y}$ such that

$$Y_i = R_i + Rt'_i = (L'+R)t'_i + \rho_i \quad (14)$$
$$Y_{i,j} = \frac{Y_i}{R}t'_i + \rho_{i,j} \quad (15)$$

Using these definitions and after some algebra we obtain

$$q_{,i} = -\frac{1}{2}\left\{2\rho_i\left(\ln(L'+R) - \frac{1}{2}\right) + \frac{\rho^2 t'_i}{(L'+R)} + Y_i\right\} \quad (16)$$

and

$$q_{,ij} = -\frac{1}{2}\left\{2\left(\delta_{ij} - t'_i t'_j\right)\ln(L'+R) + \frac{2\rho_i Y_j + Y_j(L'+R)t'_i + 2R\rho_j t'_i + (L'-R)t'_i Y_j}{R(L'+R)}\right\} \quad (17)$$

$$= -\left\{\left(\delta_{ij} - t'_i t'_j\right)\ln(L'+R) + \frac{\left(\rho_i t'_j + \rho_j t'_i + L' t'_i t'_j\right)}{(L'+R)} + \frac{R_j\left(\rho_i + L' t'_i\right)}{R(L'+R)}\right\} \quad (18)$$

$$= -\left(\delta_{ij} - t'_i t'_j\right)\ln(L'+R) - \frac{\left(\rho_i t'_j + \rho_j t'_i + L' t'_i t'_j\right)}{R} - \frac{\rho_i \rho_j}{R(L'+R)} \quad (19)$$

Accordingly, the third-order derivatives of q are

$$q_{,qq} = -2\ln(L'+R) - 1 \tag{20}$$

$$q_{,qqm} = -2\left(\frac{Y_m}{R(L'+R)}\right) \tag{21}$$

and

$$q_{,ijm} = -\rho_{i,j}\frac{Y_m}{R(L'+R)} - \frac{(\rho_{i,m}t'_j + \rho_{j,m}t'_i + t'_m t'_i t'_j)}{R} + \frac{(\rho_i t'_j + \rho_j t'_i + L' t'_i t'_j)}{R^3}R_m - \frac{\rho_{i,m}\rho_j + \rho_i\rho_{j,m}}{R(L'+R)} + \frac{\rho_i\rho_j}{R^2(L'+R)^2}\left(\frac{R_m}{R}(L'+R) + R\left(t'_m + \frac{R_m}{R}\right)\right) \tag{22}$$

To simplify the previous equation it is helpful to notice that the solutions in the form

$$\epsilon_{kmn}\, t'_k t'_m = (\mathbf{t}' \times \mathbf{t}') = 0 \tag{23}$$

do not need to be considered and all the terms multiplied by t'_m can be dropped from equation (22). Therefore, $Y_m = \rho_m = R_m$ and we obtain

$$q_{,ijm} = -\frac{\delta_{im}Y_j + \delta_{jm}Y_i}{R(L'+R)} - \rho_m\left[\frac{\rho_{i,j}}{R(L'+R)} - \frac{(\rho_i t'_j + \rho_j t'_i + L' t'_i t'_j)}{R^3} - \frac{\rho_i\rho_j}{R^2(L'+R)^2}\left(\frac{(L'+R)}{R} + 1\right)\right] \tag{24}$$

The expression (1) can be reformulated in general tensor notation with respect to an arbitrary Cartesian coordinate system, using the vector products $(\mathbf{b}' \times \mathbf{Y})$, $(\mathbf{b}' \times \mathbf{t}')$ and the mixed product **(b', r, t')**.

The computability of equation (25) is improved by defining the symmetric tensor operator

$$[\mathbf{abc}]^s_{ij} = \frac{1}{2}\left((\mathbf{a}\times\mathbf{b})_i c_j + (\mathbf{a}\times\mathbf{b})_j c_i\right) \tag{26}$$

With the help of the following relations,

$$(\mathbf{b}', \rho, \mathbf{t}') = (\mathbf{b}', \mathbf{Y}, \mathbf{t}') \tag{27}$$

$$Y^2 = 2R(L'+R) \tag{28}$$

we obtain

$$\sigma_{ij}(\mathbf{r}) = \frac{\mu}{\pi Y^2}\left[[\mathbf{b}'\mathbf{Y}\mathbf{t}']^s_{ij} - \frac{1}{(1-\nu)}[\mathbf{b}'\mathbf{t}'\mathbf{Y}]^s_{ij} - \frac{(\mathbf{b}', \mathbf{Y}, \mathbf{t}')}{2(1-\nu)}\left[\delta_{ij} + t'_i t'_j + \frac{2}{Y^2}\left[\rho_i Y_j + \rho_j Y_i + \frac{L'}{R}Y_i Y_j\right]\right]\right] \tag{29}$$

Finally, the stress field of a dislocation segment lying between the points A and B on the infinite dislocation line (cf. figure 1) is determined by subtracting the solutions of the equation (29) at this two points [10].

$$\sigma_{ij}(\mathbf{r}) = \frac{\mu}{4\pi}\frac{1}{R(L'+R)}\left[(\mathbf{b}'\times\mathbf{Y})_i t'_j + (\mathbf{b}'\times\mathbf{Y})_j t'_i - \frac{1}{(1-\nu)}\left((\mathbf{b}'\times\mathbf{t}')_i Y_j + (\mathbf{b}'\times\mathbf{t}')_j Y_i\right) - \frac{(\mathbf{b}', \rho, \mathbf{t}')}{(1-\nu)}\left[\delta_{ij} + t'_i t'_j + \frac{(\rho_i t'_j + \rho_j t'_i + L' t'_i t'_j)(L'+R)}{R^2} + \frac{\rho_i\rho_j(2+L'/R)}{R(L'+R)}\right]\right] \tag{25}$$

$$\sigma^{(AB)}_{ij}(\mathbf{r}) = \left(\left(\sigma_{ij}(\mathbf{r})\right)_{r'=B} - \left(\sigma_{ij}(\mathbf{r})\right)_{r'=A}\right) \tag{30}$$

The elastic internal stress associated with a network of connected discretized dislocation segments is simply the sum at the considered point **r** of the stress fields of each segment. Once this quantity is computed, the elastic interactions of dislocation segments are easily derived with the help of the classical Peach-Kœhler formula [5]

3. Concluding Remarks

Equations (29) and (30) are better suited for numerical models than other existing expressions (cf. e.g. [5]), since the stress tensors associated to all the dislocation segments are now expressed in the same reference frame. In addition to this advantage, equation (29) conveniently allows to separate the contributions from screw and edge segments. Thus, with pure screw segments only the first term of equation (29) needs to be considered. Similarly, only the first two terms of equation (29) are needed to compute the stress field in the dislocation glide plane. Advantage has been taken of these remarks to develop a simple discretization model of dislocation lines curvature (the 'edge-screw' model [3]) in the view of performing three-dimensional simulations of dislocation dynamics at the mesoscopic scale [1-4]. This new model associated to the present expressions for the stress field of dislocation segments allowed dynamical studies of realistic metals dislocations density ($\approx 10^{12}$ m^{-2}) inside cubic volume elements of typical side a few tens of micrometers.

Acknowledgements - The author wishes to express his deep gratitude to Pr. M. Condat for the initial idea of this work.

References

1. L.P. Kubin "Dislocation Patterning", in Treatise on Materials Science and Technology, R. W. Cahn, P. Haasen and E.J. Kramer Eds., Vol 6, Chap 4, VCH, Weinberg (1991)
2. L.P. Kubin, G. Canova, M. Condat, B. Devincre, V. Pontikis and Y. Brechet, in 'Non-linear Phenomena in Materials Science II', Eds. G. Martin and L. Kubin, Trans Tech Publication, CH-Aedermannsdorf (1992)
3. B. Devincre and M. Condat, Acta metall. mater., **40**, 2629 (1992)
4. B. Devincre, Doctoral Thesis, University Paris-Sud Orsay , N° 2838 (1993)
5. J. P. Hirth and J. Lothe, Theory of Dislocations, Wiley-Interscience Publications, 132 (1982)
6. L. M. Brown, Phil. Mag., **10**, 441 (1964)
7. T. Jossang, J. Lothe and Skylstand, Acta metall. **13**, 271 (1965)
8. G.C.T. Liu and J.C.M. Li, Phys. Stat. Sol. **18**, 517 (1966)
9. R. de Wit, Phys. Stat. Sol., **20**, 567 (1967)
10. J.C.M. Li , Phil. Mag., **10**; 1097 (1964)

ON THE USE OF PERIODIC BOUNDARY CONDITIONS IN DISLOCATION DYNAMICS SIMULATIONS

Ronan Madec, Benoit Devincre* and Ladislas Kubin*

DPTA, Commissariat à l'Energie Atomique, BP12, 91680 Bruyères-le-Châtel, France
**LEM, CNRS-ONERA, 29 Av. de la Division Leclerc, BP 72, 92322 Châtillon Cedex, France*

Abstract: The use of periodic boundary simulations in dislocation dynamics simulations results in indesirable self-annihilation events. Methods are presented for avoiding this artefact and prescribing realistic dislocation mean free-paths.

Key words: dislocation dynamics simulation, periodic boundary condition.

1. INTRODUCTION

The present work is dealing with periodic boundary conditions (PBCs) in dislocation dynamics (DD) simulations. For the so-called mass simulations, PBCs are needed in order to ensure that dislocation fluxes are balanced at the boundaries of the primary simulation cell in order to avoid undesirable size effects due to finite dimensions and artificial dislocation losses due to image forces.

Bulatov, Rhee and Cai[1] have discussed the application of PBCs to DD simulations. In short, dislocations glide in a periodic array formed by a primary simulation cell and its replicas. Every time a portion of dislocation line crosses a boundary between two cells, its images emerge in all the cells at the equivalent position on the opposite boundary. A balance of fluxes is then established through all the internal interfaces of the simulated volume.

However, the application of PBCs to linear objects is known to lead to spurious self-interactions[2]. In the case of dislocations, a given portion of line may self-annihilate with one of its images after a certain number of boundary crossings. Self-annihilation may reduce the mean free-path of dislocations, and this can have drastic consequences that have not been considered so far in the context of DD simulations. A too short effective mean free-path affects the density of mobile dislocations and their storage rate and, hence, both the arrangement of the microstructure and the strain hardening properties.

The object of the present study is to discuss several methods that have been developed in order to control this artifact. These methods apply to DD simulations in which, like in real crystals, the spacing between slip planes obeys crystallographic relations[3].

In part 2, a few definitions are given that are further used for calculating the self-annihilation distances. For particular slip geometries, self-annihilation occurs after a single boundary crossing and two methods are proposed for dealing with such situations. In part 3, it is shown that self-annihilation distances can be controlled by adequately tailoring the dimensions of orthorhombic simulation cells. Two model situations of practical interest are considered, those of isotropic and strongly anisotropic dislocation loops. Concluding remarks are presented in part 4.

2. DIRECT SELF-ANNIHILATION

2.1 Self-Annihilation: Definitions

Figure 1 shows a simple two-dimensional example of PBCs applied to a square cell of side L. Every dislocation line crossing the boundary of a simulation cell, enters all replicas at positions defined by translation vectors parallel to the cell sides, $\boldsymbol{L}_x$ or $\boldsymbol{L}_y$. These vectors are called modulo translations, as their linear combinations "fold" the microstructure developing in a slip plane into a set of images in every cell. This method has several advantages from a computational viewpoint[1]. It respects the continuity of the lines at the cell boundaries. In addition, shifting in an arbitrary manner the origin of the primary cell does not modify the above-mentioned properties, so that there is actually no boundary to deal with in the presence of PBCs. Finally, any segment can be set at the center of a primary cell for the computation of its elastic interactions with the rest of the microstructure.

As the array of cells is periodic, its section by a slip plane is also periodic, albeit with a different period. A portion of dislocation line, then, necessarily meets with one of its images after a certain glide path. For instance in the square cell of Fig. 1-*a* and for a portion of dislocation line propagating along

the second diagonal, self-annihilation occurs after two boundary crossings only. The simplest way to control these undesirable spatial correlations consists in introducing orthorhombic distortions of the square or cubic simulation cells.

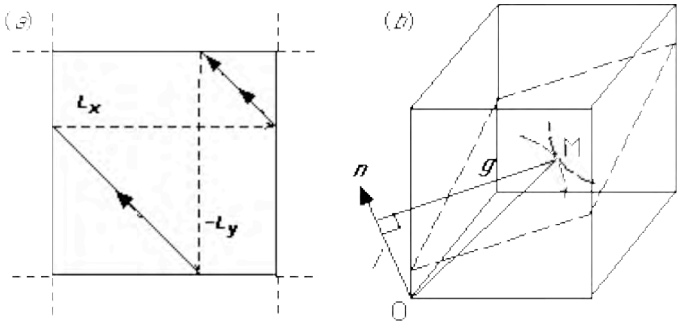

Figure 1. a - In a square cell, a point moving along a direction parallel to the second diagonal annihilates with its image after two modulo translations. *b* – Self-annihilation in three-dimensions and in a slip plane of normal ***n***.

We now consider the images of a three-dimensional trajectory in the primary cell (cf. Fig. 1-*b*). In what follows, the primary simulation cell has {100} faces and its dimensions are defined by the vectors ($\boldsymbol{L}_x$, $\boldsymbol{L}_y$, $\boldsymbol{L}_z$). The slip plane normal is denoted ***n***(*h, k, l*), and the position of a point along an expanding dislocation loop is defined by the vector ***OM***, the arbitrary origin of the expansion, O, being taken at the origin of the cell. The vector ***OM*** can be decomposed as a sum of two components, one along the in the glide plane (***g*** in Fig. 1-*b*) and the other along the slip plane normal. The latter allows distinguishing between slip planes of different heights in the simulation. For this purpose, we define a slip plane index, *i*, such that (Fig. 1-*b*):

$$i = \boldsymbol{OM}.\boldsymbol{n} \qquad (1)$$

In each cell, this index goes from zero to a maximum value. Upon self-annihilation, the two interacting segments must have same slip plane index, as they are in the same slip plane. In the case depicted in Fig. 1-*b*, self-annihilation occurs between two images in a plane with non-zero index, which is not that of the loop expanding from the origin ($i = 0$). It can also occur in the plane $i = 0$, between the loop and one of its images. These two situations will be discussed separately in section 3. Finally, we define the total translation, ***T***, as the sum of the whole set of modulo translations upon self-annihilation:

$$\boldsymbol{T} = u\boldsymbol{L}_x + v\boldsymbol{L}_y + w\boldsymbol{L}_z, \qquad (2)$$

In this expression, u, v, and w are integers counting the number of cell boundary crossings before self-annihilation. The total translation ***T*** has a glide component and a component along the normal to the slip plane. Thus, the condition for self-annihilation of a segment in a slip plane with index i is simply written $\boldsymbol{T}.\boldsymbol{n} = i$, or, in developed form:

$$huL_x + kvL_x + lwL_x = i \qquad (3)$$

In the same way, all the slip plane indexes met during the glide path ***OM*** are a linear combination of hL_x, kL_y and lL_z. The greatest common divisor of these three last quantities defines, along the normal n, a one-dimensional lattice that contains all the possible slip plane indexes available to dislocations. This property is, actually, the only one that is needed to apply the general solutions developed below to three-dimensional DD simulations. It also defines the smallest dipole height that can be met in a given slip system.

Before coming back to the general calculation of the self-annihilation distances, we examine particular slip geometries leading to very short annihilation distances.

2.2 Direct self-annihilations

In general, the modulo translations are not in a slip plane. This can, however, happen for particular slip geometries. As schematically depicted in Fig. 2-a, when a dislocation line propagates along a direction parallel to a modulo translation, self-annihilation occurs after one boundary crossing, irrespective of the cell shape, cubic or orthrhombic. This type of situation is not uncommon and is met typically with {100} and {110} slip planes in some simple cubic structures. For example, the {110} slip planes in the bcc structure contain a modulo translation parallel to <001>.

A solution to this problem consists in shifting a set of parallel boundaries by a translation Δ_{ij} (Fig. 2-a). The first index refers here to the boundary normal and the second one to the shift direction. In lattice-based simulations, the coherency of the slip planes across the interface has to be preserved and Δ_{ij} is a translation of the simulation lattice. The shift vector must also preserve the continuity of the simulated material. For instance normal shifts Δ_i are forbidden, as they introduce voids or matter overlaps. For the same reason, simultaneous symmetrical shears on different boundaries, like Δ_j and Δ_i are forbidden, and of the three non-zero shears, only two can be applied simultaneously. Thus, in three dimensions, the problem can be solved for two boundaries only. Another solution is, then, needed, for the case of {100} slip, where direct self-annihilation can occur in three different directions.

An alternative solution consists in rotating the crystallographic orientations with respect to the primary cell (Fig. 2-b), in order to tilt the slip planes away from the direction of the modulo translation. In discretized

simulations, the rotated lattice must be such that the summits of the unit cell have integer Miller indexes, in order to ensure crystallographic compatibility between the primary cell and its replicas. In cubic or orthorhombic structures, a convenient solution consists in rotating the crystallographic axes around simple crystallographic directions, for instance <001>. This method can be employed alone, as one rotation can be applied along each <100> direction, at the expense of some complexity, or in combination with shifts. The optimization of the cell dimensions presented below can be carried out in the presence of shifts and rotations (cf. section 3.4).

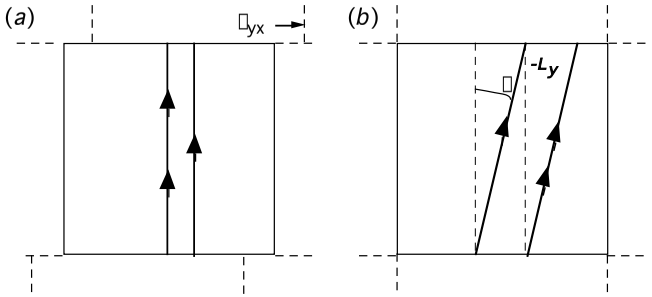

Figure 2. Two-dimensional sketches of direct self-annihilations after a single boundary crossing. *a* – A vertical slip direction is transformed into itself after one boundary crossing (single arrow). The problem is solved by shifting the neighboring cells with respect to each other (here by $\square_{yx}$) so that the glide path and its image (double arrow) do not coincide. *b* – The same problem is solved by introducing a rotation $\square$ of the crystallographic axes with respect to the primary cell.

3. CONTROLLING SELF-ANNIHILATIONS

1.1 Isotropic and Anisotropic Dislocation Loops

In three-dimensions, the self-annihilation distance of a dislocation segment in a given slip plane depends on its propagation direction. Its minimum value, which is achieved for a particular direction, corresponds to the first self-annihilation occurring during a simulation. This quantity is the one that should be controlled for a proper use of PBCs. Two model situations are considered in what follows, which correspond to common configurations found in the practice. In fcc crystals, dislocation loops expand with rather isotropic shapes and mean-free paths of the order of a several tens of microns[4]. At low temperatures in bcc crystals and for prismatic slip in hcp crystals, screw dislocations experience a strong lattice friction and

non-screw segments are comparatively highly mobile. These segments can have long mean-free paths, perhaps up to one hundred of microns or more in pure crystals; their propagation results in the formation of loops with very anisotropic shapes[5].

3.2 Geometry in the Extended Slip Plane

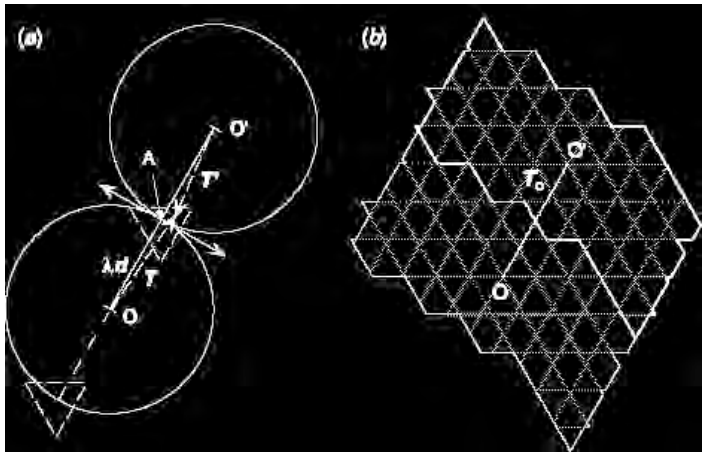

Figure 3. a - A circular dislocation loop expands from the origin O in a slip plane of normal ***n***. Along a direction ***d***, and for a certain radius $\square$, the first self-annihilation occurs in A with an image that moved in the opposite direction (see text for other details). *b* - Tiling of a (111) slip plane in the fcc structure by polygonal intersections with a periodic array of orthorhombic simulation cells. The latter have here dimensions proportional to the set of incommensurate numbers (40, 30, 31). Two supercells are shown, of which the boundaries were computed from the condition that each supercell only contains polygons with different indexes.

Figure 3-*a*, schematically depicts the self-annihilation of an isotropic dislocation loop expanding by glide from the origin O of the primary cell (initial index $i_o = 0$). As indicated in section 2.1 the origin can be chosen in an arbitrary manner without loss of generality. The first self-annihilation event occurs along a direction $\boldsymbol{d}(d_x, d_y, d_z)$, after a glide path or self-annihilation radius $\square$.

The intersections of a slip plane with the periodic array of simulation cells define a tiling of contiguous polygons with various indexes and shapes. This tiling is necessarily periodic since there is a finite number of possible indexes i , which corresponds to an equivalent number of distinct polygonal intersections. One can thus define in the slip plane a periodic array of supercells, of which the periodicity in any direction is defined by the periodicity of the indexes of the polygonal intersections. The supercells have complex shapes, as shown in the example given in Figure 3-b. This example

also illustrates the problems met with non-optimal cell dimensions: the self-annihilation radius is rather small in this case (1.27 times a cell diagonal) and the supercell is rather anisotropic, which means that self-annihilation occurs along different directions in the various {111} slip planes.

In Fig. 3-*a*, self-annihilation occurs when a portion of the expanding loop meets in the same polygonal intersection with an image propagating in the opposite direction. The two segments meet with a common tangent and a common normal parallel to the propagation direction $\boldsymbol{d}$. Thus, the first self-annihilation event on the dislocation loop occurs along the direction of the shortest distance between images of the origin in the superlattice, $\boldsymbol{T}_o = \boldsymbol{OO'}$ (cf. Fig. 3-*b*). The self-annihilation diameter is then $2\Box = \boldsymbol{T}_o$, and the self-annihilation radius, $\Box$, is half this value (Fig. 3-*a*). As already mentioned, the two total translations $\boldsymbol{T}$ and $\boldsymbol{T'}$ (dashed lines in Fig. 3-*a*) are not in the slip plane. Further, they do not necessarily correspond to symmetrical sequences of modulo translations. For instance, a portion of loop expanding in the primary cell starts with a glide sequence, whereas its images start by crossing cell boundaries, which implies one additional modulo translation.

The geometrical considerations developed in the previous sections are now used to calculate a relation between the self-annihilation radius and the cell dimensions. The practical applications are outlined in section 3.4.

3.3 Self-Annihilation of Isotropic Loops

The direction of first self-annihilation is that of the smallest vector connecting two neighboring supercells, $\boldsymbol{T}_o$. Considering the total translations $\boldsymbol{T}$ and $\boldsymbol{T'}$, we see from Fig. 3-*a* that $\boldsymbol{T}_o = \boldsymbol{T} - \boldsymbol{T'}$ and, further, that $\boldsymbol{T}_o = 2\Box\boldsymbol{d}$, so that the condition for first self-annihilation is written:

$$2\Box\boldsymbol{d} + \boldsymbol{T}_o = 0. \qquad (4)$$

In projection along the slip plane normal, we have $\boldsymbol{T}_o.\boldsymbol{n} = 0$, or:

$$huL_x + kvL_x + lwL_x = 0 \qquad (5)$$

In this expression, the unknows are the numbers of boundary crossings u, v and w. Linear equations, of which the solutions searched for are integer numbers, like Eq. (5), are known under the name of first-degree Diophantine equations (after Diophantes of Alexandria, cf. Bashmakova 1997); their solutions can be obtained with the help of various algorithms. The first self-annihilation corresponds to the set of integers (u, v, w) leading to the translation vector between supercell origins of smallest magnitude, $\boldsymbol{T}_o$. The self-annihilation diameter is then obtained from Eq. (4):

$$2\Box = \sqrt{(uL_x)^2 + (vL_y)^2 + (wL_z)^2} \qquad (6)$$

3.4 Self-annihilation of Anisotropic Loops

The anisotropic loops have in practice quasi-rectangular shapes and the fast moving portions, of small length, can be approximated by segments of infinitesimal length propagating along the direction $\pm\boldsymbol{d}$. In contrast with the previous case, the direction $\boldsymbol{d}$ is fixed by a physical argument and is not necessarily connecting the origins of neighboring supercells. Anisotropic loops or segments can, thus, cross several supercells before self-annihilating. As a consequence, their trajectories have one interesting property, which is not formally developed here by lack of space. Every time the boundary of a supercell is crossed by a small segment, an image of the latter appears in all the supercells through the operation of the PBCs. The successive images are shifted by a constant amount, due to the fact that the propagation direction is not, in general, parallel to direction connecting the origins of neighboring supercells. It follows that the images of the trajectories of anisotropic loops in a slip plane are equidistant. Then, a necessary condition for treating the short segments as infinitesimal ones is that their length be smaller than the spacing between their trajectories.

If an edge segment is emitted in only one direction, its return glide distance is $\Box$. There is then no annihilation, but a spurious spatial correlation is introduced (to simplify notations, we still call $\Box$ a self-annihilation radius). Each segment starts from the origin (i = 0) and self-interacts with an image at the origin of another supercell. Equation (3) of section 2.1, taken with i= *0* applies to this situation. However, Eq. (3), which is also a first-order Diophantine equation, does not explicitly include the propagation direction $\boldsymbol{d}$ and yields solutions for all directions in a given slip plane. A more transparent solution can be derived as follows.

The position of the self-annihilation event in the extended plane is brought back into the primary cell by subtracting the total translation from the self-annihilation radius. Then (cf. section 2.1 and Fig. 1-*b*):

$$\boldsymbol{OM} = \Box\boldsymbol{d} - \boldsymbol{T} \qquad (7)$$

Upon self-annihilation at the origin, we have $\boldsymbol{OM} = 0$ and Eq. (7) reduces to $\Box\boldsymbol{d} - \boldsymbol{T} = 0$, or, in developed form :

$$\frac{\Box}{\sqrt{d_x^2 + d_y^2 + d_z^2}} = \frac{uL_x}{d_x} = \frac{vL_y}{d_y} = \frac{wL_z}{d_z}, \qquad (8)$$

where the d_i are integer crystallographic indexes. This equation reduces to Eq. (3) by introducing the condition $\boldsymbol{d}.\boldsymbol{n} = 0$, which expresses that the direction $\boldsymbol{d}$ is in the slip plane of normal $\boldsymbol{n}$. The set of integer numbers (*u, v, w)* is obtained from the three equations at the right-hand side of Eq. (8):

$$v = u\frac{L_x d_y}{L_y d_x}; \quad w = u\frac{L_x d_z}{L_z d_x} . \tag{9}$$

This equation has an infinite number of solutions. The first self-annihilation is obtained through the additional condition that it corresponds to the total translation vector $\boldsymbol{T}$ of smallest magnitude, i.e., to the smallest distance between cell origins. The self-annihilation radius is then determined from the left-hand side of Eq. (8).

3.5 Implementation

In practice, several conditions are initially prescribed. The average dimension of the primary cell should be large with respect to the typical length scale of interest, for instance an average distance between dislocations or the diameter of a dislocation cell. This leads to average dimensions of typically 10 μm for standard mass simulations. The value of the self-annihilation radius is then prescribed according to the physical situation considered. The orthorhombic cell should not be too much distorted with respect to the cubic shape, so that all crystallographically equivalent active slip planes have equal weight in the simulation. The cell dimensions should then be proportional to a set of three incommensurate numbers centered around an average value.

In the anisotropic case, several possible solutions can be obtained directly from Eqs. (8) and (9). In the isotropic case, The coupled equations (5) and (6) are solved numerically, which also leads to several possible solutions. The condition that the supercells have isotropic shapes ensures that all equivalent slip planes of a same family have comparable self-annihilation radii. It is used to select the optimal solution.

Several situations related to self-annihilation can also be treated via first-order Diophantine equations. This includes, in particular, the formation of dipoles with small heights, which can be troublesome during model simulations with small initial dislocation densities. The condition for self-annihilation is then replaced by the condition that self-interaction occurs in a cell where the interacting segments have nearest-neighboring indexes.

Finally, these solutions can easily be extended to the particular slip geometries where one has to use shifts and rotations to avoid premature self-annihilation (section 2.2). Rotations of the crystallographic lattice are cared of by carrying out calculations in the rotated lattice. Shifts applied to the boundaries are accounted for by replacing the modulo translations L_i by translations ($\boldsymbol{L}_i$+□$_j$) incorporating the shift on the face i.

4. CONCLUDING REMARKS

The self-annihilation of dislocation lines caused by the use of PBCs is an artifact that can be turned into an advantage. Indeed, the methods outlined in the present work allow setting the values of the self-annihilation distances and, in the same time, making sure that the effective dislocation mean-free paths are conform to physical expectations. This last length scale has a strong influence on the development of dislocation microstructures and its control allows drawing quantitative estimates from DD simulations[3,7].

The two situations considered here, those of isotropic and anisotropic loops cover most of the cases of practical interest. To avoid severe artifacts occurring with particular slip geometries, two methods are proposed that consist in modifying the periodic arrangement of the simulation cells. These methods can be implemented in any DD simulation, discretized or not. The self-interaction distances of dislocations are prescribed through a choice of the dimensions of an orthorhombic simulation cell based on a quantitative analysis. To be implemented, the latter only involves the requirement that the slip planes available to the moving dislocations be located on a set of equidistant heights in the simulation cell.

ACKNOWLEDGEMENTS

The authors gratefully thank Pr. Robert Rudd (Lawrence Livermore National Laboratory) for sharing his views on the question of PBCs. Part of this work was conducted by one of the authors (RM) at the Centre Européen de Calcul Atomique et Moléculaire (CECAM) during a post-doctoral stay.

REFERENCES

1. Bulatov VV, Rhee M, Cai W., in Multiscale Modeling of Materials 2000, LP Kubin, R. Selinger, JL Bassani J.L. and K Cho eds, Warrendale, PA: Materials Research Society 2000, Symposium Proceedings Vol. 653, p. z1-3.
2. Schwarz K.W. 1988, Phys. Rev. B 85:108.
3. Madec R., Devincre B., Kubin L.P. 2002, Phys. Rev. Lett. 89:255508.
4. Ambrosi P., Shwink Ch.. 1978, Scripta Metall. 12:303.
5. Tang M., Kubin, L.P., Canova, G.R. 1998, Acta Mater. 46:9.
6. Bashmakova, I.G., *Diophantes and Diophantine Equations*. Washington DC: Math. Assoc. Amer.
7. Madec R., Devincre, B., Kubin, L.P. 2002, Scripta Mater. 47:689.

Dislocation Intersections and Reactions in FCC and BCC Crystals

Ladislas P. Kubin, Ronan Madec[1] and Benoit Devincre
Laboratoire d'Etude des microstructures, CNRS-ONERA,
29 Av. de la Division Leclerc, BP 72, 92322 Chatillon Cedex, France
[1]Now at: DPTA, Commissariat à l'Energie Atomique, BP12, 91680 Bruyères-le-Châtel, France

ABSTRACT

The various types of configurations formed in face-centered cubic (fcc) and body-centered cubic (bcc) structures by two interacting, non-coplanar, dislocation segments of various orientations are examined and discussed. The focus is on junction formation and on a particular interaction, the collinear interaction, which deserves much more attention than paid up to now.

INTRODUCTION

As first stated by Taylor [1], strain hardening in crystals stems from dislocation interactions. Within the widely accepted "forest model" [2, 3], the formation and the destruction of junctions or locks produced by attractive interactions between non-coplanar dislocations contribute to most of the flow stress in conditions of multiple slip. The stability of junctions is governed by self-energies, which are mainly elastic in nature since the contribution of the dislocation cores is comparatively negligible. This allowed performing studies on particular junction configurations in several simple crystal structures, fcc [4, 5], see also [6], bcc [7, 8] and hexagonal close-packed [9]. More recent studies of individual junction configurations at the atomic scale [10, 11] and at the mesoscopic scale [12-15] have confirmed the validity of such elastic approaches. At the mesoscale, however, analytical elastic calculations cannot fully account for the mutual distortions of interacting dislocations lines. This is why dislocation dynamics (DD) simulations are particularly suited for a more precise treatment of such problems.

The aim of the present study is to provide a global insight into the interactions and reactions of two dislocation segments in fcc and bcc crystals, stressing their dependence on the initial orientation of the lines. Some aspects of the simulation technique used in the present study are summarized. Mappings of dislocation reactions are then presented and discussed, with emphasis on an intersection process which has been largely ignored up to now and has recently be found to be of prominent importance, the collinear interaction. Concluding remarks are finally presented.

METHODOLOGY

Use is made of a DD simulation, in which segments with a finite set of orientations are embedded into an elastic medium and move by discrete translations in an underlying mesoscopic lattice with same symmetry elements as the considered crystal. An early version of this simulation, in which continuous dislocation shapes were discretized into edge and screw segments, has been described is some detail [16, 17]. The updated version used in the present work is based on the same principles, which are discussed in [15, 18], but makes use of an improved description of the dislocation lines. This allows one to treat dislocation reactions in a very precise, parameter-free, manner by incorporating the directions of dislocation reactions in the elementary base of vectors of the simulation [19, 20]. We focus here on the procedure for producing the intersection mappings shown in the next parts.

Optimized Discretization of the Dislocation Lines

Figure 1 illustrates, through the example of Frank-Read sources in fcc and bcc crystals, how the discretization of the dislocation lines in the DD simulation can be adapted to different crystallographic structures. An extension to the treatment of prismatic and first-order pyramidal slip in hcp crystals will be described in a separate publication (Monnet et al., to be published).

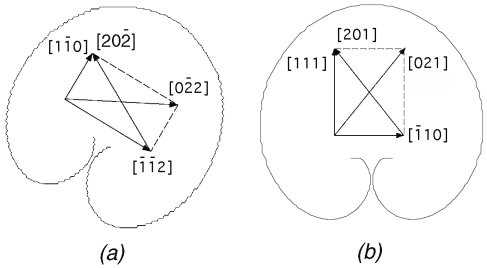

Figure 1. Frank-Read sources expanding under stress in their slip planes in the absence of lattice friction. The source segments are of edge character and of length 4 μm. The detail of the loops shapes is mostly determined by the loading conditions. (*a*) - 1/2[1 $\bar{1}$ 0](111) slip in a fcc crystal (Cu). (*b*) – 1/2[111](11$\bar{2}$) slip in bcc Ta. The <021> directions are those obtained by reaction of the slip systems [111](11$\bar{2}$) and [1 $\bar{1}$ $\bar{1}$] (1 $\bar{1}$ 2).

In the fcc structure (Fig. 1-a), the glide loops are described using a base of 8 line directions per slip plane, namely the edge, screw, π/3 and 2π/3 directions with their two signs. In the bcc structure, 6 line directions per slip plane (two screw and four mixed) are sufficient if only {110} slip is accounted for. In order to treat all the junction formed by dislocations gliding in {110} and {112} planes, 12 and 20 lines directions are needed in {110} and {112} planes, respectively. The <021> directions shown in Fig. 1-b are those obtained by reaction of the slip systems 1/2[111](11$\bar{2}$) and 1/2[1 $\bar{1}$ $\bar{1}$] (1 $\bar{1}$ 2).

Mappings of Dislocation Reactions

We consider the two slip systems (1) and (2) defined by their Burgers vectors $\boldsymbol{b}_i$ ($i = 1, 2$) and their slip plane normal $\boldsymbol{n}_i$. Along the intersection of the two slip planes, where junctions potentially form, a reference direction is chosen, $\boldsymbol{l}_j$. The interacting segments, each in one slip

plane, have line direction $\boldsymbol{l}_i$ (i = 1, 2). They are initially of same length and intersect each other in their midpoints (Fig. 2), making angles ϕ_1 and ϕ_2, respectively, with respect to $\boldsymbol{l}_j$. These angles are measured in reference frames such that $\boldsymbol{n}_1 = -\boldsymbol{b}_1 \times \boldsymbol{l}_1$ and $\boldsymbol{n}_2 = \boldsymbol{b}_2 \times \boldsymbol{l}_2$. With this convention, two dislocation lines parallel to $\boldsymbol{l}j$, ($\phi_1 = \phi_2 = 0$) and with opposite Burgers vector are attractive.

After relaxation, three types of configurations are obtained, which are illustrated in Fig. 2. Figs. 2-a and 2-c show two configurations corresponding to junction formation and repulsive interaction, respectively. A third type of configuration occurs, in which although two segments are attractive, the formation of a junction is not observed because it is not energetically favored. An example of such configuration is shown in Fig. 2-b; it is called a crossed-state after Wickham et al. [12]. The occurrence of crossed-states can be understood from a simple geometrical argument given by Friedel [3]. When a junction is formed, equilibrium at the triple nodes corresponds to a certain angle between the arms of the initial segments. This angle is necessarily larger than its value before junction zipping (cf. Fig. 2-a). Thus, if the two interacting segments initially make an angle larger than the equilibrium value, and even if they are attractive, no line tension equilibrium can be achieved and no junction can be formed. A last type of configuration consists of a few neutral states that cannot be characterized due to the too small magnitude of the interactions. For the sake of simplicity, neutral states and crossed-states are lumped into a common category of weak obstacles.

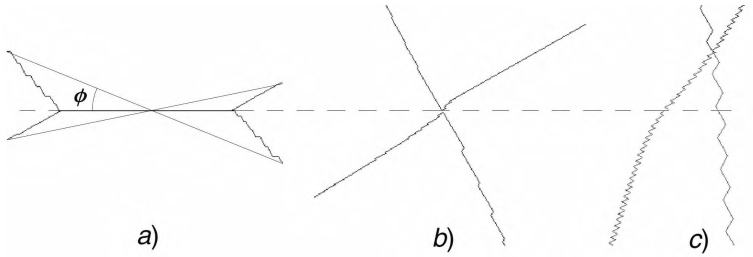

Figure 2. Three simulated configurations of intersecting non-coplanar segments gliding in different slip planes. The dashed line represents the direction of intersection of the two slip planes. (*a*) - Attractive interaction: junction formation. The thick lines represent the initial configuration. (*b*) - Crossed-state: although the two segments are attractive, junction formation is not energetically favored. (*c*) - Repulsive interaction: the two segments move away from each other.

The simulation of dislocations interactions and reactions is performed as follows. For a given set of interacting slip systems and for a couple of initial orientations of the dislocation lines, an initial configuration is built up. We consider two straight segments pinned at their extremities in order to mimic strong interactions occurring in real crystals with other forest dislocations. For the same reason, the initial length of the segments is taken to be $l_i \approx \rho_f^{-1/2} = 1$ µm, the typical length associated with a forest density $\rho_f = 10^{12}$ m^{-2}. To discuss the influence of the segment's length, another length of 30 µm is also used in Fig. 7, below. This second type of configuration is dedicated to a comparison with simplified analytical models, which consider infinite dislocation lines. In the initial state, the midpoints of the two segments are placed at an approach distance of $d \approx l_i/100$. Then, the two segments are let to relax and reach an equilibrium configuration such that the Peach-Koehler force on each discretized segment describing the lines is equal to zero. To speed up relaxation, the stress vs. velocity law is in all cases the one defined for fcc crystals, which entails high dislocation mobility. Isotropic elasticity is used throughout the present work. The simulated model materials are defined by their Burgers vector, Poisson's ratio, ν, and isotropic shear modulus, μ. The values used are $b = 0.256$ nm, $\nu = 0.347$ and $\mu = 42$ GPa for fcc crystals and $b = 0.286$ nm, $\nu = 0.33$ and $\mu = 68.5$ GPa for bcc crystals. However, within the restriction of isotropic elasticity, all the mappings presented in the next sections are generic and apply to all materials of same crystallographic structure. The reason is that within the present context, the configurations investigated depend on elastic interaction and line tension forces that scale with the product μb. Changes in the Poisson's coefficient from one material to the other induce only minor modifications.

The boundary conditions of the simulations are chosen in order to investigate the properties of two isolated dislocations embedded into an infinite elastic medium. This configuration can easily be obtained with the help of periodic boundary conditions in a reference cell at least two times larger than the initial length of the dislocation lines. The nature of the relaxed configuration is identified as follows. If the two dislocation lines superimpose each other over a fraction of their length, the formation of a junction is stated. If the shortest approach distance between the dislocations has increased after relaxation, the configuration is necessarily repulsive. All the intermediate cases not accounted for by the above two criteria, are considered as cross-states.

The output of the simulations is presented for each couple of angles (ϕ_1, ϕ_2) in the form of a mapping indicating the nature of the final state, like in previous works on bcc metals [7, 12]. The properties of junctions, like their length or critical unzipping stress, can be derived easily from these results [15, 18], but will not be reported here in detail by lack of space.

Comparison With Elastic Calculations

Two elastic solutions, which derive from simplified models, yield boundaries that are superimposed to the computed mappings presented below. They are aimed at providing a guide and a check from elastic solutions less sophisticated than those given by the simulations. A first boundary is the locus of the points where junction formation is neutral, i.e., neither favored nor forbidden. This criterion can be obtained either by a condition of line energy minimization or equivalently by the condition of line tension equilibrium at the triple nodes. It is calculated for straight segments, in isotropic elasticity and with an orientation-dependent line tension that does not include the usual logarithmic term. The corresponding expression can be derived easily [21]. The second boundary delimitates the border between initially attractive and repulsive segments. It is calculated from the interaction force along the shortest approach distance of two rigid, infinite, lines. Kroupa [22] gave a simple solution to this problem (see also [23]). Both models assume that the interacting segments are rigid but, as discussed below (cf. Fig. 4), they may also lead to opposite predictions regarding the nature of the final state. The comparison with the simulations is nevertheless useful for the interpretation of the results.

JUNCTIONS IN FCC AND BCC CRYSTALS

Junctions in FCC Crystals

Figure 3 shows the mappings obtained for the three types of slip systems interactions leading to perfect junctions in the fcc structure: - the Lomer junction, of 1/2<110> type, which is sessile, - the glissile junction, also of 1/2<110> type, which is glissile in one of the two intersecting slip planes, and - the Hirth lock, where the interacting Burgers vectors are orthogonal and the reaction product is of the <200> type. The solutions of the two simple elastic models mentioned above are superimposed to the simulation results.

The three configurations depicted in Fig. 2 are found in these graphs. The mappings are periodic with a period ($\phi_1 = \pm\pi$, $\phi_2 = \pm\pi$), since these translations leave the initial configuration unchanged (cf. Fig. 2-a). The domain of junction formation takes the form of lobes encircling the origin. These lobes depart from a circular shape due to the orientation-dependence of the line tension and approximately follow the predictions of the elastic models (thick lines in Fig. 3). The boundary between attractive states, i.e., junctions and crossed-states, and repulsive states is also relatively well accounted for by Kroupa's formula (thin lines in Fig. 3). The assumptions made in the two elastic estimates also manifest themselves for some orientations through conflicting predictions, as is clearly seen in the case of the glissile junction. In Fig. 3-b, on top of the central lobe, junctions are formed between attractive segments, whereas for rigid segments the reaction is energetically unfavorable. Inversely, at the bottom of the upper lobe at right, junction formation is energetically favorable for rigid segments, but does not occur because the segments are repulsive. Such discrepancies stem from the fact that the two elastic estimates reflect in an imperfect manner two aspects of the same global behavior. The junction lobes derive from a simplified calculation of the energies of the initial and final states, whereas the boundary between attractive and repulsive states derives from a calculation of the initial interaction force, i.e., of the initial derivative of energy vs. reaction coordinate. As illustrated by 4, the two estimates may yield opposite predictions in the presence of an energy barrier. Whether or not the latter can be overcome by the dislocations depends on some complex balance between line tension and interaction forces, as will be discussed in the next part.

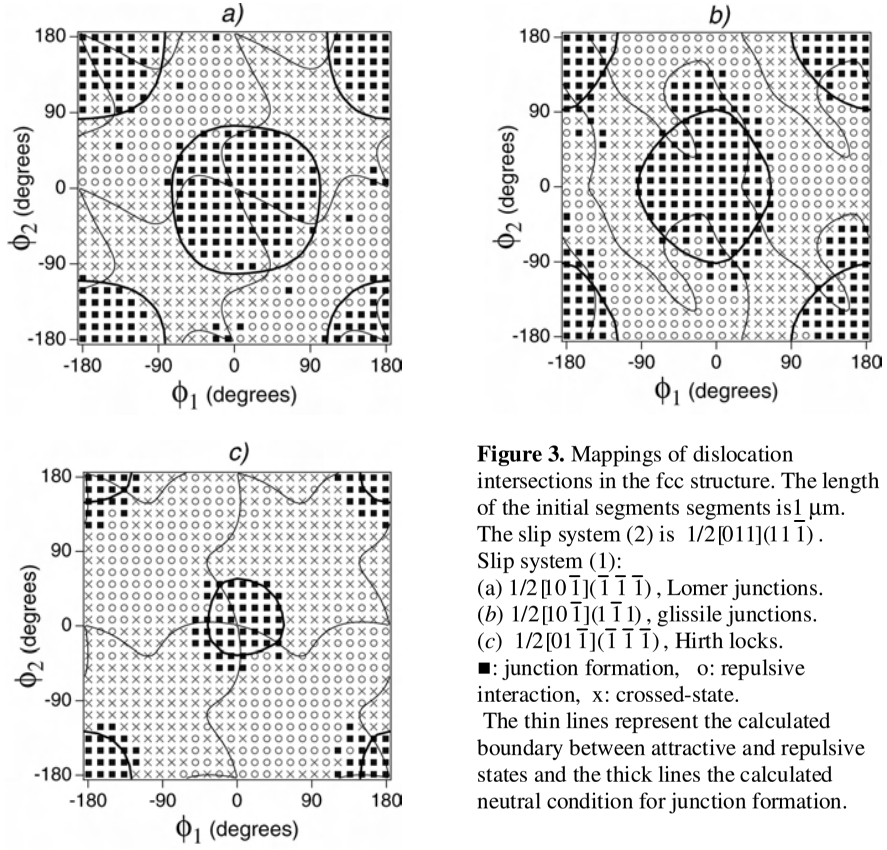

Figure 3. Mappings of dislocation intersections in the fcc structure. The length of the initial segments segments is 1 μm. The slip system (2) is $1/2[011](1\,1\,\bar{1})$. Slip system (1):
(a) $1/2[10\,\bar{1}](\bar{1}\,\bar{1}\,\bar{1})$, Lomer junctions.
(*b*) $1/2[10\,\bar{1}](1\,\bar{1}\,1)$, glissile junctions.
(*c*) $1/2[01\,\bar{1}](\bar{1}\,\bar{1}\,\bar{1})$, Hirth locks.
■: junction formation, o: repulsive interaction, x: crossed-state.
The thin lines represent the calculated boundary between attractive and repulsive states and the thick lines the calculated neutral condition for junction formation.

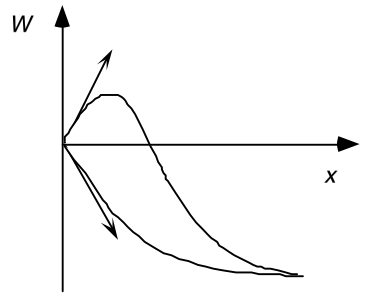

Figure 4. Schematic diagram of elastic energy (*W*) vs. reaction coordinate (*x*) for junction formation. A calculation of elastic energy predicts junction formation if the final state has a lower energy than the initial state. The initial slope yields the initial interaction force. If it is positive, the initially repulsive dislocation can reach the state of minimum energy only if they are able to overcome an energy barrier.

According to the forest model [2, 4], the strength of junctions is, in first approximation, inversely proportional to the length of the initial segments. It also exhibits a geometrical dependence on the angles (ϕ_1, ϕ_2), which is slightly anisotropic due to the orientation dependence of the line tension. One may note that the strength of a junction is by definition zero at the transition between junctions and other states, so that the periphery of the junction lobes corresponds to the weakest configurations. This strength diverges at the origin, since the two parallel lines are fully recombined. Indeed, the length of residual arms being zero, an infinite stress is required to unzip the junction. Assuming than the global strength of an interaction is mostly due to junctions and depends on the area enclosed by the junction lobes, we see that the glissile and Lomer junctions should have rather comparable strengths, whereas the Hirth lock, whose stability is due to the orientation-dependence of the line tension, is a rather weak obstacle. Many other details can be inferred from simple considerations. For instance the lobe of the glissile junction is elongated along the y-axis because the segment (2) is of edge character at $\phi_2 = \pi/2$. It has a high elastic energy, which favors junction formation.

Junctions in BCC Crystals

In bcc crystals, dislocations of Burgers vector 1/2<111> principally glide in {110} and {112} planes. Püschl [7], has classified the different types of interactions in the course of a detailed study of the stability of junctions in anisotropic elasticity. The reaction product is always found to be of the <100> type. For dislocations reacting in {110} planes and forming stable junctions, three different types of mapping configurations are obtained. By reason of symmetry it is sufficient to consider the interaction of a primary system, for example $1/2[111](\bar{1}10)$, with any other Burgers vector and the three slip planes that contain it, for example $1/2[1\bar{1}1](011)$, $1/2[1\bar{1}1](\bar{1}01)$ and $1/2[1\bar{1}1](110)$. One can easily check that in the first case, the [010] junction is sessile and of mixed character ($\boldsymbol{l}_j = [11\bar{1}]$). In the second case, it is also of mixed character ($\boldsymbol{l}_j = [111]$), but glissile in $(\bar{1}01)$. Wickham et al. [12] have studied the two related mappings. The third case is illustrated by Fig. 5-a; it corresponds to a sessile edge junction of line direction $\boldsymbol{l}_j = [001]$. Due to the multiplicity of additional reactions arising when {112} slip systems are accounted for, only one example is shown here (Fig. 5-b).

The qualitative considerations developed in the previous section also apply to the present case. From the viewpoint of junction stability, the main difference between fcc and bcc crystals resides in the higher energy of the reaction product in bcc crystals, since its Burgers vector squared is larger than that of the parent segments by a factor of 4/3. This results in smaller junction lobes, as compared to those of the glissile or Lomer junctions (cf. Figs. 3-a and 3-b).

At low temperature and in the presence of a lattice friction on screw dislocations, dislocation loops become elongated in the screw direction, which is that of the less mobile species. As plastic flow is mostly governed by the properties of screw dislocations, strain hardening essentially depends on the interactions between screw dislocations and the forest. Then, the mappings reduce to a set of horizontal and vertical data lines drawn for segments with screw orientation, from which one can deduce the characters of the forest dislocation lines that strongly interact with screw dislocations.

Finally, in bcc metals and at low temperature, the flow stress is a complex superposition of friction stress and forest density, and it is not proportional to the square root of the forest density as in fcc crystals [24]. A screw dislocation line pinned between two obstacles does not achieve equilibrium bowed-out shapes under increasing stress. Rather, the screw portions move forwards by the thermally assisted nucleation of kink-pairs. Thus, all the dislocation movements associated with junction formation and unzipping are sensitive to the applied strain rate or temperature and kinetic effects can no longer be ignored. In short, the mappings presented here are only meaningful in the absence of lattice friction, i.e., at high temperatures.

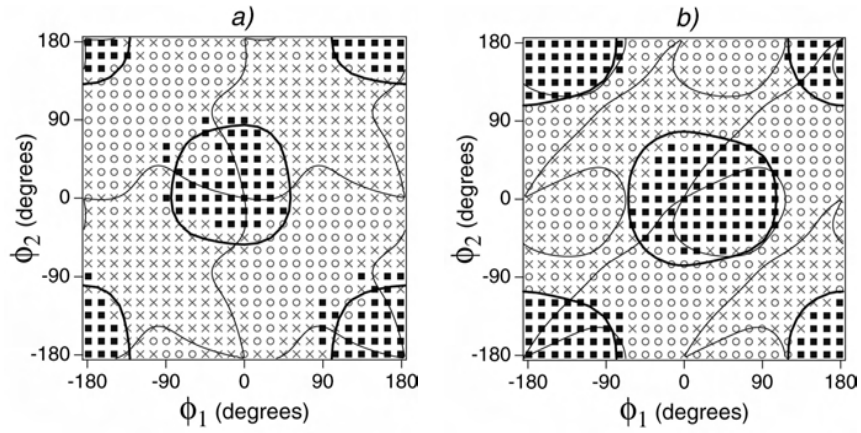

Figure 5. Mappings of dislocation intersections in the bcc structure. The symbols have same meaning as in Fig. 3. The length of the interacting segments is 1 µm. Slip system (1): $1/2[111](\bar{1}10)$. System (2) : (*a*) $1/2[1\bar{1}1](\bar{1}\,\bar{1}0)$, (*b*) $1/2[1\bar{1}\,\bar{1}](\bar{1}\,\bar{1}2)$.

THE COLLINEAR INTERACTION

To each slip system is associated a cross-slip system with same (collinear) Burgers vector; the two slip planes intersect along a line parallel to their common Burgers vector. The non-screw dislocations of each system play the role of forest obstacles with respect to the dislocations of the other system and their interaction is called the collinear interaction. Upon intersection, mutual annihilation of the lines can take place according to the reaction $\boldsymbol{b}_1 - \boldsymbol{b}_1 = 0$, which is equivalent to the formation of a highly stable junction with zero Burgers vector. A simulated sequence of collinear annihilation is shown in Fig. 6.

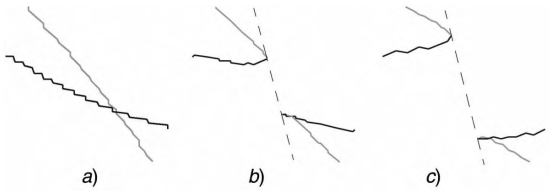

Figure 6. Simulation of collinear annihilation in the fcc structure. (*a*) – The initial configuration consists of two non-coplanar, attractive lines, of mixed character and with Burgers vectors of opposite sign. (*b*) – Annihilation takes place along the direction of intersection of the two slip planes (dashed line), which is parallel to $\boldsymbol{b}$. (*c*) - The final configuration is made up of two composite segments in equilibrium at double nodes along the intersection of the two slip planes.

For the collinear interaction in fcc crystals, there is only one type of mapping per Burgers vector. Figs. 7-a and 7-b, were obtained for segments of respective lengths 30 and 1 microns, respectively, in order to illustrate a length effect that is discussed below. If one considers the interactions of {110} and {112} slip systems in bcc crystals, there are three different

configurations for the collinear interaction: one only for the interaction between crystallographically equivalent slip systems and two between {110} and {112} slip planes, of which one is shown in Fig. 7-c.

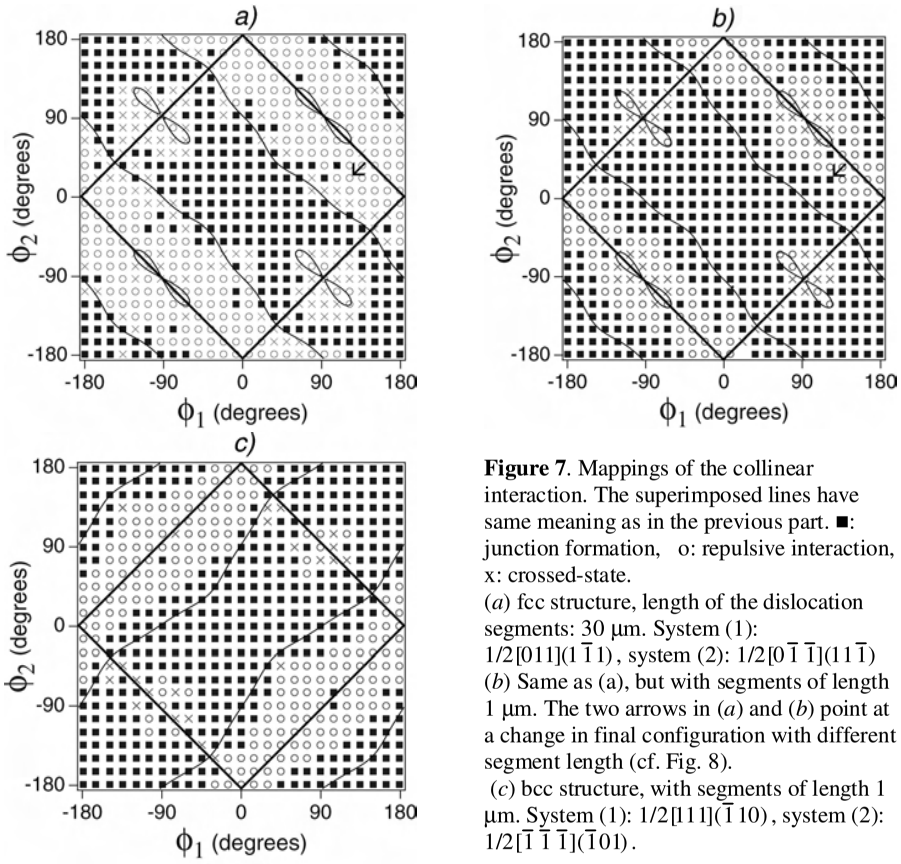

Figure 7. Mappings of the collinear interaction. The superimposed lines have same meaning as in the previous part. ■: junction formation, o: repulsive interaction, x: crossed-state.
(*a*) fcc structure, length of the dislocation segments: 30 µm. System (1): $1/2[011](1\bar{1}1)$, system (2): $1/2[0\bar{1}\bar{1}](11\bar{1})$
(*b*) Same as (a), but with segments of length 1 µm. The two arrows in (*a*) and (*b*) point at a change in final configuration with different segment length (cf. Fig. 8).
(*c*) bcc structure, with segments of length 1 µm. System (1): $1/2[111](\bar{1}10)$, system (2): $1/2[\bar{1}\,\bar{1}\,\bar{1}](\bar{1}01)$.

As in the previous part, predictions from the elastic theory of dislocations are superimposed to the simulation results. In contrast to the case of junctions, the total elastic energy is always reduced by the collinear annihilation, except along the singular lines $\phi_1 \pm \phi_2 = \pm\pi$. Along these lines, the two initial segments have same character and their projected line tensions exactly balance in projection along $\boldsymbol{l}_i$. Thus, the initial configuration is already in equilibrium. According to Kroupa's formula, the repulsive and attractive states are localized in parallel bands of same total area since half of the configurations are repulsive (or attractive). There are, in Figs. 7-a and 7-b, four small double lobes centered on the orientation $\phi_1 = \phi_2 = \pm\pi/2$, inside which the interaction changes sign. This orientation corresponds to non-interacting initial segments perpendicular to $\boldsymbol{l}_i$ and of edge character. The bcc mapping (Fig. 7-c) is rather similar, except that the boundary between attraction and repulsion no longer includes small localized domains where the interaction changes sign, but very flat local minima.

For long interacting segments (Fig. 7-a), the simplified elastic predictions are in very good agreement with the simulated results. The neutral states and crossed-states are localized near the singular lines and small lobes defined above. In contrast, with shorter segments length (Fig. 7-b, see also Fig. 7-c), the domain of collinear annihilation largely expands into the previous domain of neutral and repulsive states. The repulsive and neutral states are now localized around the regions of weak interaction and null energy balance. This predominance of collinear annihilations is due to the increased flexibility of the short dislocation lines, as induced by the logarithmic factor in the line tension [4, 15, 25]. This results in a reduction of the energy barrier opposing annihilation that is depicted in Fig. 4. Figure 8 illustrates this effect in the case of two initially repulsive straight lines. Thus, the average strength of the collinear interaction should be significantly larger than that of junctions, due to both the larger probability of occurrence of the reaction, as can be checked by comparing Figs. 3 and 7, and the higher stability of the final configuration. The interest of the collinear annihilation resides in the fact that it occurs in an athermal manner and induces annihilation events even in the absence of cross-slip. Other consequences of this interaction on dislocation microstructures and plastic flow will be discussed in a separate publication (Madec et al., submitted).

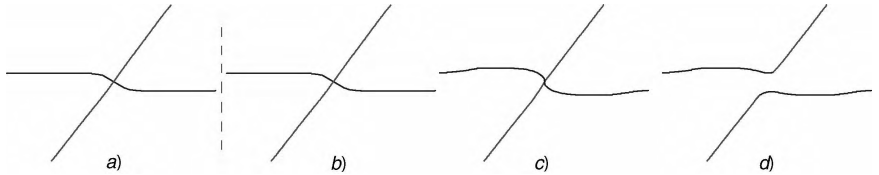

Figure 8. Interaction of two initially repulsive straight segments ($\phi_1 = 115°$, $\phi_2 = 22°$, see arrows in Figs. 7-a and 7-b). The configurations are seen along the slip plane of the horizontal line. (*a*) - With segments of length 30 µm, a stable repulsive state is obtained. (*b*) to (*d*) - With segments of length 1 µm, the saddle point associated with the repulsive interaction can be overcome owing to a smaller line tension. The dislocation lines are then able to reach their minimum energy configuration corresponding to mutual annihilation.

CONCLUDING REMARKS

The present study shows that DD simulations are well suited for predicting accurately the outcome of the interaction between two non-coplanar dislocation segments, in the absence of lattice friction. Checking the properties of these individual configurations is, in fact, a mandatory step, preliminary to any attempt at a quantitative investigation of forest hardening.

Although the present work was performed in isotropic elasticity, there are two manners to

perform a more refined treatment in anisotropic elasticity. An approximate procedure, which should capture most of the effects of anisotropy, consists in simply tabulating the anisotropic local line tension in DD simulations. Rigorous solutions can be obtained through the use of coupled DD and Finite Element codes. An illustration of the use of both methods can be found in [26].

The mappings presented here were obtained in the absence of applied stress. They are necessarily modified in the presence of an applied stress, from which one can infer for instance which types of junctions are unzipped the most easily. However, as the flow stress of a crystal depends on complex averages over individual configurations that are less simple than the symmetrical ones examined here, the question of forest hardening can be treated quantitatively only by performing mass simulations on large dislocation densities [15].

A detailed study of the collinear annihilation has been presented at the scale of individual configurations, showing that the annihilation of dislocations gliding in slip and cross-slip systems can occur easily and in an athermal manner. As this interaction leads to extremely stable reaction products, it has a significant impact on microstructures and flow properties (Madec et al., to be published). Its study also reveals a strong influence of the average length of the interacting lines through line tension effects. This effect also manifests itself on all the critical stresses for remobilizing dislocations segments blocked after a reaction. It is in no way negligible if one considers that the average dislocation density and segments length evolve by orders of magnitude along a stress-strain curve.

ACKNOWLEDGEMENTS

The authors would like to thank Drs. Thierry Hoc and Ghiath Monnet for helpful discussions and contributions to the present work. RM gratefully acknowledges the support of the Centre Européen de Calcul Atomique et Moléculaire (CECAM).

REFERENCES

1. G.I. Taylor, *Proc. Roy. Soc. A* **145**, 362 (1934).
2. G. Saada, *Acta Metall.* **8**. 841 (1960).
3. J. Friedel, 1967, *Dislocations* (Pergamon Press, 1964), p. 43.
4. G. Schoeck and R. Frydman, 1972, *Phys. Stat. Sol. (b)* **53**, 661 (1972).
5. W. Püschl, R. Frydman and G. Schoeck, *Phys. Stat. Sol. (a)* **74**, 211 (1982).
6. L. Dupuy and M. Fivel, *Acta Mat.* **50**, 4873 (2002).
7. W. Püschl, *Phys. Stat. Sol.* **90**, 181 (1985).
8. W. Püschl, *Phil. Mag. Lett.* **80**, 199 (2000).
9. W. Püschl and G. Schoeck, *Crystal Res. and Technology* **19**, 303 (1984).
10. V.V. Bulatov, F.F. Abraham, L.P. Kubin, B. Devincre and S. Yip, *Nature* **391**, 669 (1998).
11. D. Rodney and R. Phillips, *Phys. Rev. Lett.* **82**, 1704 (1999).
12. L.K. Wickham, K.Schwarz, and J.S. Stölken, Phys. Rev. Lett. **83**, 4574 (1999).
13. V.B. Shenoy, R.V. Kukta and R. Phillips, *Phys. Rev. Lett.* **84**, 1491 (2000).
14. C. Shin, M. Fivel, D. Rodney, R. Phillips, V.B. Shenoy and L. Dupuy, *J. Phys IV* (France) **11**, 19 (2001).
15. R. Madec, B. Devincre and L.P. Kubin, *Phys. Rev. Lett.* **89**, 255508 (2002).
16. L.P. Kubin, G. Canova, M. Condat, B. Devincre, V. Pontikis and Y. Bréchet, *Solid State Phenomena* **23-24**, 455 (1992).
17. B. Devincre and L.P. Kubin, 1997, *Mat. Sci. Eng. A* **234-236**, 8 (1997).
18. R. Madec, B. Devincre and L.P. Kubin, *Scripta Mater.* **47**, 689 (2002).
19. R. Madec, B. Devincre and L.P. Kubin, in *Multiscale Modeling of Materials – 2000*, ed. L.P. Kubin, R. Selinger, J.L. Bassani and K. Cho (Materials Research Society, 2000), Symposium Proceedings Vol. 653, p. z1-8.
20. R. Madec, *Ph.D. Dissertation*, University of Orsay (2001).
21. R. Madec, B. Devincre and L.P. Kubin, 2002c, *Comp. Mater. Sci.* **23**, 219 (2002).
22. F. Kroupa, 1961, *Czech. J. Phys. B* **11**, 847 (1961).
23. J. Hirth and J. Lothe, *Theory of Dislocations* (Krieger, 1982), p. 123.
24. M. Tang, B. Devincre, and L.P. Kubin, *Model. Simul. in Mat. Sci. Eng.* **7**, 893 (1999).
25. S.J. Basinski and Z.J. Basinski, in: *Dislocations in Solids*, ed. FRN Nabarro (North Holland, 1979), Vol. 4, p. 261.
26. S. Groh, B. Devincre, L. Kubin, A. Roos, F. Feyel and J.-L. Chaboche, *Phil. Mag. Lett.*, **83**, 303, 2003.

Modelling Simul. Mater. Sci. Eng. **7** (1999) 893–908. Printed in the UK PII: S0965-0393(99)05406-6

Simulation and modelling of forest hardening in body centre cubic crystals at low temperature

M Tang†, B Devincre‡ and L P Kubin‡

† Lawrence Livermore National Laboratory, PO Box 808, L-415, Livermore CA 94550, USA
‡ LEM, CNRS-ONERA, 29 Avenue de la Division Leclerc, BP 72, 92322 Châtillon Cedex, France

Received 15 February 1999, accepted for publication 17 June 1999

Abstract. In body centred cubic (bcc) crystals at low temperatures, the thermally activated motion of screw dislocations by the kink-pair mechanism governs the yield properties and also affects the strain hardening properties. In this work, the average strength of dislocation junctions is derived and numerically estimated in the case of Nb and Ta crystals. This allows us to extend an existing simulation of dislocation dynamics in bcc crystals to the case of the motion of a screw dislocation line through a random distribution of forest obstacles. Numerical results are presented in the case of Ta crystals and at two temperatures, 160 K and 215 K. They are complemented by a simple model that applies quite generally to bcc metals at low temperatures. It is shown that forest hardening is made up of two contributions, a free-length effect that depends on the length of the mobile screw segments and whose dependence on forest obstacle density is logarithmic and a line tension effect linearly proportional to the obstacle density. As a result of the thermally activated character of screw dislocation mobility, the relative weight of the two contributions to forest hardening depends on the temperature and strain rate.

1. Introduction

In face centred cubic (fcc) crystals, the hardening due to forest dislocations intersecting the glide planes of mobile dislocations is governed by the formation and unzipping of attractive dislocation junctions [1, 2]. This process is naturally described in terms of line tension and obstacle strength [3]. The average distance between forest obstacles, defined as the inverse of the square root of the forest density, is then found to be inversely proportional to the external stress (see e.g. [4] for an extended review and discussion). The forest density is essentially a density of stored dislocations and, as a consequence, the strain dependence of strain hardening is governed by storage and recovery rates [5].

In body centred cubic (bcc) crystals, the strain hardening properties can be treated in a very similar manner in the high-temperature domain, i.e. in the temperature range above the so-called 'athermal temperature', T_a. In this domain, the usual relationship between the stress and the square root of the dislocation density holds [4], the stress–strain curves exhibit the usual three-stage hardening behaviour and a dislocation cell structure is formed in multiple slip conditions. At low temperatures, the particular core properties of screw dislocations induce a thermally activated mobility (cf [6] and the recent review [7]). A strongly temperature-dependent effective stress, substantially larger than the athermal stress for dislocation junction unzipping, is then needed to move the screw dislocations by the kink-pair mechanism. In a transition range ($T_c < T < T_a$ where T_c is the critical temperature), the two stress values

ble and a mixed regime combining kink pair formation and forest hardening in a nner is obtained (see [6] for more detail).

follows, numerical estimates will be given in the case of tantalum, for which . and $T_c = 380$ K [6]. The temperature domain below T_c is the concern of the y. In this temperature range, line tension effects no longer govern the flow stress, torage is not effective until large strains [8], the spatial distribution of dislocations id the stress–strain curves adopt a pseudo-parabolic shape. Several questions can d. What are the mechanisms of strain hardening? Is the relation between stress ensity the same as in fcc crystals? Is it still possible to decompose the external e sum of a lattice friction on screws and of a forest hardening?

ective of the present work is to answer these basic questions through simple of model configurations. While strain hardening is a three-dimensional (3D) st of its basic mechanisms can be understood with the help of two-dimensional odels as exemplified by several studies on fcc crystals (cf e.g. [9–11]). Thus, rest hardening' here refers to the hardening recorded when a dislocation line is gh random distributions of obstacles with increasing density. The simulation of dynamics in bcc crystals used in the present work is the same as the one used s study [6]. In section 2, junction properties are introduced into the simulation d. In section 3, the simulation results are presented. A geometrical relationship, ne base of all strain hardening models in bcc crystals at low temperatures [12, 13], ly checked. Next, forest hardening is investigated as a function of the density of ection 4 is devoted to the analysis and modelling of these results. Two mechanisms contribute to hardening, which have both been discussed in earlier studies. One the influence of the free length of the screw segments on their velocity [12], due to line tension effects [13]. The contributions of these two mechanisms to ning are estimated as a function of the density of forest obstacles and temperature. antitatively compared to the simulated results. Finally, the concluding section 5 he present lack of experimental data on dislocation densities at low temperatures s a few additional effects involved in the relation between forest hardening and ning.

strength in bcc metals

ion of dislocation dynamics in bcc crystals

ion dynamics (DD) simulation of bcc crystals is based on the 'edge-screw' model ne dislocation configurations are decomposed into successive edge and screw at move in a discretized lattice. The latter has same symmetry elements as the rystal, which allows one to include the slip geometry. The lattice parameter is ew nanometres, thus delimiting a boundary between the elastic properties of the and contact or core properties. The former are conveniently treated within an otropic continuum, while the latter are accounted for by introducing local rules in n. In bcc crystals at low temperatures, the screw segments tend to align themselves se-packed $\langle 111 \rangle$ directions of their slip planes. In the simulation, this property mobility rules. The thermally activated motion of screw dislocations over the is described by an Arrhenius form, which is numerically fitted to the yield stress erature dependence of pure Ta crystals

$$v \propto L \exp - \left(\frac{\Delta H(\tau^*)}{kT} \right) \tag{1}$$

where ΔH is the activation enthalpy for kink-pair formation, τ^* is the effective stress, k is the Boltzmann constant, T is the absolute temperature and L is the length of the screw segments. Other quantities entering the prefactor are discussed in [6]. The non-screw portions of the dislocation lines have a glissile core structure and a mobility comparable to that of dislocations in fcc crystals, which is orders of magnitude larger than that of the long screw segments. A convenient simplification consists, then, of not accounting for their free-flight time between two obstacles. While this approximation greatly enhances the efficiency of the DD simulation by allowing use of large time steps (10^{-2} s), it limits its domain of validity to the domain of low temperatures, i.e. below the critical temperature T_c. More detail on the DD simulation of bcc crystals and on its application to deformation in single glide conditions can be found in [2, 6]. The numerical conditions used in the present work are given in section 3.

Due to the particular geometry of the dislocation configurations in bcc metals at low temperatures (cf figure 1), the treatment of line tension requires some care. The bent portions of the dislocation lines immobilized at forest obstacles are produced by the piling up of elementary kinks. They can be treated in a simple manner (cf section 2.3) provided that the critical conditions for junction destruction are adequately implemented. For the long screw dislocation lines, a more refined treatment is needed as their line tension properties contribute to forest hardening (cf section 4). Since no approximation based on the local curvature can be used, the line tension stress is derived from the gradient of the elastic self-energy. The expression implemented in the simulation and further used in the model discussed in section 4 is similar to the one used for the treatment of dislocations in silicon crystals [16]. This expression was first derived by Devincre and Condat [17] from an expression for the self-energy obtained by de Wit [18]

$$\tau_{\Gamma s} = -\frac{k\mu b}{L} \tag{2a}$$

with

$$k = \frac{1}{4\pi(1-\nu)}\left[\ln\left(\frac{2X_1}{b}\right) + \ln\left(\frac{2X_2}{b}\right) + \frac{3-2\nu}{2(1-\nu)}\right] \tag{2b}$$

where L is the length of the screw segment and X_1 and X_2 are the lengths of the two segments adjacent to the screw dislocation line, which are of edge character, μ and ν are respectively the shear modulus and Poisson ratio, and b is the modulus of the Burgers vector.

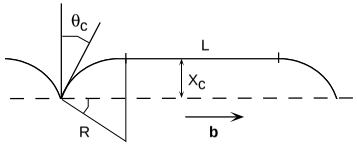

Figure 1. Schematic drawing of the critical configuration of an initial screw dislocation line pinned at its ends by two junction-forming forest obstacles in a bcc metal at low temperature.

2.2. Junction strength

The way junctions are implemented into DD simulations has been extensively discussed in a recent publication [2]. When two dislocation segments moving in non-coplanar slip planes intersect each other, a junction is formed if the Frank criterion, involving a comparison of the Burgers vectors squared before and after reaction, is fulfilled. A sessile segment is then introduced, whose destruction occurs when the work of the local stress τ_u applied to one arm of the parent dislocations, of length ℓ_u, is sufficient to unzip the junction. If the formation

energy of the latter is W_j per unit length, one has $W_j = \tau_u b \ell_u$, where b is the modulus of the Burgers vectors of the parent dislocations. The total energies are obtained by multiplying both sides of the expressions by the junction length ℓ_j. The formation energy can be written in the reduced form $W_j = \beta\mu b^2$, where β is a dimensionless material constant describing the 'junction strength'. Then

$$\beta = \frac{\tau_u \ell_u}{\mu b}. \tag{3}$$

In fcc crystals, the length of the unzipping arm, ℓ_u, depends on the forest density through $\ell_u \propto \rho_f^{-1/2}$, hence the local stress and, by extension, the flow stress are proportional to the square root of the forest density.

In bcc crystals at low temperatures, the dislocation structures formed during plastic deformation are quite anisotropic due to the lack of mobility of the screw dislocations. As a result, the density of mobile dislocations essentially consists of straight segments of screw character, locally pinned by junctions formed with strong forest obstacles. The energetically favourable reaction of two dislocations with Burgers vector $\frac{1}{2}\langle 111\rangle$ produces, in general, a junction with $\langle 100\rangle$ Burgers vector [19–21]. The typical configuration of a screw dislocation line gliding past forest obstacles is schematically depicted in figure 1. In contrast to fcc crystals, the screw dislocation line is not immobilized as a whole by the pinning points. It continuously moves, producing elementary kinks that accumulate near the junctions, thus forming two curved lines of non-screw character. Junction breaking occurs when a critical angle θ_c is reached, which corresponds to a certain critical distance X_c for the thermally activated motion of the screw segment. Due to the fact that the two bent segments near the forest obstacle are connected by a straight screw segment, the mobility of screw dislocations participates in the hardening process. As a consequence, forest hardening is likely to be temperature and strain-rate dependent.

In such conditions, it is more convenient to describe the junction strength using the critical distance X_c rather than the length of the unzipping arm, ℓ_u. Indeed, X_c/b is the number of kinks nucleated when the junction unzips. As can be seen from figure 1, ℓ_u is simply the length of a bent non-screw segment. If R is the curvature radius of the latter, simple geometrical considerations (cf figure 1) lead to $\ell_u = R(\pi/2 - \theta_c)$ and $X_c = R(1 - \sin\theta_c)$. By eliminating the curvature radius between these two expressions, one obtains a simple scaling relation

$$\frac{\ell_u}{X_c} = \frac{\pi/2 - \theta_c}{1 - \sin\theta_c} \tag{4}$$

and (3) can then be rewritten in a form that does not depend on the details of the local geometrical configuration

$$\beta' = \frac{\tau_u X_c}{\mu b}. \tag{5}$$

In the following, the junction strength will be defined by the coefficient β'. As the critical distance X_c is not directly related to the forest density, the constancy of the obstacle strength no longer entails a simple relation like the one found in fcc crystals.

The destruction of a junction then occurs when the distance travelled by a screw segment reaches the critical value X_c given by (5). To implement this rule, the simulation must be able to track the instantaneous height of the bowed-out portions of the dislocation lines (cf figure 1), which is not possible if the latter are made up of several discrete segments. Thus, no line tension is applied to the non-screw segments, so that the latter agglomerate into one single edge segment whose length is measurable. The resulting configurations are shown in figure 2 and correspond to the typical approximation of low-temperature behaviour, as discussed in section 4.1.

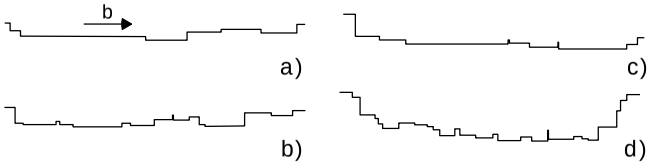

Figure 2. Typical configurations of the mobile dislocation line interacting with forest obstacles. (a) $T = 160$ K, $\rho_f = 10^{12}$ m^{-2}; (b) $T = 160$ K, $\rho_f = 2.4 \times 10^{12}$ m^{-2}; (c) $T = 215$ K, $\rho_f = 0.8 \times 10^{12}$ m^{-2}; and (d) $T = 215$ K, $\rho_f = 2.41 \times 10^{12}$ m^{-2}. A magnification by a factor of 5 was applied along the direction of propagation of the lines. This allows one to observe some end effects at large densities due to the piling up of macrokinks at the boundaries of the slip area. The latter are treated as strong obstacles.

Table 1. Calibration of the junction strength β' in Nb single crystals, according to equation (3) of the text. The values of the critical distance X_c at three temperatures are extracted from *in situ* T.E.M. measurements [12]. The corresponding stress values are taken from Christian [22].

	Temperature T (K)		
	110	180	230
X_c^{Nb} (10^{-2} μm)	2.93	6.83	15.6
τ (MPa)	157	68.5	28.5
β'	0.435	0.442	0.42

2.3. Calibration of junction strength

In the absence of theoretical or *ab initio* data on junction strength in bcc crystals, a calibration has to be performed with respect to experimental measurements. For this purpose, we base ourselves on one set of measurements of the critical distance X_c that was performed by Louchet *et al* [12] in niobium crystals by *in situ* deformation in a high-voltage electron microscope. The values measured at three different temperatures are reproduced in table 1. The corresponding resolved yield stress values of Nb crystals shown in table 1 are extracted from a review article by Christian [22] (cf in figure 3(b) of [22] the data for the purest crystals). To compute the value of the junction strength β' at each temperature we make use of (5) with $\mu_{Nb} = 37$ GPa and $b_{Nb} = 0.286$ nm. As can be seen from table 1, β' is indeed found to be a constant ($\beta' \approx 0.43$) between 110 K and 230 K. This justifies the way the average junction strength is treated in the DD simulation and provides a numerical value for the case of niobium crystals. Equation (5) can also be applied to a continuously curved dislocation line bowing out between two forest obstacles in a fcc crystal. For copper crystals, making use of the numerical values discussed in [2], one obtains a value much smaller than the one derived for niobium: $\beta'_{Cu} \approx 0.12$. This apparent difference between the junction strengths of fcc and bcc crystals certainly deserves further examination.

It should be noted that one has to be careful not to use (5) as a scaling law to derive the junction strength in other bcc crystals. For instance, Ta and Nb have same lattice parameter and a ratio of shear moduli $\mu_{Ta}/\mu_{Nb} = 1.89$. According to table 1, the yield stress of Nb crystals is 160 MPa at 110 K and a scaling by the shear modulus would predict a yield stress of 300 MPa for Ta crystals. This value is, however, larger than the yield stress of Ta crystals at 0 K, which is of the order of 250 MPa [6, 23, 24]. This discrepancy is obviously due to differences in the core structure of the screw dislocations in the two crystals, possibly also to

the fact that we make use here of isotropic elasticity (the coefficient of elastic anisotropy of Nb is 0.5 and that of Ta 1.56).

As the bcc crystal investigated here is tantalum, we perform a scaling via strain hardening coefficients measured in the high-temperature domain, taking advantage of the fact that the junction strength is a material constant. According to Wässerbach [24], the maximum work hardening coefficient at the end of stage II is $\mu/550$ for Nb and $\mu/620$ for Ta crystals (cf figure 10 of [24]). As these values should be directly proportional to the strength of forest obstacles, we have $\beta'_{Ta} = \beta'_{Nb} 550/620 = 0.38$ for Ta crystals.

3. Simulation of forest hardening

3.1. Simulation conditions

A dislocation line initially of screw character and Burgers vector $a/2[111]$ was moved in a $(10\,\bar{1})$ slip plane through a random distribution of forest trees with Burgers vector $a/2[\bar{1}\,11]$, mobile in (101) slip planes. As in [6], {110} slip was assumed for convenience, in the absence of a realistic input predicting the nature of the active slip system [8]. The present results would not be modified, however, if slip was assumed to occur in the equally frequent {112} planes (in the soft twinning sense). Since the dislocation microstructures found in bcc metals deformed at low temperature mostly consist of screw dislocation lines, the forest obstacles were taken of screw character. The size of the simulation box was $(100\ \mu\text{m})^3$ and the slip plane considered was the one going through the centre of the simulation cube. In this plane, a slip area of size $84.18 \times 59.5\ \mu\text{m}^2$ was defined and the length of the mobile segment was initially $L_0 = 84.18\ \mu$m. As shown in (1), the stress against velocity law of the screw segments includes a linear dependence of the velocity on the free-length of the considered segment. In the following, this 'free-length' effect is occasionally relaxed in order to check its influence on hardening. This is performed by setting $L = L_0$ in (1). A constant strain rate was applied along the $[\bar{4}\,8\,19]$ easy glide direction (Schmid factor 0.49 on the active slip system) in order to immobilize the forest dislocations. The applied strain rate was 7.5×10^{-8} s^{-1}. With such a value, the velocity of the single mobile segment (typically 3 μm s^{-1}) is comparable to the velocities achieved in real crystals or 3-D simulations, which involve larger mobile densities and applied strain rates [6]. By doing so, the recorded flow stresses are also in the range obtained in 3-D. The material constants were those of Ta: $b = 0.286$ nm, $\mu = 68.5$ GPa, $\nu = 0.38$.

The total number of forest obstacles N_f was varied in the range from 4×10^3 to 1.2×10^4. To fix the ideas, these values can be converted into equivalent dislocation densities through the relation $\rho_f = N_f/A_0$, where A_0 is the slip area. Then $N_f = 10^3$ corresponds to a density $\rho_f = 2 \times 10^{11}$ m^{-2}. Values of the forest density that are too small lead to large statistical fluctuations and to end effects on the screw segment. This sets a lower limit to the number of obstacles, 4×10^3, corresponding to about 14 simultaneous pinning events along the mobile line, thus limiting the fluctuations on the free-length of the screw segments (cf figure 4(b)). The upper limit stems from the fact that with large obstacle densities, the predominant screw character of the dislocations is no longer preserved and bcc crystals enter a transition range similar to that observed at high temperatures. In order to check a possible dependence of forest hardening on temperature, two temperature values were selected, 160 K and 215 K. The junction strength was implemented as discussed in the previous section. The critical values of X_c were defined from (5) and allowed to evolve according to the local stress. In fact, the simulation tends to yield average values of X_c overestimated by a constant factor for two reasons. There is an overshooting of the critical positions because a dislocation line can only stop at the end of a time step. In addition, the coalescence of sliding macro-kinks with

immobile kinks may produce junction unzipping with a total macro-kink height larger than X_c. This defect is taken into account and corrected in the modelling part.

Figure 2 shows typical shapes of the mobile dislocation line interacting with forest obstacles at the two temperatures investigated and with two different obstacle densities. A magnification was applied along the $[1\bar{2}1]$ propagation direction, in order to better illustrate the increase of the line roughness with increasing obstacle density and increasing temperature.

3.2. Results

Figure 3 shows the stress against time step curves recorded at 160 K and 215 K for different values of the equivalent forest density. The average stress levels are different at the two temperatures, as screw dislocations become less and less mobile as temperature decreases. In comparison to the high yield-stress values, forest hardening seems rather modest. However, a reference stress value has to be defined, which is carried out below, to allow for a precise measurement of forest hardening.

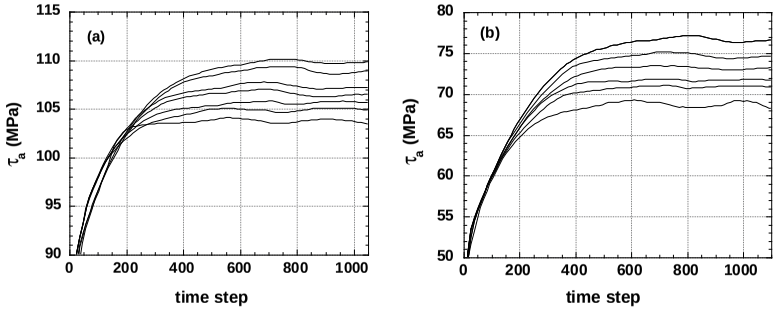

Figure 3. Flow stress against number of time steps at constant strain rate (7.5×10^{-8} s^{-1}) for different forest dislocation densities. (a) $T = 160$ K, the forest dislocation densities (in units of 10^{12} m^{-2}) are, from bottom to top, 1.0, 1.21, 1.4, 1.61, 1.8, 2.2, and 2.4. (b) $T = 215$ K. The forest dislocation densities are, from bottom to top, 0.8, 1.2, 1.4, 1.6, 2.0, and 2.4.

Figure 4(a) shows the free-length of the mobile segments in steady state, L, averaged at each time step, as a function of time step and for different forest obstacle densities at 160 K. After a transient during which the strain rates reach the imposed value, the average free-lengths reach stable values. The latter are plotted in figure 4(b) as a function of obstacle density for the two temperatures investigated. The free-length decreases with increasing density of obstacles, as expected, and with increasing temperature or decreasing stress. This is expected too, since the relative densities of edge and screw segments must increase with increasing temperature. These dependences can be rationalized in a simple manner, making use of a simple geometrical relation that was derived in [12] and is discussed in detail in section 4.1. In essence, this relation expresses that the area LX_c associated with one critical unzipping event is equal to the average area associated with one forest obstacle $1/\rho_f$ (figure 1 and (6), below). It must be noted that unzipping may occur either by the motion of a screw segment reaching its critical distance or by the sliding of a macro-kink. As a consequence, junctions can be formed either on the long screw segments or on the sliding macro-kinks.

The check of this geometrical relation is presented in figure 5 where the quantity LX_c is plotted as a function of $1/\rho_f$ for the two temperatures investigated, with and without the

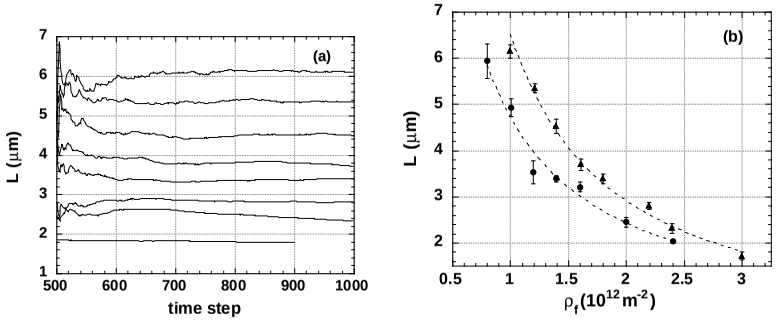

Figure 4. (a) Time-averaged mean screw-dislocation length against the number of time steps at 160 K. The corresponding densities (in units of 10^{12} m^{-2}) are, from top to bottom, 1.0, 1.21, 1.40, 1.61, 1.8, 2.2, 2.4 and 3.0. The curve for the largest density is terminated early, a segment having reached the boundary of the slip area. Nevertheless, the steady-state rate is reached and good statistics are obtained. (b) Averaged screw-dislocation length against forest dislocation densities at 160 K (full triangles) and 215 K (full circles). Broken curves are to guide the eyes.

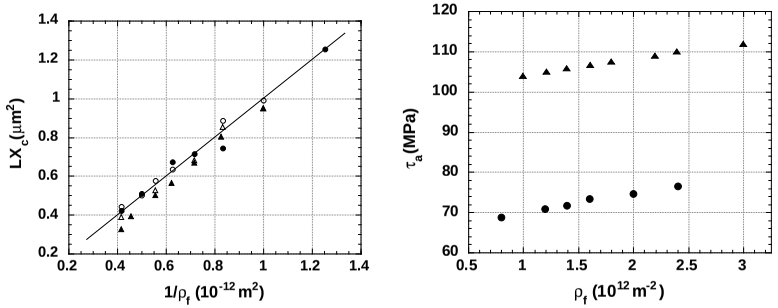

Figure 5. Plot of LX_c against $1/\rho_f$. The values of L are the time-averaged mean screw-dislocation lengths obtained from the simulations with and without length effect (see text for detail). The X_c values are obtained from the simulations directly. Full and open symbols correspond respectively to data points with and without the length effect. Triangles are for data at 160 K and circles are for data at 215 K. The solid line represents the relation $LX_c = 1/\rho_f$.

Figure 6. Flow stress against forest dislocation densities at 160 K (full triangles) and 215 K (full circles).

free-length effect on screw-dislocation velocity. The predicted geometrical relationship (cf equation (6)) between the three quantities L, X_c and $1/\rho_f$ is perfectly checked. Another quantity of interest is the ratio of the respective contributions of screw and non-screw segments to the total strain or strain rate. Although the non-screw segments are in small density (cf figure 2), they achieve very large velocities (actually infinite velocities in the simulation, as discussed in section 2.1). It has been predicted that at low temperature the two contributions to the strain rate should be of same order, irrespective of the forest obstacle density [12].

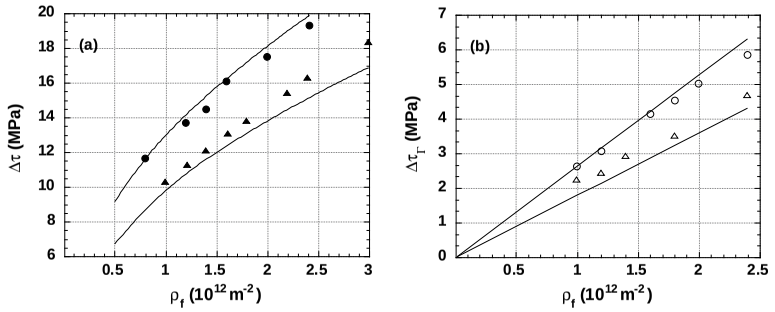

Figure 7. Forest hardening (i.e. flow-stress increment with respect to the reference state) against forest dislocation densities at 160 K (triangles) and 215 K (circles). The full lines correspond to the predictions of the model discussed in section 4. (a) Total hardening with length effect included. (b) Line tension hardening, $\Delta\tau_\Gamma$, obtained without length effect.

This is essentially a consequence of the fact that whenever a junction is unzipped by a moving screw segment, a macro-kink is liberated that travels, on average, a free-flight distance L (cf section 4.1). This prediction was checked and the two contributions were never found to statistically depart from each other by more than 20%.

Figure 6 shows the variation of the flow stress against the density of forest obstacles at the two temperatures investigated. Actually, such a plot is misleading. The reason is that the contribution of forest hardening to the flow stress in not directly related to the effective stress, since the latter is governed by a different mechanism. Indeed, it is not the flow stress but the difference between the flow stress and the yield stress that reflects the effect of forest obstacles. Hence, in order to estimate the forest hardening, one has to define a reference stress value in the absence of forest density. The corresponding reference state was defined as that of the long dislocation line ($L_0 = 84\ \mu$m) moving in an obstacle-free slip area. In such conditions, the measured stress levels are 93.6 MPa and 57.3 MPa at 160 K and 215 K, respectively. Identical values were calculated from the Arrhenius form giving the strain rate as a function of stress and temperature (cf [6] for more detail).

Forest hardening could then be estimated and is plotted in figure 7(a) as a function of the forest density for the two temperatures investigated. Figure 7(b) shows the hardening obtained without the free-length effect on dislocation velocities. It clearly appears that two different mechanisms contribute to forest hardening. One stems from a 'free-length effect': an increased obstacle density reduces the average length of the screw segments, thereby reducing their velocity and increasing their effective stress. The second contribution is a line tension effect on the screw segments (cf (2) and next section). The exact dependence of these two contributions on forest density is not easy to assess, due to the small range of densities accessible to the numerical experiment. However, one can notice that in figure 7(b) the extrapolations of the numerical data, to a good approximation, pass through the origin. Since the reference state was defined in an independent manner, this indicates that the line tension contribution to hardening is likely to be linearly dependent on forest obstacle density. The length effect must then have a different dependence (actually a logarithmic one, as shown below), since the linear back extrapolation of the total hardening to zero obstacle density does not pass through the origin.

4. The modelling of forest hardening

In this part, the hardening $\Delta\tau$ produced in bcc crystals by a density of forest obstacles is calculated. In the case of low temperatures, as considered here, some simplifications can be made. The length of the screw segments is much larger than that of the non-screw segments pinned at the forest obstacles (i.e. $X_c \ll L$). In addition, the effective stress on screw dislocations contributes to the major part of the flow stress and the forest hardening is comparatively small (i.e. $\Delta\tau < \tau_a$). The long-range elastic stresses on dislocations are neglected since they statistically average out to zero in the absence of a self-organized microstructure.

4.1. Geometrical configuration in a steady state

A steady-state argument [12] allows one to establish a relation between the density of forest obstacles and the average values of the two geometrical parameters, the critical distance X_c and the length of the screw segments L. In a steady state, the number of junctions present along the moving dislocation line is constant, so that every time a junction is destroyed another is formed. Whenever a junction is destroyed, a dislocation segment of either screw or non-screw character moves until it meets another forest obstacle, thus sweeping a certain area. It follows from the steady-state argument that this area is, in both cases, the same as the one associated, on average, with one forest obstacle, $1/\rho_f$. As illustrated by figure 8, this process can occur in two different manners. The area A_s swept by a screw segment during its interaction with the obstacles can be visualized from figure 1. This area can be decomposed into two terms, one stemming from the area below the screw line, LX_c, the other corresponding to the area under the bowed-out segments. While an exact calculation of A_s can easily be performed [13], the former contribution to the swept area largely dominates in the temperature range considered here. Indeed, when the temperature decreases and when the stress increases, the average length of the screw segments increases while the area below the bowed-out segments becomes negligible. Then, $A_s = LX_c$.

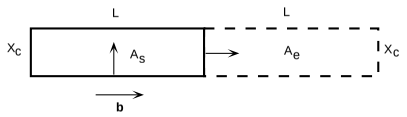

Figure 8. The average area LX_c associated with one junction-unzipping event (schematic). This area can be considered as being swept by one screw segment of length L moving a distance X_c or, alternatively, by a macro-kink of height X_c sliding over a distance L.

When a junction is destroyed, a macro-kink is produced, which slides with a high velocity, annihilates the screw dislocation line and creates a new segment of screw character. The moving macro-kink can be blocked by a forest obstacle and form a junction, or it can be recombined or annihilated at other bowed-out segments. This corresponds to a second contribution to the total strain through the swept area A_e. The steady-state argument implies that A_e is also, on average, the area associated with one forest obstacle, $1/\rho_f$ [12] (cf figure 8). Hence, we have $1/\rho_f = A_e = A_s$ and

$$LX_c = 1/\rho_f \tag{6}$$

This geometrical relation should hold irrespective of temperature and was checked from *in situ* experiments [12]. The present simulations confirm this result (cf figure 5) and confirm that the areas A_e and A_s yield practically identical contributions to the total strain (cf section 3.2).

The local stress inducing the curvature of the non-screw segments (cf equation 5) can be assimilated to the external stress τ_a. This is fully justified at low temperature since the elastic interaction stresses do not significantly contribute to the flow stress. It follows that the average length of the screw segments, L, is governed by the obstacle density and by the critical distance, the latter depending on both the junction strength and the applied stress. Moreover, the value of L is also related to the effective stress on the screw segments through the rate equation (1) describing the mobility of the latter.

4.2. Rate equation

The total length of a dislocation line, of initially screw character, propagating through the forest obstacles can, in practice, be considered as a constant, irrespective of the density of the forest. This is equivalent to assuming low-temperature conditions such that most of the mobile density is of screw character. In addition, the contribution of non-screw and screw dislocations to the total strain rate is a constant and of the same value as shown by the simulations (section 3.2). Then, it is equivalent to impose either the total strain rate, or the global velocity of the dislocation line or the velocity of individual screw segments of average length. In the Arrhenius rate equation (1), the effective stress on screw dislocations is the algebraic sum of the applied stress and of the line tension stress as given by (2), $\tau^* = \tau_a + \tau_\Gamma$ (notice that the line tension stress is in fact negative). Since the line tension stress is a small contribution to the flow stress, the activation energy can be expanded in the form

$$v_a \propto L \exp\left(-\frac{\Delta H(\tau_a)}{kT}\right) \exp\left(\frac{\tau_{\Gamma_s}}{S}\right) \tag{7}$$

where S is the strain rate sensitivity ($S = kT/V$, where V is the corresponding activation volume for kink-pair formation, cf [6]).

4.3. Forest hardening

The hardening due to a forest density ρ_f can be estimated by comparison with the reference state discussed in section 3.2. The latter is an approximation of the obstacle-free crystal with a large free-length of the screw segments L_0. The corresponding line tension stress is then small and it can be neglected. Denoting by τ_{a0} the reference stress, we have

$$v_a \propto L_0 \exp\left(-\frac{\Delta H(\tau_{a0})}{kT}\right) \tag{8}$$

Combining (7) and (8), we obtain

$$\frac{\Delta H(\tau_a) - \Delta H(\tau_{a0})}{kT} = \ln\left(\frac{L_0}{L}\right) - \frac{\tau_{\Gamma s}}{S}. \tag{9}$$

Various coefficients entering the prefactor of the Arrhenius equation vanish, so that it is not necessary to consider their possible stress dependence. This expression can be simplified by expanding the activation enthalpies around the reference value, thus defining a hardening $\Delta\tau = (\tau_a - \tau_{a0})$. With the line tension stress being given by (2*a*), we eventually obtain

$$\Delta\tau = S_0 \ln\left(\frac{L_0}{L}\right) + k\frac{\mu b}{L}. \tag{10}$$

Here, it was assumed that the strain rate sensitivity S does not significantly differ from its value in the reference state S_0. With the help of the expression defining the junction strength (equation (5)) and that of the geometrical relation (6), the length of the screw segments can be expressed as a function of the density of forest obstacles, $L = \tau_{a0}/\beta'\mu b\rho_f$. The forest hardening is then written as

$$\Delta\tau = S_0 \ln\left(\frac{\rho_f}{\rho_{f0}}\right) + k\mu\frac{\mu\rho_f}{\tau_{a0}\rho_0} \tag{11}$$

where $\rho_0 = 1/\beta' b^2$ is a scaling density that depends on the obstacle strength and $\rho_{f0} = b\tau_{a0}\rho_0/\mu L_0$ is the vanishingly small obstacle density corresponding to an average free-length L_0 of the screw segments. The dimensionless coefficient k is practically a constant at a fixed temperature and depends on temperature through the stress dependence of the critical length X_c (cf equation (2*b*)). We see that forest hardening in bcc metals at low temperatures is a combination of two contributions: (i) a logarithmic term, which stems from the proportionality of the screw segment velocities to their length. This free-length effect has been discussed by Louchet *et al* [12]: (ii) a practically linear line tension contribution, similar to the one considered by Rauch [13]. A more accurate, but more complex, form for the total hardening can be obtained by relaxing some of the approximations relevant to the low-temperature regime. However, it must be kept in mind that as soon as the forest hardening is no longer small compared to the yield stress, the deformed specimen enters the mixed regime where both line tension and lattice friction govern the mechanical properties.

Equation (11) contains two quantities related to the reference state that are strongly temperature dependent. One is the reference stress τ_{a0} whose temperature and strain rate dependence is similar to that of the yield stress of the bcc crystal considered. The other is the strain rate sensitivity, S_0, which governs the free-length component of hardening. Therefore, a second characteristic feature of the low-temperature forest hardening in bcc crystals is its sensitivity to strain rate and temperature.

4.4. Numerical checks and predictions

In a first step, the simulation results are checked with the help of (11). The free-length contribution is calculated by estimating the free-length L from the geometrical relation of (6), taking the critical distance values from the simulation. The strain rate sensitivities in the reference state are calculated from the Arrhenius form describing the mobility of the screw segments (1), or alternatively measured from the simulation in the reference conditions. In both cases $S_0 = 3.17$ MPa at 160 K and 3.61 MPa at 215 K.

As far as the line tension contribution is concerned, it can be estimated from the simulation which yields a global average over all the instantaneous configurations. An exact calculation would be quite complex, since it should involve a statistical study of the lengths of the edge-segments lengths X_1 and X_2 that are nearest neighbours of a screw segment (cf equation (2*b*)) and of the free-lengths L (the average of $1/L$ is not that of L). Here, we take advantage of the simulation results to fix the value of one unknown coefficient of statistical origin. We can assume that the average values of X_1 and X_2 are about $X_c/2$. Then an effective value, k_{eff}, is defined to take into account in (2*b*) the fluctuations in the lengths of the screw segments. At the two temperatures investigated, it is found that this introduces a constant factor of $\frac{1}{3}$. Hence, (2*b*) is rewritten in the form

$$k_{eff} = \frac{1}{3}\frac{1}{4\pi(1-\nu)}\left[2\ln\left(\frac{X_c}{b}\right) + \frac{3-2\nu}{2(1-\nu)}\right]. \tag{12}$$

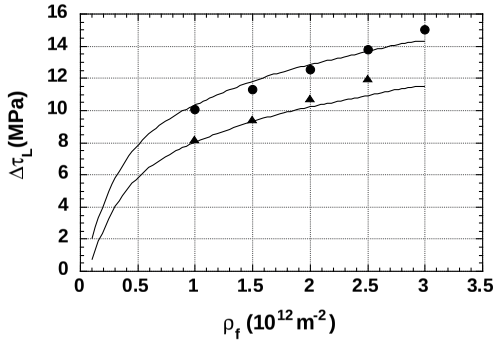

Figure 9. Prediction of the model for the contribution of the free-length effect to forest hardening as a function of obstacle density (full curves). The data points represent values deduced from the simulation results of figures 7(a) and (b) at 160 K (full triangles) and 215 K (full circles).

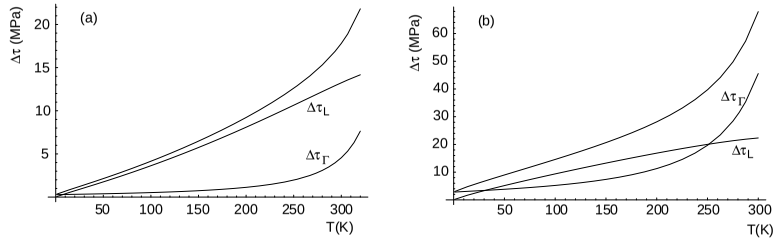

Figure 10. Predicted dependence of forest hardening, line tension hardening, $\Delta\tau_\Gamma$, and free-length hardening, $\Delta\tau_L$, on temperature for two values of the density of forest obstacles: (a) $\rho_f = 10^{12}$ m^{-2} and (b) $\rho_f = 10^{13}$ m^{-2}.

The total hardening and the line tension stress contribution can then be calculated and are shown in figures 7(a) and (b), respectively. The apparently linear dependence of the forest hardening on forest density simply results from the small range of obstacle densities accessible to the simulation. Globally, the model is in fair agreement with the simulated results, provided that a fit is made of the unknown statistical factor. Therefore, the simple arguments used to estimate the line tension stress will be assumed to be generally valid. The contribution from the length effect is shown in figure 9 for the two temperatures investigated and can be compared with the simulation results.

The model predictions for the forest hardening as a function of temperature are presented in figures 10(a) and 10(b) for two values of the density of forest obstacles, 10^{12} m^{-2} and 10^{13} m^{-2}, respectively. Here, use was made of (12) and the values of X_c were calculated according to the model presented above. The temperature dependences of the stress- and of the strain-rate sensitivity in the reference state were calculated from the activation enthalpy for the screw dislocation velocity (cf equation (1) and [6] for the analytical form), with an applied strain rate of 5×10^{-5} s^{-1}. Two effects dominate the relative magnitude of the two

contributions: the line tension effect increases the fastest with obstacle density since it involves a linear dependence; and the strain rate sensitivity vanishes at absolute zero temperature, passes through a maximum at intermediate temperatures (about 250 K in Ta) and vanishes again at the athermal temperature. As a result, the line tension effects are predominant at very low temperatures and at high temperature, all the more as the forest density is large. In a rather broad range of temperatures (typically 30–250 K for $\rho_f = 10^{13}$ m^{-2}) the free-length term is the largest. These features cannot be compared directly to strain hardening properties, however, since the relation between dislocation densities and strain cannot be derived from the present study. A further investigation involving 3-D simulations is therefore necessary, in order to establish the complete strain hardening properties of bcc crystals at low temperatures.

The increase of the line tension stress with increasing temperature or obstacle density sets a limit between the low-temperature behaviour and the intermediate regime where the interactions between dislocations are sufficiently large to induce dislocation patterning. Such a situation is met when the free-length of the screw segments becomes of same order as the critical distance, so that the typical low-temperature approximations no longer hold. Then, from (6), $L \approx X_c \approx \rho_{fc}^{-1/2}$, where ρ_{fc} is the obstacle density at this transition. With the help of (5) defining the obstacle strength, we have

$$\tau_{a0} = \beta' \mu b \sqrt{\rho_{fc}}/2 \tag{13}$$

Here, we took the line tension stress of the same magnitude as the reference stress, so that the applied stress is twice the value of τ_{a0}. It is not surprising to obtain, here, the square root relationship between the stress and the critical forest density. For the two temperatures investigated, we have $\rho_{fc} = 6.32 \times 10^{14}$ m^{-2} at 160 K and $\rho_{fc} = 2.37 \times 10^{14}$ m^{-2} at 215 K.

As the temperature decreases and the stress increases, or with smaller junction strength, a larger critical density is necessary to reach the transition. Such a behaviour was actually reported in an early study by Keh and Weissmann [8] on α-Fe polycrystals where it was found that a dislocation cell structure is formed beyond a certain critical strain that increases with decreasing temperature. The same study contains the most detailed measurements of dislocation densities available for bcc metals. Unfortunately, the plots of the flow stress against the dislocation density do not cover a sufficient range to serve as a firm base for checking a model. The same problem was noticed with the results of the simulation (cf figure 6).

5. Concluding remarks

One of the main factors governing forest hardening is the junction strength. In the present work, the latter was successfully estimated in spite of the lack of experimental or theoretical data. Then, it was shown numerically that the geometrical relationship on which all hardening models are based is effectively checked by the numerical simulations. The answers to the questions brought up in the inductory part can be summed up as follows. Both simulation and modelling confirm that forest hardening is made up of two additive contributions, a free-length effect and a line tension effect, whose relative weight depends on the obstacle density, temperature and strain rate, and whose dependences on forest density are, respectively, logarithmic and linear. A clear limit of the present model resides in the fact that it does not treat the statistical aspects of the local configurations that are critical for a rigorous calculation of the line tension contribution.

The model, as well as the DD simulation, are valid in the low-temperature regime where the length of the screw segments is large with respect to that of the bowed-out non-screw segments. A transition to the typical fcc-like behaviour is expected when this is no longer the case, i.e. not only at temperatures above T_c but also at large strains below T_c. It would be a

rather difficult task to simulate the transition between the two regimes, but further modelling is now possible since the basic mechanisms are understood in the two regimes. The results obtained here are transposable to other bcc metals provided that the junction strength is known. This points to an important input property, on which one presently has little information, the conditions for junction formation and destruction.

Since the proposed model essentially treats forest obstacles like point obstacles, it can easily be extended to the treatment of impurity hardening by interstitial atoms at low temperatures. This would, in practice, mean replacing $1/\rho_f$ by $1/c$, where c is the solute concentration, in the basic geometrical equation and introducing a thermally activated breakaway from the obstacles.

So far, we have discussed forest hardening rather than the 3-D strain hardening of real crystals. The relation between these two properties involves the knowledge of the strain dependence of the forest dislocation density. One major problem, which is not sufficiently emphasized in the current literature, stems from the occurrence of an exhaustion stage (stage 0) during the pseudo-elastic loading of the specimen. During this stage, the screw dislocations are immobile, but most of the edge segments present in the crystal move over large distances, thus producing a large density of immobile (forest) screw dislocations in all of the primary slip planes [6, 25]. As a consequence, the density of the forest at the yield stress can be orders of magnitude larger than the initial density, all the more as the temperature is low and the extent of stage 0 is large. In addition, the mean free path of the edge segments depends on the concentration of interstitial solutes that tends to reduce it [25]. Beyond stage 0, the evolution of the forest density is governed by the dislocation multiplication rate in the active slip systems and by the annihilation properties of the screw dislocations, until the forest density reaches the transition regime discussed above. While such processes are undoubtedly difficult to model, they can be simulated with the help of the 3-D version of the present DD simulation.

Another type of difficulty is associated with the present lack of knowledge of the rules governing the slip geometry of bcc crystals at low temperatures. Atomistic modelling is presently very active in this domain and may yield more information about some relevant input properties [7, 26, 27]. From the experimental point of view, controlled measurements of the dislocation densities against strain at low temperatures and *post mortem* as well as *in situ* observations of junctions would certainly be of great interest.

Acknowledgments

MT acknowledges discussions with M Fivel, L Yang, and J Moriarty. The work of MT is performed under the auspices of the US Department of Energy by the Lawrence Livermore National Laboratory under contract number W-7405-ENG-48.

References

[1] Bulatov V, Abraham F F, Kubin L P, Devincre B and Yip S 1998 *Nature* **391** 669
[2] Kubin L P, Devincre B and Tang M 1998 *J. Comput. Aided Mater. Design* **5** 31
[3] Friedel J 1967 *Dislocations* (Oxford: Pergamon)
[4] Gil Sevillano J 1993 *Plastic Deformation and Fracture of Materials (Materials Science and Technology* vol 6), ed H Mughrabi (Weinheim: VCH) p 40
[5] Kocks U F 1976 *J. Eng. Mater. Technol.* **98** 76
[6] Tang M, Kubin L P and Canova G R 1998 *Acta Mater.* **46** 3221
[7] Duesbery M and Vitek V 1988 *Acta Mater.* **46** 1481
[8] Keh A S and Weissmann S 1963 *Electron Microscopy and Strength of Crystals* ed G Thomas and J Washburn (New York: Interscience) p 231

[9] Foreman A J E and Makin J E 1966 *Phil. Mag* **14** 911
[10] Kocks U F 1985 *Dislocations and Properties of Real Materials* (Bristol: Institute of Physics) p 125
[11] Devincre B and Kubin L P 1994 *Model. Simul. Mater. Sci. Eng* **2** 559
[12] Louchet F Kubin L P and Vesely D 1979 *Phil. Mag* A **39** 433
[13] Rauch E F 1994 *Key Eng. Mater.* **97–98** 371
[14] Kubin L P, Canova G, Condat M, Devincre B, Pontikis V and Bréchet Y 1992 *Solid State Phenom.* **23–24** 455
[15] Devincre B 1996 *Computer Simulation in Materials Science (NATO ASI E 308)* (Dordrecht: Kluwer) p 309
[16] Moulin A, Condat M and Kubin L P 1997 *Acta Mater.* **45** 2339
[17] Devincre B and Condat M 1992 *Acta Metall. Mater.* **40** 2629
[18] de Wit R 1967 *Phys. Status Solidi* **20** 575
[19] Chou Y T 1972 *Mater. Sci. Eng.* **10** 81
[20] Louchet F and Kubin L P 1975 *Acta Metall.* **23** 17
[21] Hirth J P and Lothe J 1992 *Theory of Dislocations* (Malabar: Krieger) p 724
[22] Christian J W 1983 *Metall. Trans.* A **14** 1237
[23] Lachenmann R and Schultz H 1970 *Scripta Metall.* **4** 709
[24] Wasserbäch W 1996 *Tantalum* ed E Chen *et al* (Warrendale, PA: Minerals Metals and Materials Society) p 225
[25] Kubin L P 1976 *Rev. Deform. Behav. Mater.* **1** 244
[26] Xu W and Moriarty J A 1998 *J. Comput. Mater. Sci.* **9** 348
[27] Moriarty J A, Xu W, Soderlind P, Belak J, Yang L and Zhu S 1999 *J. Eng. Mater. Tech.* **121** 120

PERGAMON

Scripta Materialia 47 (2002) 689–695

Scripta MATERIALIA

www.actamat-journals.com

Simulation of dislocation patterns in multislip

R. Madec, B. Devincre, L.P. Kubin *

Laboratoire d'Etude des Microstructures, CNRS-ONERA (OM), 29 Av. de la Division Leclerc, BP 72, 92322 Châtillon Cedex, France

Accepted 12 April 2002

Abstract

Dislocation dynamics simulations of multiple slip in f.c.c. crystals lead to the formation of patterned microstructures. The mechanisms participating to dislocation storage and dynamic recovery are investigated and discussed. Cross-slip and short-range interactions are found to govern the bifurcation from uniform to ordered microstructures.

Keywords: Dislocations; Cell structures; Cross-slip; Junctions; Dynamic recovery

1. Introduction

Numerical simulations can provide an original insight into the mechanisms of dislocation cell formation in f.c.c. crystals. Dislocation dynamics (DD) simulations are at present limited to small strains, <1%, and small model volumes. Thus, this approach does not permit to check the occurrence of similitude or self-similarity properties in the microstructures. It allows, nevertheless, to examine the respective contributions from various dislocation processes to the emergence of dislocation patterns without making strong assumptions.

From early transmission electron microscopy studies, it is known that cell structures form at the onset of stage III of the deformation of single crystals, or at small strains in multislip conditions [1,2]. These last conditions are, therefore, the most suited for DD simulations. Three major contributions to patterning have been discussed in the literature and are examined in the present work. As emphasized by Kocks [3], the storage of immobile dislocations is due to strong interactions of the mobile dislocations with a "forest" of intersecting dislocations. The cross-slip mechanism has often (but not always) been assumed to be responsible for the temperature dependence of τ_{III}, the critical stress for the onset of stage III, i.e., for dynamic recovery. Within this view, the relaxation of internal stresses that characterizes stage III behavior is attributed to the mutual annihilation of mobile screw dislocations with immobile ones. In contrast, continuum spatio-temporal models tend to propose general explanations for the formation of dislocation cells. In the deterministic model by Kratochvíl and Orlová [4], an internal bending type of instability is invoked, whereas a more recent statistical model points out at long-range stress fluctuations as a possible cause of patterning, by analogy with noise-induced phase transitions [5].

In what follows, the numerical method is briefly recalled and answers provided by DD simulations to the three points mentioned above are presented and discussed.

* Corresponding author.
E-mail address: kubin@onera.fr (L.P. Kubin).

1359-6462/02/$ - see front matter © 2002 Acta Materialia Inc. Published by Elsevier Science Ltd. All rights reserved.
PII: S1359-6462(02)00185-9

2. Dislocation dynamics simulations

The present results were obtained with the help of DD simulations, in which the character of the dislocation lines is discretized into a succession of screw and edge segments (the "Edge–Screw" model), or of screw, mixed and edge segments (the "Mixed" model). Due to the reduction in the number of degrees of freedom resulting from the discretization of characters, this type of simulation provides an excellent compromise between numerical accuracy and computing efficiency. This makes it possible to treat dense configurations in material volumes with dimensions larger than those of a typical dislocation cell. The basic principles of these three-dimensional (3-D) simulations can be found in several references [6–9] and will not be detailed here.

As far as elastic properties are concerned, it is sufficient to mention that all the contributions to the effective stress on a dislocation segment are computed within isotropic elasticity theory. This includes a line tension stress, estimated from Foreman's formula [10], the elastic interactions with other segments from the same line or from other lines, a small Peierls stress ($10^{-5}\mu$, where μ is the shear modulus) and the resolved applied stress. The mobility of a segment is then governed in f.c.c. crystals by a viscous drag due to the interaction with phonons and electrons.

The formation and destruction of junctions is treated as a purely elastic problem, on the base that it is governed by a balance of line energies, to which the contribution of core energies is negligible. The only assumption made is that dislocations are not dissociated, which certainly applies to an f.c.c. crystal with a high stacking fault energy (SFE) like aluminum. Several arguments show that this simplifying assumption also applies to crystals of lower SFE like copper, or even silver, as far as junction properties are concerned. For instance, a detailed comparison of the critical stress for the unzipping of Lomer–Cottrell locks shows that very similar values are found by atomistic and DD simulations and by DD simulations of the corresponding non-dissociated configuration, the Lomer lock [11,12]. The fact that the junction strength is not sensitive to the core structure is also considered as an explanation for the relative insensitivity of stage II hardening in f.c.c. crystals to the value of the SFE.

In the present simulations, the only mechanism by which dislocations can move out of their slip plane is the cross-slip of screw dislocations. Cross-slip is implemented in a stochastic manner via an Arrhenius-like probability law, which accounts for its thermally activated character. A simplified form for the activation energy is derived from the Friedel–Escaig mechanism (see e.g. [13]), in agreement with more recent atomistic simulations [14]. It depends on the local effective stresses on the slip and cross-slip planes and on the SFE of the material through the value of τ_{III}. The way this local rule is numerically implemented is the same in all versions of the DD simulations [6,9,15].

The initial microstructure is made up of an initially random distribution of source segments, to which a prestrain and a further relaxation are sometimes applied to simulate annealed microstructures. The model crystal is deformed with a constant imposed strain rate, typically 20 s^{-1}, along a [0 0 1] stress axis (specific details will be given below for each set of numerical experiments). The boundary conditions are either those of free surfaces (Edge–Screw model) or periodic boundary conditions [9,16] for the Mixed model. In what follows, the temperature is fixed to about 400 K, the elastic constants of the material and the cross-slip properties being those of copper. Finally, one may keep in mind that local lattice rotations are not taken into account into these DD simulations.

3. Junctions and dislocations storage

In a crystal deformed in multislip conditions, dislocation storage occurs through the interaction of gliding dislocations with strong forest obstacles, particularly attractive junctions. The conditions for the formation and destruction of the three types of junctions between perfect dislocations in

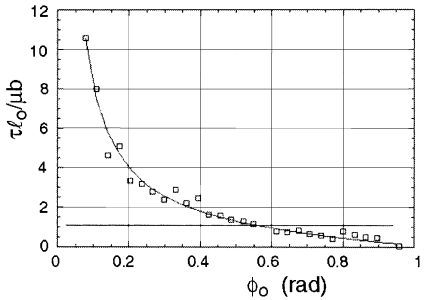

Fig. 1. The critical stress τ_0 of a symmetrical Lomer lock, scaled by $\mu b/\ell_0$, where ℓ_0 is the initial length of the interacting segments, as a function of the angle ϕ_0 between the initially straight interacting segments and the junction direction. The squares represent simulation results obtained with the Mixed model. The curve is a fit to a simplified elastic model [9]. The horizontal line corresponds to a typical (reduced) yield stress of $2.5 \times 10^{-4}\mu$.

f.c.c. crystals (the Lomer, glissile and Hirth locks) have been investigated in detail as a function of the orientation of the interacting lines [8,9,17]. Fig. 1 shows a plot of the critical stress (in reduced units) for the unzipping a symmetrical Lomer lock as a function of the common initial angle ϕ_0 of the interacting lines with the junction direction. The simulation results (squares) are fitted to a simplified elastic model. The latter contains one arbitrary constant but provides a surprisingly accurate prediction. One can see that there is a whole spectrum of junction strengths and a divergence when the lines are initially parallel to the junction direction ($\phi_0 = 0$). In this particular case, the length of the unzipping arms is zero and an infinite stress has to be applied to them to destroy the junction. The horizontal line represents, in the same reduced units, the typical flow stress of an annealed f.c.c. single crystal at small strains. Thus, most junction of smaller critical stress are destroyed under stress, whereas those of larger critical stress are stored and can contribute to patterning. The flow stress is, therefore, such that a sufficient fraction of all the junctions present at a given moment can be destroyed, in order to allow the mobile density to produce the imposed plastic strain rate. Within the Mixed model, the scaling relationship $\tau = \alpha\mu b\sqrt{\rho_f}$ between the resolved flow stress and the square root of the forest density in multiple slip is spontaneously obtained (b is the modulus of the $1/2\langle 1\,1\,0\rangle$ Burgers vector). A mean value of $\alpha = 0.38$ comes out without any adjustment [9], which compares well with the experimental data on copper and silver compiled by Basinski and Basinski [18].

4. Influence of cross-slip on pattern formation

Fig. 2 shows two simulated microstructures obtained in multiple slip with the Mixed model. The numerical conditions and the initial configurations are exactly the same, except that the cross-slip probability is set to zero in Fig. 2a. An early stage of organization appears in Fig. 2b, where well-defined dislocation-dense regions can be observed. These regions are in the form of veins, rather than walls, with preferential $\langle 1\,1\,0\rangle$ directions, parallel to the intersections of the active slip systems. Their average spacing is $d \approx 10$ μm, to be compared to the periodicity of about $10\sqrt{2}$ μm imposed along the $\langle 1\,1\,0\rangle$ directions by the boundary conditions. To fix the ideas, the axial stress is $\sigma = 2.7 \times 10^{-4}\mu$ and with a Burgers vector $b = 0.255$ nm, we have $d \approx 11\mu b/\sigma$ for these emerging structures. Similar microstructures were obtained previously with the Edge–Screw model [19], in simulated volumes of 15 μm^3 with free surfaces. The dislocation-dense regions are anchored on an underlying skeleton of stable junctions; they also contain cross-slipped segments, jogs and debris. In contrast, in the absence of cross-slip, the organization is much less well-marked and the formation of observable patterns is either delayed to larger strains or suppressed (cf. Fig. 2a). Although one may assume that the rearrangement of the microstructure by cross-slip contributes to the refinement of the dislocation-dense regions and their 3-D extension, the detail of the mechanisms that cooperate to produce the pattern of Fig. 2b remain to be investigated. Thus, this numerical experiment essentially confirms that cross-slip strongly favors the emergence of ordered dislocation microstructures. Within 5%, the total dislocation density is the same in the two situations

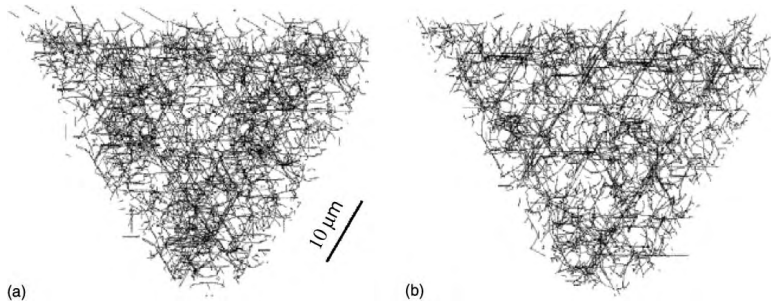

Fig. 2. (1 1 1) foils of thickness 5 μm extracted at the same position from simulated crystal of approximately cubic shape ($9.8 \times 11.6 \times 8.4$ μm^3), strained along a [1 0 0] stress axis (the microstructures are under stress). The simulation conditions are identical (initial density 10^{12} m^{-2}, imposed strain rate 20 s^{-1}, total plastic strain $\varepsilon \approx 2 \times 10^{-3}$), except that the cross-slip probability is set to zero in (a). In (b) and in the presence of cross-slip, sharp dislocation-dense regions are observed along the three $\langle 1\,1\,0\rangle$ directions of the (1 1 1) plane. Sections of the simulated volume and of one layer of replicas stemming from periodic boundary conditions are shown.

depicted in Fig. 2 and the corresponding simulated stress–strain curves do not substantially differ (cf. Fig. 4b below). This confirms the relative insensitivity of the flow stress on the arrangement of the microstructure, which has been noted by many authors [20,21].

5. Internal stresses

Fig. 3a shows another emerging microstructure obtained in the presence of cross-slip, in conditions similar to those of Fig. 2b. This figure is obtained by superimposing a large number of successive gray images. The black areas are, therefore, those where storage resulted in stable dislocation-dense regions. Fig. 3b shows a mapping of the resistive internal stress resolved in one of the active slip systems. The amplitude of these stresses, whose sign is opposite to that of the resolved applied stress, increases with increasing darkness up to -2 times the applied shear or more in the black areas. These negative internal stresses approximately correspond to the dislocation-poor areas of Fig. 3a. In the same way, the complementary mapping of the positive internal stresses (Fig. 3c) delineates

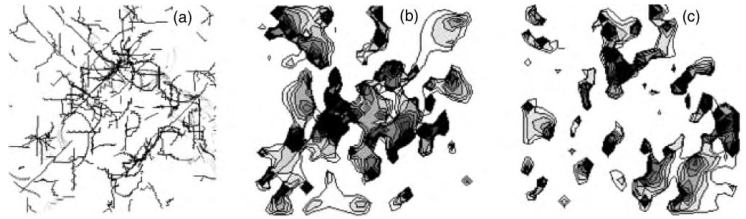

Fig. 3. (a) A simulated microstructure obtained from the Edge–Screw model in conditions similar to those of Fig. 2b ([1 0 0] foil of thickness 2 μm extracted from a simulation box of linear dimension 15 μm). This picture was obtained by superimposing successive gray images, in order to better visualize the regions where dislocations are permanently stored. The dense veins are parallel to the $\langle 1\,1\,0\rangle$ directions of the foil plane. (b) A mapping of the resistive (negative) internal shear stresses in one of the active slip plane (the dark areas are those where the modulus of the internal stress is the largest). (c) A mapping of the positive internal stresses on the same slip plane.

areas that approximately correspond to the dislocation-dense regions. This picture is qualitatively consistent with Mughrabi's composite model [19], according to which the continuity of plastic strain between the hard dislocation-dense regions and the soft dislocation-poor regions induces positive internal stresses in the former and negative ones in the latter. The high local stress levels in the walls enhance the cross-slip probability, since the latter is stress-dependent. We attribute to this effect the progressive refinement of the walls, which can be seen by comparing the gray and dark contrasts in Fig. 3a, and their stabilization by the relaxation of the local peaks of internal stress.

6. Influence of long- and short-range stresses on pattern formation

Numerical experiments were designed in order to check the influence of close and distant interactions between dislocations on the evolution of the microstructure and on the flow stress [7]. A cut-off radius was introduced of the order of $\rho^{-1/2}$ (about 1 μm). In one test, only the elastic interactions situated inside this cut-off were computed and in a second one only those situated outside the cut-off. In both case intersection and junction processes were included. Fig. 4a shows a microstructure obtained in the case where short-range elastic interactions are cut out. The dislocations are uniformly distributed in space and no trace of emerging structure is found. In the case where only short-range interactions are accounted for, a central dislocation-poor region is formed [7]. Its radius is larger than the cut-off radius, so that this structure is not an artifact due to the truncation of the elastic interactions (in contrast to a common belief, such artifacts arise only on microstructures that are let to relax in the absence of applied stress). These results are interpreted as follows. The largest internal stresses are produced by short-range dislocation interactions. Since the cross-slip probability is strongly stress-sensitive, omitting these interactions is equivalent to de-activating cross-slip. As shown above, this prevents the emergence of an organized microstructure. Thus, we conclude that, although long-range interactions do play a role once dislocation patterns are well formed, they cannot be the cause of pattern formation.

Fig. 4b compares four stress–strain curves in [1 0 0] multislip, with cross-slip included (bold

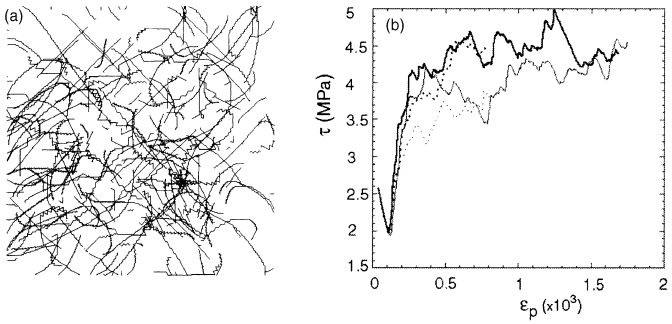

Fig. 4. (a) A simulated microstructure obtained in conditions similar to those of Fig. 2b ([1 0 0] foil of thickness 4 μm extracted from a simulation box of linear dimension 15 μm, Edge–Screw model). Elastic interactions between segments are computed only at distances larger than the mean dislocation spacing, $\rho^{-1/2} \approx 1$ μm. Short-range interactions are truncated but junction processes are operative. A uniform dislocation distribution results. (b) Simulated resolved stress vs. plastic shear strain curves obtained in [1 0 0] multislip conditions using the Mixed model with cross-slip (bold curve), with cross-slip and only short-range interactions (bold dotted curve), without cross-slip (thin curve) or without cross-slip and with only short-range interactions (dotted thin curve). The initial stage corresponds to a relaxation of the initial configuration.

curves) or not (thin curves) and with long-range interactions truncated (dotted curves) beyond a distance $\rho^{-1/2} = 0.75$ μm, or not truncated. Cross-slip induces a small upwards shift in flow stress, which is attributed to the increased density of the forest via multiplication by double cross-slip and to the formation of jogs and debris. The long-range stresses do not significantly contribute to the flow stress. These conclusions are, of course, only valid in the small strain range considered here.

7. Discussion and concluding remarks

These results show that early stages of the organization of the microstructure can be investigated with the help of DD simulations. The dislocation arrangements obtained in this study share some properties of well-formed cells. Although it is not presently possible, by lack of computing power, to check how they evolve with increasing applied stress, they are associated with internal stress field patterns that behave as predicted by Mughrabi's composite model. Nevertheless, the flow stress of the simulated materials is governed by the forest mechanism, i.e., by short-range and contact interactions. These patterns are stable within the small strain range investigated here. The dislocation processes that concur to the formation of these microstructures are, nevertheless, rather complex and have not been examined yet in detail.

As far as the modeling of dislocation pattern formation at low and medium temperatures is concerned, it seems essential to take into account not only the storage of dislocations by their interaction with the forest but also the cross-slip mechanism. Because cross-slip is stress-dependent, it is mostly sensitive to short-range dislocation interactions. Its effect is to decrease the mean internal stress by relaxing local peaks in its distribution, thus stabilizing the configurations of stored dislocations. All these features also characterize dynamic recovery, so that, in the absence of any obvious alternative, the present results support the view according to which the cross-slip mechanism is responsible for dynamic recovery. Cross-slip favors non-planar glide and the present results also confirm that pattern formation is either delayed or suppressed in conditions of purely planar glide. Finally, long-range internal stresses, as well as local lattice rotations that are not included in these DD simulations, do not seem to critically influence the emergence of a cell structure.

There are virtually no transmission electron microscopy studies on single crystals deformed in multiple slip at small plastic strains, typically in the range of 0.5–1%. It would certainly be desirable to undertake such a study in order to check the present conclusions regarding the bifurcation from an initially uniform dislocation structure to an organized one.

References

[1] Hirsch PB. In: Hirsch PB, editor. The physics of metals: II defects. Cambridge: Cambridge University Press; 1975. p. 193.
[2] Jackson PJ. Progr Mater Sci 1984;29:139.
[3] Kocks UF. In: Dislocations and properties of real materials. London: The Institute of Metals; 1985. p. 125.
[4] Kratochvíl J, Orlová A. Philos Mag 1990;A61:281.
[5] Zaiser M. Mater Sci Eng A 2001;309–310:304.
[6] Kubin LP, Canova G, Condat M, Devincre B, Pontikis V, Bréchet Y. Solid State Phenomena 1992;23–24:455.
[7] Devincre B, Kubin LP, Lemarchand C, Madec R. Mater Sci Eng A 2001;309–310:211.
[8] Madec R, Devincre B, Kubin LP. Multiscale Modeling of Materials, p. z1.8.1. In: Kubin L, Selinger R, Bassani J, Cho K, editors. MRS Symp Proc, vol. 653, Warrendale (PA): Materials Research Society, 2001.
[9] Madec R. Doctorate Thesis, Orsay University, 2001.
[10] Gómez-García D, Devincre B, Kubin LP. J Comput Aided Mater Design 1999;6:157.
[11] Bulatov V, Abraham F, Kubin LP, Devincre B, Yip S. Nature 1998;391:669.
[12] Shin CS, Fivel MC, Rodney D, Phillips R, Shenoy VB, Dupuy L. In: Forest S, van der Giessen E, Kubin L, editors. Scale transitions from atomistics to continuum plasticity. F-Les Ulis: EDP Sciences; 2001. p. 19.
[13] Bonneville J, Escaig B, Martin JL. Acta Metall 1988;36:1989.
[14] Vegge T, Rasmussen T, Leffers T, Pedersen OB, Jacobsen KW. Philos Mag Lett 2001;81:137.
[15] Devincre B. In: Kirchner HOK, Pontikis V, Kubin LP, editors. Computer simulation in materials science. Amsterdam: North Holland; 1996. p. 309, NATO ASI Series E308.

[16] Bulatov VV, Rhee M, Cai W. Multiscale modeling of materials, p. z1.3.1. In: Kubin L, Selinger R, Bassani J, Cho K, editors. MRS Symp Proc, vol. 653, Warrendale (PA): Materials Research Society, 2001.
[17] Madec R, Devincre B, Kubin LP. Comput Mater Sci, 2002;23:219–224.
[18] Basinski SJ, Basinski ZS. In: Nabarro FRN, editor. Dislocations in solids, vol. 4. Amsterdam: North-Holland; 1979. p. 261.
[19] Devincre B, Kubin LP. Mater Sci Eng A 1997;234–236:8.
[20] Mughrabi H. Acta Metall 1983;31:1367.
[21] Neuhaus R, Schwink C. Philos Mag A 1992;65:1463.

DISCRETE-CONTINUUM MODELING OF METAL MATRIX COMPOSITES PLASTICITY

S. Groh[1], B. Devincre[1], F. Feyel[2], L. Kubin[1], A. Roos[2] and J.-L. Chaboche[2]

[1]*LEM, CNRS-ONERA, BP 72, 29 av. de la division Leclerc, 92322 Chatillon Cedex, France*

[2]*LCME, ONERA, BP 72, 29 av. de la division Leclerc, 92322 Chatillon Cedex, France*

Abstract A computing methodology is reported for modeling the plastic deformation of Metal Matrix Composites. Use is made of a discrete-continuum model based on a coupling between Dislocation Dynamics and Finite Element simulations, which provides a parameter-free quantitative description of the mechanical properties. The model and the first simulation results on MMCs are presented and briefly discussed.

Keywords: Metal Matrix Composite, Plastic deformation, Dislocation Dynamics simulation, Finite Element simulation

1. INTRODUCTION

The recent interest on materials with increasingly small characteristic length scales has clearly revealed some shortcomings in the modeling of size effects in materials plasticity. These effects, which are explicit in dislocation theory, are usually not reproduced by continuum approaches. For this reason, the prediction of the plastic properties of Metal Matrix Composites (MMCs) is sometimes considered as a bench test for theoretical or numerical models. Indeed, in MMCs the stress-strain behavior is size-dependent for reinforcement sizes and volume fractions in the micrometer range. Further, the matrix stress-strain behavior that needs to be assumed to reproduce experimental results differs from the stress-strain behavior of the unreinforced material [1–3].

As theory and experiment often do not fit very well, some authors [4–6] proposed to validate the predictions of their own theory by comparison with a Dislocation Dynamics (DD) simulation by Cleveringa et al. [7, 8], on a 2D composite material with periodic rectangular reinforcements. Such exercises

were extremely instructive but, nevertheless, care should be exercized when extrapolating two-dimensional models to experiment.

The simulation of dislocation dynamics in 3D MMCs is a challenging problem, which goes much deeper than the usual question of CPU time limitation. One has, in addition, to define precisely the conditions for mechanical equilibrium in such complex hetero-structures (see [9] for detail). Several solutions to this problem are now potentially available [9–14] and a critical comparison of these approaches can be found in ref. [15]. In the present work, use is made of the Discrete-Continuum Model (DCM) [10, 11]. The model and its specific implementation in the case of MMCs are shortly described in part 2. Parts 3 and 4 are dedicated to a presentation of the simulation results and part 5 to concluding remarks.

2. THE DISCRETE-CONTINUUM MODEL

In essence, the DCM, is made up of an FE code (ZeBuLon), in which a DD simulation replaces the constitutive formulation for plastic properties. On the one hand, the FE code treats the boundary value problem and cares of the conditions of local equilibrium in a meshed volume element. On the other hand, the DD code cares of the topology and motion of the dislocation lines in the same volume element, hence of the plastic strain, $\underline{\varepsilon}_p$. The coupling is realized with the help of two procedures that control the traffic between the "discrete" and "continuum" codes, a homogenization procedure for the calculation of $\underline{\varepsilon}_p$ and an interpolation procedure for the calculation of the stress tensor $\underline{\sigma}$ at any point of the simulated volume (cf. [11, 15]).

2.1 Dislocation Self-Stress Fields

In agreement with Mura's Eigenstrain theory [16], the DCM can theoretically capture all details of the dislocation stress fields in isotropic or anisotropic elasticity. It is then mainly a matter of computation to design a FE mesh for computing the complex stress field of a dislocation line close to its singularity. Unfortunately, for "mass" simulations involving many dislocations, this brute force approach is numerically untractable.

For instance, considering the computational constraints discussed in part 4, the largest regular mesh that can be handled by a good workstation has $(10 \times 16 \times 6)$ quadratic cubic elements of linear length $0.137\mu m$. The mesh length may then be larger than the mean distance between dislocations and the shape function used to interpolate the stress can only reproduce the smooth variations of the dislocation stress fields far from their singularities. Indeed, the Eigenstrains associated to dislocations are homogenized in a small volume surrounding the lines, in order to remove stress singularities. For this rea-

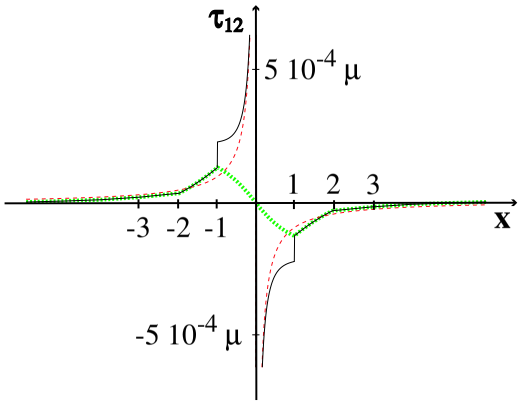

Figure 1. Isotropic shear stress field of a rigid screw dislocation calculated along a direction normal to the line. For the sake of comparison, the distances in abscissa are plotted in units of the linear dimension of the quadratic elements used in the present work. Dashed line: theoretical solution. Dotted line: solution yielded by the DCM. Continuous line: DCM solution with a short-distance correction.

son, the previous version of the DCM was restricted to problems of plastic relaxation implying no short-distance reactions between dislocations (see for instance [17]).

A simple solution is proposed to overcome this limitation. In the DD part of the DCM, the analytical (isotropic) self-stress field of a dislocation is superimposed to the stress prediction yielded by the FE code within a small volume surrounding the singularity (see Fig. 1). This volume is limited to the homogenized core region, so that the homogenization volume in the DCM is identical to the volume where the stress correction is performed. Hence, in conformity with dislocation theory, we introduce in the DCM framework the equivalent of an "elastic core surface traction" [18], which does not affect the total mechanical equilibrium (by construction the integral of the additional stress is zero), but improves the local description of dislocation interactions. In other terms, the amount of elastic energy lost in the homogenization procedure is locally restored in the DD code without affecting the consistency of the FE calculations. This correction is an essential one if one wishes to realistically reproduce the strength of dislocation reactions (cf. part 4). It must be noticed that whereas this improvement is easy to implement, it significantly increases the computational burden. This is why the small discontinuity of the stress field generated at the border of the homogenization volume (see Fig. 1) has not been removed so far. This is feasible in technical terms, but does not appears to be critical.

2.2 Initial and Boundary Conditions

The need to consider a reference cell as small as possible in order to optimize computations strongly suggests applying periodic boundary conditions (PBCs) in the case of MMCs simulations. Topological problems related to the use of these conditions, when applied with DD simulations, are discussed in [19]. Here, we restrict ourselves to the question of implementing PBCs in a FE code and to some related problems that may affect the simulation results.

As shown in Fig. 2, the simulation cell used for the study of MMCs is a parallelepipedic volume of dimension $(1.368 \times 2.188 \times 0.820)\ \mu m^{-3}$ including four half-fibers of square cross-section at the center of the vertical faces (the edges of the fibers are rounded off in the FE mesh to eliminate local stress concentrations). Modifying the dimensions of the fibers allows obtaining various volume fractions in the simulated cell. By periodic three-dimensional replication of the simulation cell, one obtains a composite material with an hexagonal arrangement of infinitely long fibers. The displacement ($\mathbf{u}$) and strain ($\underline{\varepsilon}$) fields that verify the periodic solution in the reference cell are as follows:

$$\underline{\varepsilon}(\mathbf{u}(\mathbf{r})) = \underline{\bar{\varepsilon}} + \underline{\varepsilon}(\mathbf{u}'(\mathbf{r})) \quad \text{with} \quad \mathbf{u}(\mathbf{r}) = \underline{\varepsilon} \cdot \mathbf{r} + \mathbf{u}'(\mathbf{r}) \tag{1}$$

where $\underline{\bar{\varepsilon}}$ is the mean deformation expected if the material is homogeneous and $\underline{\varepsilon}(\mathbf{u}')$ is a fluctuating quantity that accounts for the presence of the periodic hetherogeneities (in the present case, the fibers). This last term derives from a displacement field $\mathbf{u}'$, *i.e.*, whose values are periodically repeated at the cell boundaries in the directions of the translation vectors. Hence, the mechanical equilibrium in the simulated volume element must satisfy the following equations:

$$\langle \underline{\varepsilon}(\mathbf{u}'(\mathbf{r})) \rangle = \underline{0} \quad \text{and} \quad \langle \underline{\varepsilon} \rangle = \underline{\bar{\varepsilon}} \tag{2}$$

$$div \underline{\sigma}(\mathbf{r}) = \underline{0} \quad \text{and} \quad \underline{\sigma}(\mathbf{r_1}).\mathbf{n} = -\underline{\sigma}(\mathbf{r_2}).\mathbf{n}, \tag{3}$$

where $\mathbf{r_1}$ and $\mathbf{r_2}$ are opposite points at the boundary of the simulation cell and $\mathbf{n}$ is the corresponding boundary translation vector.

The main difficulty encountered when setting up proper initial conditions stems from the fulfillment of the above stress and strain conditions in the presence of a dislocation microstructure. In order for the FE code to account for the elastic fields of dislocations, the latter must imperatively be generated by a Volterra process. This implies that the DCM can only deal with closed dislocation loops. To globally satisfy the equilibrium conditions, the solution that is implemented consists in expanding the initial dipolar loops from random positions in the simulation cell (see Fig. 2-a). All the loops have same diameter, which is taken much larger than the mean distance between dislocations in order to avoid artificial screening effects. The total density is equally distributed

on the twelve slip systems of the fcc structure and the total plastic shear during the Volterra process is set to zero by balancing the signs of the Burgers vectors. In the case of the unreinforced material (cf. part 3), this type of initial microstructure induces a mechanical state very close to equilibrium and only a small relaxation is observed at the beginning of the simulations. The case of the MMCs simulations is more critical and particular attention must be paid to the displacement and strain fields associated to the initial configuration (see Fig. 2-b), particularly with large volume fractions of fibers. Indeed, the fiber-matrix interfaces, which are assumed to be impenetrable barriers to dislocation glide, alter the symmetries of the initial dislocation microstructure. For this reason, it is necessary to check that the randomly generated configuration does not induce high internal stresses that could artificially modify the dynamics. In what follows, we only consider initial microstructures with an initial internal stress sufficiently small not to induce an artificial asymmetry between tension and compression tests. It is worth noting that it could be interesting in some cases to use alternative initial microstructures, for instance for reproducing the residual stresses generated during the processing of MMCs [1].

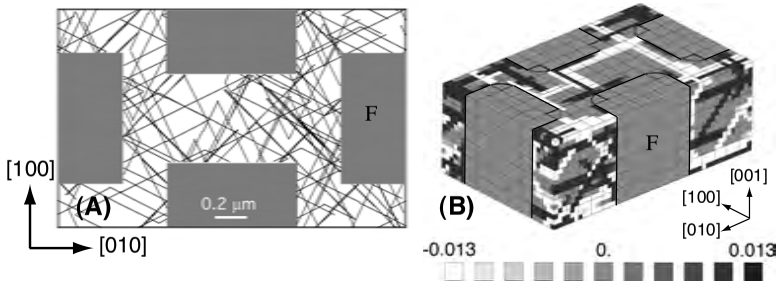

Figure 2. Initial conditions for the MMCs problem. A) A random distribution of dipolar dislocation loops generated by Volterra processes in a simulation cell. Whatever the loop positions, the dislocation lines cannot penetrate the fibers (denoted F). B) Surface mapping of the component ε_{33} of the initial strain field (the mean value is close to zero, as can be seen from the gray scale). Notice that special elements are used at the fiber's edges to avoid local stress concentrations.

Finally, whereas conventional DD simulations with PBCs make use of a cut-off distance for the stress field computations [20], the dislocation dynamics part of the DCM accounts for the totality of the periodic fields. The two types of simulations should then yield slightly different results when long-range elastic effects come into play.

3. VALIDATION TESTS

In order to validate the short-distance stress correction discussed in Sec. 2.1, simulated tensile tests have been carried out on copper crystals. The flow stress of pure fcc metals being controlled by dislocation reactions [20], such tests should be critical ones. An equivalent simulation, not reproduced here, were performed on an aluminum crystal, to determine the plastic properties of unreinforced matrix in Al_2O_3/Al MMCs. The results are very similar in both cases.

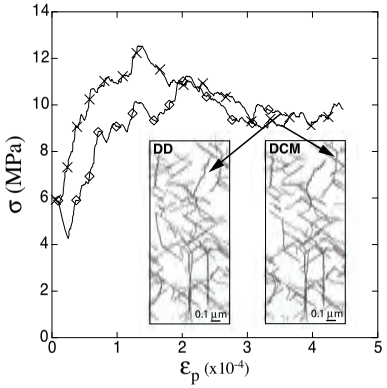

Figure 3. Tensile [100] stress-strain curves for a copper crystal, as obtained by DD ($\Diamond$) and DCM ($\times$) simulations with periodic boundary conditions. In both cases, the dimension of the reference cell is about $(10\mu m)^3$, the initial dislocation density is $10^{12}\ m^{-2}$ and the simulated specimen is deformed with a total imposed strain rate of $20\ s^{-1}$. The insets show thin foils extracted from the two simulations. One can check that the dislocation microstructures and the positions of the junctions at the end of the two simulations are nearly identical.

Figure 3 shows the results of DD and DCM simulations on a copper crystal with same loading conditions. In both cases the yield stress is exactly the one experimentally measured for a dislocation density of $10^{12}\ m^{-2}$ [20]. As a result of the small differences between PBCs in the two simulations (cf. Sec. 2.2), the two stress-strain curves slightly differ at low strains. This, actually, results from the truncation of the long-range stresses in the DD simulations. Beyond the yield stress, these differences vanish and the very good agreement between the two computations is interpreted as follows. In fcc crystals, long range interactions do not significantly contribute to the flow stress. The latter is controlled by the dislocation line tension and the numerous dislocation reactions taking place at the intersections between active slip planes.

This well-known result is illustrated in Fig. 3 by two thin foils extracted from the two simulated stress-strain curves at the same strain value. The same junctions are found at the same places in the two simulated microstructures and one has to look closely to find differences in the detail. From this result, we conclude that the local stress correction discussed in Sec. 2-1 is efficient and allows reproducing in the DCM the short-range interactions of dislocations, i.e., essentially the zipping and unzipping of junctions and dipoles. In addition, we verify that the energetic and dynamic aspects of the DCM are now consistent with their equivalents in DD simulations.

4. LONGITUDINAL TENSILE TEST IN Al_2O_3/Al

4.1 Simulation Conditions

In the present study, an Al matrix with infinitely long Al_2O_3 fibers is considered as a generic model for MMCs with long reinforcements. The mechanical properties for this composite are well documented in the literature [3], which allows performing direct comparisons with experiment. To be consistent with the dislocation microstructures generated during the processing of such MMCs, the initial dislocation density is set, in all cases, to the rather large value of $\rho_0 \approx 0.7\ 10^{14}\ m^{-2}$. Three different volume fractions of fibers are investigated, 5%, 20% and 45%, with respective fiber cross-sections of $(0.274 \times 0.274)\ \mu m^2$, $(0.547 \times 0.547)\ \mu m^2$ and $(0.828 \times 0.828)\ \mu m^2$. The distances between the centers of the fibers is constant and equal $1.29\ \mu m$, in order to check the possible occurrence of size effects. As most of the existing analyses of experimental results make use of isotropic elasticity, two isotropic matrices of elastic constants are used in the FE part of the DCM. The Young's moduli and Poisson's ratio for the two phases are, respectively, E_{Al} = 71.3 GPa, $E_{Al_2O_3}$ = 373 GPa, $\nu_{Al} = 0.347$ and $\nu_{Al_2O_3} = 0.235$.

4.2 Results

In a first step, the simulation results are compared with the simple rule of mixtures, which assimilates the material to a composition in series of two elastic phases stressed in uniaxial tension. Hence, along the tensile axis:

$$\sigma = E\varepsilon \quad \text{and} \quad E = E_{Al_2O_3}V + E_{Al}(1-V) \tag{4}$$

where V is the volume fraction of fibers.

The composite behavior, as reproduced by the simulation, is in very good agreement with experiment on the same material [1, 3]. As shown in Fig. 4,

the composite material deformed in the longitudinal direction and with a large volume fraction of fibers deforms quasi-elastically. The rule of mixtures then provides a reasonable prediction of the stress-strain dependency. A smooth deviation from the purely elastic prediction is nevertheless recorded, even at very small strains. Such behavior, viz. the absence of an initial elastic stage, is commonly observed experimentally in Al_2O_3/Al composites. In the present case, the Al matrix is soft, as it has the mechanical properties of a pure single crystal; thus, it starts plastically deforming at rather low applied stresses. As expected, this phenomenon manifests itself all the more as the volume fraction of fibers decreases.

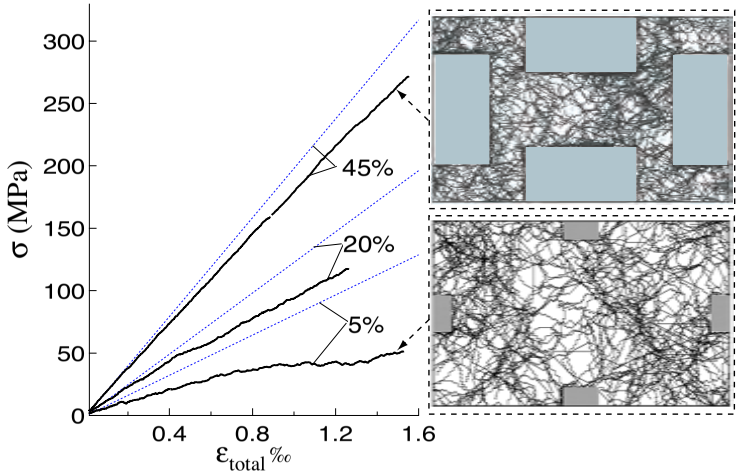

Figure 4. Longitudinal tensile stress-strain curves for Al_2O_3/Al MMCs with different fiber dimensions in a simulation cell of constant size. The volume fraction of fibers is V = 5%, 20% and 45%. The dotted lines refer to elastic predictions from the rule of mixtures. The two simulated microstructures show [001] views of the composites parallel to the fiber axis at a strain $\varepsilon = 0.15\%$. The dislocation density is about $1.35\ 10^{14}\ m^{-2}$ for $V = 5\%$ and $1.7\ 10^{14}\ m^{-2}$ for $V = 45\%$. Notice the early departure from elastic behavior for the smallest volume fraction.

When plastic deformation proceeds in the matrix, the dislocation density rapidly increases and a microstructure is formed, which contains many junctions (Fig. 4). The observed persistence of junctions at all the investigated strains is an indirect proof that the stresses developed in the matrix are still compatible with a mechanism of forest hardening. This result is again in agreement with experimental observation [1]. Nevertheless, as illustrated by Fig. 4, the differences in microstructure arrangement and dislocation density between

the two volume fractions $V = 5\%$ and $V = 45\%$ strongly suggest that there is an additional hardening process. By lack of space, the analysis of this effect, which is actually size-dependent, is postponed to a future publication where the in-situ properties of the Al matrix will be investigated in full detail.

Finally, a careful observation of the simulation output reveals the progressive accumulation of a large dislocation density at the interfaces between the fibers and the matrix. In contrast with 2D simulations results, however, no pile-up of dislocation loops is formed around the fibers. This result can be explained in simple terms. In a 3D MMC structure, the dislocations can by-pass the fibers by an Orowan process, irrespective of the volume fraction, whereas this process cannot be accounted for in two dimensions. Hence, if the mean free-path of the dislocations is large enough, a large amount of plastic strain can be produced by each dislocation loop and the sources are much less active in 3D than in 2D. This is why in multi-slip conditions, but also in single slip conditions too, the probability for finding at the interfaces dislocations emitted in the same plane by a dislocation source is rather low.

5. CONCLUDING REMARKS

An improvement to the DCM is proposed and tested, which gives access to "massive" simulations of dislocation dynamics accounting for complex boundary value problems. The comparison between conventional DD simulations and the DCM in the case of pure fcc single crystals shows that the interactions of the dislocations at short distances, and especially their reactions, are now quantitatively reproduced.

The first original calculations of this improved version of the DCM have been dedicated to the study of a MMC. It was checked that the DCM, which is a parameter-free simulation, reproduces well the tensile properties of Al_2O_3/Al composites in the longitudinal direction. A simple comparison of 2D and 3D simulation results makes it clear that the hardening processes involved in MMCs are, in essence, three-dimensional.

This first study allows considering many future developments, which, globally, aim at discriminating between dislocation or metallurgical effects and mechanical effects through a coupled analysis of the simulated microstructures and of the stress and displacement fields. A detailed in situ investigation of the strain hardening of the aluminum matrix is under way. Since, however, the stress-strain behavior of Al_2O_3/Al composites deformed along the fiber direction is mainly elastic, size effects can more conveniently be examined by straining along the transverse direction. Lastly, experimental studies suggest the existence of a significant Baushinger effect. Its examination by the DCM could be of interest with reference to kinematic hardening in MMCs.

References

[1] J.A. Isaacs and A. Mortensen. *Metall. Trans. A*, 23A:1207-1219, 1992.

[2] C.-W. Nan and D.R. Clarke. *Acta mater.*, 44:3801-3811, 1996.

[3] P. Bystricky, H. Bjerregard, and A. Mortensen. *Metall. and Mater. Trans. A*, 30A:1843-1866, 1999.

[4] J.L. Bassani, A. Needleman, and E. Van der Giessen. *Int. J. Sol. Struct.*, 38:833-853, 2001.

[5] S. Yefimov, I. Groma, and E. Van der Giessen. *J. Phys. IV France*, 11:103-110, 2001.

[6] E. Bittencourt, A. Needleman, M.E. Gurtin, and E. Van der Giessen. *J. Mech. Phys. Solids*, 51:281-310, 2003.

[7] H.H.M. Cleveringa, E. van der Giessen, and A Needleman. *Acta mater.*, 45:3163-3179, 1997.

[8] H. H. M. Cleveringa, E. van der Giessen, and A Needleman. *Phil. Mag. A*, 79:893-920, 1999.

[9] E. van der Giessen and A Needleman. *Model. Simul. Mater. Sci. Eng.*, 3:689-735, 1995.

[10] C. Lemarchand, B. Devincre, L. P. Kubin, and J. L. Chaboche. In V.V. Bulatov et al., eds., *Multiscale Modelling of Materials*, volume 538, pp. 63-68. MRS, Warrendale, PA, 1999.

[11] C. Lemarchand, B. Devincre, and L.P. Kubin. *J. Mech. Phys. Solids*, 49:1969, 2001.

[12] D. Weygand, E. Van der Giessen, and A. Needleman. *Mat. Sci. Eng.*, A309-310:420, 2001.

[13] H. Yasin, H.M. Zbib, and M.A. Khaleel. *Mat. Sci. Eng.*, A309-310: pp. 294-299, 2001.

[14] C.S. Shin, M.C. Fivel, and K.H. Oh. In S. Forest et al., editor, *Scale Transitions from Atomistics to Continuum Plasticity*, vol. 11, p. 27, 2001.

[15] B. Devincre, A. Roos, and S. Groh. In A.. Finel et al., eds., *Thermodynamics, Microstructures and Plasticity*, NATO SCIENCE SERIES: II: Mathematics, Physics and Chemistry: Vol. 108, Kluwer Academic Publishers, The Netherlands, 2003.

[16] T. Mura. *Micromechanics of defects in Solids*. Kluwer Academic Publishers, Dordrecht, Netherlands, 1993.

[17] S. Groh, B. Devincre, L.P. Kubin, A. Roos, F. Feyel, and J.-L. Chaboche. *Phil. Mag. Lett.*, 83:303-313, 2003.

[18] R. Bullough and A.J.E. Foreman. *Phil. Mag.*, 9:315-329, 1964.

[19] R. Madec, B. Devincre, and L.P. Kubin. *This volume*.

[20] R. Madec, B. Devincre, and L.P. Kubin. *Phys. Rev. Lett.*, 89: 255508, 2002.

Bibliographie

[1] V. V. Bulatov and L. P. Kubin. Dislocation modeling at atomistic and mesoscopic scales. *Current Opinion in Sol. Stat. and Mat. Sci.*, 3 :558, 1998.

[2] A. Needleman. Computational mechanics at the mesoscale. *Acta mater.*, 48 :105–124, 2000.

[3] T. Diaz de la Rubia and V. Bulatov. Materials research by means of multiscale computer simulations. *MRS Bulletin*, 26(3) :169–170, 2001.

[4] D. Walgraef and E.I. Aifantis. Dislocation patterning in fatigued metals as a result of dynamical instabilities. *J. Appl. Phys.*, 58 :688, 1985.

[5] C. Schiller and D. Walgraef. Numerical simulation of persistent slip band formation. *Acta metall.*, 36 : 563, 1988.

[6] J. Kratochvil and M. Saxlova. Sweeping mechanism of dislocation pattern formation. *Scripta met.*, 26 (113), 1992.

[7] A. Franek, R. Kalus, and J. Kratochvil. Model of early stage of dislocation structure formation in cyclically deformed metal crystals. *Phil. Mag. A*, 64 :497, 1991.

[8] P. Hähner and M. Zaiser. From mesoscopic heterogeneity of slip to macroscopic fluctuations of stress and strain. *Acta Mater.*, 45 :1067–1075, 1997.

[9] M. Zaiser, K. Bay, and P. Hähner. Fractal analysis of deformation-induced dislocation patterns. *Acta Mater.*, 47(47) :2463–2476, 1999.

[10] A. El-Azab. Statistical mechanics treatment of the evolution of dislocation distributions in crystals. *Phys. Rev. B*, 61 :11956—11966, 2000.

[11] I. Groma and B. Bako. Dislocation patterning : from micro- to mesoscale description. *Phys. Rev. Lett.*, 84(7) :1487–1490, 2000.

[12] M. Zaiser, M.-Carmen Miguel, and I. Groma. Statistical dynamics of dislocation systems : The influence of dislocation-dislocation correlations. *Phys. Rev. B*, 64 :224102, 2001.

[13] N.A. Fleck, G.M. Muller, M.F. Ashby, and J.W. Hutchinson. Strain gradient plasticity : Theory and experiment. *Acta metall. mater.*, 42 :475–487, 1994.

[14] Y. Estrin. Unified constitutive laws of plastic deformation. In A.S. Krauss and K. Krauss, editors, *Dislocation-density-related constitutive modeling*, pages 69–105. Academic Press, 1996.

[15] J.L. Bassani, A. Needleman, and E. Van der Giessen. Plastic flow in a composite : a comparison of nonlocal continuum and discrete dislocation predictions. *International Journal of Solids and Structures*, 38 :833–853, 2001.

[16] H. Mughrabi and T. Ungar. Long-range internal stresses in deformed single-phase materials : The composite model and its consequences. In F.R.N. Nabarro and M.S. Duesbery, editors, *Dislocations in Solids*, volume 11, chapter 60, pages 343–411. Elsevier Science B.V., Amsterdam, 2002.

[17] L.M. Brown. The self-stress of dislocations and the shape of extended nodes. *Phil. Mag.*, 10 :441–466, 1964.

[18] A. J. E. Foreman. The bowing of a dislocation segment. *Phil. Mag.*, 15 :1011–1021, 1967.

[19] D. Bacon. A method for describing a flexible dislocation. *Phys. Stat. Sol.*, 23 :527, 1967.

[20] D. Bacon, D.M. Barnett, and R.O. Scattergood. Anisotropic continuum theory of lattice defects. *Progress in Materials Science*, 23 :51, 1979.

[21] J. P. Hirth and J. Lothe. *Theory of Dislocations*. MacGraw-Hill, New York, 1982.

[22] B. Devincre. Three dimensional stress field expressions for straight dislocation segments. *Solid State Communications*, 93 :875, 1995.

[23] N. M. Ghoniem, S.H. Tong, and L. Z. Sun. Parametric dislocation dynamics : A thermodynamics-based approach to investigations of mesoscopic plastic deformation. *Phys. Rev. B*, 139(2) :913–927, 2000.

[24] M. Rhee, J.S. Stolken, V.V. Bulatov, T. Diaz de la Rubia, N. Zbib, and J.P. Hirth. Dislocation stress fields for dynamic codes using anisotropic elasticity : methodology and analysis. *Mater. Sci. Eng. A*, 309-310 :288–293, 2001.

[25] C. Lemarchand, B. Devincre, and L.P. Kubin. Homogenization method for a discrete-continuum simulation of dislocation dynamics. *J. Mech. Phys. Solids*, 49 :1969, 2001.

[26] H.M. Zbib, M. Rhee, and J.P. Hirth. On plastic deformation and the dynamics of 3D dislocations. *Int. J. Mech. Sci.*, 40 :113–127, 1998.

[27] K.W. Schwarz. Simulation of dislocations on the mesoscopic scale : I methods and examples and examples. *J. Appl. Phys.*, 1999.

[28] R. V. Kukta and L. B. Freund. 3-D numerical simulation of interacting dislocations in a strained epitaxial surface layer. *Mat. Res. Soc. Symp. Proc.*, 538 :99–105, 1999.

[29] O. Politano and J. M. Salazar. A 3D mesoscopic approach for discrete dislocation dynamics. *Mater. Sci. Eng. A*, 309-310 :261–264, 2001.

[30] B. Devincre and M. Condat. Model validation of a 3d simulation of dislocation dynamics : discretization and line tension effects. *Acta metall. mater.*, 40 :2629–2637, 1992.

[31] T.A. Khraishi, J.P. Hirth, H.M. Zbib, and T. Diaz de la Rubia. The stress field of a general circular Volterra dislocation loop : analytical and numerical approaches. *Phil. Mag. Letters*, 80(2) :95–105, 2000.

[32] L.P. Kubin, G. Canova, M. Condat, B. Devincre, V. Pontikis, and Y. Bréchet. Dislocation microstructures and plastic flow : A 3D simulation. *Solid State Phenom.*, 23-24 :455–472, 1992.

[33] M. Fivel, M. Verdier, and G. R. Canova. 3D simulation of a nanoindentation test at a mesoscopic scale. *Mater. Sci. Eng.*, A234-236 :923–926, 1997.

[34] A. Moulin, M. Condat, and L. P. Kubin. Simulation of Frank – Read sources in silicon. *Acta mater.*, 45 :2339–2348, 1997.

[35] M. Tang, L. P. Kubin, and G. R. Canova. Dislocation mobility and the mechanical response of bbc single crystals : a mesoscopic approach. *Acta mater.*, 46 :3221, 1998.

[36] R. Madec, B. Devincre, and L.P. Kubin. New line model for optimized dislocation dynamics simulations. In *Mat. Res. Soc. Symp. Proc. Vol 653*, page Z1.8.1. Materials Research Society, 2001.

[37] S. Groh, B. Devincre, F. Feyel, L.P. Kubin, A. Roos, and J.-L. Chaboche. Discrete-continuum modeling of metal matrix composites plasticity. In H. Kitagawa and Y. Shibutani, editors, *IUTAM Symposium on Mesoscopic Dynamics of Fracture Process and Materials Strength*, volume 115 of *Solid Mechanics and its Applications*. Kluwer Academic Publishers, NL-Dordrecht, 2004.

[38] B. Devincre and S. Roberts. 3-D simulation of dislocations-crack interactions in bcc metals at the mesoscopic scale. *Acta metall.*, 74 :2891, 1996.

[39] R. Phillips. *Crystals, Defects and Microstructures*. Cambridge University Press, 2001.

[40] T. Mura. *Micromechanics of defects in Solids*. Kluwer Academic Publishers, Dordrecht, the Netherlands, 1993.

[41] J. Friedel. *Dislocations*. Oxford, Pergamon press., 1964.

[42] A. J. E. Foreman and M.J. Makin. Dislocation motion through random arrays of obstacles. *Phil. Mag.*, 14 :911–924, 1966.

[43] L.M. Brown and R.K. Ham. Dislocation-particle interactions. In A. Kelly and R.B. Nicholson, editors, *Strengthening Methods in Solids*, chapter 2, pages 9–135. Applied Science Publishers, Barking, Essex (UK), 1971.

[44] D. Gomez-Garcia, B. Devincre, and L. P. Kubin. Dislocation dynamics in confined geometry. *J. Comp. Aided Mat. Design*, 6 :157–164, 1999.

[45] L. Dupuy and M.C. Fivel. A study of dislocation junctions in fcc metals by an orientation dependent line tension model. *Acta mater.*, 50 :4873–4885, 2002.

[46] K. W. Schwarz. Local rules for approximating strong dislocation interactions in discrete dislocation dynamics. *Modelling Simul. Mater. Sci. Eng.*, 115 :609–625, 2003.

[47] B. Devincre. *Simulation de la dynamique des dislocations à une echelle mesoscopique*. PhD thesis, Université Paris XI, Orsay, 1994.

[48] R. Madec. *Des interactions entre dislocations à la plasticité du monocristal cfc ; une étude par dynamique des dislocations*. PhD thesis, Université Paris XI Orsay, 2001.

[49] D. Weygand, E. Van der Giessen, and A. Needleman. Discrete dislocation modeling in 3D confined volumes. *Mat. Sci. Eng.*, A309-310 :420, 2001.

[50] W.T. Read. *Dislocations in Crystals*. McGraw-Hill, New York, 1992.

[51] W. Cai, V. V. Bulatov, J. Chang, J. Li, and S. Yip. Anisotropic elastic interactions of a periodic dislocation array. *Phys. Rev. Lett.*, 86(25) :5727–5730, 2001.

[52] J. Douin, P. Veyssière, and P. Beauchamp. Dilsocation line stability in Ni3Al. *Phil. Mag. A*, 54(3) : 375–393, 1986.

[53] S. Groh. *Simulation de la plasticité des matériaux cristallins par le modèle discret-continu*. PhD thesis, Université Paris-Sud Orsay, 2003.

[54] M. Fivel and A. El-Azab. Linking continuum mechanics and 3D discrete dislocation simulations. *J. de Phys IV*, 9 :278, 1999.

[55] J. Lepinoux and L. P. Kubin. The dynamic organization of dislocation structures : A simulation. *Scripta met.*, 21 :833, 1987.

[56] N. M. Ghoniem and R. J. Amodeo. Dislocation dynamics. i. a proposed methodology for deformation micromechanics. *Phys. Rev. B*, 41 :6958, 1989.

[57] A.N. Gulluoglu, D.J. Srolovitz, R. LeSar, and P.S. Lomdahl. Dislocations distributions in two dimensions. *Scripta met.*, 23 :1347, 1989.

[58] D. Gomez-Garcia, B. Devincre, and L. P. Kubin. Forest hardening and boundary conditions in 2D simulations of dislocations dynamics. In Robertson et al., editor, *Multiscale Phenomena in materials-experiments and modeling*, volume 578, pages 131–136. MRS, Warrendale, Pennsylvania, 2000.

[59] V. V. Bulatov, M. Rhee, and W. Cai. Periodic boundary conditions for dislocation dynamics simulations in three dimensions. In *Mat. Res. Soc. Symp. Proc.*, volume 653, page Z1.3.1, 2001.

[60] R. Madec, B. Devincre, and L.P. Kubin. On the use of periodic boundary conditions in dislocation dynamics simulations. In H. Kitagawa and Y. Shibutani, editors, *IUTAM Symposium on Mesoscopic Dynamics of Fracture Process and Materials Strength*, volume 115 of *Solid Mechanics and its Applications*, pages 35–44. Kluwer Academic Publishers, NL-Dordrecht, 2004.

[61] L. Greengard and V. Rokhlin. A fast algorithms for particle simulations. *J. Comput. Phys.*, 73 :325–348, 1987.

[62] L. Greengard. Fast algorithms for classical physics. *Science*, 265 :909–914, 1994.

[63] R. LeSar and J.M. Rickman. Multipole expansion of dislocation interactions : Application to discrete dislocations. *Phys. Rev. B*, page 144110, 2002.

[64] Z. Wang, N. M. Ghoniem, and R. Lesar. Multipole representation of the elastic field of dislocation ensembles. *Phys. Rev. B*, 69 :174102, 2004.

[65] W. Cai, V. V. Bulatov, T.G. Pierce, M. Hiratani, M. Rhee, M. Bartelt, and M. Tang. Massively-parallel dislocation dynamics simulations. In K. Kitawaga and Y. Shibutani, editors, *Mesoscopic Dynamics of fracture process and materials strength*, pages 1–11. Kluwer Academic Publishers, 2004.

[66] C.S. Shin. *3D discrete dislocation dynamics applied to dislocation-precipitate interactions.* PhD thesis, INPG, 2004.

[67] E. van der Giessen and A. Needleman. Discrete dislocation plasticity : a simple planar model. *Modelling Simul. Mater. Sci. Eng.*, 3 :689–735, 1995.

[68] J. Christiansen, K. Morgenstern, J. Schiotz, K. Jacobsen, K.-F. Braun, K.-H. Rieder, E. Laegsgaard, and F. Besenbacher. Atomic-scale structure of dislocations revealed by scanning tunneling microscopy and molecular dynamics. *Phys. Rev. Lett.*, 88(20) :206106, 2002.

[69] P.M. Hazzledine, H.P. Karnthaler, and E. Wintner. Non-parallel dissociation of dislocations in thin films. *Phil. Mag. A*, 31 :81–97, 1975.

[70] X. H. Liu, F. M. Ross, and K. W. Schwarz. Dislocated epitaxial islands. *Phys. Rev. Lett.*, 85(19) : 4088–4091, 2000.

[71] M. de Koning, R. Miller, V. V. Bulatov, and F. F. Abraham. Modelling grain-boundary resistance in intergranular dislocation slip transmission. *Phil. Mag. A*, 82(13) :2511–2527, 2002.

[72] M. de Koning, R. J. Kurtz, V. V. Bulatov, C. H. Henager Jr, R.G. Hoagland, W. Cai, and M. Nomura. Modeling of dislocation–grain boundary interactions in fcc metals. *Journal of Nuclear Materials*, 323 : 281–310, 2003.

[73] D. Chidambarrao, X. H. Liu, and K. W. Schwarz. Combined dislocation and process modeling for local oxidation of silicon structure. *J. Appl. Phys.*, 92(10) :6278–6286, 2002.

[74] M. Verdier, M. Fivel, and I. Groma. Plasticity in fine scale semi-coherent metallic films and multilayers. *Scripta met.*, 50 :769–773, 2004.

[75] M. C. Fivel, T. J. Gosling, and G. R. Canova. Implementing image stresses in a 3D dislocation simulation. *Modelling Simul. Mater. Sci. Eng.*, 4 :581, 1996.

[76] A. Hartmaier, M.C. Fivel, G. R. Canova, and Gumbsch P. Image stresses in a free-standing thin film. *Modelling Simul. Mater. Sci. Eng.*, 795 :781–794, 1999.

[77] T.A. Khraishi, H.M. Zbib, and T. Diaz de la Rubia. The treatment of traction-free boundary conditions in three-dimensional dislocation dynamics using generalized image stress analysis. *Mater. Sci. Eng.*, A309-310 :283–287, 2001.

[78] T.A. Khraishi and H.M. Zbib. Dislocation dynamics simulations of the interaction between a short rigid fiber and a glide circular dislocation pile-up. *Computational Materials Science*, 24 :310–322, 2002.

[79] L. Yan, T.A. Khraishi, Y.-L. Shen, and M.F. Horstemeyer. A distributed-dislocation method for treating free-surface image stresses in three-dimensional dislocation dynamics simulations. *Modelling Simul. Mater. Sci. Eng.*, XX :S289–S301, 2004.

[80] H.H.M. Cleveringa, E. van der Giessen, and A Needleman. Comparison of discrete dislocation and continuum plasticity predictions for a composite material. *Acta mater.*, 45 :3163–3179, 1997.

[81] V.S. Deshpande, A Needleman, and E. van der Giessen. Discrete dislocation modeling of fatigue crack propagation. *Acta mater.*, 50 :831–846, 2002.

[82] H. H. M. Cleveringa, E. van der Giessen, and A Needleman. A discrete dislocation analysis of residual stresses in a composite material. *Phil. Mag. A*, 79(4) :893–920, 1999.

[83] M. Fivel, C. F. Robertson, G. R. Canova, and L. Boulanger. 3-D modeling of indent-induced plastic zone at a mesoscale. *Acta mater.*, 46 :6183–6194, 1998.

[84] M. Fivel and G. R. Canova. Developing rigourous boundary conditions to simulations of discrete dislocation dynamics. *Modelling Simul. Mater. Sci. Eng.*, 7 :753–768, 1999.

[85] C.S. Shin, M.C. Fivel, and K.H. Oh. Nucleation and propagation of dislocations near a precipitate using 3d discrete dislocation dynamics simulations. In S. Forest, E. Van der Giessen, and L. Kubin, editors, *Scale Transitions from Atomistics to Continuum Plasticity*, volume 11, page 27, 2001.

[86] D. Weygand, L. H. Friedman, and E. van der Giessen. Aspect of boundary-value problem solutions with 3D dislocation dynamics. *Modelling Simul. Mater. Sci. Eng.*, 10 :437–468, 2002.

[87] H. Yasin, H.M. Zbib, and M.A. Khaleel. Size and boundary effects in discrete dislocation dynamics : coupling with continuum finite element. *Mat. Sci. Eng.*, A309-310 :294–299, 2001.

[88] R. Martinez and N. M. Ghoniem. The infuence of crystal surfaces on dislocation interactions in mesoscopic plasticity : A combined dislocation dynamics - finite element approach. *J. Comp. Meth. Engr. Science*, 3, 2002.

[89] C. Lemarchand, B. Devincre, L. P. Kubin, and J. L. Chaboche. Coupled meso-macro simulations of plasticity : Validation tests. In V. Bulatov, T. Diaz de la Rubia, T. Phillips, R. andKaxiras, and N. Ghoniem, editors, *Multiscale Modelling of Materials*, volume 538, pages 63–68. MRS, Warrendale, Pennsylvania, 1999.

[90] B. Devincre, A. Roos, and S. Groh. Boundary problems in DD simulations. In A. Finel, D. Mazière, and M. Véron, editors, *Thermodynamics, Microstructures and Plasticity*, pages 275–284, Dordrecht, 2003. NATO Science Series, Kluwer Academic Publishers.

[91] V.I. Alshits and V.L. Indenbom. Mechanisms of dislocation drag. In F.R.N. Nabarro, editor, *Dislocations in Solids*, volume 6, chapter 34, pages 43–111. Elsevier Science B.V., Amsterdam, 1986.

[92] K.D. Fusenig and Nembach E. Dynamic dislocation effects in precipitation hardened materials. *Acta metall. mater.*, 41 :3181–3189, 1993.

[93] D. Mordehai, Y. Ashkenazy, I. Kelson, and G. Makov. Dynamic properties of screw dislocations in Cu : A molecular dynamics study. *Phys. Rev. B*, 67 :024112–1–9, 2003.

[94] E. Bitzek, D. Weygand, and Gumbsch P. Atomistic study of edge dislocations in fcc metals : Drag and inertial effects. In H. Kitagawa and Y. Shibutani, editors, *IUTAM Symposium on Mesoscopic Dynamics of Fracture Process and Materials Strength*, volume 115 of *Solid Mechanics and its Applications*, pages 45–57. Kluwer Academic Publishers, NL-Dordrecht, 2004.

[95] A. Granato and K. Lücke. Application of dislocation theory to internal friction phenomena at high frequency. *J. Appl. Phys.*, 27 :789–805, 1956.

[96] R. V. Kukta. *Observations on the Kinetics of Relaxation in Epitaxial Films Grown on Conventional and Compliant Substrates A Continuum Simulation of Dislocation Glide Near an Interface*. PhD thesis, Brown University, 1998.

[97] G. Saada. Sur le durcissement dû à la recombinaison des dislocations. *Acta Metall.*, 8 :841–847, 1960.

[98] V. V. Bulatov, F. F. Abraham, L. P. Kubin, B. Devincre, and S. Yip. Connecting atomistic and mesoscale simulations of crystal plasticity. *Nature*, 391 :669–672, 1998.

[99] D. Rodney and R. Phillips. Structure and strength of dislocation junctions : An atomic level analysis. *Phys. Rev. Lett.*, 82 :1704–1707, 1999.

[100] V. B. Shenoy, R. V. Kukta, and R. Phillips. Mesoscopic analysis of structure and strength of dislocation junctions in fcc metals. *Phys. Rev. Lett.*, 84 :1491–1494, 2000.

[101] L. K. Wickham, K. W. Schwarz, and J. S. Stölken. Rules for forest interactions between dislocations. *Phys. Rev. Lett.*, 83 :4574–4577, 1999.

[102] R. Madec, B. Devincre, and L.P. Kubin. On the nature of attractive dislocation crossed states. *Computational Materials Science*, 23 :219–224, 2002.

[103] B. Devincre. Mesco-scale simulation of the dislocation dynamics. In H. O. Kirchner, V. Pontikis, and L. P. Kubin, editors, *Computer Simulation in Materials Science*, pages 309–323. Kluwer Academic Publishers, Amsterdam, North-Holland, 1996.

[104] W. Püschl. Models for dislocation cross-slip in close-packed crystal structures : a critical review. *Progress in Materials Science*, 47 :415–461, 2002.

[105] D. Caillard and J.-L. Martin. *Thermally Activated Mechanisms in Crystal Plasticity*. Pergamon Materials Series. Pergamon (Elsevier), Amsterdam, 2003.

[106] B. Escaig. L'activation thermique des déviations sous faibles contraintes dans les structures h.c. et c.c. *Phys. Stat. Sol.*, 28 :461–473, 1968.

[107] B. Escaig. Sur le glissement dévié des dislocations dans la structure cubique à faces centrées. *J. Physique*, 29 :225–239, 1968.

[108] J. Friedel. Regarding Seeger's paper on work hardening. In *Dislocations and Mechanical Properties of Crystals*, page 330, New York, 1957. J. Wiley and Sons.

[109] G. Saada. Cross-slip and work hardening of f.c.c. crystals. *Mat. Sci. Eng. A*, 137 :177–183, 1991.

[110] M.S. Duesbery, N.P. Louat, and K. Sadananda. The mechanics and energetics of cross-slip. *Acta Metall. Mater.*, 40 :149–158, 1992.

[111] J. Bonneville and B. Escaig. Cross-slipping process and the stress-orientation dependence in pure copper. *Acta Metall.*, 27 :1477–1486, 1979.

[112] U. Essmann and H. Mughrabi. Annihilation of dislocations during tensile and cyclic deformation and limits of dislocation densities. *Phil. Mag. A*, 40 :731–756, 1979.

[113] T. Vegge and K.W. Jacobsen. Atomistic simulations of dislocation processes in copper. *J. Phys. : Condens. Matter*, 14 :2929–2956, 2002.

[114] T. Vegge, T. Rasmussen, T. Leffers, O.B. Pedersen, and K.W. Jacobsen. Atomistic simulations of cross-slip of jogged screw dislocations in copper. *Phil. Mag. Lett.*, 81 :137–144, 2001b.

[115] T. Rasmussen, K.W. Jacobsen, T. Leffers, and O.B. Pedersen. Simulations of the atomic structure, energetics and cross-slip of screw dislocations in copper. *Phys. Rev. B*, 56 :2977–2990, 1997b.

[116] J. Bonneville, B. Escaig, and J.L. Martin. A study of cross-slip activation parameters in copper. *Acta Metall.*, 36 :1989–2002, 1988.

[117] A. Moulin, M. Condat, and L. P. Kubin. Perfect and partial Frank − Read sources in silicon. *Phil. Mag. A*, 79 :1995–2011, 1999.

[118] C.S. Shin, M. Fivel, D. Rodney, V. B. Phillips, R. Shenoy, and L. Dupuy. Formation and strength of dislocation junctions in fcc metals. *J. Phys. IV*, 11(5) :19–26, 2001.

[119] J.P. Chateau, D. Delafosse, and T. Magnin. Numerical simulations of hydrogen-dislocation interactions in fcc stainless steels : Part I. *Acta mater.*, 50 :1507–1522, 2002.

[120] W. Cai and V. V. Bulatov. Mobility laws in dislocation dynamics simulations. *Mat. Sci. Eng.*, A387–389 : 277—281, 2004.

[121] J. Godet, L. Pizzagalli, S. Brochard, and P. Beauchamp. Theoretical study of dislocation nucleation from simple surface defects in semiconductors. *Phys. Rev. B*, 70 :054109(1–8), 2004.

[122] A.P. Sutton and R.W. Balluffi. *Interfaces in Crystalline Materials*. Monographs on the physics and chemistry of materials. Clarendon Press, Oxford, 1996.

[123] K.J. Van Vliet, T. Li, J.and Zhu, S. Yip, and S. Suresh. Quantifying the early stages of plasticity through nanoscale experiments and simulations. *Phys. Rev. B*, 67 :104105–15, 2003.

[124] J. Weertman and J. Weertman. Moving dislocations. In F. R. N. Nabarro, editor, *Dislocations in Solids*, volume 3, pages 1–59. Amsterdam :North-Holland, 1980.

[125] P. Haasen. *Physical Metallurgy*. Cambridge University Press, 1996.

[126] P. Haasen. Solution hardening in f.c.c. metals. In F.R.N. Nabarro, editor, *Dislocations in Metallurgy*, volume 4 of *Dislocations in Solids*, pages 155–189. North-Holland, Amsterdam, 1979.

[127] H. Suzuki. Solution hardening in body-centred cubic alloys. In F.R.N. Nabarro, editor, *Dislocations in Metallurgy*, volume 4, pages 191–217. North-Holland, Amsterdam, 1979.

[128] H. Neuhäuser and Ch. Schwink. Solid solution strengthening. In H. Mughrabi, editor, *Plastic Deformation and Fracture of Materials*, volume 6 of *Materials Science and Technology*, chapter 5, pages 191–250. VCH, Weinheim (FRG), 1993.

[129] V. Gerold. Precipitation hardening. In F.R.N. Nabarro, editor, *Dislocations in Metallurgy*, volume 4, pages 219–260. North-Holland, Amsterdam, 1979.

[130] E. Nembach. *Particle Strengthening of Metals and Alloys*. John Wiley and Sons, New York, 1996.

[131] J.W. Martin. *Precipitation Hardening*. Butterworth-Heinemann, Oxford, 1998.

[132] B. Legrand. Structure du coeur des dislocations vis dans le titane. *Phil. Mag. A*, 52 :83–97, 1985.

[133] J. Diehl. Zugverformung von kupfer-einkristallen. i. verfestigungskurven und oberflachenerscheinungen. *Z. Metallkde*, 47 :331–343, 1956.

[134] T. Takeuchi. Work hardening of copper single crystals with multiple glide orientations. *Trans. JIM*, 16 : 629–640, 1975.

[135] U.F. Kocks, A.S. Argon, and M.F. Ashby. *Thermodynamics and kinetics of slip*. Pergamon Press, 1975.

[136] U.F. Kocks and H. Mecking. Physics and phenomenology of strain hardening : the fcc case. *Progress in Materials Science*, 48 :171–273, 2003.

[137] C. Teodosiu, J.L. Raphanel, and L. Tabourot. Finite element simulation of the large elastoplastic deformation of multicrystals. In C. Teodosiu, J.L. Raphanel, and F. Sidoroff, editors, *Large Plastic Deformations*, pages 153–175, Rotterdam, 1993. A.A. Balkema.

[138] M. Fivel, L. Tabourot, E. Rauch, and G. R. Canova. Identification through mesoscopic simulations of macroscopic parameters of physically based constitutive equations for the plastic behaviour of fcc single crystals. *J. Phys. IV*, 8, 1998.

[139] T. Hoc, B. Devincre, and L.P. Kubin. Deformation stage i of fcc crystals : Constitutive modelling. In C. et al. Gundlach, editor, *Evolution of Deformation Microstructures in 3D*, pages 43–59, Roskilde, Denmark, 2004. RisøNational Laboratory.

[140] P. Ambrosi and C. Schwink. Slip line length of copper single crystals oriented along 100 and 111. *Scripta Metall.*, 12 :303–308, 1978.

[141] S.J. Basinski and Z.S. Basinski. Plastic deformation and work hardening. In F.R.N. Nabarro, editor, *Dislocations in Metallurgy*, volume 4 of *Dislocations in Solids*, chapter 16, pages 261–362. North-Holland, Amsterdam, 1979.

[142] T. Hoc, C. Rey, and J.L. Raphanel. Experimental and numerical analysis of localization during sequential test for if-ti steel. *Acta Mater.*, 49 :1385–1846, 2001.

[143] A. Franciosi, P. et Zaoui. Multislip in f.c.c. crystals a theoretical approach compared with experimental data. *Acta Metall.*, 30 :1627–1637, 1982.

[144] S.V. Raj and G.M. Pharr. A compilation and analysis of data for the stress dependence of the subgrain size. *Mat. Sci. Eng. A*, 81 :217–237, 1986.

[145] J. G. Sevillano. Flow stress and work hardening. In H. Mughrabi, editor, *Materials Science and Technology*, volume 6, page 19. Weinheim, VCH, 1993.

[146] A.E. Matthews, J.W. ; Blakeslee. Defects in epitaxial multilayers defects in epitaxial multilayers defects in epitaxial multilayers. *J. Cryst. Growth*, 27 :118, 1974.

[147] S.P. Baker, A. Kretschmann, and E. Arzt. Thermomechanical behavior of different texture components in cu thin films. *Acta mater.*, 49 :2145–2160, 2001.

[148] C. Woodward. First principles simulations of dislocation cores. *Mat. Sci. Eng. A, in press*, 2005.

[149] V. Vitek, M. Mrovec, and J. Bassani. Influence of non-glide stresses on plastic flow : from atomistic to continuum modeling. *Mater. Sci. Eng.*, A365 :31–37, 2004.

[150] L.P. Kubin, R. Madec, and B. Devincre. Dislocation intersections and reactions in fcc and bcc crystals. In H. Zbib, D. Lassila, L. Levine, and K. Hemker, editors, *Multiscale Phenomena in Materials-Experiments and Modeling Related to Mechanical Behavior*, volume 779 of *Mat. Res. Soc. Symp. Proc.*, page W1.6. MRS, Warrendale, Pennsylvania, 2003.

[151] M. Tang, Devincre B., and L.P. Kubin. Simulation and modelling of forest hardening in body centred cubic crystals at low temperature. *Model Simul. Mater. Sci. Eng.*, 7 :893–908, 1999.

[152] R. Madec, B. Devincre, and L.P. Kubin. Simulation of dislocation patterns in multislip. *Scripta Mat.*, 47 :689–695, 2002.